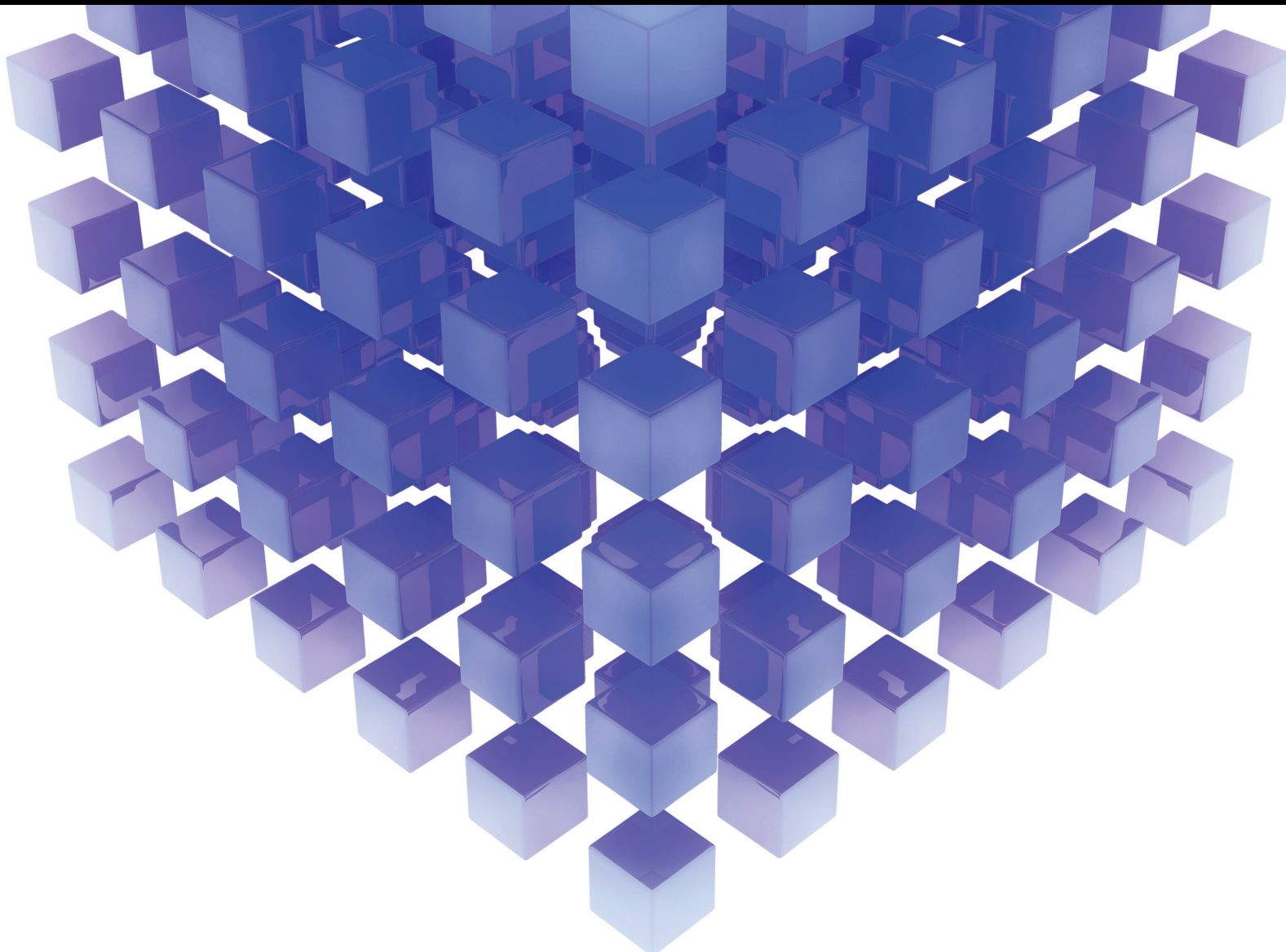


Mathematical Problems in Engineering

# Mathematical Problems in Failure Mechanism of Rock Mass under Water-Heat-Mechanical Coupling Environment

Lead Guest Editor: Fuqiang Ren

Guest Editors: Menglong Dong and Jinzhou Bai





---

**Mathematical Problems in Failure Mechanism  
of Rock Mass under Water-Heat-Mechanical  
Coupling Environment**

Mathematical Problems in Engineering

---

**Mathematical Problems in Failure  
Mechanism of Rock Mass under  
Water-Heat-Mechanical Coupling  
Environment**

Lead Guest Editor: Fuqiang Ren

Guest Editors: Menglong Dong and Jinzhou Bai



---

Copyright © 2023 Hindawi Limited. All rights reserved.

This is a special issue published in “Mathematical Problems in Engineering.” All articles are open access articles distributed under the Creative Commons Attribution License, which permits unrestricted use, distribution, and reproduction in any medium, provided the original work is properly cited.

# Chief Editor

Guangming Xie , China

## Academic Editors

Kumaravel A , India  
Waqas Abbasi, Pakistan  
Mohamed Abd El Aziz , Egypt  
Mahmoud Abdel-Aty , Egypt  
Mohammed S. Abdo, Yemen  
Mohammad Yaghoub Abdollahzadeh  
Jamalabadi , Republic of Korea  
Rahib Abiyev , Turkey  
Leonardo Acho , Spain  
Daniela Addessi , Italy  
Arooj Adeel , Pakistan  
Waleed Adel , Egypt  
Ramesh Agarwal , USA  
Francesco Aggogeri , Italy  
Ricardo Aguilar-Lopez , Mexico  
Afaq Ahmad , Pakistan  
Naveed Ahmed , Pakistan  
Elias Aifantis , USA  
Akif Akgul , Turkey  
Tareq Al-shami , Yemen  
Guido Ala, Italy  
Andrea Alaimo , Italy  
Reza Alam, USA  
Osamah Albahri , Malaysia  
Nicholas Alexander , United Kingdom  
Salvatore Alfonzetti, Italy  
Ghous Ali , Pakistan  
Nouman Ali , Pakistan  
Mohammad D. Aliyu , Canada  
Juan A. Almendral , Spain  
A.K. Alomari, Jordan  
José Domingo Álvarez , Spain  
Cláudio Alves , Portugal  
Juan P. Amezcua-Sanchez, Mexico  
Mukherjee Amitava, India  
Lionel Amodeo, France  
Sebastian Anita, Romania  
Costanza Arico , Italy  
Sabri Arik, Turkey  
Fausto Arpino , Italy  
Rashad Asharabi , Saudi Arabia  
Farhad Aslani , Australia  
Mohsen Asle Zaem , USA

Andrea Avanzini , Italy  
Richard I. Avery , USA  
Viktor Avrutin , Germany  
Mohammed A. Awadallah , Malaysia  
Francesco Aymerich , Italy  
Sajad Azizi , Belgium  
Michele Bacciocchi , Italy  
Seungik Baek , USA  
Khaled Bahlali, France  
M.V.A Raju Bahubalendruni, India  
Pedro Balaguer , Spain  
P. Balasubramaniam, India  
Stefan Balint , Romania  
Ines Tejado Balsera , Spain  
Alfonso Banos , Spain  
Jerzy Baranowski , Poland  
Tudor Barbu , Romania  
Andrzej Bartoszewicz , Poland  
Sergio Baselga , Spain  
S. Caglar Baslamisli , Turkey  
David Bassir , France  
Chiara Bedon , Italy  
Azeddine Beghdadi, France  
Andriette Bekker , South Africa  
Francisco Beltran-Carbajal , Mexico  
Abdellatif Ben Makhlof , Saudi Arabia  
Denis Benasciutti , Italy  
Ivano Benedetti , Italy  
Rosa M. Benito , Spain  
Elena Benvenuti , Italy  
Giovanni Berselli, Italy  
Michele Betti , Italy  
Pietro Bia , Italy  
Carlo Bianca , France  
Simone Bianco , Italy  
Vincenzo Bianco, Italy  
Vittorio Bianco, Italy  
David Bigaud , France  
Sardar Muhammad Bilal , Pakistan  
Antonio Bilotta , Italy  
Sylvio R. Bistafa, Brazil  
Chiara Boccaletti , Italy  
Rodolfo Bontempo , Italy  
Alberto Borboni , Italy  
Marco Bortolini, Italy

Paolo Boscariol, Italy  
Daniela Boso , Italy  
Guillermo Botella-Juan, Spain  
Abdesselem Boulkroune , Algeria  
Boulaïd Boulkroune, Belgium  
Fabio Bovenga , Italy  
Francesco Braghin , Italy  
Ricardo Branco, Portugal  
Julien Bruchon , France  
Matteo Bruggi , Italy  
Michele Brun , Italy  
Maria Elena Bruni, Italy  
Maria Angela Butturi , Italy  
Bartłomiej Błachowski , Poland  
Dhanamjayulu C , India  
Raquel Caballero-Águila , Spain  
Filippo Cacace , Italy  
Salvatore Caddemi , Italy  
Zuowei Cai , China  
Roberto Caldelli , Italy  
Francesco Cannizzaro , Italy  
Maosen Cao , China  
Ana Carpio, Spain  
Rodrigo Carvajal , Chile  
Caterina Casavola, Italy  
Sara Casciati, Italy  
Federica Caselli , Italy  
Carmen Castillo , Spain  
Inmaculada T. Castro , Spain  
Miguel Castro , Portugal  
Giuseppe Catalanotti , United Kingdom  
Alberto Cavallo , Italy  
Gabriele Cazzulani , Italy  
Fatih Vehbi Celebi, Turkey  
Miguel Cerrolaza , Venezuela  
Gregory Chagnon , France  
Ching-Ter Chang , Taiwan  
Kuei-Lun Chang , Taiwan  
Qing Chang , USA  
Xiaoheng Chang , China  
Prasenjit Chatterjee , Lithuania  
Kacem Chehdi, France  
Peter N. Cheimets, USA  
Chih-Chiang Chen , Taiwan  
He Chen , China

Kebing Chen , China  
Mengxin Chen , China  
Shyi-Ming Chen , Taiwan  
Xizhong Chen , Ireland  
Xue-Bo Chen , China  
Zhiwen Chen , China  
Qiang Cheng, USA  
Zeyang Cheng, China  
Luca Chiapponi , Italy  
Francisco Chicano , Spain  
Tirivanhu Chinyoka , South Africa  
Adrian Chmielewski , Poland  
Seongim Choi , USA  
Gautam Choubey , India  
Hung-Yuan Chung , Taiwan  
Yusheng Ci, China  
Simone Cinquemani , Italy  
Roberto G. Citarella , Italy  
Joaquim Ciurana , Spain  
John D. Clayton , USA  
Piero Colajanni , Italy  
Giuseppina Colicchio, Italy  
Vassilios Constantoudis , Greece  
Enrico Conte, Italy  
Alessandro Contento , USA  
Mario Cools , Belgium  
Gino Cortellessa, Italy  
Carlo Cosentino , Italy  
Paolo Crippa , Italy  
Erik Cuevas , Mexico  
Guozeng Cui , China  
Mehmet Cunkas , Turkey  
Giuseppe D'Aniello , Italy  
Peter Dabnichki, Australia  
Weizhong Dai , USA  
Zhifeng Dai , China  
Purushothaman Damodaran , USA  
Sergey Dashkovskiy, Germany  
Adiel T. De Almeida-Filho , Brazil  
Fabio De Angelis , Italy  
Samuele De Bartolo , Italy  
Stefano De Miranda , Italy  
Filippo De Monte , Italy

José António Fonseca De Oliveira  
Correia , Portugal  
Jose Renato De Sousa , Brazil  
Michael Defoort, France  
Alessandro Della Corte, Italy  
Laurent Dewasme , Belgium  
Sanku Dey , India  
Gianpaolo Di Bona , Italy  
Roberta Di Pace , Italy  
Francesca Di Puccio , Italy  
Ramón I. Diego , Spain  
Yannis Dimakopoulos , Greece  
Hasan Dinçer , Turkey  
José M. Domínguez , Spain  
Georgios Dounias, Greece  
Bo Du , China  
Emil Dumic, Croatia  
Madalina Dumitriu , United Kingdom  
Premraj Durairaj , India  
Saeed Eftekhari Azam, USA  
Said El Kafhali , Morocco  
Antonio Elipse , Spain  
R. Emre Erkmen, Canada  
John Escobar , Colombia  
Leandro F. F. Miguel , Brazil  
FRANCESCO FOTI , Italy  
Andrea L. Facci , Italy  
Shahla Faisal , Pakistan  
Giovanni Falsone , Italy  
Hua Fan, China  
Jianguang Fang, Australia  
Nicholas Fantuzzi , Italy  
Muhammad Shahid Farid , Pakistan  
Hamed Faruqi, Iran  
Yann Favennec, France  
Fiorenzo A. Fazzolari , United Kingdom  
Giuseppe Fedele , Italy  
Roberto Fedele , Italy  
Baowei Feng , China  
Mohammad Ferdows , Bangladesh  
Arturo J. Fernández , Spain  
Jesus M. Fernandez Oro, Spain  
Francesco Ferrise, Italy  
Eric Feulvarch , France  
Thierry Floquet, France

Eric Florentin , France  
Gerardo Flores, Mexico  
Antonio Forcina , Italy  
Alessandro Formisano, Italy  
Francesco Franco , Italy  
Elisa Francomano , Italy  
Juan Frausto-Solis, Mexico  
Shujun Fu , China  
Juan C. G. Prada , Spain  
HECTOR GOMEZ , Chile  
Matteo Gaeta , Italy  
Mauro Gaggero , Italy  
Zoran Gajic , USA  
Jaime Gallardo-Alvarado , Mexico  
Mosè Gallo , Italy  
Akemi Gálvez , Spain  
Maria L. Gandarias , Spain  
Hao Gao , Hong Kong  
Xingbao Gao , China  
Yan Gao , China  
Zhiwei Gao , United Kingdom  
Giovanni Garcea , Italy  
José García , Chile  
Harish Garg , India  
Alessandro Gasparetto , Italy  
Stylianos Georgantzinou, Greece  
Fotios Georgiades , India  
Parviz Ghadimi , Iran  
Ştefan Cristian Gherghina , Romania  
Georgios I. Giannopoulos , Greece  
Agathoklis Giaralis , United Kingdom  
Anna M. Gil-Lafuente , Spain  
Ivan Giorgio , Italy  
Gaetano Giunta , Luxembourg  
Jefferson L.M.A. Gomes , United Kingdom  
Emilio Gómez-Déniz , Spain  
Antonio M. Gonçalves de Lima , Brazil  
Qunxi Gong , China  
Chris Goodrich, USA  
Rama S. R. Gorla, USA  
Veena Goswami , India  
Xunjie Gou , Spain  
Jakub Grabski , Poland

Antoine Grall , France  
George A. Gravvanis , Greece  
Fabrizio Greco , Italy  
David Greiner , Spain  
Jason Gu , Canada  
Federico Guarracino , Italy  
Michele Guida , Italy  
Muhammet Gul , Turkey  
Dong-Sheng Guo , China  
Hu Guo , China  
Zhaoxia Guo, China  
Yusuf Gurefe, Turkey  
Salim HEDDAM , Algeria  
ABID HUSSANAN, China  
Quang Phuc Ha, Australia  
Li Haitao , China  
Petr Hájek , Czech Republic  
Mohamed Hamdy , Egypt  
Muhammad Hamid , United Kingdom  
Renke Han , United Kingdom  
Weimin Han , USA  
Xingsi Han, China  
Zhen-Lai Han , China  
Thomas Hanne , Switzerland  
Xinan Hao , China  
Mohammad A. Hariri-Ardebili , USA  
Khalid Hattaf , Morocco  
Defeng He , China  
Xiao-Qiao He, China  
Yanchao He, China  
Yu-Ling He , China  
Ramdane Hedjar , Saudi Arabia  
Jude Hemanth , India  
Reza Hemmati, Iran  
Nicolae Herisanu , Romania  
Alfredo G. Hernández-Díaz , Spain  
M.I. Herreros , Spain  
Eckhard Hitzer , Japan  
Paul Honeine , France  
Jaromir Horacek , Czech Republic  
Lei Hou , China  
Yingkun Hou , China  
Yu-Chen Hu , Taiwan  
Yunfeng Hu, China  
Can Huang , China  
Gordon Huang , Canada  
Linsheng Huo , China  
Sajid Hussain, Canada  
Asier Ibeas , Spain  
Orest V. Iftime , The Netherlands  
Przemyslaw Ignaciuk , Poland  
Giacomo Innocenti , Italy  
Emilio Insfran Pelozo , Spain  
Azeem Irshad, Pakistan  
Alessio Ishizaka, France  
Benjamin Ivorra , Spain  
Breno Jacob , Brazil  
Reema Jain , India  
Tushar Jain , India  
Amin Jajarmi , Iran  
Chiranjibe Jana , India  
Łukasz Jankowski , Poland  
Samuel N. Jator , USA  
Juan Carlos Jáuregui-Correa , Mexico  
Kandasamy Jayakrishna, India  
Reza Jazar, Australia  
Khalide Jbilou, France  
Isabel S. Jesus , Portugal  
Chao Ji , China  
Qing-Chao Jiang , China  
Peng-fei Jiao , China  
Ricardo Fabricio Escobar Jiménez , Mexico  
Emilio Jiménez Macías , Spain  
Maolin Jin, Republic of Korea  
Zhuo Jin, Australia  
Ramash Kumar K , India  
BHABEN KALITA , USA  
MOHAMMAD REZA KHEDMATI , Iran  
Viacheslav Kalashnikov , Mexico  
Mathiyalagan Kalidass , India  
Tamas Kalmar-Nagy , Hungary  
Rajesh Kaluri , India  
Jyotheeswara Reddy Kalvakurthi, India  
Zhao Kang , China  
Ramani Kannan , Malaysia  
Tomasz Kapitaniak , Poland  
Julius Kaplunov, United Kingdom  
Konstantinos Karamanos, Belgium  
Michal Kawulok, Poland

Irfan Kaymaz , Turkey  
Vahid Kayvanfar , Qatar  
Krzysztof Kecik , Poland  
Mohamed Khader , Egypt  
Chaudry M. Khalique , South Africa  
Mukhtaj Khan , Pakistan  
Shahid Khan , Pakistan  
Nam-Il Kim, Republic of Korea  
Philipp V. Kiryukhantsev-Korneev ,  
Russia  
P.V.V Kishore , India  
Jan Koci , Czech Republic  
Ioannis Kostavelis , Greece  
Sotiris B. Kotsiantis , Greece  
Frederic Kratz , France  
Vamsi Krishna , India  
Edyta Kucharska, Poland  
Krzysztof S. Kulpa , Poland  
Kamal Kumar, India  
Prof. Ashwani Kumar , India  
Michal Kunicki , Poland  
Cedrick A. K. Kwuimy , USA  
Kyandoghere Kyamakya, Austria  
Ivan Kyrchei , Ukraine  
Márcio J. Lacerda , Brazil  
Eduardo Lalla , The Netherlands  
Giovanni Lancioni , Italy  
Jaroslaw Latalski , Poland  
Hervé Laurent , France  
Agostino Lauria , Italy  
Aimé Lay-Ekuakille , Italy  
Nicolas J. Leconte , France  
Kun-Chou Lee , Taiwan  
Dimitri Lefebvre , France  
Eric Lefevre , France  
Marek Lefik, Poland  
Yaguo Lei , China  
Kauko Leiviskä , Finland  
Ervin Lenzi , Brazil  
ChenFeng Li , China  
Jian Li , USA  
Jun Li , China  
Yueyang Li , China  
Zhao Li , China

Zhen Li , China  
En-Qiang Lin, USA  
Jian Lin , China  
Qibin Lin, China  
Yao-Jin Lin, China  
Zhiyun Lin , China  
Bin Liu , China  
Bo Liu , China  
Heng Liu , China  
Jianxu Liu , Thailand  
Lei Liu , China  
Sixin Liu , China  
Wanquan Liu , China  
Yu Liu , China  
Yuanchang Liu , United Kingdom  
Bonifacio Llamazares , Spain  
Alessandro Lo Schiavo , Italy  
Jean Jacques Loiseau , France  
Francesco Lolli , Italy  
Paolo Lonetti , Italy  
António M. Lopes , Portugal  
Sebastian López, Spain  
Luis M. López-Ochoa , Spain  
Vassilios C. Loukopoulos, Greece  
Gabriele Maria Lozito , Italy  
Zhiguo Luo , China  
Gabriel Luque , Spain  
Valentin Lychagin, Norway  
YUE MEI, China  
Junwei Ma , China  
Xuanlong Ma , China  
Antonio Madeo , Italy  
Alessandro Magnani , Belgium  
Toqeer Mahmood , Pakistan  
Fazal M. Mahomed , South Africa  
Arunava Majumder , India  
Sarfranz Nawaz Malik, Pakistan  
Paolo Manfredi , Italy  
Adnan Maqsood , Pakistan  
Muazzam Maqsood, Pakistan  
Giuseppe Carlo Marano , Italy  
Damijan Markovic, France  
Filipe J. Marques , Portugal  
Luca Martinelli , Italy  
Denizar Cruz Martins, Brazil

Francisco J. Martos , Spain  
Elio Masciari , Italy  
Paolo Massioni , France  
Alessandro Mauro , Italy  
Jonathan Mayo-Maldonado , Mexico  
Pier Luigi Mazzeo , Italy  
Laura Mazzola, Italy  
Driss Mehdi , France  
Zahid Mehmood , Pakistan  
Roderick Melnik , Canada  
Xiangyu Meng , USA  
Jose Merodio , Spain  
Alessio Merola , Italy  
Mahmoud Mesbah , Iran  
Luciano Mescia , Italy  
Laurent Mevel , France  
Constantine Michailides , Cyprus  
Mariusz Michta , Poland  
Prankul Middha, Norway  
Aki Mikkola , Finland  
Giovanni Minafò , Italy  
Edmondo Minisci , United Kingdom  
Hiroyuki Mino , Japan  
Dimitrios Mitsotakis , New Zealand  
Ardashir Mohammadzadeh , Iran  
Francisco J. Montáns , Spain  
Francesco Montefusco , Italy  
Gisele Mophou , France  
Rafael Morales , Spain  
Marco Morandini , Italy  
Javier Moreno-Valenzuela , Mexico  
Simone Morganti , Italy  
Caroline Mota , Brazil  
Aziz Moukrim , France  
Shen Mouquan , China  
Dimitris Mourtzis , Greece  
Emiliano Mucchi , Italy  
Taseer Muhammad, Saudi Arabia  
Ghulam Muhiuddin, Saudi Arabia  
Amitava Mukherjee , India  
Josefa Mula , Spain  
Jose J. Muñoz , Spain  
Giuseppe Muscolino, Italy  
Marco Mussetta , Italy

Hariharan Muthusamy, India  
Alessandro Naddeo , Italy  
Raj Nandkeolyar, India  
Keivan Navaie , United Kingdom  
Soumya Nayak, India  
Adrian Neagu , USA  
Erivelton Geraldo Nepomuceno , Brazil  
AMA Neves, Portugal  
Ha Quang Thinh Ngo , Vietnam  
Nhon Nguyen-Thanh, Singapore  
Papakostas Nikolaos , Ireland  
Jelena Nikolic , Serbia  
Tatsushi Nishi, Japan  
Shanzhou Niu , China  
Ben T. Nohara , Japan  
Mohammed Nouari , France  
Mustapha Nourelfath, Canada  
Kazem Nouri , Iran  
Ciro Núñez-Gutiérrez , Mexico  
Włodzimierz Ogryczak, Poland  
Roger Ohayon, France  
Krzysztof Okarma , Poland  
Mitsuhiro Okayasu, Japan  
Murat Olgun , Turkey  
Diego Oliva, Mexico  
Alberto Olivares , Spain  
Enrique Onieva , Spain  
Calogero Orlando , Italy  
Susana Ortega-Cisneros , Mexico  
Sergio Ortobelli, Italy  
Naohisa Otsuka , Japan  
Sid Ahmed Ould Ahmed Mahmoud , Saudi Arabia  
Taoreed Owolabi , Nigeria  
EUGENIA PETROPOULOU , Greece  
Arturo Pagano, Italy  
Madhumangal Pal, India  
Pasquale Palumbo , Italy  
Dragan Pamučar, Serbia  
Weifeng Pan , China  
Chandan Pandey, India  
Rui Pang, United Kingdom  
Jürgen Pannek , Germany  
Elena Panteley, France  
Achille Paolone, Italy

George A. Papakostas , Greece  
Xosé M. Pardo , Spain  
You-Jin Park, Taiwan  
Manuel Pastor, Spain  
Pubudu N. Pathirana , Australia  
Surajit Kumar Paul , India  
Luis Payá , Spain  
Igor Pažanin , Croatia  
Libor Pekař , Czech Republic  
Francesco Pellicano , Italy  
Marcello Pellicciari , Italy  
Jian Peng , China  
Mingshu Peng, China  
Xiang Peng , China  
Xindong Peng, China  
Yueqing Peng, China  
Marzio Pennisi , Italy  
Maria Patrizia Pera , Italy  
Matjaz Perc , Slovenia  
A. M. Bastos Pereira , Portugal  
Wesley Peres, Brazil  
F. Javier Pérez-Pinal , Mexico  
Michele Perrella, Italy  
Francesco Pesavento , Italy  
Francesco Petrini , Italy  
Hoang Vu Phan, Republic of Korea  
Lukasz Pieczonka , Poland  
Dario Piga , Switzerland  
Marco Pizzarelli , Italy  
Javier Plaza , Spain  
Goutam Pohit , India  
Dragan Poljak , Croatia  
Jorge Pomares , Spain  
Hiram Ponce , Mexico  
Sébastien Poncet , Canada  
Volodymyr Ponomaryov , Mexico  
Jean-Christophe Ponsart , France  
Mauro Pontani , Italy  
Sivakumar Poruran, India  
Francesc Pozo , Spain  
Aditya Rio Prabowo , Indonesia  
Anchasa Pramuanjaroenkij , Thailand  
Leonardo Primavera , Italy  
B Rajanarayan Prusty, India

Krzysztof Puszynski , Poland  
Chuan Qin , China  
Dongdong Qin, China  
Jianlong Qiu , China  
Giuseppe Quaranta , Italy  
DR. RITU RAJ , India  
Vitomir Racic , Italy  
Carlo Rainieri , Italy  
Kumbakonam Ramamani Rajagopal, USA  
Ali Ramazani , USA  
Angel Manuel Ramos , Spain  
Higinio Ramos , Spain  
Muhammad Afzal Rana , Pakistan  
Muhammad Rashid, Saudi Arabia  
Manoj Rastogi, India  
Alessandro Rasulo , Italy  
S.S. Ravindran , USA  
Abdolrahman Razani , Iran  
Alessandro Reali , Italy  
Jose A. Reinoso , Spain  
Oscar Reinoso , Spain  
Haijun Ren , China  
Carlo Renno , Italy  
Fabrizio Renno , Italy  
Shahram Rezapour , Iran  
Ricardo Rianza , Spain  
Francesco Riganti-Fulginei , Italy  
Gerasimos Rigatos , Greece  
Francesco Ripamonti , Italy  
Jorge Rivera , Mexico  
Eugenio Roanes-Lozano , Spain  
Ana Maria A. C. Rocha , Portugal  
Luigi Rodino , Italy  
Francisco Rodríguez , Spain  
Rosana Rodríguez López, Spain  
Francisco Rossomando , Argentina  
Jose de Jesus Rubio , Mexico  
Weiguo Rui , China  
Rubén Ruiz , Spain  
Ivan D. Rukhlenko , Australia  
Dr. Eswaramoorthi S. , India  
Weichao SHI , United Kingdom  
Chaman Lal Sabharwal , USA  
Andrés Sáez , Spain

Bekir Sahin, Turkey  
Laxminarayan Sahoo , India  
John S. Sakellariou , Greece  
Michael Sakellariou , Greece  
Salvatore Salamone, USA  
Jose Vicente Salcedo , Spain  
Alejandro Salcido , Mexico  
Alejandro Salcido, Mexico  
Nunzio Salerno , Italy  
Rohit Salgotra , India  
Miguel A. Salido , Spain  
Sinan Salih , Iraq  
Alessandro Salvini , Italy  
Abdus Samad , India  
Sovan Samanta, India  
Nikolaos Samaras , Greece  
Ramon Sancibrian , Spain  
Giuseppe Sanfilippo , Italy  
Omar-Jacobo Santos, Mexico  
J Santos-Reyes , Mexico  
José A. Sanz-Herrera , Spain  
Musavarah Sarwar, Pakistan  
Shahzad Sarwar, Saudi Arabia  
Marcelo A. Savi , Brazil  
Andrey V. Savkin, Australia  
Tadeusz Sawik , Poland  
Roberta Sburlati, Italy  
Gustavo Scaglia , Argentina  
Thomas Schuster , Germany  
Hamid M. Sedighi , Iran  
Mijanur Rahaman Seikh, India  
Tapan Senapati , China  
Lotfi Senhadji , France  
Junwon Seo, USA  
Michele Serpilli, Italy  
Silvestar Šesnić , Croatia  
Gerardo Severino, Italy  
Ruben Sevilla , United Kingdom  
Stefano Sfarra , Italy  
Dr. Ismail Shah , Pakistan  
Leonid Shaikhet , Israel  
Vimal Shanmuganathan , India  
Prayas Sharma, India  
Bo Shen , Germany  
Hang Shen, China

Xin Pu Shen, China  
Dimitri O. Shepelsky, Ukraine  
Jian Shi , China  
Amin Shokrollahi, Australia  
Suzanne M. Shontz , USA  
Babak Shotorban , USA  
Zhan Shu , Canada  
Angelo Sifaleras , Greece  
Nuno Simões , Portugal  
Mehakpreet Singh , Ireland  
Piyush Pratap Singh , India  
Rajiv Singh, India  
Seralathan Sivamani , India  
S. Sivasankaran , Malaysia  
Christos H. Skiadas, Greece  
Konstantina Skouri , Greece  
Neale R. Smith , Mexico  
Bogdan Smolka, Poland  
Delfim Soares Jr. , Brazil  
Alba Sofi , Italy  
Francesco Soldovieri , Italy  
Raffaele Solimene , Italy  
Yang Song , Norway  
Jussi Sopanen , Finland  
Marco Spadini , Italy  
Paolo Spagnolo , Italy  
Ruben Specogna , Italy  
Vasilios Spitas , Greece  
Ivanka Stamova , USA  
Rafał Stanisławski , Poland  
Miladin Stefanović , Serbia  
Salvatore Strano , Italy  
Yakov Strelniker, Israel  
Kangkang Sun , China  
Qiuqin Sun , China  
Shuaishuai Sun, Australia  
Yanchao Sun , China  
Zong-Yao Sun , China  
Kumarasamy Suresh , India  
Sergey A. Suslov , Australia  
D.L. Suthar, Ethiopia  
D.L. Suthar , Ethiopia  
Andrzej Swierniak, Poland  
Andras Szekrenyes , Hungary  
Kumar K. Tamma, USA

Yong (Aaron) Tan, United Kingdom  
Marco Antonio Taneco-Hernández , Mexico  
Lu Tang , China  
Tianyou Tao, China  
Hafez Tari , USA  
Alessandro Tasora , Italy  
Sergio Teggi , Italy  
Adriana del Carmen Téllez-Anguiano , Mexico  
Ana C. Teodoro , Portugal  
Efstathios E. Theotokoglou , Greece  
Jing-Feng Tian, China  
Alexander Timokha , Norway  
Stefania Tomasiello , Italy  
Gisella Tomasini , Italy  
Isabella Torricollo , Italy  
Francesco Tornabene , Italy  
Mariano Torrisi , Italy  
Thang nguyen Trung, Vietnam  
George Tsiatas , Greece  
Le Anh Tuan , Vietnam  
Nerio Tullini , Italy  
Emilio Turco , Italy  
Ilhan Tuzcu , USA  
Efstratios Tzirtzilakis , Greece  
FRANCISCO UREÑA , Spain  
Filippo Ubertini , Italy  
Mohammad Uddin , Australia  
Mohammad Safi Ullah , Bangladesh  
Serdar Ulubeyli , Turkey  
Mati Ur Rahman , Pakistan  
Panayiotis Vafeas , Greece  
Giuseppe Vairo , Italy  
Jesus Valdez-Resendiz , Mexico  
Eusebio Valero, Spain  
Stefano Valvano , Italy  
Carlos-Renato Vázquez , Mexico  
Martin Velasco Villa , Mexico  
Franck J. Vernerey, USA  
Georgios Veronis , USA  
Vincenzo Vespri , Italy  
Renato Vidoni , Italy  
Venkatesh Vijayaraghavan, Australia

Anna Vila, Spain  
Francisco R. Villatoro , Spain  
Francesca Vipiana , Italy  
Stanislav Vitek , Czech Republic  
Jan Vorel , Czech Republic  
Michael Vynnycky , Sweden  
Mohammad W. Alomari, Jordan  
Roman Wan-Wendner , Austria  
Bingchang Wang, China  
C. H. Wang , Taiwan  
Dagang Wang, China  
Guoqiang Wang , China  
Huaiyu Wang, China  
Hui Wang , China  
J.G. Wang, China  
Ji Wang , China  
Kang-Jia Wang , China  
Lei Wang , China  
Qiang Wang, China  
Qingling Wang , China  
Weiwei Wang , China  
Xinyu Wang , China  
Yong Wang , China  
Yung-Chung Wang , Taiwan  
Zhenbo Wang , USA  
Zhibo Wang, China  
Waldemar T. Wójcik, Poland  
Chi Wu , Australia  
Qihong Wu, China  
Yuqiang Wu, China  
Zhibin Wu , China  
Zhizheng Wu , China  
Michalis Xenos , Greece  
Hao Xiao , China  
Xiao Ping Xie , China  
Qingzheng Xu , China  
Binghan Xue , China  
Yi Xue , China  
Joseph J. Yame , France  
Chuanliang Yan , China  
Xinggang Yan , United Kingdom  
Hongtai Yang , China  
Jixiang Yang , China  
Mijia Yang, USA  
Ray-Yeng Yang, Taiwan

Zaoli Yang , China  
Jun Ye , China  
Min Ye , China  
Luis J. Yebra , Spain  
Peng-Yeng Yin , Taiwan  
Muhammad Haroon Yousaf , Pakistan  
Yuan Yuan, United Kingdom  
Qin Yuming, China  
Elena Zaitseva , Slovakia  
Arkadiusz Zak , Poland  
Mohammad Zakwan , India  
Ernesto Zambrano-Serrano , Mexico  
Francesco Zammori , Italy  
Jessica Zangari , Italy  
Rafal Zdunek , Poland  
Ibrahim Zeid, USA  
Nianyin Zeng , China  
Junyong Zhai , China  
Hao Zhang , China  
Haopeng Zhang , USA  
Jian Zhang , China  
Kai Zhang, China  
Lingfan Zhang , China  
Mingjie Zhang , Norway  
Qian Zhang , China  
Tianwei Zhang , China  
Tongqian Zhang , China  
Wenyu Zhang , China  
Xianming Zhang , Australia  
Xuping Zhang , Denmark  
Yinyan Zhang, China  
Yifan Zhao , United Kingdom  
Debao Zhou, USA  
Heng Zhou , China  
Jian G. Zhou , United Kingdom  
Junyong Zhou , China  
Xueqian Zhou , United Kingdom  
Zhe Zhou , China  
Wu-Le Zhu, China  
Gaetano Zizzo , Italy  
Mingcheng Zuo, China

## Contents

---

### **Research on the Theory and Numerical Simulation of Mine Pressure Behavior in Steeply Inclined Thick Coal Seams**

Yuxi Huang  and Xiaoyang Cheng 

Research Article (15 pages), Article ID 7742125, Volume 2023 (2023)

### **Exploration of Tunnel Lining Falling Block Remediation Using Polyurea Material**

Changyu Yang, Xun Yuan , Fang Wang, Yong Zhu, Ang Chen, Jieyuan Zheng, Yi Yang, Hui Wang, and Jijun Guo

Research Article (23 pages), Article ID 9190865, Volume 2023 (2023)

### **Research on Development Mechanism and Criterion of Upward Fractures in Longwall Face Mining**

Jian Cao , Haitao Su , Jianwei Li , Xiangye Wu , and Eryu Wang 

Research Article (11 pages), Article ID 6776734, Volume 2023 (2023)

### **Deformation Characteristics and Control Mechanisms of Deep High-Stress Large-Span Roadways**

Bo Yang  and Jing Chai 

Research Article (10 pages), Article ID 1384964, Volume 2023 (2023)

### **Mechanism and Safety Mining Technology of Overall Instability-Induced Rockbursts of Multi-Coal Seam Spatially Isolated Working Face**

Bo Sun, Sitao Zhu , Fuxing Jiang, and Gao'ang Wang

Research Article (14 pages), Article ID 1038139, Volume 2022 (2022)

### **Water Inrush Mechanism of Roof Induced by the Fault Weakening Effect in the Coal Mining**

Qing Qiu , Lulin Zheng , Hong Lan, Wen Zhang, Hengyi He, Chun Zhao, Youwen Tian, Hao Liu, and Ruipeng Li 

Research Article (13 pages), Article ID 5737738, Volume 2022 (2022)

## Research Article

# Research on the Theory and Numerical Simulation of Mine Pressure Behavior in Steeply Inclined Thick Coal Seams

Yuxi Huang <sup>1</sup> and Xiaoyang Cheng <sup>2,3,4</sup>

<sup>1</sup>School of Mining, Liaoning Technical University, Fuxin 123000, China

<sup>2</sup>China Coal Research Institute, Beijing 100013, China

<sup>3</sup>State Key Laboratory of the Gas Disaster Detecting, Preventing and Emergency Controlling, Chongqing 400037, China

<sup>4</sup>China Coal Technology and Engineering Group Chongqing Research Institute, Chongqing 400037, China

Correspondence should be addressed to Yuxi Huang; [huangyuxi1900@126.com](mailto:huangyuxi1900@126.com)

Received 18 October 2022; Revised 24 November 2022; Accepted 15 April 2023; Published 26 May 2023

Academic Editor: Fuqiang Ren

Copyright © 2023 Yuxi Huang and Xiaoyang Cheng. This is an open access article distributed under the Creative Commons Attribution License, which permits unrestricted use, distribution, and reproduction in any medium, provided the original work is properly cited.

This paper aims to study the law of pressure behavior and the characteristics of mutual influence in the process of steeply inclined coal seam mining. Based on the geological and engineering conditions of the B8 coal seam in Nanshan coal mine, this paper explores the law of mine pressure behavior in the process of steeply inclined coal seam mining by means of theoretical analysis and FLAC3D numerical simulation. Based on this, this paper also examines the influence of the interaction range between coal seams, the reasonable setting size of the section coal pillar, and the mining distance of the working face on the return air roadway. The results suggest as follows: (1) With an increase in the coal seam dip angle, the difference in the abutment pressure plastic zone between upper and lower coal pillars increases, and when mining in steeply inclined coal seams, the stress concentration in the lower and upper part of the working face deviates to the roof and floor respectively, which is obviously different from that of gently inclined coal seams. (2) The vertical stress above the section coal pillar changes in three stages with an increase in the width of the coal pillar, and the width of the coal pillar in the second stage can be taken as the reasonable size of the width of the coal pillar. The numerical simulation results are consistent with the theoretical calculation results, which indicate the high reliability of this method in determining the reasonable coal pillar size. (3) With an increase in the mining distance in steeply inclined coal seams, the maximum pressure around the working face and above the return air roadway has gone through three stages. When the distance between the working face and the adjacent return air roadway is close, the pressure above the return air roadway increases sharply, and disturbance is stronger.

## 1. Introduction

As the primary energy of consumption, coal plays a critical role in China's energy structure and national economy. With a decrease in high-quality coal resources in China, the mining activities of large dip coal seams are gradually increasing [1]. The steeply inclined coal seam generally refers to the coal seam with a buried dip angle of  $35^{\circ}\sim 55^{\circ}$  [2] and is universally considered to be the most difficult coal seam to mine in the mining field [3]. The mine pressure behavior caused by mining in steeply inclined coal seams is obviously different from that in gently inclined coal seams. Therefore, it is of great significance to develop a reasonable mining plan

to accurately grasp the mine pressure behavior in the mining process of steeply inclined coal seams. For this reason, many scholars have studied the mine pressure behavior and the disturbance in the process of mining of steeply inclined seams from different angles.

Liu et al. [4] pointed out that, in steeply inclined coal seams, the stress exerted by the surrounding rock on the roof can be divided into the normal stress perpendicular to the rock stratum and the shear stress parallel to the rock stratum, and the shear stress is greater than the normal stress. Due to the large inclination angle, the direct roof of the upper part of the working face tends to collapse on the goaf and backfill its lower space, thus forming the support to the lower roof

[5–7] when the upper roof is suspended. Therefore, the overlying strata are subjected to asymmetric stress in tendency, resulting in asymmetric separation and caving, which brings difficulties to the management of surrounding rock. Qi et al. [8] studied the deformation and failure characteristics of surrounding rock, aiming at the phenomenon of misalignment and large deformation and failure that often occur after excavation and support of roadway in steep coal seams. Based on the small-deflection theory for elastic thin plates, Tu et al. [9] established a working face mechanical analysis model for the first time before roof fracture after coal seam mining with a large dip angle. Yang and Liu [10] used the natural arch theory to analyze the cave-in mechanism of horizontal coal roadway in steep coal seams and studied the stress distribution characteristics and failure law of surrounding rock of fully mechanized mining roadway in steep coal seams. Hong-Sheng et al. [11] pointed out that the stability of the lower roof of the working face is higher than that of the upper roof in the mining of high dip coal seams. With a gradual increase in the dip angle, the ability of rock mass to withstand slip-induced instability increases, but the ability to withstand deformation-induced instability decreases. Wu et al. [12] studied the mechanical properties and microstructure of cemented rockfill reinforced by carbon nanotubes and fractal aggregates through macroscopic mechanical and microscopic scanning tests, which can provide certain support for surrounding rock support when mining coal seams with a large dip angle. Through the above analysis, this paper reveals the disturbance influence on the confining pressure in the mining process of the steeply inclined coal seam, which provides a certain theoretical basis for on-site construction.

Based on FLAC3D numerical simulation software, Xue et al. [13] studied the variation characteristics of surrounding rock stress and energy in the mining process of the steeply inclined coal face. The results show that the working face is in a high stress state affected by the leading abutment pressure, the energy accumulation area of the roof is located in the lower end and the middle and upper part of the working face, and the energy accumulation area of the floor is located in the lower end of the working face. Lu et al. [14] studied the characteristics of pressure behavior in the process of shallow steeply inclined coal seam mining through two-dimensional numerical simulation. The results show that the law of pressure behavior in the mining process of the steeply inclined coal seam is obviously different from that of the gently inclined coal seam and the uneven settlement of the steeply inclined coal seam floor is more serious than that of the coal seam roof. Zhang and Shi [15] carried out the numerical simulation of combined mining of a large dip angle and a short-distance coal seam by a finite element method. By discussing the deformation and failure characteristics of surrounding rock, they revealed the scientific nature of combined mining of steeply inclined close coal seams. Zhang et al. [16] studied the stress redistribution and coal seam deformation characteristics under the goaf of a high-dip coal seam by using 3DEC software. The results show that, in the process of upper slicing mining, more than 75% of the coal in lower slicing is located in the effective

pressure relief area. Wu et al. [17] analyzed the influence of the mining process of steeply inclined coal seams on coal seam roadway through the numerical simulation and pointed out that the difference in the rock structure on both sides of steeply inclined coal seam roadway is the root cause of roadway asymmetric failure. Qi et al. [8] studied the failure mechanism and control technology of roadway surrounding rock in deep steeply inclined coal seams under the influence of a weak structural plane by the FLAC3D numerical simulation and explored the reasonable support scheme of roadway according to the results of the numerical simulation.

The above analysis suggests that the disturbance and pressure behavior of steeply inclined coal seam mining have their own characteristics. Moreover, theoretical analysis and numerical simulation methods play a significant role in revealing the disturbance mechanism in the process of steeply inclined coal seam mining. However, at present, the law of pressure behavior and disturbance characteristics in the process of steeply inclined coal seam mining is rarely studied. In particular, there are few studies on the interaction between coal seams and the effect of coal seam mining on section coal pillars in steeply inclined coal seam mining. In the process of coal seam mining, the law of mining pressure manifestation in different regions is different. How to systematically study the characteristics of mining pressure manifestation in different regions in the process of large dip coal seam mining is the key research content of this paper, which is also the important innovation of this paper. Based on this, the paper explores the law of pressure behavior in the process of mining steeply inclined thick coal seams by focusing on the interaction between coal seams and the reasonable width of the coal pillar in steeply inclined coal seam mining and the relationship between face mining distance and roadway mining, which is expected to provide a theoretical basis and reference value for the development of on-site engineering.

## 2. Theoretical Analysis on the Law of Mine Pressure Behavior in Working Face

Coal and rock mass are not manually disturbed before coal mining, and the stress is in a state of equilibrium. At this point, the measured rock mass stress is the original rock stress. After coal mining, the mining stress field is formed, and the vertical pressure acting on coal seam, rock strata, and gangue within the range of surrounding rock stress redistribution is called abutment pressure. The accurate calculation of the distribution law and the range of the abutment pressure in stope have a significant application value for the adoption of reasonable support modes and methods for stope, the determination of reasonable excavation location and time of adjacent roadway, and the prevention of accidents related to the abutment pressure.

*2.1. Distribution Law of Inclined Abutment Pressure in Working Face.* There is a pressure peak in the abutment pressure distribution range, and the abutment pressure

distribution is divided into the plastic zone and elastic zone according to the pressure peak. The structural mechanic model is established, as shown in Figure 1.

According to the mechanical model of the inclined supporting pressure structure shown in Figure 1, the range of the plastic zone of the inclined abutment pressure in the working face is established:

$$\begin{cases} x_{\text{上侧}} = \frac{M\beta}{2 \tan \varphi_0} \ln \left[ \frac{\beta(\sigma_{y1} \cos \alpha \tan \varphi_0 + 2c_0 - M\gamma_0 \sin \alpha)}{\beta(2c_0 - M\gamma_0 \sin \alpha) + 2P_x \tan \varphi_0} \right], \\ x_{\text{下侧}} = \frac{M\beta}{2 \tan \varphi_0} \ln \left[ \frac{\beta(\sigma_{y1} \cos \alpha \tan \varphi_0 + 2c_0 + M\gamma_0 \sin \alpha)}{\beta(2c_0 + M\gamma_0 \sin \alpha) + 2P_x \tan \varphi_0} \right], \end{cases} \quad (1)$$

where  $x_{\text{upperside}}$  refers to the range of the plastic zone of the inclined abutment pressure on the upper side of the stope,  $M$  refers to the thickness of the mining coal seam,  $\beta$  refers to the lateral pressure coefficient of the face where the ultimate strength is located,  $\varphi_0$  refers to the friction angle at the interface between the coal seam and the roof and the floor,  $\sigma_{y1}$  refers to the peak value of the abutment pressure,  $\alpha$  refers to the dip angle of the coal seam,  $c_0$  refers to the cohesion at the interface between the coal seam and the roof and the floor,  $\gamma_0$  refers to the average volume force of coal, and  $P_x$  refers to the binding force of roadway support on the coal wall along the  $x$  direction.

The upper side of the stope means that the coal pillar of the goaf is located on the upper side of the upwind roadway, and the lower side of the stope means that the coal pillar of the goaf is located on the lower side of the conveyor roadway. It can be observed from formula (1) that the range of the plastic zone of the inclined abutment pressure correlated with the dip angle of the coal seam. Such a correlation is not noticeable when the dip angle of the coal seam is small, but with an increase in the dip angle of the coal seam, the difference in the plastic zone of the abutment pressure between the upper side and the lower side of the coal pillar increases.

In the subsequent analysis of the mining pressure of the working face, coal pillars in sections, and the interaction between coal seams, the stress values at different positions were calculated according to the abutment pressure model shown in Figures 1 and 2. At the same time, the yield condition and the plastic zone range of coal and rock are judged according to the corresponding criterion.

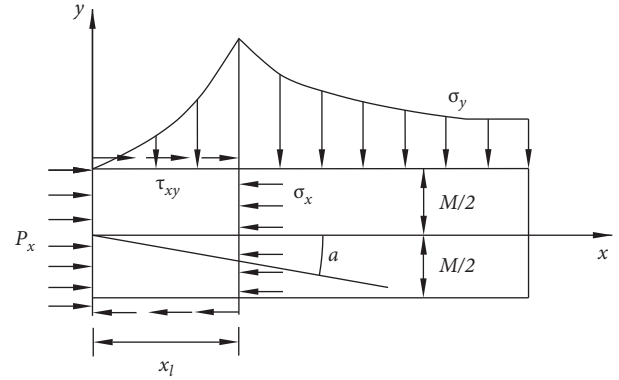


FIGURE 1: Mechanical model diagram of inclined abutment pressure structure [18].

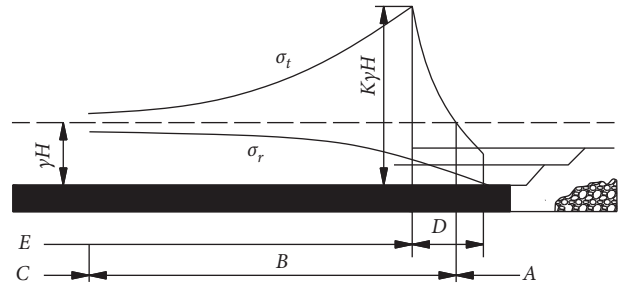


FIGURE 2: Distribution of strike abutment pressure in the mining face: (a) stress reduction area; (b) stress increase area; (c) original rock stress area; (d) limit equilibrium zone; (e) elastic zone [19].

**2.2. Distribution Law of Strike Abutment Pressure in Working Face.** The movement and stress redistribution of the strata around the stope caused by coal seam mining have a great impact on the deformation and failure of the surrounding rock of the steeply inclined coal seam. When backstopping in the working face, the strata in the irregular caving zone are in a loose state and the overlying strata are largely in a suspended state, which makes it necessary to transfer the weight of the suspended strata to the coal body in front of the working face. At this point, the goaf is a lower area than the original rock stress, and the abutment pressure of the coal in front of the working face is much higher than that of the original rock, as shown in Figure 2.

The range of the plastic zone of strike support pressure in the working face is established according to the mechanical model of the strike support pressure structure shown in Figure 2:

$$x_0 = \frac{M}{2fk_p} \ln \left[ \frac{K\gamma H \cos \alpha + (2Ck_p + M_0S_t/2fk_p) - (M_0S_t/2fk_p)e^{(2fk_p/M_0S_t)(\sigma_c - \sigma_c^*)}}{k_p p_x + \sigma_c^* + (l)} \right]. \quad (2)$$

In the formula,  $M$  refers to the coal seam mining thickness,  $f$  refers to the friction coefficient between the coal seam and the roof and floor,  $f = \tan \varphi$  ( $\varphi$  refers to the internal

friction angle at the coal-rock contact),  $K$  refers to the stress concentration factor,  $H$  refers to the buried depth of the coal seam,  $\alpha$  refers to the coal seam dip angle,  $\gamma$  refers to the bulk

density of the overlying strata,  $C$  refers to the cohesion of the coal layer,  $M_0$  refers to the softening modulus of the coal,  $S_t$  refers to the strain gradient of the coal in the plastic zone,  $p_x$  refers to the protective force of the supporting plate of the working face to the coal wall,  $\sigma_c$  refers to the uniaxial compressive strength of coal, and  $k_p$  refers to the internal friction angle of coal.

### 3. Analysis and Discussion of Numerical Simulation Results

**3.1. Introduction of the Project and the Establishment of the Model.** Taking the B8 coal seam of Xiaogou coal mine in Nanshan coal mine in Shihezi city in China as the research object, this paper examines the law of pressure behavior of the steeply inclined coal seam. The dip angle of the B8 coal seam is  $38^\circ\sim 42^\circ$ , the thickness of the coal seam is 4.2 m, the old roof is 14.6 m fine sandstone, the direct roof is 20.2 m siltstone, and the direct bottom is 1.2 m fine sandstone. In this paper, through field sampling, the corresponding physical and mechanical properties of rock are measured by using indoor rock mechanic testing machine, and then, the corresponding model is established by using FLAC3D numerical simulation software. In FLAC3D numerical simulation software, the abutment pressure distribution model in Figures 1 and 2 is used to study the pressure behavior law of a high-dip coal seam. The Mohr–Coulomb plastic constitutive relation and the yield criterion are adopted in the numerical simulation process, and the plastic flow of rock mass is not considered. The discriminant expression is

$$f_s = \sigma_1 - A\sigma_3 + 2B\sqrt{N_\varphi}, \quad (3)$$

where  $\sigma_1$  and  $\sigma_3$  are the maximum and minimum principal stresses, respectively,  $B$  and  $\varphi$  are cohesion and the internal friction angle, respectively, and  $N_\varphi = (1 + \sin\varphi)/(1 - \sin\varphi)$ . When  $f_s \geq 0$ , the material is in a plastic flow state. When  $f_s < 0$ , the material is in the elastic deformation stage. The values of physical and mechanical parameters in the simulation process are shown in Table 1.

**3.2. Research on the Law of Mine Pressure Behavior in Mining Face.** According to the theoretical model shown in Figure 2, the rock pressure behavior law of the mining face is studied by using the FLAC3D numerical simulation software, as shown in Figure 3.

After extracting the specific values from the numerical simulation results, the vertical stress variation curves at different positions of the mining face are obtained, as shown in Figure 4.

As can be observed in Figures 3 and 4, after mining, the stress concentration in the lower part of the working face deviates to the roof, the stress concentration in the upper face deviates to the floor, the influence range of stress in the lower part of the working face is 20 m, and the stress concentration appears in the position of about 3 m. These characteristics are obviously different from those of the gently inclined coal seam. The area within 0–3 m from the lower part of the working face is the stress reduction area, the

area within 3–20 m is the stress increase area, and the area beyond 20 m from the lower part of the working face is the stress stable area. In the process of mining large dip coal seams, the maximum stress is about 18 MPa and the location is about 5 m from the lower part of the working face.

#### 3.3. Research on the Pressure Behavior of the Coal Pillar in the Coal Seam with a Steeply Inclined Angle

**3.3.1. Research on the Stress and Deformation Characteristics of the Section Coal Pillar.** In order to explore the influence of the angle on the pressure behavior of the coal pillar in coal seams with a steeply incline angle, the models of a coal seam dip angle of  $35^\circ$ ,  $40^\circ$ , and  $45^\circ$  and a section pillar of 20 m were established by using FLAC3D numerical simulation software. Based on the existing research results, verification is completed and good results are obtained. The numerical simulation results are shown in Figure 5 [20].

The results of the numerical simulation cloud map in Figure 5 suggest that the maximum concentrated stress of the coal pillar in the working face of the steeply inclined coal seam is located at the top of the coal pillar near the roof of the upper working face. In order to further quantitatively characterize the effects of different dips and distances, the results in Figure 3 are extracted, as shown in Figure 6 [20].

As can be observed in Figure 6, with an increase in the dip angle, the concentrated stress action point shifts to the upper part of the roof (the upper end of the coal pillar) and to the coal wall of the working face, and the influence range of vertical stress becomes smaller with an increase in the dip angle. When the dip angle of the working face is  $45^\circ$ , the saddle-shaped stress distribution curve appears in the coal pillar, indicating that the stress in the working face and the lateral stress of the coal pillar are no longer superimposed.

**3.3.2. Research on Stress and Deformation Characteristics of the Coal Pillar with Different Width.** In order to study the law of deformation and failure of the coal pillar in different width sections under a large dip angle, numerical models with a coal pillar width of 5 m, 10 m, 15 m, 20 m, 25 m, and 30 m are established, respectively, for numerical simulation analysis under the condition that the dip angle of the coal seam is  $40^\circ$  and that the range of the goaf is constant, as shown in Figure 7 [20].

In order to better reflect the law in Figure 7, the variation results of vertical stress under the coal pillar with different widths with roadway distance are extracted, as shown in Figure 8 [20].

As shown in Figures 7 and 8, the upper side of the coal pillar, that is, the side near the goaf, is affected by the upper goaf, resulting in stress concentration. From the vertical stress curve, it can be observed that when the width of the coal pillar is about 0–10 m, the overall bearing pressure of the coal pillar is larger, and on one side of the roadway, the stress value is obviously higher than that of other width coal pillars. When the width of the coal pillar is 5 m, the maximum stress is 14.4 MPa, and when the width of the coal pillar is 10 m, the maximum stress is 20 MPa. When the width of the coal pillar is 15–30 m, the maximum stress is

TABLE 1: Physical and mechanical parameters in the simulation process.

Rock stratum	Elastic modulus (GPa)	Cohesion (MPa)	Internal friction angle (°)	Tensile strength (MPa)
Old roof	48.6	5.7	36	4.2
Direct roof	52.1	2.2	32	4.0
Coal	2.9	2.0	30	0.35
Direct bottom	47.8	5.6	35	4.1

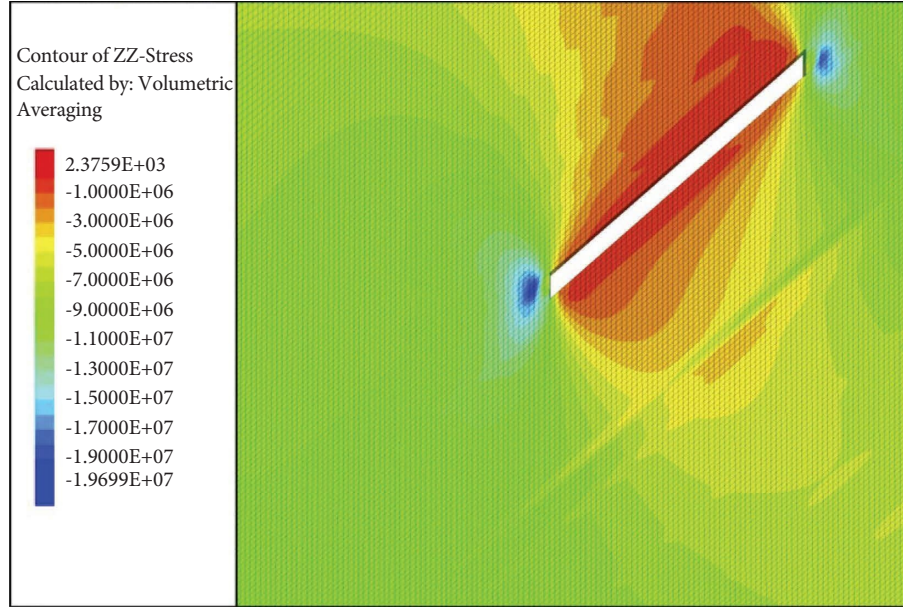


FIGURE 3: Cloud map of stress distribution in mining face.

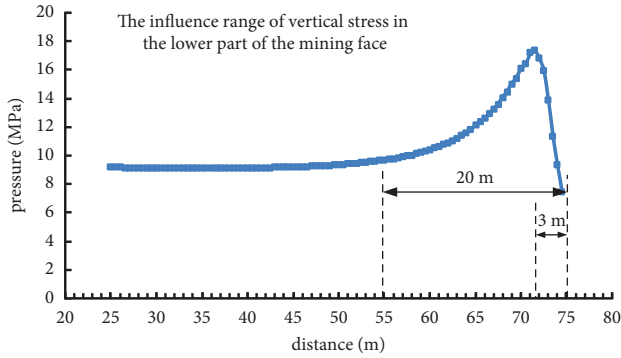


FIGURE 4: Stress distribution diagram at different positions of mining face.

18 MPa. Although the maximum stress when the coal pillar width is 15~30 m is greater than that when the coal pillar width is 5 m, with an increase in the coal pillar width, the maximum stress value is gradually far away from the roadway and the influence of the goaf roof on the roadway starts to decrease, thus ensuring the safe operation of the roadway. When the width of the coal pillar is more than 20 m, the “saddle-shaped” stress on the side of the coal pillar is no longer superimposed on each other. Therefore, based on the numerical simulation results and the recovery rate, the reasonable width of the roadway is set as 15 m~20 m.

**3.3.3. Theoretical Study on the Reasonable Size of the Section Coal Pillar.** In Section 3.3.2, the force and deformation characteristics of the coal pillar with different widths are numerically simulated, through which the reasonable width of the coal pillar is determined to be 15~20 m. In order to further verify the stability and reliability of the numerical simulation results, a theoretical study on the mine pressure behavior of the section coal pillar was carried out. The stress diagram of the section coal pillar is shown in Figure 9.

The coal strata at the upper end of the goaf area in the upper part of the working face are defined as the sliding rock mass. The force  $F_1$  along the normal direction of the overlying strata of the sliding rock mass acts on the vertical plane of the sliding rock mass, and  $F_2$  acts on the sliding rock mass along the bedding direction. At the same time, the sliding rock mass is also affected by its own gravity component  $F_4$  along the normal direction, inclination component  $F_3$ , and friction on the upper and lower surfaces. The stress relationship along the dip direction when the sliding rock mass is stable is as follows:

$$F_1 f_1 + (F_1 + F_4) f_1 \geq F_2 + F_3. \quad (4)$$

In the formula,  $F_1 = q_5 L_0 \cos \alpha$ ,  $L_0$  refers to the width of the coal pillar,  $q_5$  refers to the load of the overlying strata on the sliding rock mass,  $\alpha$  refers to the dip angle of the coal seam,  $F_1 = q_5 L_0 \cos \alpha$ ,  $F_3 = \gamma_1 \Sigma h_i L_0 \sin \alpha$ ,  $\gamma_1$  refers to the average volume force of the sliding rock mass,  $\Sigma h_i$  refers to the total

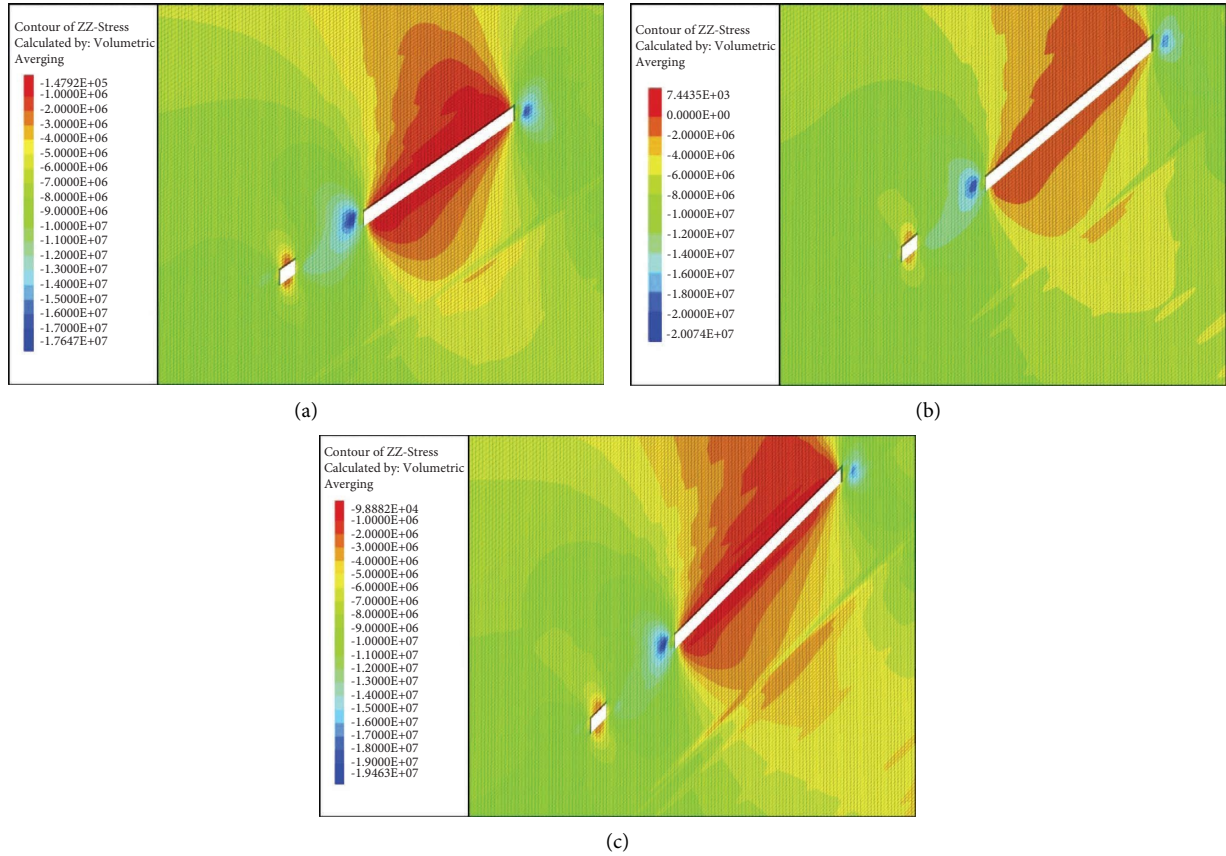


FIGURE 5: Cloud map of vertical stress distribution of the coal pillar at different dip angles: (a) 35°; (b) 40°; (c) 45°.

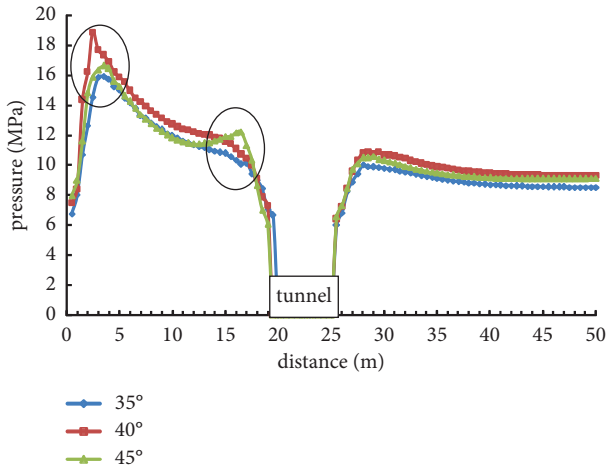


FIGURE 6: Stress distribution curve of the coal pillar in the coal seam with different angles.

thickness of the sliding rock mass in the upper part of the working face,  $F_4 = \gamma_1 \Sigma h_i L_0 \cos \alpha$ , and  $f_1$  and  $f_2$  refer to the friction coefficients between the upper and lower surfaces of the sliding rock mass, respectively. The following expression can be obtained by bringing the above values into formula (4):

$$q_5 \geq \frac{\sin \alpha - f_2 \cos \alpha}{(f_1 + f_2) \cos \alpha - \sin \alpha} \gamma_1 \Sigma h_i. \quad (5)$$

When the dip angle of the coal seam is greater than 45°, the right molecule of formula (5) is a real number greater than zero, and when the dip angle of the coal seam is less than 90°, the action load  $q_5$  of the overlying strata on the sliding rock mass is a real number greater than zero. Therefore, when  $(f_1 + f_2) \cos \alpha - \sin \alpha$  is negative,  $q_5 \geq 0$  is always workable. Thus, it can be concluded that there is no slip and instability of the coal pillar in the section when  $\alpha \leq \arctan(f_1 + f_2)$  and that there is a danger of slip when  $\alpha \geq \arctan(f_1 + f_2)$ .

In the above formula  $h_1 = H_m + M$ ,  $M$  is the coal seam mining height of the working face. The particularity of the occurrence condition of the steeply inclined coal seam determines that the movement form of the overlying rock in the working face is different from that in the near-horizontal coal seam. When the hanging width of the upper strata of the working face is less than the fracture step of the overlying strata, the overlying strata stop falling, the length of the roof no longer changes, and the total thickness of the falling strata can be measured. Therefore,  $H_m$  can be determined according to the actual occurrence conditions of coal strata in the specific working face.

A balanced pressure arch structure can be formed among the upper old roof of the high inclination face, the gangue filling in the lower part of the working face, and the coal pillar in the upper section of the working face. At equilibrium, the total weight of the overlying strata is supported by

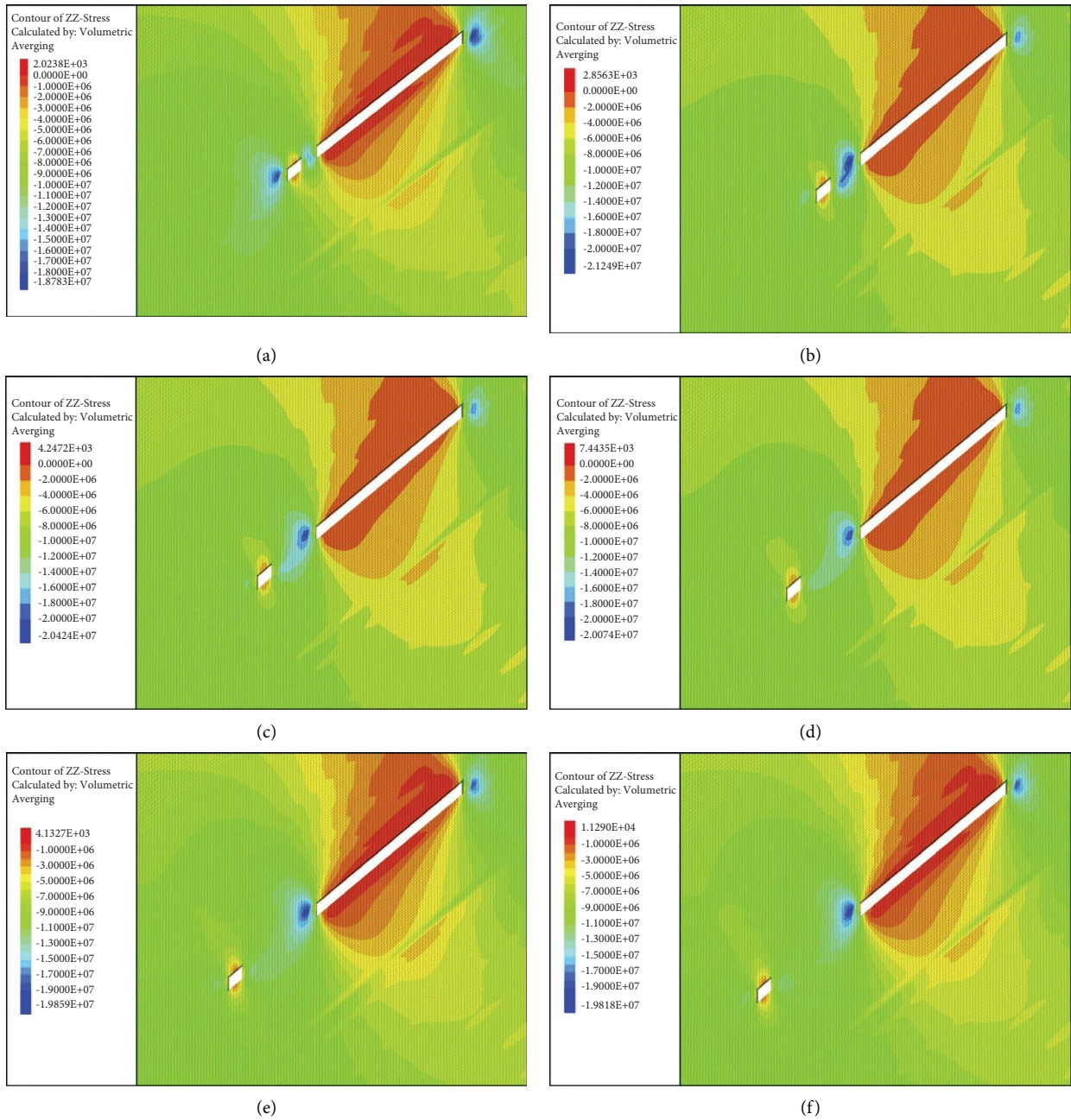


FIGURE 7: Cloud map of stress distribution of the coal pillar in different width sections: (a) 5 m; (b) 10 m; (c) 15 m; (d) 20 m; (e) 25 m; (f) 30 m.

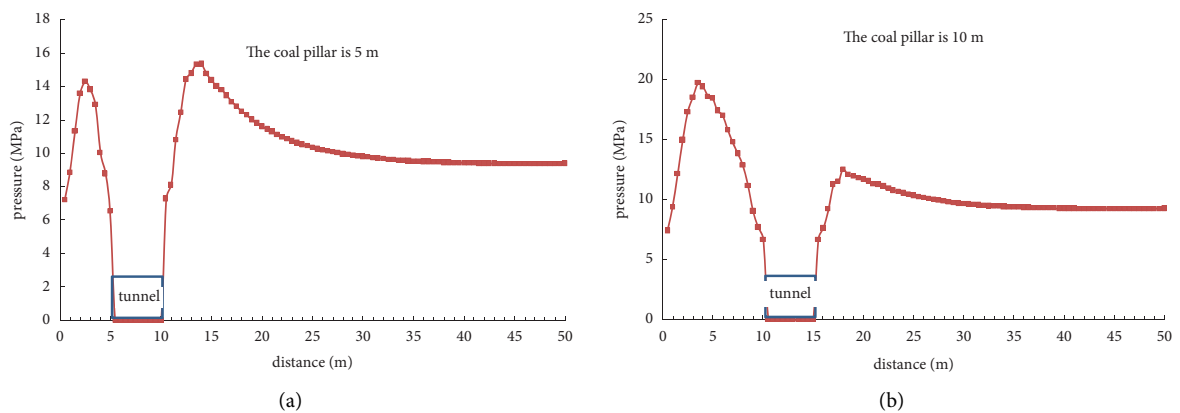


FIGURE 8: Continued.

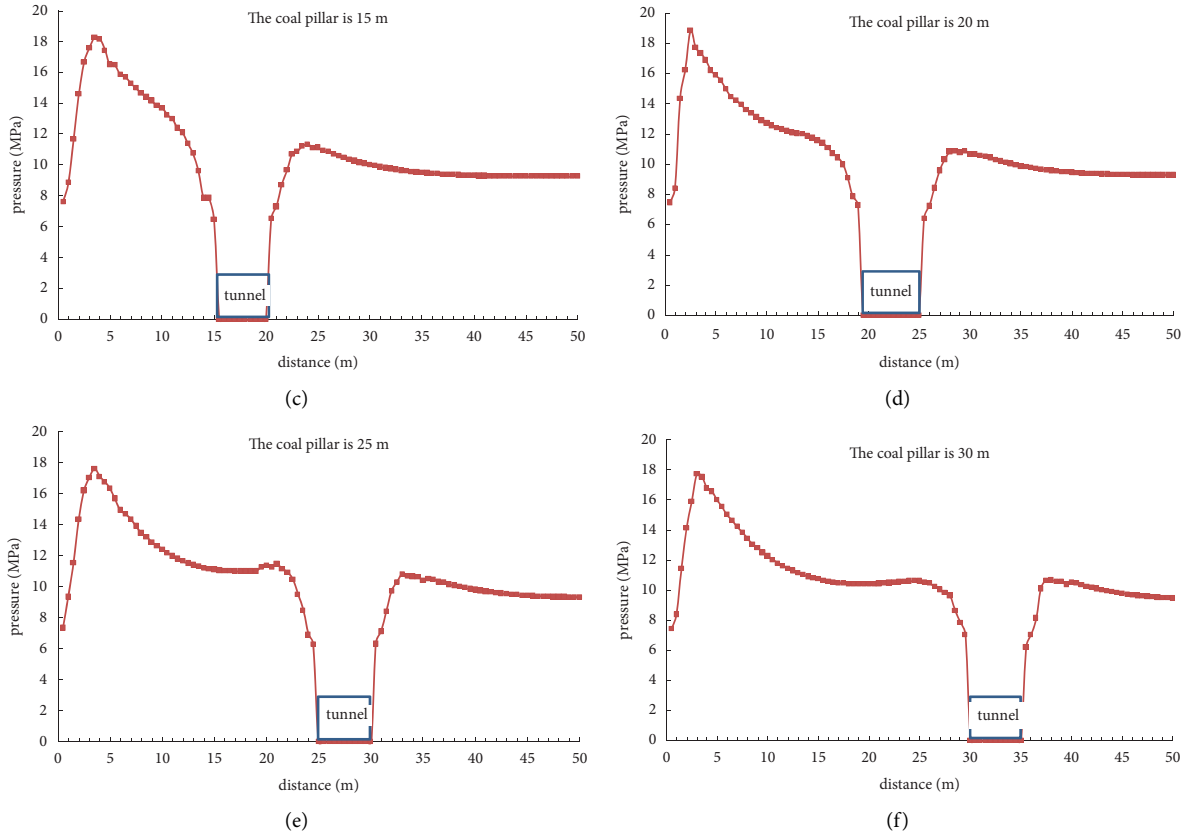


FIGURE 8: Vertical stress distribution curve of the coal pillar with different widths: (a) 5 m; (b) 10 m; (c) 15 m; (d) 20 m; (e) 25 m; (f) 30 m.

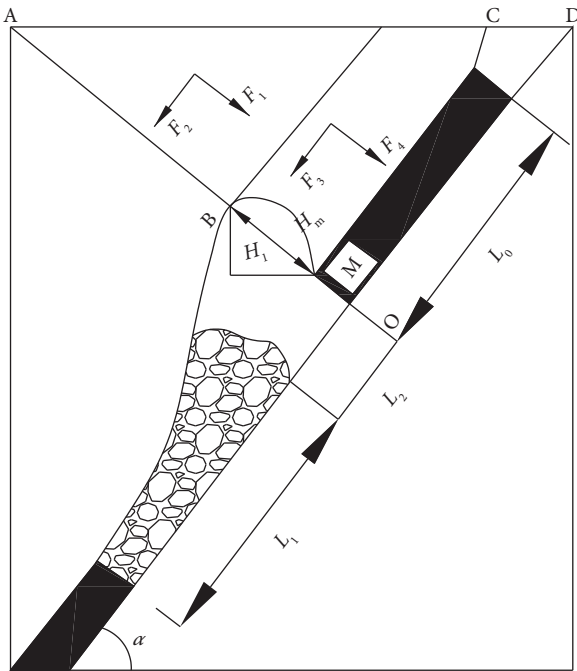


FIGURE 9: Stress diagram of the section coal pillar.

the section coal pillar and lower filling gangue of the working face (the support force of the bracket is negligible in comparison), as shown in Figure 10.

From the force relationship in Figure 10, it can be obtained that  $q_5$  is

$$q'_5 = \gamma H_q \frac{(L + L_0)}{L + L_0} + \frac{1}{2} \gamma \frac{(L + L_0)^2}{L_1 + L_0} \sin \alpha. \quad (6)$$

In the formula,  $q_5$  refers to the acting force of the overlying strata on the section coal pillar. With the self-weight of the coal pillar being excluded, it can be known from the relationship between the acting force and the reaction force that the acting force of the overlying strata on the section coal pillar is equal to that of the underlying strata on the coal pillar.  $\gamma$  refers to the average volume force of the overlying strata,  $H_q$  refers to the buried depth at the upper end of the coal pillar,  $L$  refers to the length of the working face, and  $L_1$  refers to the width of the filling in the lower part of the working face.

When the section coal pillar is stable, the resultant moment of each component of the section coal pillar is supposed to be balanced, and the following equation can be obtained by calculating the O point in Figure 10:

$$\frac{1}{2} F_1 L_0 + \frac{1}{2} F_4 L_0 + f_1 \sum h_i = F_2 \sum h_i + \frac{1}{2} F_3 \sum h_i. \quad (7)$$

Since the thickness of the coal seam is smaller than the buried depth of the working face and the total thickness of the goaf above the working face, it can be assumed that

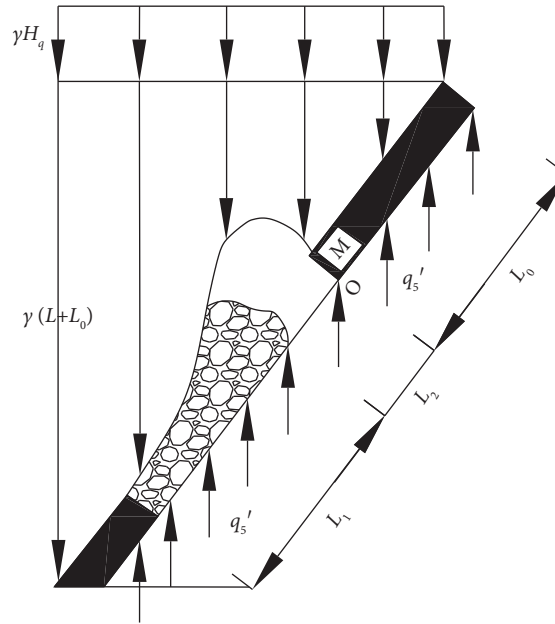


FIGURE 10: Stress diagram of the overlying strata.

$\gamma = \gamma_1$ . By substituting  $\gamma = \gamma_1$  into formula (7) and simplifying it, the following equation can be obtained:

$$q_5 = \frac{L_0 \sum h_i - (\sum h_i)^2 \tan \alpha}{2 \sum h_i \tan \alpha + 2 f_1 \tan \alpha - L_0} \gamma. \quad (8)$$

The following equation can be obtained by combining formulas (7) and (8):

$$\begin{cases} L_0 = \frac{P_1 + \sqrt{P_1^2 + 8 \sin \alpha \tan \alpha ((\sum h_i)^2 + (2H_q + L \sin \alpha)(f_1 + \sum h_i))}}{2 \sin \alpha}, \\ P_1 = 2 f_1 \sin \alpha \tan \alpha - 2 \sum h_i + 2 \sum h_i \sin \alpha \tan \alpha - 2 H_q - L \sin \alpha. \end{cases} \quad (9)$$

According to formula (9), the relationship between the setting width of the section coal pillar and the dip angle of the coal seam and the mining height of the working face can be obtained. It can be seen that when the coal seam dip angle is greater than  $60^\circ$ , the setting size of the coal pillar in the working face is greatly affected by the dip angle, and when the coal seam dip angle is less than  $60^\circ$ , the setting size of the coal pillar in the working face section is less affected by the inclination angle. The reasonable setting size of the coal pillar width is linearly proportional to the mining height of the working face.

We set the height of the working face as 4.2 m, and the reasonable reserved size of the section coal pillar at different dip angles can be obtained from formula (9), as shown in Figure 11.

From Figure 11, it can be concluded that when the coal seam dip is  $38^\circ$ – $42^\circ$ , the reasonable coal pillar size is 15 m~20 m. Therefore, the theoretical calculation result of the reserved size of the coal pillar in the reasonable section of Xiaogou subore in Nanshan coal mine is 15~20 m. The

consistency between the theoretical calculation results and the numerical simulation results reflects the stability and reliability of the numerical simulation results.

#### 3.4. Analysis of the Mining Influence Law of B4 Coal Seam and B8 Coal Seam.

In the process of coal seam mining, the pressure behavior law above the working face is not only affected by the current abutment pressure above the working face but also related to the mining of adjacent or similar coal seams. In addition, the pressure behavior of the roadway above the working face is greatly affected by the adjacent mining face in the process of tunneling. Therefore, the study of the change law of rock pressure behavior caused by the interaction between mining not only has important theoretical significance but also has clear practical significance. This section examines the influence of similar mining coal seams on the pressure behavior in the mining process of a large inclination face by carrying out the FLAC3D

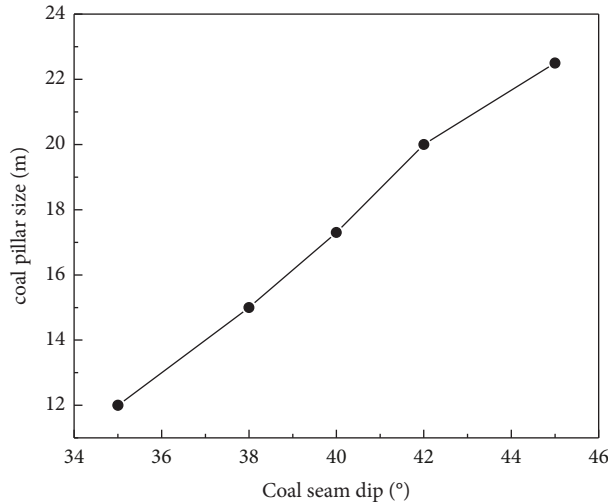


FIGURE 11: Variation law of reasonable coal pillar size with a dip angle of the coal seam.

numerical simulation. At the same time, the influence of the mining process of the steeply inclined working face on the ground pressure behavior above the heading roadway of the adjacent face is numerically stimulated.

**3.4.1. Analysis of the Influence of B4 Coal Seam Mining on B8 Coal Seam.** The thickness of the B4 coal seam is between 1.6 m and 2.26 m, the average thickness is 1.82 m, and the dip angle of the coal seam is about 40°. Most of the strata between B4 and B8 coal seams are sandstone interbeds, and the average distance between them is 66.08 m. In the process of the numerical simulation, the thickness of the B4 coal seam is 2 m and the mining length of the working face is 120 m. The model is shown in Figure 12.

According to the model established in Figure 12, the influence of B4 coal seam mining on the B8 coal seam is numerically simulated from four dimensions: plastic zone distribution, vertical displacement change, overlying strata density change, and vertical stress distribution. The results are shown in Figure 13.

The results in Figure 13 show the following:

- (1) The plastic zone of B4 coal seam mining is primarily caused by shear failure and tensile failure, and the plastic zone is mainly distributed in the roof and the floor of the two cross headings. There is no plastic failure in the B8 coal seam in the middle of the B4 working face, so it is believed that the mining of the B4 coal seam does not affect the B8 coal seam.
- (2) The vertical displacement primarily occurs at the upper side and roof of the upper cross heading. From the distribution of the vertical displacement of the roof, the roof deformation of the B4 coal seam does not affect the B8 coal seam, and the influence range of the B4 coal seam roof is mainly in the middle and upper parts.
- (3) The change area of density primarily occurs in the position of the roof and floor, and its density does not affect the B8 coal seam from the variation range of roof density.

- (4) The maximum vertical stress is in the solid coal of the two cross headings, the second is mainly distributed in the roof and floor, and the general stress distribution in the roof is larger in the middle and upper parts, which is consistent with the field ground pressure observation data of the B8 coal seam face. The simulation results show that the roof stress of the B4 coal seam has an influence on the B8 coal seam after mining, but the influence is not significant. From the numerical simulation results, when the distance between the two coal seams gradually decreases, this interaction will become increasingly significant. In addition, the maximum stress value and influence range of different coal seam spacing can be obtained from Figure 13(d). Therefore, this method can be used to judge the range of interaction of different spacing coal seams, but the precondition is to combine with specific geological conditions.

Therefore, as can be seen in Figure 13, under the assumption that the overlying strata are hard strata, after B4 coal seam mining, the plastic zone distribution, vertical displacement change, overlying strata density distribution, and vertical stress distribution do not affect or slightly affect the B8 coal seam, and the scope of influence is limited to the middle and upper parts. Although the simulation results show that the mining of the B4 coal seam has little influence on the B8 coal seam, this is mainly based on the conclusion of the actual geological conditions of Nanshan coal mine. However, the numerical simulation analysis reveals the influence range of B4 coal seam mining on the overlying coal seam, which is where the significance of this study lies.

**3.4.2. Analysis of the Influence of Mining in Working Face on the Air Return Way of Adjacent Working Face.** The three-dimensional numerical model is based on the layout plan of the B8 working face and the sketch drawing of +1190 m horizontal transport cross heading, and the conditions are appropriately simplified. The length of the numerical model

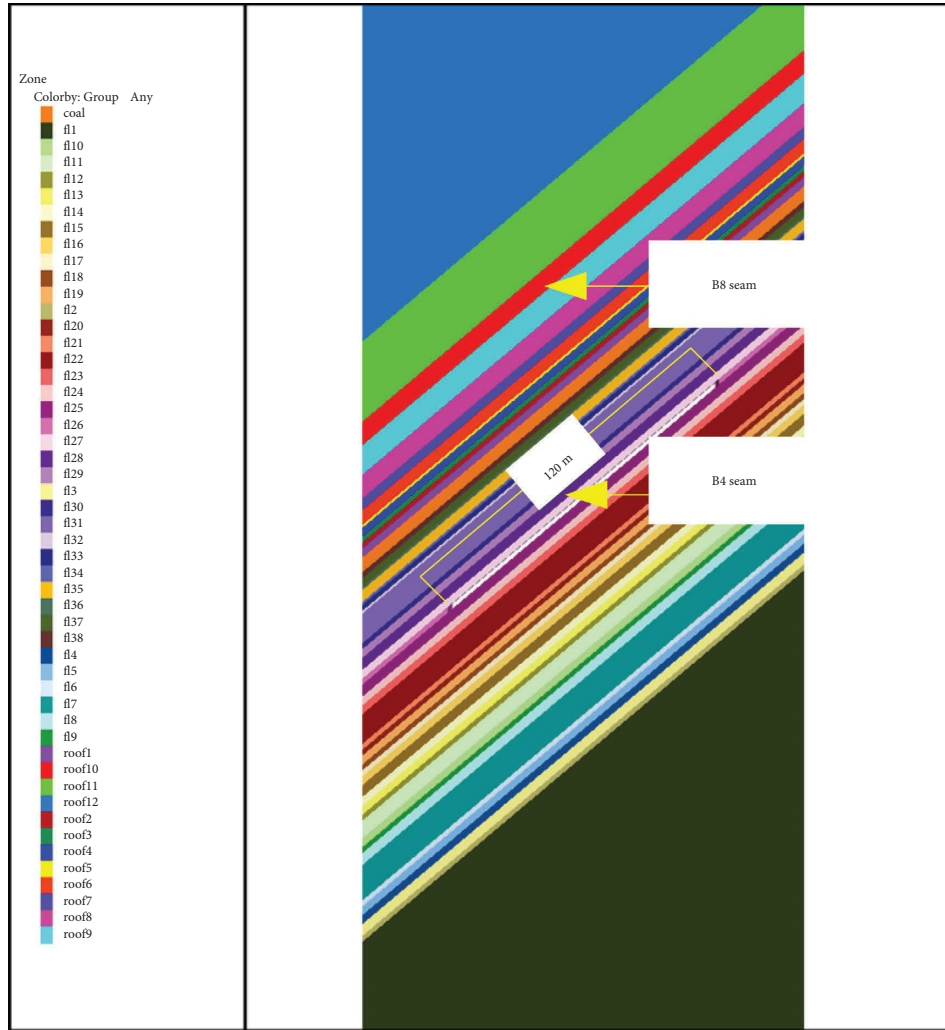


FIGURE 12: Simulation model diagram.

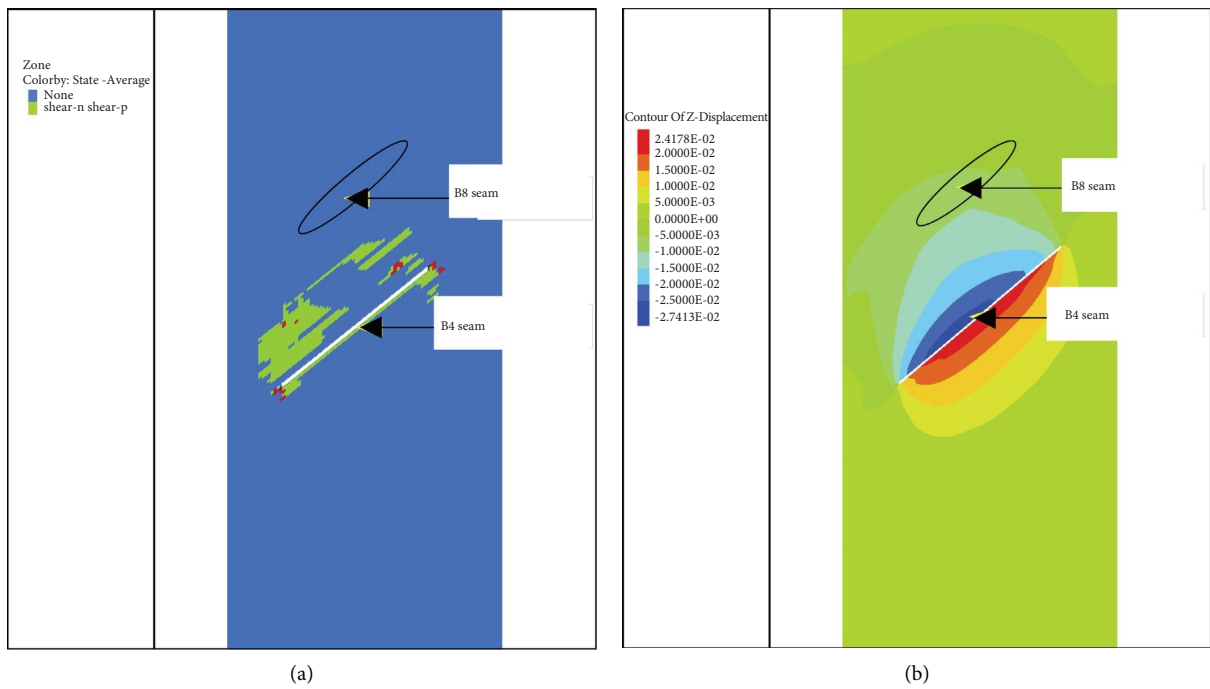


FIGURE 13: Continued.

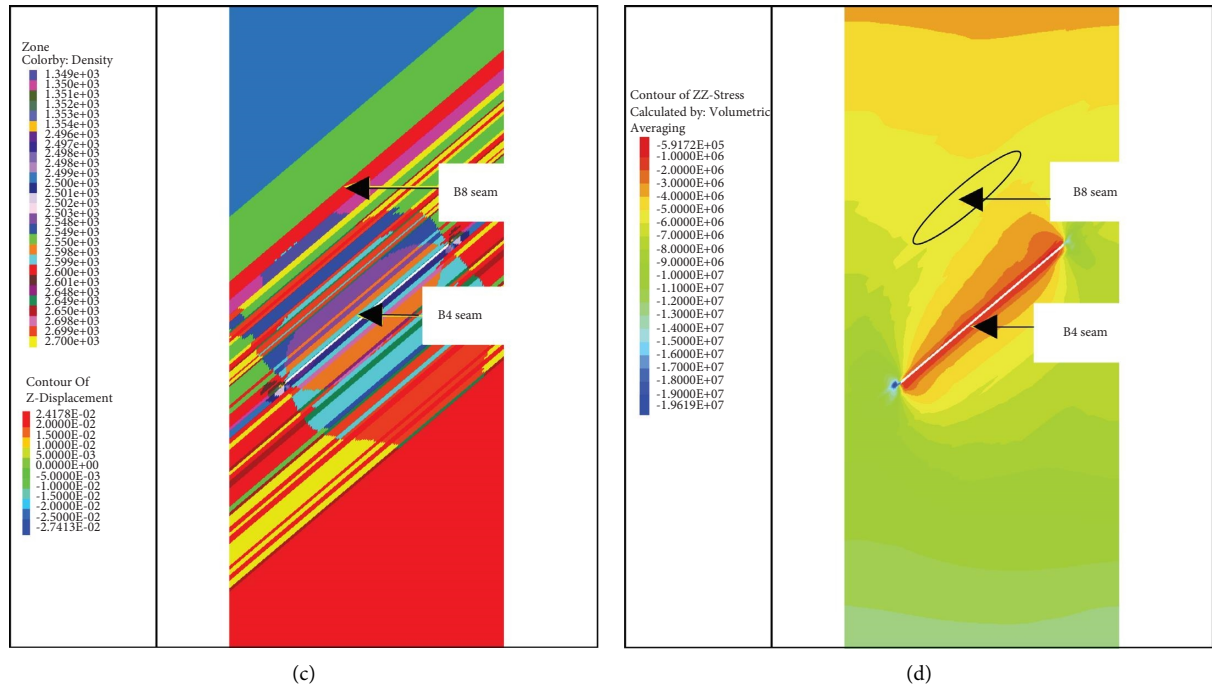


FIGURE 13: Cloud map of the influence of B4 coal seam mining on B8 coal seam: cloud map of (a) plastic zone distribution, (b) vertical displacement distribution, (c) density variation distribution, and (d) vertical stress distribution.

is 700 m, the width is 250 m, the height is 322 m, and the excavation length of the working face is 114 m. The specific model is shown in Figure 14.

First of all, on the basis of the initial model, the working face is excavated 100 m, and the return air roadway of the adjacent lower face is tunneled 100 m. At this point, the distance between the mining face and the heading face is 400 m, and the equilibrium is calculated. After mining 40 m in each working face, the distance between the two sides is shortened by 40 m until the mining face tunnels the heading face; that is, the distance between the two sides is  $-120$  m. The influence of two-sided disturbance is simulated, and some of the results are shown in Figure 15.

As shown in Figure 15, when the mining distance of the working face is 100 m and 180 m, the maximum pressure around the working face is 11 MPa and 13.5 MPa, respectively, which is located on the side of the transport roadway. At this point, the maximum pressure of the return air roadway of the adjacent working face is 6 MPa, and the two sides do not disturb each other. When the mining face is 300 m, the maximum pressure around the working face is 16.3 MPa, which is located on the side of the two roadways. The pressure in front of the working face is less than that of the two roadways, and the maximum value is 11.2 MPa. At this point, the maximum pressure of the return air roadway in the adjacent working face is 6.2 MPa, and there is some disturbance on the two sides. When the mining face is 540 m, the pressure around the working face obviously affects the return air roadway of the adjacent working face.

In order to further reveal the influence of working face mining on the adjacent return air roadway, the numerical simulation results are extracted. When the working face is

advanced at different distances, the maximum pressure around the working face and on the return air roadway is shown in Figure 16.

It can be observed from Figure 16 that the maximum pressure around the working face and above the return air roadway has gone through three stages with an increase in the mining distance of the working face. The first stage is when the mining distance of the working face is less than 260 m. In this stage, the maximum pressure around the working face increases linearly with an increase in the mining distance and the maximum pressure above the return air roadway remains unchanged, so there is no disturbance on both sides. The second stage is when the mining distance of the working face is more than 300 m and less than 500 m. In this stage, the maximum pressure around the working face increases gradually with an increase in the mining distance and the increasing speed gradually slows down; the maximum pressure above the return air roadway increases gradually with an increase in the mining distance but does not increase significantly, so there is a slight disturbance on both sides. The third stage is when the mining distance of the working face is more than 500 m. In this stage, the maximum pressure around the working face changes only slightly with an increase in the mining distance, and the maximum pressure above the return air roadway increases sharply with an increase in the mining distance and gradually approaches the maximum pressure around the mining face, so there is serious disturbance on both sides. According to the results shown in Figure 16, when the distance between the working face and the return air roadway gradually shortens during the advancing process of the working face, the interaction between the two gradually

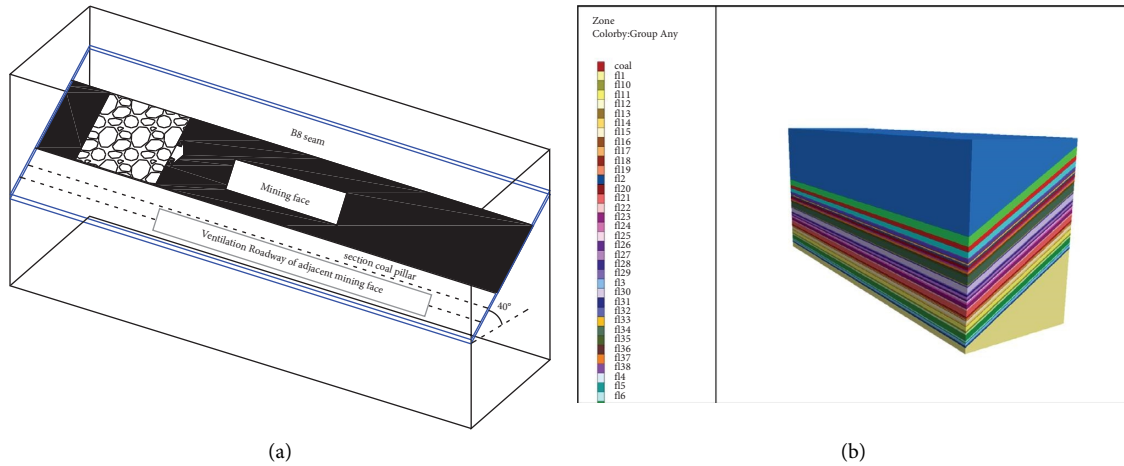


FIGURE 14: Model diagram of the working face and numerical simulation: (a) model diagram of the working face; (b) numerical model diagram of the working face.

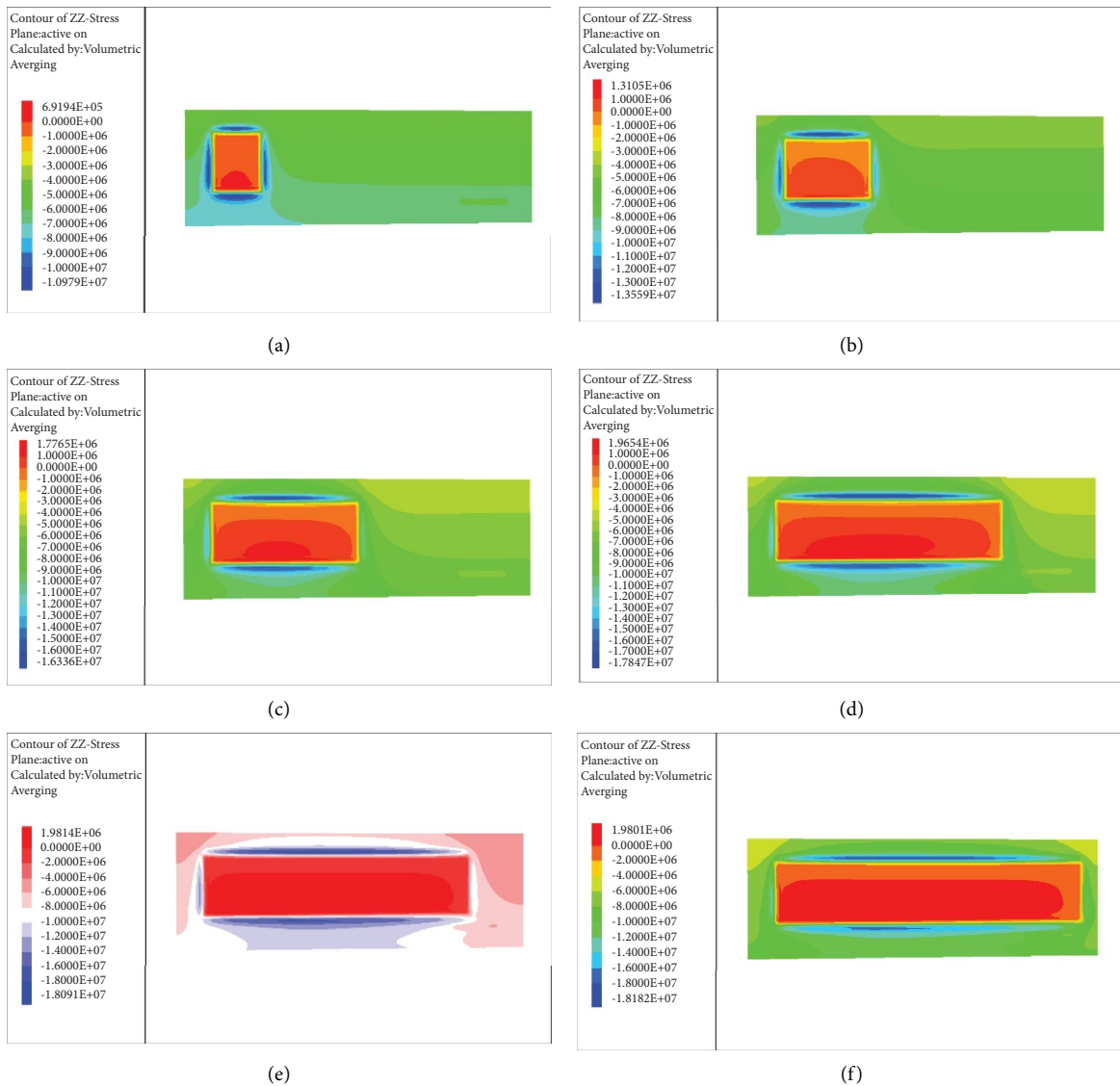


FIGURE 15: Cloud map of vertical stress distribution at different mining distances in the working face: (a) working face mining 100 m; (b) working face mining 180 m; (c) working face mining 300 m; (d) working face mining 460 m; (e) working face mining 540 m; (f) working face mining 620 m.

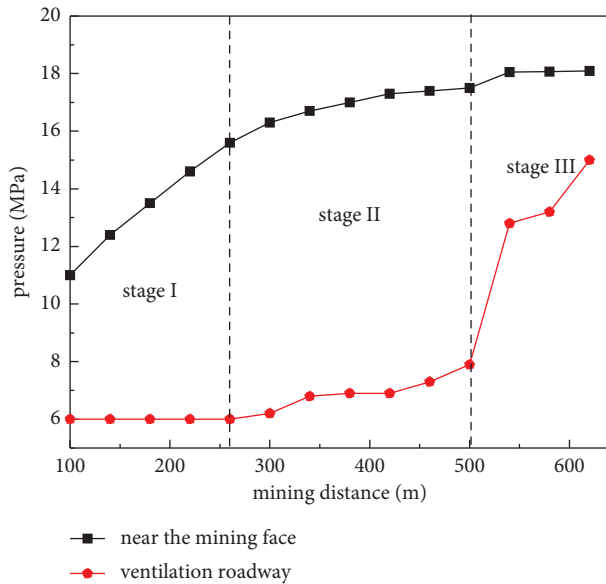


FIGURE 16: Variation of the maximum pressure of the working face and return air roadway with the mining distance of the working face.

increases. At this time, the pressure above the working face and the roadway gradually increases, which may cause a series of safety problems. Therefore, measures such as accelerating the advancing speed of the working face, shortening the roof overhang time, and reducing the top control distance of the working face can be actively taken to reduce the concentration of the abutment pressure. At the same time, when the distance between the working face and the return air roadway is within the range of the third stage, reasonable support measures should be taken.

It is worth noting that the numerical simulation results are obtained according to the specific geological and mining conditions of Xiaogou coal mine. Based on the above analysis, the mining pressure behavior law of the working face, the coal pillar with different widths, and interaction between coal seams in the Xiaogou coal mine mining process are obtained. At the same time, the influence of coal seam mining on the adjacent air return roadway is analyzed. The specific numerical results of the above analysis are only applicable to Xiaogou coal mine, however, the above simulation and theoretical analysis methods can be applied to the mining of large dip coal seams under different geological conditions.

#### 4. Conclusions

Taking the B8 coal seam of Xiaogou coal mine in Nanshan coal mine as the research object, this paper explores the law of pressure behavior in the mining process of steeply inclined coal seams. Through the methods of the theoretical analysis and numerical simulation, this paper delves into the pressure behavior law of the coal pillar above and the section of the mining face in a high-dip coal seam, as well as the interaction between steeply inclined coal seams and the pressure behavior during the interaction between the mining face and adjacent return air roadway. The main conclusions are as follows:

- (1) The range of the plastic zone of the inclined abutment pressure of the working face is related to the dip angle of the coal seam, which is not noticeable when the dip angle of the coal seam is small, but with an increase in the dip angle of the coal seam, the difference in the plastic zone of the abutment pressure between the upper side and the lower side of the coal pillar increases. During the mining of the steeply inclined coal seams, the stress concentration in the lower part of the working face deviates to the roof and the stress concentration in the upper face deviates to the floor, which is obviously different from that in the gently inclined coal seams.
- (2) The vertical stress above the coal pillar in the section changes in three stages with an increase in the width of the coal pillar: In the first stage, the overall bearing pressure of the coal pillar is larger and is on one side of the roadway when the width of the coal pillar is small. In the second stage, with an increase in the width of the coal pillar, the peak stress is far from the roadway and the influence of the roof of the goaf on the roadway begins to decrease. In the third stage, when the width of the roadway coal pillar continues to increase, the stress on the side of the coal pillar is no longer superimposed on each other. Therefore, based on the numerical simulation results and the recovery rate, this paper proposes a reasonable solution of leaving section coal pillars; that is, the coal pillar width of the second stage is taken as the section coal pillar width. Through the numerical simulation and theoretical analysis, the reasonable width of the section coal pillar is analyzed quantitatively, and the results are consistent, which show the reliability and stability of this method. When mining the working face of large inclined seams on-site, corresponding pressure relief measures should be taken at the lower roof and upper floor of the working face to reduce the effect of the abutment pressure.
- (3) In the process of mining steeply inclined coal seams, the maximum pressure around the working face and above the return air roadway goes through three stages with an increase in the mining distance of the working face: the stage of no mutual influence, the stage of slight mutual influence stage, and stage of serious mutual influence. When the distance between the working face and the return air roadway is within the range of the third stage during the field mining of large dip coal seams, measures such as speeding up the advancing speed of the working face, shortening the roof extension time, and reducing the control distance of the top of the working face should be taken to reduce the top surface pressure concentration. At the same time, reasonable support measures shall be taken.

#### Data Availability

The data can be obtained from the corresponding author on request.

## Conflicts of Interest

The authors declare that they have no conflicts of interest.

## Acknowledgments

This study was supported by the National Science Foundation for Young Scientists of China (Grant no. 52004170).

## References

- [1] J. Zhang, J. Wang, W. Weijie, C. Yi, and Z. Song, "Experimental and numerical investigation on coal drawing from thick steep seam with longwall top coal caving mining," *Arabian Journal of Geosciences*, vol. 11, no. 5, pp. 1–19, 2018.
- [2] Y. Wu, H. Jingyu, P. Xie, B. Hu, and K. Liu, "Mechanism of instability of section coal pillar in steeply dipping seam based on large-scale strata control technology," *Journal of China Coal Society*, vol. 43, no. 11, pp. 3062–3071, 2018.
- [3] W. Yang, B. Lin, Y. Qu et al., "Mechanism of strata deformation under protective seam and its application for relieved methane control," *International Journal of Coal Geology*, vol. 85, no. 3-4, pp. 300–306, 2011.
- [4] C. Y. Liu, J. X. Yang, and F. F. Wu, "A proposed method of coal pillar design, goaf filling, and grouting of steeply inclined coal seams under water-filled strata," *Mine Water and the Environment*, vol. 34, no. 1, pp. 87–94, 2015.
- [5] S. L. Zaitsev, "Physiological evaluation of the work of facemen and crew of the combine brigade in the Donbass mines with steeply sloping coal seams," *Gigiena Truda i Professionalnye Zabolevaniia*, vol. 15, no. 3, pp. 24–27, 1971.
- [6] F. Ren, X. Lai, and M. Cai, "Dynamic destabilization analysis based on AE experiment of deep-seated, steep-inclined and extra-thick coal seam," *Journal of University of Science and Technology Beijing, Mineral, Metallurgy, Material*, vol. 15, no. 3, pp. 215–219, 2008.
- [7] D. Deb, C. Sunwoo, and Y. Jung, "Pit optimization for steep coal seams at Pasir coal mine, Indonesia," *Journal of the Korean Society of Mineral and Energy Resources Engineers*, vol. 46, no. 5, pp. 509–520, 2009.
- [8] X. Qi, R. Wang, and W. Mi, "Failure characteristics and control technology of surrounding rock in deep coal seam roadway with large dip angle under the influence of weak structural plane," *Advances in Civil Engineering*, vol. 2020, Article ID 6623159, 17 pages, 2020.
- [9] H. Tu, S. Tu, D. Zhu, D. Hao, and K. Miao, "Force-fracture characteristics of the roof above goaf in a steep coal seam: a case study of xintie coal mine," *Geofluids*, vol. 2019, Article ID 7639159, 11 pages, 2019.
- [10] P. Yang and C. Liu, "Failure law and control technology of surrounding rock in fully mechanized mining gateway of steep seam," *Disaster Advances*, vol. 6, pp. 172–181, 2013.
- [11] T. Hong-Sheng, T. Shi-Hao, Z. Cun, Z. Lei, and Z. Xiao-Gang, "Characteristics of the roof behaviors and mine pressure manifestations during the mining of steep coal seam," *Archives of Mining Sciences*, vol. 62, no. 4, pp. 871–891, 2017.
- [12] J. Wu, H. Jing, Y. Gao, Q. Meng, Q. Yin, and Y. Du, "Effects of carbon nanotube dosage and aggregate size distribution on mechanical property and microstructure of cemented rock-fill," *Cement and Concrete Composites*, vol. 127, Article ID 104408, 2022.
- [13] C. Xue, A. Cao, G. Wenhao et al., "Energy evolution law and rock burst mechanism of deep thick seams with large inclination," *Journal of Mining and Safety Engineering*, vol. 38, no. 5, pp. 876–885, 2021.
- [14] W. B. Lu, Y. Wu, J. Chen, and H. Fu, "Safety analysis of tunnel in gob of high steep thick coal seam (1)-2-D numerical simulation for response," *Applied Mechanics and Materials*, vol. 71–78, pp. 1532–1538, 2011.
- [15] J. Zhang and W. Shi, "Deformation and failure features of surrounding rock for combining mining in steep and close seam," *Applied Mechanics and Materials*, vol. 327, pp. 338–341, 2013.
- [16] H. Zhang, L. Xu, M. Yang, C. Deng, and Y. Cheng, "Pressure relief mechanism and gas extraction method during the mining of the steep and extra-thick coal seam: a case study in the yaojie No. 3 coal mine," *Energies*, vol. 15, no. 10, pp. 3792–3817, 2022.
- [17] Y. Wu, P. Xie, and S. Ren, "Analysis of spatial asymmetric structure characteristics of surrounding rock in large dip seam mining," *Journal of Coal Industry*, vol. 35, no. 2, pp. 182–184, 2010.
- [18] G. Xie, K. Yang, and Q. Liu, "Study on distribution laws of stress in inclined coal pillar for fully-mechanized top-coal caving face," *Chinese Journal of Rock Mechanics and Engineering*, vol. 25, no. 3, pp. 545–549, 2006.
- [19] J. Xie and J. Xu, "Effect of key stratum on the mining abutment pressure of a coal seam," *Geosciences Journal*, vol. 21, no. 2, pp. 267–276, 2017.
- [20] J. Cao, "Study on reasonable size of coal pillars in large dip angle coal seam," in *Proceedings of the 2019 International Conference on Environmental Protection*, pp. 71–74, Coal Industry and Metallurgical Mine Safety, Rome, Italy, April 2019.

## Research Article

# Exploration of Tunnel Lining Falling Block Remediation Using Polyurea Material

Changyu Yang,<sup>1</sup> Xun Yuan ,<sup>1</sup> Fang Wang,<sup>1</sup> Yong Zhu,<sup>1</sup> Ang Chen,<sup>1</sup> Jieyuan Zheng,<sup>1</sup> Yi Yang,<sup>2</sup> Hui Wang,<sup>3</sup> and Jijun Guo<sup>3</sup>

<sup>1</sup>China Railway Eryuan Engineering Group Co. Ltd., Chengdu 610031, China

<sup>2</sup>China Railway Chengdu Group Co. Ltd., Chengdu 610081, China

<sup>3</sup>Chongqing Construction Headquarters of China Railway Chengdu Group Co. Ltd., Chongqing 400000, China

Correspondence should be addressed to Xun Yuan; [yuanxun3@ey.crec.cn](mailto:yuanxun3@ey.crec.cn)

Received 27 September 2022; Revised 28 October 2022; Accepted 24 November 2022; Published 17 May 2023

Academic Editor: Fuqiang Ren

Copyright © 2023 Changyu Yang et al. This is an open access article distributed under the Creative Commons Attribution License, which permits unrestricted use, distribution, and reproduction in any medium, provided the original work is properly cited.

Tunnel lining falling blocks can cause great threats to traffic safety, resulting in traffic interruptions or speed limits and endangering operational safety. Traditional lining disease remediation measures have low efficiency and high costs and are time consuming. Combining the research methods used in the literature, indoor testing, and model experiments, a very normal material, namely, polyurea spray film material, is proposed as a means by which to remediate the lining falling block disease in tunnels. A 1:1 tunnel lining structure model was established at the site, and four experimental conditions were tested. The experiments revealed that the tensile stress was less than the tensile strength and that no tensile fracture occurred in the polyurea spray film material under the joint action of the block's self-weight and aerodynamic loads. Factors such as side seam treatment, surface sanding, and spray temperature may influence the bond strength of the polyurea spray film material. In order to remediate the issue of lining blocks falling, we recommended increasing the bond strength between the spray film material and the concrete or increasing the thickness of the polyurea spray film material.

## 1. Introduction

By the end of 2020, China's railway operating mileage reached 145,000 km. A total of 16,798 railway tunnels have been put into operation, with a total length of about 19,630 km. The total length of the high-speed railways that have been put into operation is about 37,000 km, and the total number of tunnels is 3,631, with a total length of about 6,003 km, as shown in Table 1 [1].

The railways have a wide distribution range, a high proportion of tunnels, and complex geological and hydrological conditions [2]. Tunnel lining with high reliability is the key to ensuring the safety of high-speed railways. In recent years, most of the new operating railways have been high-density and high-speed electrified trunk and passenger-dedicated railways [3]. Tunnel lining that contain falling blocks can cause great threats to traffic safety, resulting in traffic interruptions or speed limits, endangering operational safety [4].

In the construction process, under-excavation control, the installation of subwindows into the mold, centralized vibrating, mold grouting, equipment modifications, and construction method improvements are carried out [5]. However, tunnel vault lining back voids, crack leakage, block drops, and other issues continue to appear, threatening the safety of railway traffic seriously [6].

Due to the influence of hydrogeological conditions, terrain, climate, natural disasters, and various unfavorable factors in the design, construction, operation, and management of tunnels can face various issues after being put into use, such as lining cracks and block drops [7]. These issues shorten the maintenance cycle and service life of the tunnel and seriously threaten the safety of traffic and pedestrians in the tunnel [8]. In recent years, safety accidents caused by tunnel diseases have abounded. In 1999, there were three lining block accidents in Japanese railway tunnels [9]. In July 2006, a tunnel in the Boston Central Tunnel Project collapsed

TABLE 1: Statistical table of China's high-speed rail tunnel profile.

High-speed rail status	Tunnel number	Tunnel cumulative length (km)
Under operation	3671	6003
Under construction	1811	2750
Planning	3525	7966

on top of a concrete slab [10]. Once a falling block accident occurs in an operational tunnel, the consequences are often very serious; this has attracted the attention of the transportation departments and tunnel engineering and technical personnel of various countries [11]. They have carried out inspections and treatments of tunnel diseases. Since the concrete block drop accident in the tunnels in Fukuoka Prefecture in June 1999, the Japan Transport Ministry has required the inspection of 3,360 km of tunnels among the 4,826 tunnels that are part of the national railway line [12]. Most of the tunnels in Italy were built in the 1960s, and inspections revealed that a large number had varying degrees of lump-dropping disease due to aging, load variability, environmental influences, and other influences [13].

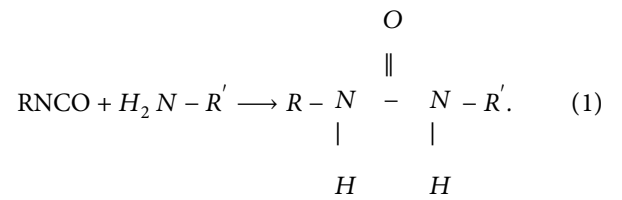
At present, lining disease remediation measures include adding bushings, the integral removal of arches, partial dismantling, polymer repair mortar filling, corrugated plate reinforcement, carbon fiber cloth reinforcement, steel belt plus anchor reinforcement, and lining inner grouting [14]. The existing measures are commonly applied, and the technologies are relatively mature. However, for the operation of tunnels, disease remediation can only be carried out using skylight time. By deducting the inspection time both inside and outside of the tunnel, the actual construction time of each skylight was found to be only a few hours [15]. The construction process, such as cast-in-place concrete or polymer mortar, is complex, the labor operation intensity is large, and the survival speed is slow, resulting in the existing remediation measures having low efficiency and high costs [16].

In view of the skylight operation time being short, time-consuming, inefficient, and with high remediation costs and other issues for existing lining disease remediation, a polymer spray film reinforcement material, namely, polyurea, is proposed in this paper. Tunnel lining disease can be rectified through surface spraying and other means. At present, there is little use of polyurea in railway engineering. It is mostly used for bridge deck waterproofing. This study combines the working environment and disease remediation requirements of tunnel lining and adopts the research methods used in the literature, such as indoor testing and model testing, to study the material performance indicators, construction process, mechanical equipment configuration, acceptance standards, construction efficiency, and economic efficiency. Finally, a complete set of spray film reinforcement technologies and construction methods for lining disease remediation are formed.

## 2. Application Status of Polyurea Spray Film Materials

*2.1. Function Mechanism.* Polyurea materials are polymers based on the chemical reaction of isocyanates, which are

generated by the reaction of isocyanates with amino compounds [17]. The reaction of isocyanate with amines is part of the gradual addition and polymerization of hydrogen transfer, which is caused by the nucleophilic center of the amine attacking the positive carbon ions of the isocyanate group [18]. The hydrogen atoms in the active hydrogen compound are transferred to the N atoms in the -NCO group, and the remaining groups and carbonyl C atoms are combined to form a urea group, the essence of which is the reaction of the semi-prepolymer with the amino polyether and amine chain extender [19]. Due to the high activity of amino polyether and the alkalinity of the N atom, the reaction does not require a catalyst and can be cured and formed in a very short time. The reaction process is shown in the following formula (1):



The formation principle of spray film is impact mixing. The A and R component liquids with high reactivity collide with each other under a high-pressure drive. The liquids are mixed by turbulence in the gun body mixing room, atomized by the spray gun, and then mixed evenly and sprayed on the substrate surface in a very short application period. Finally, an overall seamless polyurea elastomer spray layer is formed [20].

Coating adhesion strength refers to the degree of firmness of the coating film and the surface of the substrate, which are bound together by physical and chemical forces [21]. The intensity of the adhesion strength depends on the number of the polymer polar groups and the polar groups on the surface of the substrate in the coating, as well as their interaction, which is mainly determined by chemical bonds, intermolecular forces, and mechanical forces [22]. The essence of adhesion is an interfacial force, including the cohesion of the coating itself and the adhesion of the coating film to the substrate, as well as the internal stress after the coating is formed [23]. Together, these three factors affect the adhesion of the coating to the substrate. Coating cohesion is the characteristic of the coating itself. The adhesion is generated by the physicochemical action of the coating and the substrate [24]. The stress on the coating comes from two aspects: one is caused by external forces, and the other is generated when the film is formed. Therefore, the adhesion of the coating to the substrate is mainly affected by the following two factors:

- (1) The substrate surface treatment, which includes physical and chemical methods. The chemical method is to pickle and then carry out grinding and phosphating. The physical methods include hand sanding, sand blasting, or blasting. Both the physical and chemical methods require close and sufficient contact between the coating substance and the surface

material of the substrate. If there are oil stains, rust, or other substances on the surface of the substrate, these will hinder the close contact between the coating and the surface of the substrate [25]. Therefore, the substrate surface must be treated before coating. In addition, in order to increase the contact area between the coating and the substrate surface, the substrate surface is sand-blasted or shot-blasted to improve the adhesion of the coating to the substrate.

- (2) The spraying temperature. The porosity and fracture rate of the adhesive surface of the coating can have a certain impact on the adhesion of the coating and the corrosion resistance of the coating. Therefore, in the painting process, it is necessary to reduce the porosity of the coating to improve the performance of the coating [26]. Porosity is related to the formulation of the coating on the one hand and the spray temperature on the other hand. The coating process of the paint involves the coexistence of physical and chemical processes. During the coating process, the coating is heated and melted on the substrate while the curing reaction of the epoxy resin occurs. The spraying temperature refers to the temperature of the substrate when the powder is sprayed on the substrate. If the spraying temperature is low, the viscosity of the resin after melting will be high, the gelling time will be long, the curing reaction speed will be slow, the wetting time with the substrate will be long, and the cohesion of the formed coating will be high. On the contrary, if the spraying temperature is high, the resin melt viscosity will be low, the gelling time will be short, the curing reaction speed will be fast, the wetting time with the substrate will be short, and the cohesion of the resulting coating will be low. If considered from the perspective of full wetting of the coating and the substrate, the wetting effect due to low-viscosity and a long wetting time is good. However, low-viscosity and long-term wetting are contradictory in the process of powder coating because the speed of the curing reaction is proportional to the curing temperature. If the spraying temperature is high, the melt viscosity will be low, but the time for cross-linking and curing will be shortened at the same time. It is more important to choose a relatively reasonable temperature in the spraying process. When the shear stress of the coating is greater than the adhesion force of the coating to the substrate, the coating is easily peeled off of the substrate. Increasing the temperature of the coating can improve the movement of the electron cloud, which is conducive to the formation of covalent bonds between the substrate and the coating, thereby improving the adhesion of the coating. However, the porosity of the coating, especially the porosity of the bonded surface, will increase with the increase in the spraying temperature, and the increase in porosity will affect the adhesion of the coating to the substrate [27].

*2.2. Prospect of Polyurea Material for Use in Tunnel Falling Block Disease Remediation.* The advantages of the polyurea protective coating mainly include excellent mechanical properties, 100% solid content (zero VOC), green environmental protection, convenient spraying construction, seamless overlapping, and an ultra-long service life. Due to these excellent properties, spray polyurea elastomer technology has previously been used in structures such as the Boston Subway Tunnel and offshore drilling platforms. Bo [28] studied the corrosion resistance of anticorrosion coatings in different corrosive environments, and the results showed that the corrosion resistance of polyurea coatings in wet and dry circulation, brine soaking, and wet and hot corrosive environments was far superior to the corrosion resistance of polyurethane coatings and epoxy cloud iron coatings. Lü [29] et al. synthesized a new type of polyaspartic polyurea elastomer with polyaspartic acid grease. Through the study of its accelerated aging, dynamic mechanical behavior, and marine aging behavior, it was concluded that polyaspartic polyurea elastomer has good mechanical properties and corrosion resistance. Liu [30] studied the resistance to chloride ion permeation of polyurea coatings under stress conditions and without stress, and the results showed that spraying polyurea coatings on concrete surfaces can significantly improve chloride ion permeability. Yang [31] studied the acid and alkali resistance and frost resistance of concrete protected by polyurea coating and polyurethane coating, and the results showed that the acid and alkali resistance and frost resistance of polyurea coating were better than those of polyurethane coating. Li et al. [32] studied the application of polyurea in offshore concrete protection, analyzed the influencing factors of adhesion, studied the corrosion resistance of polyurea protection on the Qingdao Bay Bridge, and discussed the frost resistance and chloride ion permeation resistance of coated concrete. Wang [33] studied the effects of substrate strength, maintenance age, primer type, and temperature and humidity on the adhesion of polyurea coatings on concrete substrates.

Based on the excellent properties of polyurea materials, they have been widely used in China, such as in the Beijing Olympic Venues, Qingdao Jiaozhou Bay Cross-Sea Bridge, Beijing-Shanghai High-Speed Railway, and The Immersed Tube Tunnel part of the Hong Kong-Zhuhai-Macao Cross-Sea Bridge. Polyurea has been recognized by an increasing number of people and has been increasingly applied in major projects. Polyurea technology has gradually become one of the most promising materials of this century. According to the existing research and applications, polyurea spray film reinforcement materials are currently mostly used for waterproofing of new projects in the field of underground engineering. They are less frequently used in tunnel disease remediation, and the only cases mainly concern water leakage. There are many types of railway tunnel diseases, and diseases such as hollows and falling blocks are especially important as they endanger driver's safety. There is no research on or application of polyurea spray film materials in this field. From the perspective of improving the efficiency of rectification and reducing the cost of remediation, the

research on the use of spray film reinforcement materials for tunnel lining disease remediation technology is of very important theoretical significance and practical engineering value.

### 3. Analysis and Assumptions of the Mechanical Properties of Polyurea Materials

*3.1. The Main Function of Polyurea Spray Film Material.* Regarding spray film reinforcement materials used for tunnel lining disease remediation, the main role of polyurea spray film is to cover the lining block to prevent falling blocks and their threat to the safety of driving.

As shown in Figure 1, on the concrete lining with a thickness of  $T$ , there is a circular concrete test block  $AA'BB'$  with a diameter of  $r_1$  and a mass of  $m$ . At the initial moment, the test block is not separated from the lining and is supported by a polyurea elastomer with a diameter of  $r_1 + 2r_2$  and a bond strength of  $\psi$ . It can be seen that the protective effect of the spray polyurea elastomer on the separated concrete test block on the lining is essentially the support force provided by the ring polyurea elastomer with width  $r_2$ , while the polyurea elastomer with the diameter of the  $r_1$  part at the bottom of the test block does not provide force. Therefore, the most dangerous points of the entire care system are point  $A$  and point  $A'$ .

Since the polyurea spray film is a flexible material, the vertical and horizontal directions of the load at point  $A$  and point  $A'$  do not provide the supporting force that the rigid body does. The support of the test block depends on the adhesion of the spray polyurea elastomer and the dragging force of the film after the spray film is disengaged.

*3.2. Loads on the Spray Film Material.* Under different test conditions, the spray film material was mainly subjected to tensile pressure and shear effects caused by the self-weight of the arch drop block and the additional aerodynamic effect.

*3.2.1. Self-Weight of the Arch Drop Block.* When lining block falling occurs, the spray film material must first withstand the gravity applied by the self-weight of the falling block, which is determined by the concrete bulk weight and the size of the test block.

*3.2.2. Aerodynamic Loads.* When the multiple unit (EMU) passes through a short tunnel, the impact of aerodynamic loads on the pressure change inside the vehicle is small, while the impact on the tunnel structure and its ancillary facilities cannot be ignored. The high-speed passage of the train in the tunnel causes a drastic change in the air pressure inside the tunnel, and the aerodynamic effect generated has a great impact on the spray film material. High-speed trains produce an aerodynamic fatigue load when running in the tunnel. The role of the pneumatic fatigue load is to cause the spray film material and the initial stable small crack on the lining to quickly develop. At the same time, new cracks can also occur around the periphery of the existing cracks. The

new cracks extend towards the weak points in the material and connect with the existing cracks, causing macroscopic damage to the material.

*3.3. Stress Model Assumptions.* The antifall block of lining in this study refers to the loosening area of the lining locally. Under the premise of not affecting the overall stability of the lining structure, the spray film material is used to achieve the purpose of creating an antifall block. Focusing on the tensile strength of the spray film and the bonding strength between it and the concrete, the calculation ignores the friction between the test block and the lining wall.

#### 3.3.1. Calculation of the Spray Film Material Force of the Circular Concrete Test Block

*(1) Spray Film Bond Strength When Only the Self-Weight of the Test Block is Considered.* The bonding strength and tensile strength of the spray film material to the lining concrete surface on the concrete test block at the top of the lining is calculated according to the principle of the minimum circumference of the circular boundary, as shown in Figure 2. Combined with the actual situation of the tunnel section, the diameters of the test block  $r_1$  are 0.5 m, 1 m, 2 m, 3 m, 4 m, 5 m, and 6 m, respectively. The thickness is  $T = 0.5$  m, and the concrete bulk weight is  $\gamma = 23$  kN/m<sup>3</sup>. The bond strength of the spray film material  $\psi$  is assumed to be outside the boundary of the falling block according to the force area,  $L_1 = 0.01$  m. The tensile strength is calculated under the assumption that faulting of the block end is  $h_1 = 0.005$  m after spraying, and it is assumed that the material is still within the elastic range at this time.

According to the principle of force balance, in order to prevent the test block from falling, the following conditions must be met:

$$\gamma\pi\frac{r_1^2}{4}T = \pi r_1 L_1 \psi. \quad (2)$$

From this, the calculation formula for the spray film bond stress  $\psi$  is as follows:

$$\psi = \frac{\gamma r_1 T}{4L_1}. \quad (3)$$

*(2) Bond Strength of the Spray Film When Both the Block Weight and Aerodynamic Loads are Taken into Account.* According to the additional pressure recommendation values for auxiliary facilities in tunnels as found in the China high-speed railway design code, the bond strength of the spray film material to the concrete surface is shown in Table 2 under the condition of single and double lines at different speeds.

According to Table 2, the worst operating condition is when trains meet in double lines with a speed of 350 km/h. The bond strength of the sprayed film material to the surface of the lined concrete should be greater than 14.8 kPa

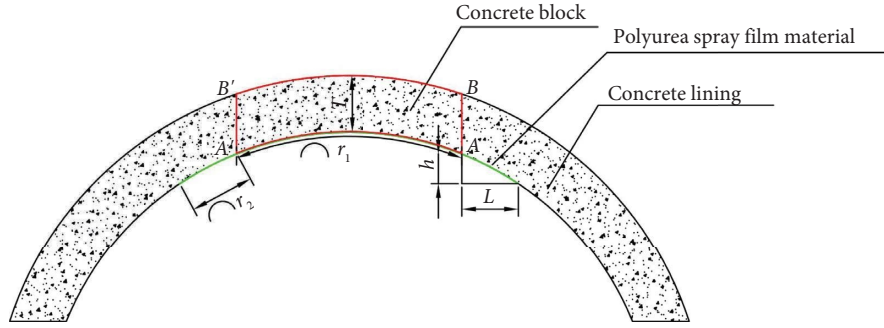


FIGURE 1: Schematic diagram of the calculation of the bearing of the spray polyurea material.

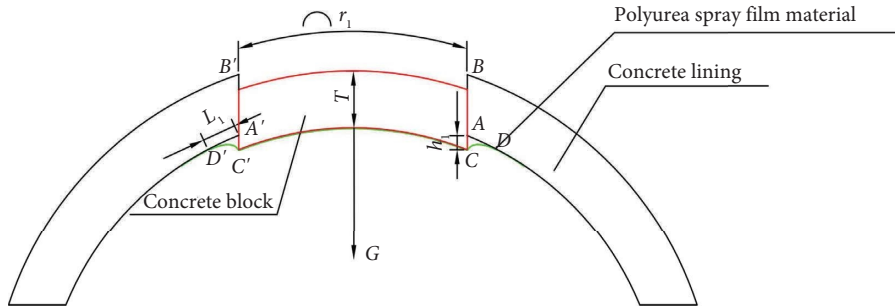


FIGURE 2: Schematic of the calculation when only gravity is considered.

TABLE 2: Additional pressure recommendation values in high-speed rail tunnels.

Nos	Operating condition	Positive peak pressure (kPa)	Passive peak pressure (kPa)	Bond stress requirement (kPa)
1	Single line, 70 m <sup>2</sup> , 300 km/h,	2.6	-3.9	>6.4
2	Single line, 70 m <sup>2</sup> , 350 km/h	3.4	-5.1	>8.5
3	Double lines, 100 m <sup>2</sup> , 300 km/h	1.6	-2.8	>4.4
4	Double lines, 100 m <sup>2</sup> , 350 km/h	2.2	-3.5	>5.7
5	Double lines, 100 m <sup>2</sup> , 350 km/h, trains meet	5.9	-8.9	>14.8
6	Double lines, 92 m <sup>2</sup> , 250 km/h	1.2	-1.8	>3.0
7	Double lines, 92 m <sup>2</sup> , 250 km/h, trains meet	3.5	-5.4	>8.9
8	Single line, 58 m <sup>2</sup> , 250 km/h	2.2	-3.3	>5.5

(0.0148 MPa). Therefore, the aerodynamic loads on the test block under the most unfavorable operating conditions can be calculated as follows:

$$P = 14.8\pi \frac{r_1^2}{4}. \quad (4)$$

A schematic diagram for the calculation of the bond strength of the spray film material, taking into account both the self-weight of the test block and the aerodynamic load, is shown in Figure 3.

Combining equations (3) and (4) with Figure 3, the spray film bond stress calculation formula under this condition is as follows:

$$\psi = \frac{(\gamma T + 14.8)r_1}{4L_1}. \quad (5)$$

(3) *Tensile Strength of the Spray Film When Both the Block Weight and Aerodynamic Loads are Taken into Account.* The

tensile strength  $\xi$  of the spray film is calculated according to Figure 4. When the test block falls, it is caught by the drag action of the spray film. The component of the spray film tension in the vertical direction is canceled out by the gravity and aerodynamic load of the test block, and the components of the ring spray film tension in the horizontal direction cancel each other out. The entire care system reaches a balanced state.

Width of the torn spray film can be calculated as follows:

$$l = \sqrt{L_1^2 + h_1^2}. \quad (6)$$

Angle between spray film and test block can be calculated as follows:

$$\theta = \arctan \frac{L_1}{h_1}. \quad (7)$$

The component of the spray film tension in the vertical direction can be calculated as follows:

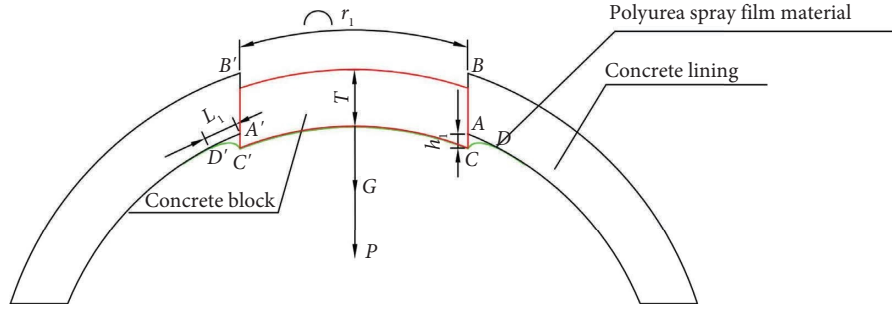


FIGURE 3: Schematic diagram of the calculation of bond stress taking into account both gravity and aerodynamic loads.

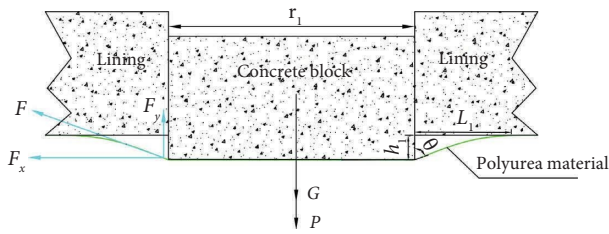


FIGURE 4: Calculation schematic diagram of spray film tensile stress.

$$F_y = F \cos \theta. \quad (8)$$

Spray film tension can be calculated as follows:

$$F = \pi r_1 l \xi. \quad (9)$$

Combining formula (2) and (4) and formula (6)~(9), the tensile stress  $\xi$  of the spray film can be obtained as follows:

$$\xi = \frac{(T\gamma + 14.8)r_1}{4\sqrt{L_1^2 + h_1^2} \cos \arctan L_1/h_1}. \quad (10)$$

(4) *Tensile Strength of the Spray Film When Only the Self-Weight of the Test Block Is Considered.* When only the self-weight of the falling test block is considered, without consideration of the aerodynamic load, the schematic diagram of the force of the spray film support system is shown in Figure 5.

According to equation (10) and Figure 5, the tensile stress of the spray film at this time is calculated as follows:

$$\xi = \frac{T\gamma r_1}{4\sqrt{L_1^2 + h_1^2} \cos \arctan L_1/h_1}. \quad (11)$$

3.3.2. *Calculation of the Spray Film Material Force of the Rectangular Concrete Test Block.* According to the calculation result of the circular falling block, the force condition of the spray film material under the rectangular falling block can also be obtained.

(1) *Spray Film Bond Strength When Only the Self-Weight of the Test Block is Considered.* As can be seen from Figure 2, when the concrete test block is  $r_1$  long and  $r_2$  wide, equation (2) can be converted to

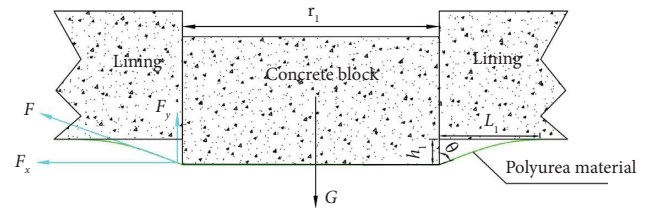


FIGURE 5: Calculation schematic diagram of spray film tensile stress when subjected to gravity alone.

$$\gamma r_1 r_2 T = [(2L_1 + r_1)(2L_1 + r_2) - r_1 r_2] \psi. \quad (12)$$

From this, it is possible to obtain the formula for calculating the bonding stress of the spray film material when considering only the self-weight of the test block:

$$\psi = \frac{\gamma T r_1 r_2}{2L_1(2L_1 + r_1 + r_2)}. \quad (13)$$

(2) *Bond Strength of the Spray Film When Both the Block Weight and Aerodynamic Loads Are Taken into Account.* For rectangular test blocks subject to aerodynamic loads, equation (3) can be converted to

$$P = 14.8 r_1 r_2. \quad (14)$$

The bond stress of the spray film material when both aerodynamic loads and the self-weight of the test block are taken into account can be calculated by combining formula (13) and formula (14):

$$\psi = \frac{r_1 r_2 (\gamma T + 14.8)}{2L_1(2L_1 + r_1 + r_2)}. \quad (15)$$

(3) *Tensile Strength of the Spray Film When Both the Block Weight and Aerodynamic Loads Are Taken into Account.* Assuming that the spray film material at this time is still in the elastic stage and is not damaged by plastic stretching, the spray film area  $S$  squeezed out by the test block is as follows:

$$S = 2(r_1 + r_2)l. \quad (16)$$

The tensile stress calculation formula of the spray film material under this condition can be obtained as follows:

$$\xi = \frac{(T\gamma + 14.8)r_1r_2}{2(r_1 + r_2)\sqrt{L_1^2 + h_1^2} \cos \arctan L_1/h_1}. \quad (17)$$

(4) *Tensile Strength of the Spray Film When only the Self-Weight of the Test Block is Considered.* At this point, the aerodynamic load is subtracted in equation (17) to obtain the tensile stress calculation formula for spray film materials that only consider the self-weight of the test block:

$$\xi = \frac{T\gamma r_1 r_2}{2(r_1 + r_2)\sqrt{L_1^2 + h_1^2} \cos \arctan L_1/h_1}. \quad (18)$$

3.4. *The Main Required Mechanical Properties of Spray Film Materials.* The mechanical properties of the spray film material should be calculated according to the most unfavorable circular test block to provide a sufficient safety factor in actual construction. Based on this principle, the calculation results are described below.

#### 3.4.1. Circular Test Block

(1) *When only Self-Weight is Considered.* The calculation results are shown in Table 3.

The results show that the minimum bond strength of the sprayed film material and the lining concrete is positively correlated with the diameter of the falling block. The theoretical analysis suggests that the minimum bond strength requirement is no less than 1.73 MPa and that the minimum tensile strength is no less than 3.45 MPa.

(2) *When Both Self-Weight and Aerodynamic Loads Are Considered.* The calculation results are shown in Table 4. According to the analysis of the calculation results, the single-hole, double-line 100 m<sup>2</sup> tunnel with a speed of 350 km per hour when trains meet is the most unfavorable working condition. The required minimum bond strength is no less than 3.95 MPa, and the minimum tensile strength is no less than 7.89 MPa.

Considering the aerodynamic effect, the dragging effect of the spray film layer on the falling block, and the use of the spray film layer to ensure that the lining cracks meet the specification limits, it is recommended that the bonding strength of the spray film material and the concrete be no less than 3.95 MPa and that the tensile strength of the spray film material be no less than 7.89 MPa. In addition, if the structure is subjected to a large external force load and needs to meet the crack width limit requirements, the tensile strength of the spray film material still needs to be analyzed according to the specific force situation.

#### 3.4.2. Rectangular Test Block

(1) *When Only Self-Weight is Considered.* The calculation results after the substitution of the parameters are shown in Table 5.

TABLE 3: Mechanical indicators of film spray film materials for circular falling blocks under self-weight.

Nos	Block diameter (m)	Minimum bond strength (MPa)	Minimum tensile strength (MPa)
1	0.5	0.14	0.287
2	1.0	0.29	0.575
3	2.0	0.58	1.150
4	3.0	0.86	1.725
5	4.0	1.15	2.300
6	5.0	1.44	2.875
7	6.0	1.73	3.450

The theoretical analysis suggests that the minimum bond strength requirement is no less than 1.565 MPa and that the minimum tensile strength is no less than 1.69 MPa when only the self-weight of the test block is taken into account.

(2) *When Both the Self-Weight and Aerodynamic Loads Are Considered.* The calculation results are shown in Table 6.

It can be seen that for rectangular lining drop blocks, the bonding strength of the spray film material should not be less than 3.580 MPa and the tensile strength should be no less than 3.865 MPa when considering both the self-weight and aerodynamic load of the test block.

## 4. Lining Disease Remediation Model Experiment Using Polyurea Spray Film Material

In order to verify the actual strength of the spray film material under the action of the self-weight of the concrete test block and aerodynamic load and whether it can support the tunnel lining block to achieve the purpose of disease remediation, a 1:1 tunnel lining structure model was established at the site to simulate the disease of the tunnel lining block. Through this model experiment, the consistency of the material performance indicators and the theoretical analysis were verified, and the antilining blocking effect of the polyurea spray film material was clarified.

### 4.1. Model Experiment Scheme

4.1.1. *Purpose of the Experiment.* According to the construction of the tunnel model and the construction process of spray film reinforcement, a total of four working-condition experiments were carried out. The lining thickness was 0.5 m with a rectangular test block of 2 × 3 m in size and a circular test block of  $\Phi = 2$  m in diameter. The thickness of the polyurea spray film in each set of test blocks was 5 mm, and the spray film was extended along the edge of the test block for 2 m, as shown in Figure 6. Sandbags were used in the test to simulate aerodynamic loads.

When implemented, the on-site cast-in-place reinforced concrete test model was poured 20 m at a time, and the facility joint was installed every 10 m with a waterstop belt. When the concrete was poured, it was divided by steel plates to form an independent test block, which was suspended

TABLE 4: Spray film bond stress and tensile strength requirements under different circular drop diameters.

No	Block diameter (m)	Minimum bond strength (MPa)	Minimum tensile strength (MPa)
1	0.5	0.33	0.6575
2	1.0	0.66	1.315
3	2.0	1.32	2.630
4	3.0	1.97	3.945
5	4.0	2.63	5.260
6	5.0	3.29	6.575
7	6.0	3.95	7.890

TABLE 5: Mechanical indicators of film spray film materials for rectangular falling blocks under self-weight.

Nos	Block size (m)	Minimum bond strength (MPa)	Minimum tensile strength (MPa)
1	1 × 2	0.381	0.413
2	2 × 3	0.687	0.620
3	3 × 4	0.983	1.062
4	4 × 5	1.275	1.377
5	5 × 6	1.565	1.690

TABLE 6: Spray film bond stress and tensile strength requirements under different rectangular drop sizes.

Nos	Block size (m)	Minimum bond strength (MPa)	Minimum tensile strength (MPa)								
1	1 × 2	0.871	0.945								
2	2 × 3	1.572	1.700								
3	3 × 4	2.248	2.430 </tr <tr> <td>4</td> <td>4 × 5</td> <td>2.916</td> <td>3.149</td> </tr> <tr> <td>5</td> <td>5 × 6</td> <td>3.580</td> <td>3.865</td> </tr>	4	4 × 5	2.916	3.149	5	5 × 6	3.580	3.865
4	4 × 5	2.916	3.149								
5	5 × 6	3.580	3.865								

under the gantry crane after reaching the edge. The polyurea material was sprayed on the inner edge of the arch to simulate the remediation of lining diseases. After the polyurea spray film material reached its strength, the suspension was lifted; thus, the disease of the tunnel lining falling block was simulated. The testing and monitoring was carried out at the same time.

**4.1.2. Experimental Conditions.** According to the purpose of the model test and the actual service status of the tunnel lining, the shape of the test block was considered according to the most unfavorable consideration. Therefore, the rectangular and circular test blocks were adopted. The experimental conditions are shown in Table 7.

#### 4.2. Model Experimental Structural Design

**4.2.1. Model Size.** According to the model test scheme, the China Reference Diagram of the Lining Structure of a two-line tunnel at a Speed of 160 km/h was used as the benchmark for the real simulation of the tunnel structure. The inner contour of the tunnel is shown in Figure 7.

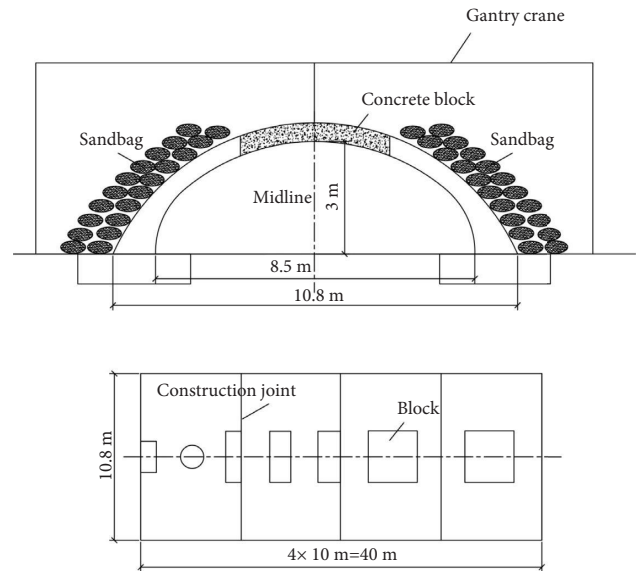


FIGURE 6: Schematic diagram of the model experiment.

We mainly studied the remediation effect of polyurea spray film material on lining block drop disease, focusing on verifying the supporting effect of polyurea spray film material. Due to the certain randomness of the actual tunnel lining block drop disease, the model test considered the most unfavorable working conditions, and the drop block was set with the tunnel vault position. Considering the operating space requirements in the model, the headroom height in the model was set to 3 m, thus determining the model height. Unlike the surrounding rock constraints around the actual tunnel, the bottom of the test model had a large arch foot structure, and a bar foundation and antishear keys were set in the upper part of the arch foot to resist the horizontal thrust of the model arch foot and to ensure safety.

The dimensions of the test model are shown in Figure 8.

**4.2.2. Structural Calculation.** According to the test scheme, there were two types of loading conditions for the test model: self-weight and self-weight + aerodynamic load. The most unfavorable working conditions were self-weight + aerodynamic load, and the structural calculation was carried out according to this working condition. The additional surface loads formed by personnel and equipment on the surface of the model under the loading conditions were considered at the same time. The structural

TABLE 7: Summary of experimental conditions.

Nos	Block shape	Block size	Spray film thickness (mm)	Epitaxial range (m)	Block weight	Aerodynamic loads	Note
1	Circle	$\Phi 2$ m	5	2	✓	✓	Crack epoxy consolidation + surface epoxy consolidation + the surface is sprayed with polyurea
2	Rectangle	$2 \times 3$ m	5	2	✓	✓	The surface is sprayed with polyurea
3	Rectangle	$2 \times 3$ m	5	2	✓	✓	Crack epoxy consolidation, destruction test
4	Circle	$\Phi 2$ m	5	2	✓	✓	Crack epoxy consolidation + surface epoxy consolidation + the surface is sprayed with polyurea, destruction test



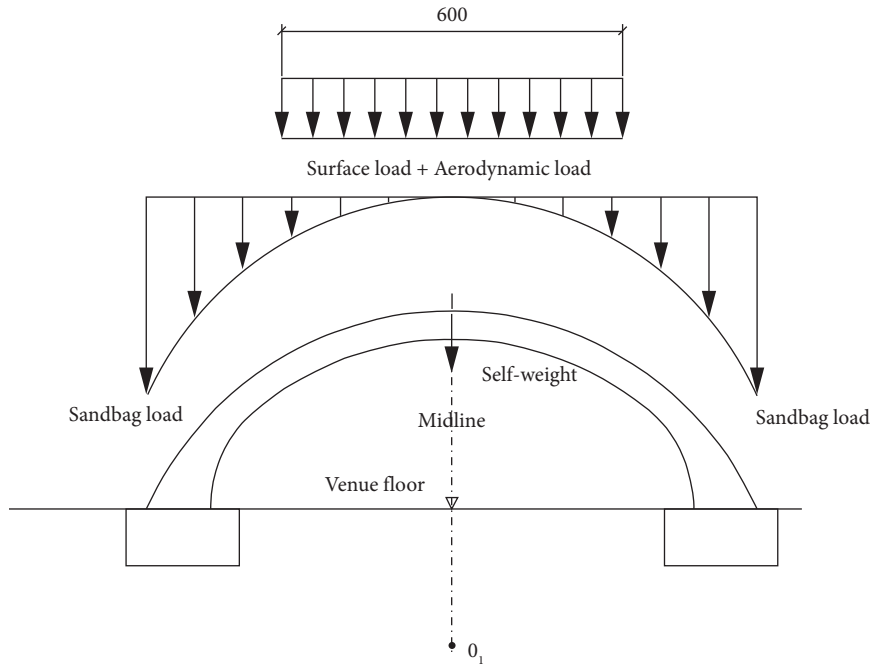


FIGURE 9: The designed model structure load.

TABLE 8: Structural calculation loads.

Model self-weight standard value (kN·m <sup>3</sup> )	Aerodynamic loads (kPa)	Additional surface loads for personnel and equipment (kPa)	Sandbag load (kN·m <sup>3</sup> )
25	15	10	20

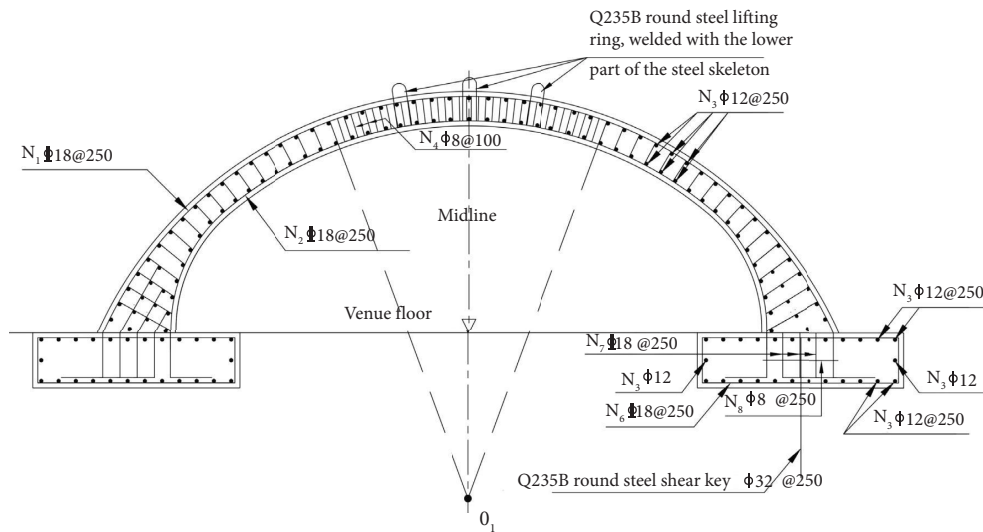


FIGURE 10: Model structure reinforcement diagram.

(2) *Safety Control.* The inside, outside, and test blocks of the tunnel model were fully enclosed and isolated by metal mesh, and safety warning signs were set up to ensure the safety of on-site construction workers and test personnel, as shown in Figure 12.

4.3.2. *Polyurea Material Spraying.* After the base surface treatment of the bottom and edge seam extension of the circular test block, 5 cm of epoxy consolidation material was infused at the edge gap between the test block and the incision. The substrate was sprayed with epoxy



FIGURE 11: Construction of the experiment model. (a) Lining formwork installation of the first plate. (b) Concrete pouring of the first plate. (c) Lining formwork installation of the second plate. (d) Concrete pouring of the second plate.



FIGURE 12: Construction safety control. (a) Tunnel model entrance isolation. (b) Tunnel model internal isolation. (c) The tunnel model was fully enclosed and isolated. (d) Warning signs around the vault test block.

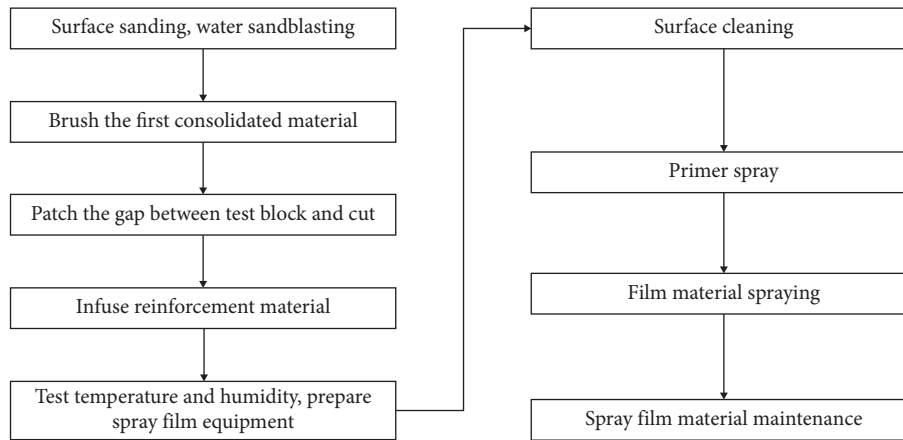


FIGURE 13: Process of polyurea material spraying.

consolidation materials, followed by primers and polyurea spray materials. The specific process is shown in Figures 13–15.

#### 4.4. Simulation Test under Different Working Conditions

**4.4.1. Tensile Stress of Polyurea Material Spray Film.** The tensile stress of the polyurea spray film material can be analyzed by testing the elastic strain of the spray film material at the measuring point under each loading condition, for which the resistive strain gauges were used to test the elastic strain of the polyurea spray film material under the corresponding loading conditions.

The arrangement of the measuring points for spray film material near the inner surface of the tunnel on the rectangular and circular test blocks and the pasting method of the strain gauges at the measuring points are shown in Figures 16 and 17, respectively.

**4.4.2. Block Sinking Measurement.** In the model test, the amount of vault sinking and staggering that occurs when the test block of the tunnel arch is supported and reinforced by the spray film material can be tested using a total station and a steel ruler, respectively. The test method for determining the amount of sinking of the test block vault and the amount of misalignment between the test block and the surrounding lining is shown in Figure 18.

The amount of vault sinking  $h_i$  can be obtained by measuring the height difference between the tunnel model vault measurement points  $A$ ,  $B$ , and  $C$  during the experimental loading process.

**4.4.3. Misalignment between the Block and Surrounding Concrete.** The misalignment  $\Delta h$  between the test block and the surrounding concrete lining in the tunnel model can be obtained by the displacement amount that occurs before and after the sinking of the test block on measurement points  $A$  and  $B$ . The specific test method is shown in Figure 19.

## 5. Experimental Results

### 5.1. Results of Experimental Condition 1

**5.1.1. The Bond Strength between the Polyurea Material and Concrete Surface.** According to the test results at different points, the average bond strength of working condition 1 was 3.83 MPa.

**5.1.2. Polyurea Material Spray Film Thickness.** According to the test results at different points, the average spray film thickness in working condition 1 was 5.7 mm.

**5.1.3. Tensile Strain and Stress of Spray Film Material.** For the cylindrical test block supported and reinforced by spray film material with a thickness of 5 mm, the largest strain values were at measuring points  $D$  and  $G$ , as shown in Figure 16(b). The spray film material was in a tensile state along the tunnel ring and in the axis direction. Taking the strain at points  $D$  and  $G$  as an example, the relationship curve of the longitudinal tensile strain with time at point  $D$  is shown in Figure 20, and the relationship curve of the lateral tensile strain with time at point  $G$  is shown in Figure 21.

As can be seen from Figures 20 and 21, under the load condition of the test block weight and with an additional load of about 8.6 t, the maximum tensile strain measured at points  $D$  and  $G$  was  $\varepsilon_t = -42.65 \mu\varepsilon$ .

According to the field test conditions, the test time under the action of the arch test blocks and sandbags with a self-weight of about 8.6 t lasted for almost 80 min. During this test, the spray film materials were in the linear elastic deformation stage, and no plastic yield or brittle fracturing occurred. The spray film material modulus of tensile elasticity  $E$  after curing was about 8 MPa. According to the stress and strain relationship of the spray film material in the elastic stage after curing, the tensile stress  $\sigma_t$  of the central part of the spray film material can be obtained as follows:

$$\sigma_t = E\varepsilon_t, \quad (19)$$

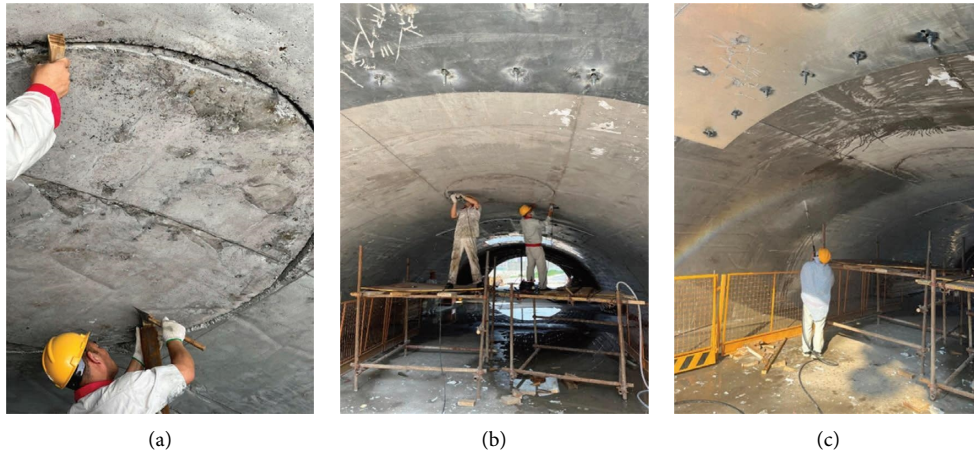


FIGURE 14: Surface treatment. (a) Adjusting the incision. (b) Burnishing. (c) Water sandblasting.

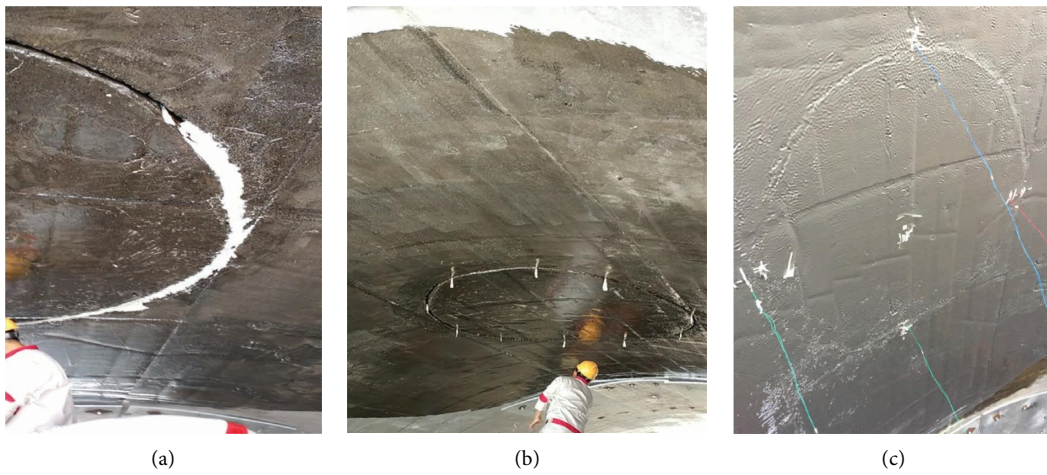


FIGURE 15: Primer spraying. (a) Greasing the side seams. (b) Epitaxial spraying. (c) Final rendering.

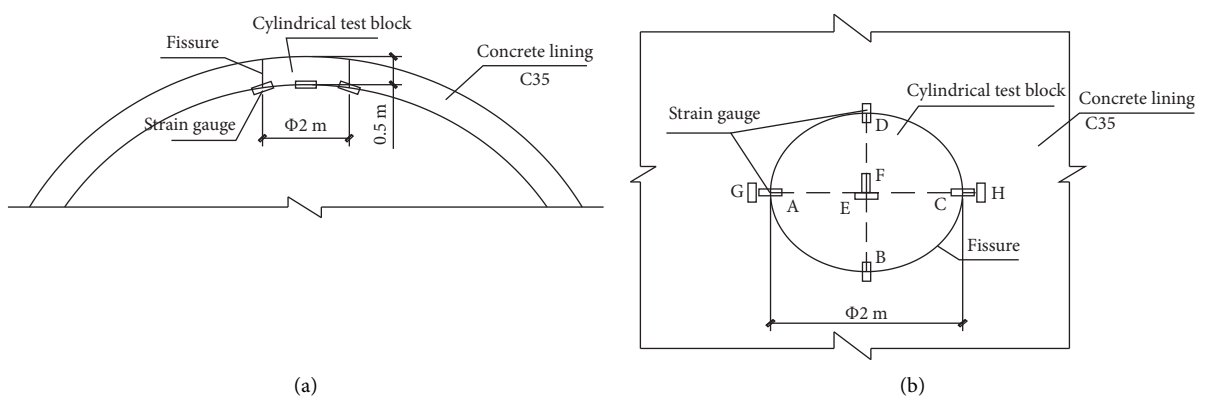


FIGURE 16: Strain measurement points on the spray film material for the circular test block. (a) Front view. (b) Top view.

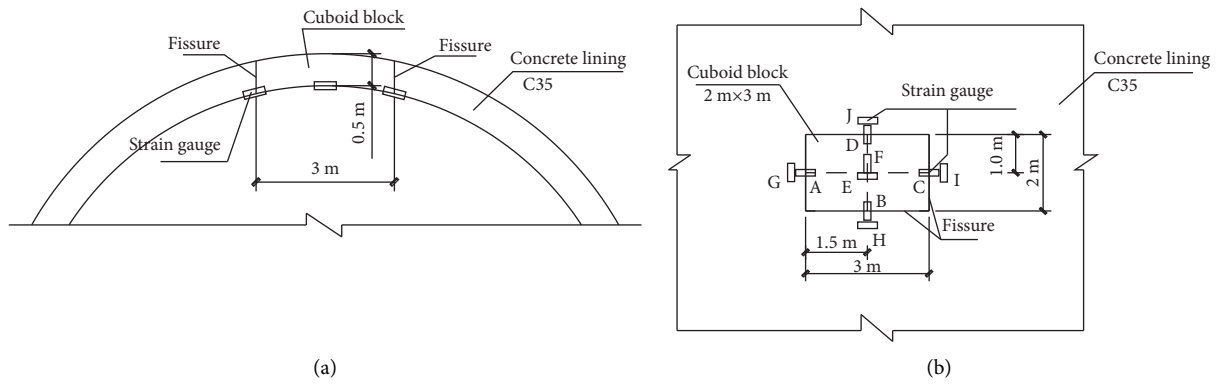


FIGURE 17: Strain measurement points on the spray film material for the rectangular test block. (a) Front view. (b) Top view.

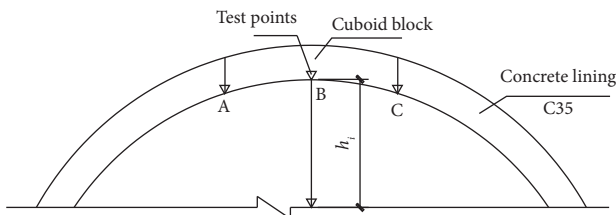


FIGURE 18: Test of lining vault block sinking.

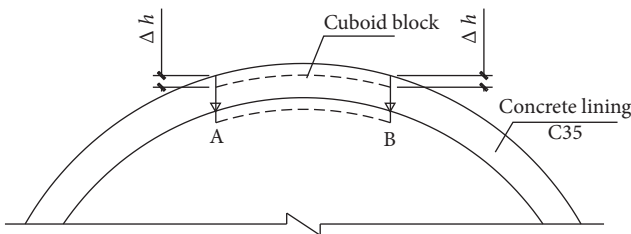


FIGURE 19: Misalignment measurement.

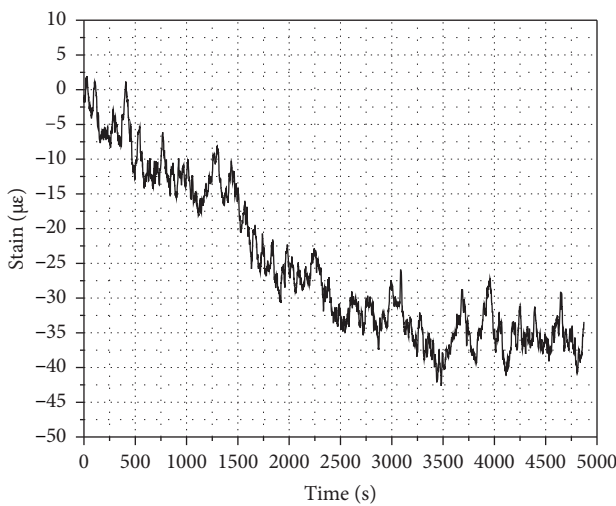


FIGURE 20: Longitudinal tensile strain curve at measurement point D.

where  $E$  is the tension elasticity modulus of the spray film material, MPa, and  $\epsilon_t$  is elastic tensile strain value produced by spray film material,  $\mu\epsilon$ .

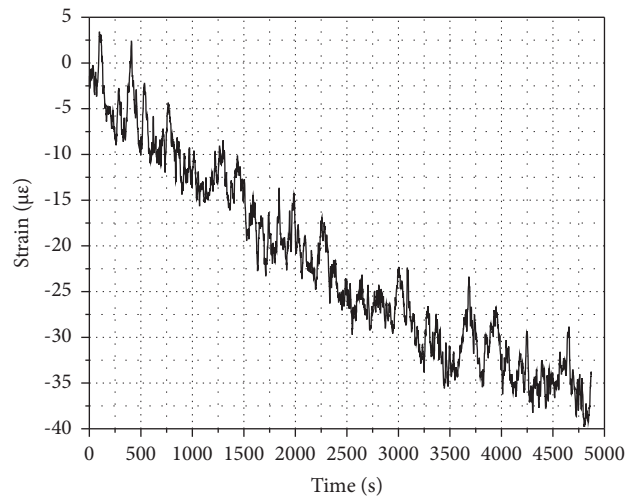


FIGURE 21: Lateral tensile strain curve at measurement point G.

The maximum tensile stress at point  $D$  can be calculated by equation (19):  $\sigma_t = 0.341$  kPa.

The tensile strength of the spray film material measured in the laboratory was 13 MPa. It can be seen that under the joint action of the  $\Phi 2.0$  m cylindrical test block with a sandbag with a weight of about 8.6 t, the maximum tensile stress ( $\sigma_t = 0.341$  kPa) of the spray film material with a thickness of 5 mm was much less than the tensile strength.

Due to the infusion of epoxy consolidation materials in the cracks, the adhesion force between the test block and the concrete around it was far greater than the weight of the test block and the load. There were no sinking or misalignment phenomena in the test block after the sling was detached. Therefore, the role of the spray polyurea in lifting the test block and the total weight of the load was not played out at all.

It was found that the 5 mm thick spray film material in the test could withstand a cylindrical test block of  $\Phi 2 \times 0.5$  m and an aerodynamic load of 8.6 t. The tensile stress was much smaller than the tensile strength, and no tensile yield or brittleness failure occurred in the spray film material during the test.

The stress analysis of the spray film material tested in working condition 1 showed that the spray film material with a thickness of 5 mm was pulled along the tunnel loop



FIGURE 22: The state of the spray film material in the inner wall of the tunnel after loading.

and the tunnel axis under the combined effect of the test block gravity and the aerodynamic effect of the high-speed railway tunnel. The spray film material was in a tensile state, and the maximum tensile stress at the measuring point was less than the tensile strength of the spray film material.

**5.1.4. Misalignment between the Block and Lining.** Because the test block did not sink during loading condition 1, its sinking amount was zero, and the amount of misalignment was also zero. The condition of the spray film surface during loading is shown in Figure 22.

Based on the model test of the tunnel lining reinforced with a spray film material with a thickness of 5 mm, combined with the analysis of the strain and stress test, the following conclusions were reached. The tensile stress was between 0.264 and 0.341 kPa under the action of the lining arch drop and the aerodynamic effect of the high-speed railway tunnel with a load of 8.6 t on the spray film material with a thickness of 5 mm. The spray film material was in a pulled state along the tunnel ring and the tunnel axis. The tensile stress of the 5 mm spray film material in the model test condition was less than its tensile strength of 13 MPa. This shows that the spray film material with a thickness of 5 mm was able to bear the combined effect of the tunnel arch lining block and aerodynamic effect without shear or tensile failure in test condition 1.

## 5.2. Results of Experimental Condition 2

**5.2.1. Bond Strength.** According to the test results at different points, the average bonding strength of working condition 2 was 4.5 MPa.

**5.2.2. Polyurea Material Spray Film Thickness.** According to the test results at different points, the average polyurea spray film thickness in condition 2 was 5.6 mm.

**5.2.3. Tensile Strain and Stress of Spray Film Material.** The dimensions of the rectangular test block used to simulate the lining of the tunnel arch in condition 2 were  $2.0 \times 3.0 \times 0.5$  m. In the test of the spray film material it strained under the combined action of the block self-weight and the aerodynamic effect. The 5 mm thick spray film

material was affected by internal tension stress during loading. At the beginning of the loading, the internal tensile strain and compressive strain were small. The tensile and compressive strain values of each measurement point changed greatly with the increase in the applied loads, and the compressive stress changed from compressive stress to tensile stress. The maximum tensile strain in the spray film material occurred at the moment when the test block was close to sinking. According to the analysis of the spray film material strain value at each measurement point, shown in Figure 17, the strain values at the three points of measurement points A, H, and J were the largest. In the process of loading the spray film material until it sank, the spray film materials at measuring points A, H, and J were in a state of tensile stress. The tensile strain curves for measuring points A, H, and J are shown in Figures 23(a)–23(c), respectively.

As can be seen from Figure 23, under the loading condition of being subjected to the block's own weight and the weight of 14 t sandbags, the maximum tensile strain of the polyurea spray film material measured was  $63334.11 \mu\epsilon$ .

According to working condition 2 of the field test, the test time under the weight of the arch test block and the sandbag with a load of about 14 t lasted for nearly 50 min. The spray film material was in the linear elastic deformation stage during the sinking process of the test block, and no brittle fracturing occurred. The tensile elastic modulus was  $E = 8$  MPa after the spray film material was cured, thus obtaining the maximum tensile stress of  $\sigma_t = 506.7$  kPa.

The tensile strength of the sprayed film material was 13 MPa. It can be seen that under the combined action of a test block of  $2.0 \times 3.0 \times 0.5$  m and a sandbag with a weight of about 14 t, the maximum tensile stress of the spray film material with a thickness of 5 mm during the sinking process of the test block was 506.7 kPa. This is still less than the tensile strength of the spray film material of 13 MPa.

In case 2, the test block sank during loading and peeled off the spray film material within a certain range around the test block. This phenomenon indicates that the bond strength between the spray film polyurea material and the tunnel lining concrete surface reduced gradually, which, in turn, caused the spray film polyurea material to be stripped from the surface of the concrete by the sinking test block.

For the spray film material with a thickness of 5 mm in case 2, it was subjected to pressure and tensile stress before

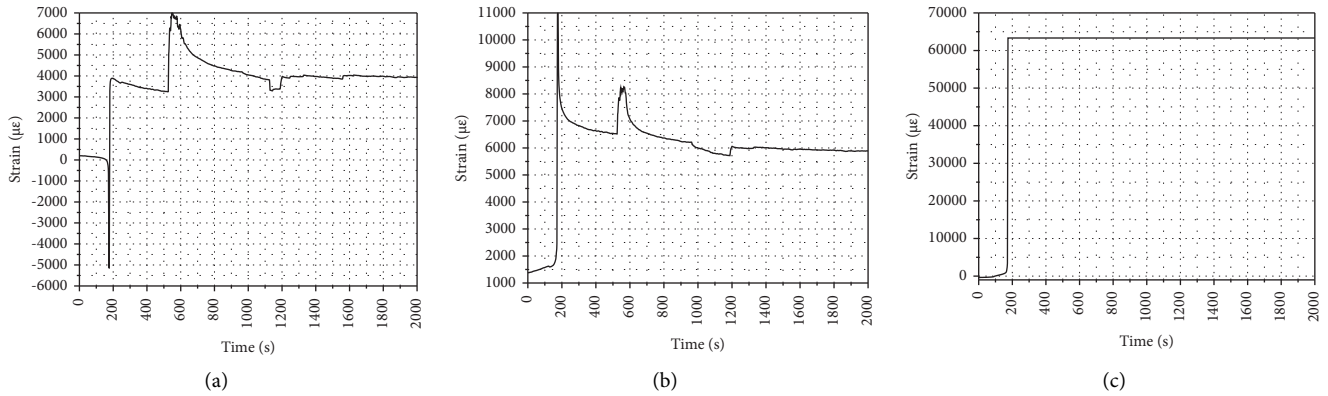


FIGURE 23: The relationship between strain and time of spray film material. (a) Measurement point A. (b) Measurement point H. (c) Measurement point J.

the test block sank under the combined action of the self-weight of the rectangular test block and the simulated aerodynamic effect of the high-speed railway tunnel with a load of about 14 t. When the test block sank, the spray film material was all in a state of tensile stress, but the maximum tensile stress obtained by the test was still less than the tensile strength of the spray film material.

The thickness of the spray film material in this loading test was 5 mm. Although there was a sinking phenomenon for the test block in condition 2 during loading, the tensile stress in the spray film material did not exceed its tensile strength during the sinking period. The failure phenomenon of tension cracking and tearing did not occur on the spray film material, which showed that the spray film material with a thickness of 5 mm in condition 2 could withstand and drag the sinking test block to prevent it from falling to the floor completely. The main reason for the sinking of the test block during loading may be due to the decrease in bond strength between the spray film material and the concrete wall, and the bonding tension caused by the increased weight of the test block could not be resisted. Therefore, in order to prevent the tunnel lining arch test block from falling, measures such as increasing the bond strength between the spray film material and the concrete or increasing the thickness of the spray film material can be taken.

**5.2.4. Test Block Misalignment and Spray Film Material Peeling Area.** During the model test, the arch cube test block sank under the combined action of its self-weight and the simulated aerodynamic effect loads, but it did not fall to the ground completely. Between the test block and the tunnel lining, there was a misalignment. The maximum settlement of the concrete block tested on-site was 29 cm, and the maximum amount of misalignment between the test block and the surrounding concrete lining was 28 cm. Due to the sinking of the test block during loading, the spray film material around the test block was stripped from the tunnel concrete lining, as shown in Figures 24–26.

The sinking amount and misalignment of the test block in condition 2 is shown in Figure 27. The maximum



FIGURE 24: The condition of the cuboid test block after sinking.

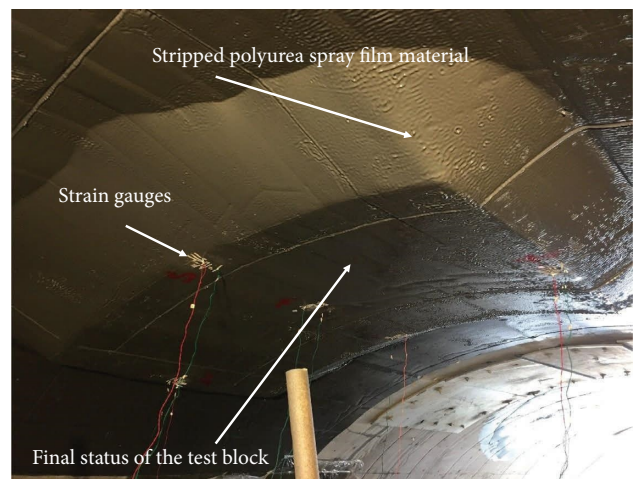


FIGURE 25: The tensile status of the spray film material after the test block sank.

settlement of the test block was 29 cm, and the misalignment between the test block and the surrounding concrete lining reached 28 cm.

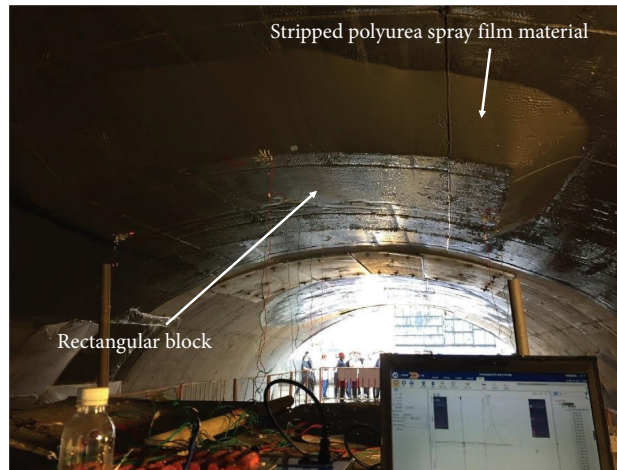


FIGURE 26: The final status of the sunken test block and the stripped spray film material.

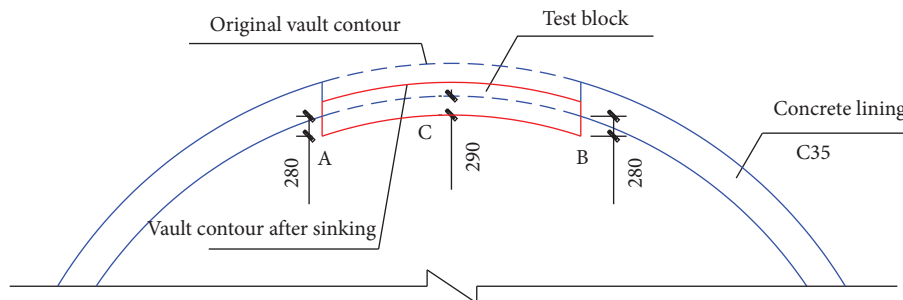


FIGURE 27: Misalignment between the block and surrounding lining (mm).

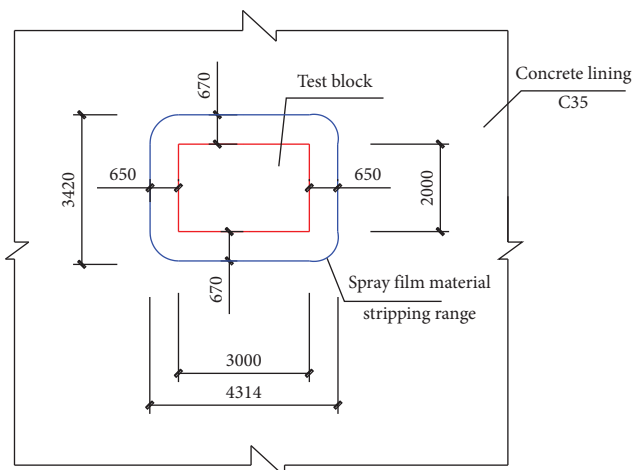


FIGURE 28: Floor plan of the peeling range of the spray film material around the rectangular test block (mm).

According to the field test, the floor plan of the stripped spray film material area around the  $3 \times 2 \times 0.5$  m rectangular test block is shown in Figure 28.

It can be seen from Figure 28 that the length of the slope of the spray film material that peeled off along the sinking of the test block was about 0.65 to 0.67 m on the horizontal plane. The projection of the spray film material sinking with

the test block on the horizontal plane was a rectangle of  $3.42 \times 4.31$  m. From this, it can be calculated that the area of the spray film material stripped from the concrete lining was about  $8.6 \text{ m}^2$ .

The cross-section of the spray film material around the test block peeled off from the lining due to the weight of the test block and sandbag load is shown as Figure 29.

From Figure 29, it can be concluded that the peeling spray film material around the test block in condition 2 was within 1.0 m.

According to the model test of the spray film material with a thickness of 5 mm used to prevent the tunnel lining falling block disease under working condition 2, the following conclusions can be made:

- (1) For the test block in working condition 2, when the 5 mm thick spray film material's extension range was 2 m, the tensile stress caused by the block drop was 506 kPa under the action of the block's self-weight and the aerodynamic effect of the high-speed railway tunnel of about 14 t. The spray film material was in a tensile and compressive state along the tunnel ring and the tunnel axis during the loading test, and the tensile stress was greater than the compressive stress. The whole spray film material was in a tensile stress state after the test block sank. The maximum tensile stress of the spray film material in model test case 2

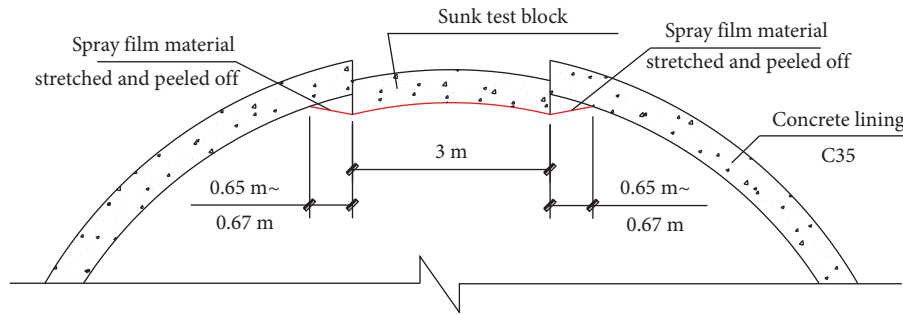


FIGURE 29: The spray film material that was peeled off around the periphery of the sunken cuboid test block.

was less than its tensile strength (13 MPa). This indicates that the spray film material with a thickness of 5 mm can bear the combined effect of the tunnel arch lining block drop and the aerodynamic effect without shear or tensile failure.

- (2) The use of 5 mm thick spray film material failed to prevent the concrete test block from sinking in model test condition 2, but the test block did not fall to the floor of the tunnel completely and was dragged and supported by the stripped spray film material. After the test block sank, the misalignment between the test block and the surrounding concrete lining reached 28 cm, and the area of the spray film material on the inner wall surface of the model tunnel concrete lining was about 8.6 m<sup>2</sup> due to the sinking and pulling of the test block.
- (3) It can be concluded that the reason for the block sinking was related to the decrease in the bond strength between the spray film material around the test block and the concrete. The range of the stripped film material around the test block was less than 1.0 m. Therefore, it is recommended that the bond strength between the spray film material and the concrete within 1.0 m of the spraying range around the test block should be appropriately increased. In addition, in order to reduce the tensile stress concentration caused by the uneven thickness of the spray film material due to the spraying construction process, it is recommended that the thickness of the spray film material should be appropriately increased.

**5.3. Results of Experimental Condition 3.** The test block in condition 3 was a cuboid block of 2 × 3 × 0.5 m. In this condition, the cracks between the test block and the surrounding concrete were treated with perfusion epoxy and were not reinforced with spray film material. Therefore, only destructive loading tests were performed on the shear-to-vandal resistance of the perfused epoxy material. However, the test block did not sink or fall under the action of its own weight or under the weight of the upper sandbag with a total load of 11.5 t during the loading period. Under the action of the 11.5 t load, the perfusion of the epoxy material was free of destruction. The test block in condition 3 did not sink or misalign, and its test value was zero.

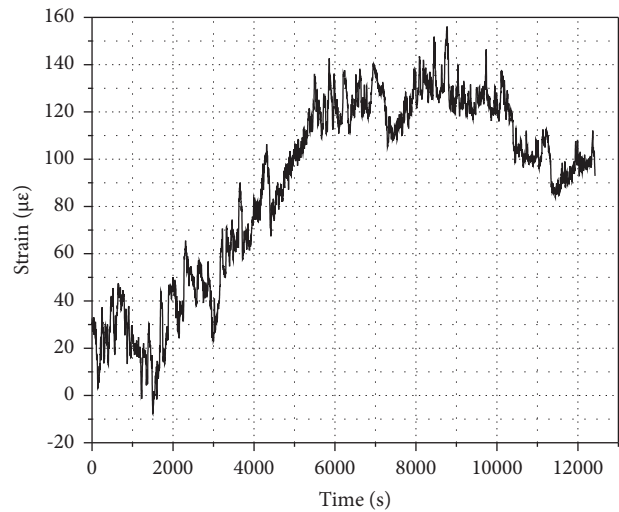


FIGURE 30: Strain curve at point B.

#### 5.4. Results of Experimental Condition 4

**5.4.1. Tensile Strain and Stress of Spray Film Material.** The loading test for working condition 4 consisted of spraying 5 mm thick polyurea material in the arch of the tunnel model and repairing the cracks between the test block and the concrete lining with infused epoxy material. The test block was a circular block of  $\Phi 2 \times 0.5$  m. The loads on the cylindrical test block included its own weight and the additional loads applied by the sandbag on its upper part, and then the load carrying capacity of the spray film material under the two loads was analyzed.

The strain values at measurement points B and C were the largest for the cylinder test block of  $\Phi 2 \times 0.5$  m, shown in Figure 16. The spray film material was in a tensile state along the tunnel ring and axis direction. The relationship curve of the longitudinal tensile strain at point B is shown in Figure 30.

As can be seen from Figure 30, the maximum tensile strain measured by the spray film material with a thickness of 5 mm at point B and point C under a sandbag load of about 9.5 t was  $\epsilon_t = 156.03 \mu\epsilon$ .

According to the conditions of the field test, the test lasted for nearly 250 min under the combined action of the arch test block weight and a sandbag load of about 9.5 t. The spray film material was in the linear elastic deformation



FIGURE 31: The appearance of the spray film material of the tunnel arch cylinder test block. (a) Before loading. (b) After loading.

stage during the test, and no plastic yield or brittle fracturing occurred, nor did any significant sinking or falling appear.

The tensile elastic modulus was  $E = 8$  MPa after the spray film material was cured. According to the stress and strain relationship of the spray film material in the elastic stage after curing, it was calculated from equation (19) that the maximum tensile strain was  $\varepsilon_t = 156.03 \mu\varepsilon$ . At the peripheral measuring point  $B$ , the tensile stress was  $\sigma_t = 1.25$  kPa. The tensile strength of the sprayed film material was 13 MPa. It can be seen that under the combined action of the  $\Phi 2.0$  m cylindrical test block weight and a total sandbag weight of about 9.5 t, the maximum tensile stress ( $\sigma_t = 1.25$  kPa) borne by the spray film material with a thickness of 5 mm was much less than the tensile strength of the spray film material.

It was found that the spray film material with a thickness of 5 mm in working condition 4 of the loading test was able to support the joint action of the cylindrical test block of  $\Phi 2 \times 0.5$  m and an additional load of about 9.5 t. The tensile stress of the spray film material was much less than its tensile strength, and the spray film material did not undergo tensile yield or brittle damage during the test, nor was there any significant sinking or falling.

**5.4.2. Misalignment between the Block and Surrounding Concrete.** After the misalignment test on the lower arch test block supported and reinforced by a 5 mm thick spray film material, the arch test block in model test condition 4 did not sink or fall during loading. The sinking amount was zero, and the amount of misalignment was also zero. The spray film material was not peeled off from the inner wall of the concrete. The condition of the spray film surface during loading is shown in Figure 31.

From the test in experimental condition 4, the following conclusions can be addressed: In the destructive test simulating the action of the railway tunnel lining arch block falling under an additional aerodynamic load of about 9.5 t, the tensile stress test value inside the spray film material was between 0.76 and 1.25 kPa. The spray film material was under tensile stress along both the tunnel ring and the tunnel axis. The tensile stress of the spray film material in the test

was less than its tensile strength of 13 MPa, indicating that the spray film material with a thickness of 5 mm in this destructive test was still able to bear the joint effect of the block weight and tunnel aerodynamic effect in the model tunnel. The spray film material did not have tensile or shear damage, and the cylindrical test block did not sink or fall.

## 6. Discussion

For all of the four model tests, only the spray film under working condition 2 fell off. Therefore, the mechanical properties of the spray film material under working condition 2 need to be verified.

**6.1. Validation of the Assumptions in the Calculation of the Spray Film Material Bond Strength.** The length and width of the rectangular test block were as follows:  $r_1 = 3$  m,  $r_2 = 2$  m; the thickness of the block:  $T = 0.5$  m; the bulk weight of the block:  $\gamma = 23$  kN/m<sup>3</sup>; the simulated aerodynamic load:  $P = mg = 14 \times 9.8 = 137.2$  kN; and the average width of the spray film material bevel that peeled off as the test block sank projecting on the horizontal plane:  $L_1 = 0.66$  m. According to the measured data, the actual bond strength of the spray film material can be calculated by equation (15).

$$\psi = \frac{2 \times 3 \times 23 \times 0.5 + 137.2}{2 \times 0.66 \times (2 \times 0.66 + 2 + 3)} = 24.72 \text{ kPa.} \quad (20)$$

From Table 6, for rectangular concrete test blocks with a length  $\times$  width = 3  $\times$  2 m, the theoretical bond strength of the polyurea spray film material was 1.572 MPa. The measured value is only 1.57% of the theoretical value. The calculations show that the supporting effect provided by the material after actual construction was much smaller than the theoretical analysis value. On the other hand, the average bond strength of the spray film material under the measured working conditions was 4.5 MPa. The test results had values much greater than the calculated values, but the polyurea spray film material failed in experimental condition 2. In view of the above situation, the reasons for this are analyzed as follows:

### 6.1.1. Differences between the Measured Bond Strength Calculation and the Theoretical Bond Strength Calculation

- ① Reasonableness of the assumptions regarding the stressed region of the spray film material:

In the theoretical analysis of Section 3.3.1, the force area of the spray film material's bond strength was assumed to be 0.01 m outside the boundary of the falling block. The actual measured spray film peeling width was 0.66 m, which is 66 times the hypothesized value. Therefore, the hypothesized value is conservative.

- ② Reasonableness of the aerodynamic load assumptions:

In the theoretical analysis, the aerodynamic load of 88.8 kN for double trains meeting at a speed of 350 km/h was given to calculate the bond strength between the spray film material and the lining concrete surface. In the model test, the aerodynamic load was simulated by accumulating 14 t sandbags, with a load of 137.2 kN. The dynamic load of the model test was 1.55 times that of the theoretical assumption, so the assumed load is small.

- ③ Reasonableness of the elasticity hypothesis:

The theoretical calculations assumed that the polyurea spray film material was still in the elastic deformation stage when peeling. However, plastic damage may occur in the spray film material during actual engineering. The elasticity assumption may therefore not be satisfied. In addition, the theoretical calculation assumed that the supporting area of the entire spray film material was evenly stressed. However, the spray film was the most stressed at the edge of the contact between the test block and the lining. There was a decreasing trend along the edge of the spray film material.

### 6.1.2. Differences between the Measured Bond Strength and the Calculated Bond Strength

- ① Test position. The actual bond strength failure occurred in the side seam position. However, in order to conduct bond strength tests, a small part of the membrane material is destroyed. To avoid this, the test position was far from the side seam. Therefore, the bond strength of the seam position in condition 2 was not detected. Affected by the test method, the bond strength of the spray film material was not measured at the edge of the test block, that is, at the most dangerous A and A' points in Figure 1. Therefore, the measured values were much larger than the theoretically calculated values.
- ② Side seam treatment process. The width of the side seam was about 1.5 cm in working condition 2. The surface of the side seam was irregular, and more special putty was used for screeding. The strength of the putty selected for the test was low, and the adhesion strengths of the primer and the film material

did not match. This resulted in the special putty being peeled off from the concrete surface first, then causing the local peeling of the membrane material. The low strength of the special putty is one of the main reasons for the failure of the local bonding strength.

- ③ Surface sanding process. The particle size and strength of the quartz sand used in condition 2 were small. Additionally, the grinding time was short. Therefore, the surface grinding process was one of the main reasons for the failure of local bond strength in condition 2.

6.2. Validation of the Assumptions in the Calculations of the Spray Film Material Tensile Strength. The amount of rectangular test block misalignment was  $h_1 = 0.28$  m. As can be seen from equation (16), the theoretical calculation of the tensile stress  $\xi$  of the spray film material at this time is as follows:

$$\xi = \frac{2 \times 3 \times 23 \times 0.5 + 137.2}{2 \times (2 + 3) \times \sqrt{0.66^2 + 0.28^2} \times \cos \arctan L_1/h_1} \quad (21)$$

$$= 103.1 \text{ kPa.}$$

The maximum tensile stress of the spray film material measured in Section 5.2 was 506.67 kPa, which shows that the tensile stress of the spray film material measured in the model test was 4.9 times that of the theoretical calculation result. The actual tensile stress was much greater than the tensile strength of the spray film material, so the spray film material was destroyed.

## 7. Conclusions

In this study, a model test of the polyurea spray film material used to prevent lining block from falling was carried out. Four different working conditions were set up, and the bond strength and tensile strength of the spray film material under each working condition were measured. According to the actual measurement results, the proposed theoretical calculation model was verified. According to the results of this study, the following main conclusions can be made:

- (1) After crack epoxy consolidation + surface epoxy consolidation + surface spray polyurea treatment, the average bonding strength measured was 3.83 MPa and the maximum tensile stress was 0.341 kPa. This bonding strength could bear the joint action of tunnel arch lining block drop and the aerodynamic effect without shear or tensile damage. The test block did not fall, and the spray film material was not peeled off.
- (2) After the surface spray polyurea treatment, the average bonding strength measured was 4.5 MPa, and the maximum tensile stress was 506.7 kPa. Under the combined action of the test block's self-weight and an aerodynamic effect of about 14 t load, the tensile stress was less than the tensile strength, and no

tensile fracture occurred in the spray film material during the test.

- (3) The test block sank during the loading process, and the spray film material within a certain range around the test block was peeled off, indicating that the bond strength within the peeling range between the spray film polyurea material and the tunnel lining concrete surface was gradually reduced. In order to prevent the tunnel lining arch test block from falling, measures such as increasing the bond strength between the spray film material and the concrete or increasing the thickness of the spray film material are recommended to be taken.
- (4) The theoretical supporting force of the polyurea spray film material is 1.572 MPa, but the measured value is only 1.57% of the theoretical value. The calculation shows that the supporting effect provided by the material in the actual construction was much smaller than the theoretical analysis value. The maximum tensile stress of the spray film material was 506.67 kPa, and the tensile stress of the spray film material measured in the model test was 4.9 times that of the theoretical calculation result.
- (5) After the crack epoxy consolidation treatment, the test block was able to withstand its own weight and the weight of the upper sandbag for a total load of 11.5 t without sinking or falling.
- (6) After crack epoxy consolidation + surface epoxy consolidation + surface spray polyurea treatment, the maximum tensile stress measured was 1.25 kPa, which was much less than the tensile strength of the spray film material.

## Data Availability

The data used to support the findings of this study are included within the article.

## Conflicts of Interest

The authors declare that they have no conflicts of interest.

## Acknowledgments

The National Natural Science Foundation of China: 51274145.

## References

- [1] H. S. Cheng, W. Ang, and H. S. Xiao, "Research on the movement law and traffic safety zoning of spalled blocks in the linings of high-speed railway tunnels," *Tunnelling and Underground Space Technology*, vol. 128, Article ID 104614, 2022.
- [2] L. Li, M. G. Duan, and Z. Cao, "Rehabilitation of highway procedures," *Proceedings of ATTES-ITA 2001 world tunnel Tunnels-Techniques and congress*, pp. 45–50, 2005.
- [3] X. S. Li, Q. H. Li, Y. J. Hu et al., "Study on three-dimensional dynamic stability of open-pit high slope under blasting vibration," *Lithosphere*, vol. 2021, Article ID 6426550, 2022.
- [4] D. Ren, X. Wang, Z. Kou et al., "Feasibility evaluation of CO<sub>2</sub> EOR and storage in tight oil reservoirs: a demonstration project in the Ordos Basin," *Fuel*, vol. 331, Article ID 125652, 2023.
- [5] M. C. He, Q. R. Sui, M. N. Li, Z. J. Wang, and Z. G. Tao, "Compensation excavation method control for large deformation disaster of mountain soft rock tunnel," *International Journal of Mining Science and Technology*, vol. 32, no. 5, pp. 951–963, 2022.
- [6] C. Zhu, X. Xu, and X. T. Wang, "Experimental investigation on nonlinear flow anisotropy behavior in fracture media," *Geofluids*, vol. 2019, Article ID 5874849, 9 pages, 2019.
- [7] Q. Wang, B. Jiang, S. Xu et al., "Roof-cutting and energy-absorbing method for dynamic disaster control in deep coal mine," *International Journal of Rock Mechanics and Mining Sciences*, vol. 158, Article ID 105186, 2022.
- [8] Q. Wang, S. Xu, Z. Xin, M. He, H. Wei, and B. Jiang, "Mechanical properties and field application of constant resistance energy-absorbing anchor cable," *Tunnelling and Underground Space Technology*, vol. 125, Article ID 104526, 2022.
- [9] Q. Yin, J. Wu, Z. Jiang et al., "Investigating the effect of water quenching cycles on mechanical behaviors for granites after conventional triaxial compression," *Geomechanics and Geophysics for Geo-Energy and Geo-Resources*, vol. 8, no. 2, 2022.
- [10] G. Feng, X. Wang, Y. Kang, and Z. Zhang, "Effect of thermal cycling-dependent cracks on physical and mechanical properties of granite for enhanced geothermal system," *International Journal of Rock Mechanics and Mining Sciences*, vol. 134, Article ID 104476, 2020.
- [11] T. Meng, X. Yongbing, J. Ma et al., "Evolution of permeability and microscopic pore structure of sandstone and its weakening mechanism under coupled thermo-hydro-mechanical environment subjected to real-time high temperature," *Engineering Geology*, vol. 280, Article ID 105955, 2021.
- [12] G. Feng, X. Wang, M. Wang, and Y. Kang, "Experimental investigation of thermal cycling effect on fracture characteristics of granite in a geothermal-energy reservoir," *Engineering Fracture Mechanics*, vol. 235, Article ID 107180, 2020.
- [13] P. Jin, Y. Hu, J. Shao, Z. Liu, G. Feng, and S. Song, "Influence of temperature on the structure of pore-fracture of sandstone," *Rock Mechanics and Rock Engineering*, vol. 53, no. 1, pp. 1–12, 2020.
- [14] B. Chiaia, A. P. Fantilli, and P. Vallini, "Combining fiber-reinforced concrete with traditional reinforcement in tunnel linings," *Engineering Structures*, vol. 31, no. 7, pp. 1600–1606, 2009.
- [15] G. Feng, Y. Kang, F. Chen, Y. Liu, and X. Wang, "The influence of temperatures on mixed-mode (I + II) and mode-II fracture toughness of sandstone," *Engineering Fracture Mechanics*, vol. 189, pp. 51–63, 2018.
- [16] E. S. Bernard, "Influence of geometric factors on the punching load resistance of early-age fibre reinforced shotcrete linings," *Tunnelling and Underground Space Technology*, vol. 26, no. 4, pp. 541–547, 2011.
- [17] Y. C. Chiu, C. H. Lee, and T. T. Wang, "Lining crack evolution of an operational tunnel influenced by slope instability," *Tunnelling and Underground Space Technology*, vol. 65, pp. 167–178, 2017.
- [18] H. M. Kroetz, N. A. Do, D. Dias, and A. T. Beck, "Reliability of tunnel lining design using the Hyperstatic Reaction Method," *Tunnelling and Underground Space Technology*, vol. 77, pp. 59–67, 2018.

- [19] K. Tsuno and K. Kishida, "Evaluation of spalling of concrete pieces from tunnel lining employing joint shear model," *Tunnelling and Underground Space Technology*, vol. 103, Article ID 103456, 2020.
- [20] J. Du, Q. Fang, G. Wang, D. Zhang, and T. Chen, "Fatigue damage and residual life of secondary lining of high-speed railway tunnel under aerodynamic pressure wave," *Tunnelling and Underground Space Technology*, vol. 111, no. 5, Article ID 103851, 2021.
- [21] D. Feng, X. Wang, and B. Zhang, "Improving reconstruction of tunnel lining defects from ground-penetrating radar profiles by multi-scale inversion and bi-parametric full-waveform inversion," *Advanced Engineering Informatics*, vol. 41, Article ID 100931, 2019.
- [22] K. Lee, D. Kim, S. H. Chang, S. W. Choi, B. Park, and C. Lee, "Numerical approach to assessing the contact characteristics of a polymer-based waterproof membrane," *Tunnelling and Underground Space Technology*, vol. 79, pp. 242–249, 2018.
- [23] K. Kovari, "History of the sprayed concrete lining method—part II: milestones up to the 1960 s," *Tunnelling and Underground Space Technology*, vol. 18, no. 1, pp. 71–83, 2003.
- [24] J. Kwasny and T. A. Aiken, "Sulfate and acid resistance of lithomarge-based geopolymer mortars," *Construction & Building Materials*, vol. 166, 2018.
- [25] S. Heidari, F. Esmailzadeh, D. Mowla, and S. Ghasemi, "Synthesis of an efficient copolymer of acrylamide and acrylic acid and determination of its swelling behavior," *Journal of Petroleum Exploration and Production Technology*, vol. 8, no. 4, pp. 1331–1340, 2018.
- [26] R. P. Johnson, F. E. Swallow, and S. Psomas, "Structural properties and durability of a sprayed waterproofing membrane for tunnels," *Tunnelling and Underground Space Technology*, vol. 60, pp. 41–48, 2016.
- [27] C. Angeloff, E. P. Squiller, and K. E. Best, "Two-component aliphatic polyurea coatings for high productivity applications," *Journal of Protective Coatings and Linings*, vol. 19, no. 8, pp. 42–47, 2002.
- [28] Z. Bo, *Study on the Corrosion Resistance of Anti-corrosion Coatings in Different Corrosive Environments*, Qingdao Technological University, Shandong, China, 2013.
- [29] P. Lü, G. Chen, and W. Huang, "Study on accelerated aging behavior of polyurea coatings of polyaspartate," *Journal of Sichuan University (Medical Science Edition): Engineering Science Edition*, vol. 39, no. 2, p. 6, 2007.
- [30] Y. Liu, *Research on the Properties and Test Methods of concrete Protective Coatings*, China Academy of Building Materials Science, Beijing, China, 2004.
- [31] H. Yang, *Effect of Sprayed Polyurea Elastomer on concrete Durability*, Qingdao Institute of Civil Engineering and Architecture, Shandong, China, 2004.
- [32] Z. Li, J. Zhang, and W. Huang, "Application of sprayed polyurea elastomer technology in offshore concrete protection," *Painting Guide*, vol. 2, no. 2, p. 5, 2010.
- [33] W. Wang, *Research on the Application of spray Polyurea Technology in the protection of Underground concrete Structures*, Qingdao Technological University, Qingdao, China, 2004.

## Research Article

# Research on Development Mechanism and Criterion of Upward Fractures in Longwall Face Mining

Jian Cao , Haitao Su , Jianwei Li , Xiangye Wu , and Eryu Wang 

*Institute of Mining Engineering and Coal, Inner Mongolia University of Science and Technology, Baotou, Inner Mongolia 014010, China*

Correspondence should be addressed to Jian Cao; 2020913@imust.edu.cn

Received 21 September 2022; Revised 15 October 2022; Accepted 24 November 2022; Published 17 April 2023

Academic Editor: Fuqiang Ren

Copyright © 2023 Jian Cao et al. This is an open access article distributed under the Creative Commons Attribution License, which permits unrestricted use, distribution, and reproduction in any medium, provided the original work is properly cited.

After mining, upward fractures develop from bottom to top, and they are key channel for groundwater and gas flow and also sand burst; therefore, it is important to study the development mechanism and criterion of upward fractures. Combining with physical simulation and theoretical analysis, the development law of mining-induced upward fractures was revealed, and the mechanism and criterion of fracture propagation was studied. The results show that the development of mining-induced upward fractures can be divided into the following three stages: with the face advances from the open cut, the vertical fractures are generated at the mining boundary, and the roof is flexural but not caved; it is “Fractures generate stage.” After roof caves, the upward fractures extend and develop upward along the caving angle with continue advances; it is “Fractures develop and extend stage.” When the face reaches critical mining, the development height of the upward fractures is at its maximum and is basically invariable; it is “Fractures stabilization stage.” Mining-induced fractures can be analyzed as mixed-type fractures in fracture mechanics; when the combined stress exceeds the critical strength of stratum, it will extend downward until penetrate through the stratum, and the upward fracture develops and extends upwards. The parameter controlling the fracture of the rock stratum is the maximum hoop tensile stress  $\sigma_{(\theta)\max}$ , at the fracture end, the theoretical model of fracture propagation was established, and the criterion of upward fractures was proposed.

## 1. Introduction

The upward fractures are the key channel of water and gas conduction. In order to realize water conservation mining and mine disaster prevention, it is important to study the criterion of upward fractures. The development essence of upward fracture is that the concentrated stress reaches the tensile strength, it develops continuously with the face advances, and it finally reaches a stable stage.

Lots of research studies relating to the development law of upward fractures by field measurement have been published. Zhu and Teng [1] concluded that the development height of the upward fracture is directly proportional to the total mining thickness. Zhang and Zhang [2] analyzed the overburden of thick coal seam mining fracture propagation mechanics and principle based on the related theories of elastic-plastic and fracture mechanics. Bai and Tu [3]

summarized the mining-induced fracture characteristics in shallow coal seam. Through engineering tests, Tan et al. [4] obtained the height of water-conducting fracturing zone. Huang et al. [5] studied the height of upward fracture by transient electromagnetic and drilling in Wanli mining area.

Besides, physical simulation, numerical calculation, and theoretical model were applied to study the development law of upward fractures. Wen et al. [6] established a fracture expansion model. By using the elasticity and Winkler foundation theory, Li et al. [7] established the numerical calculation model of fracture and the evolution of overburden strata under the condition of seepage-stress coupling and analyzed the dynamic change process of overburden strata fracture development height. By using physical simulation experiment, Bai et al. [8] revealed the failure mechanism of water-conducting fracture zone. Xu et al. [9, 10] revealed that the position of main key strata of

overlying strata will affect the upward crack development height of coal seam roof. Based on partial filling mining in shallow coal seams, Zhang and Huang [11] found that different backfilling parameters directly affect the development height of upward fractures. Zhao et al. [12] established the development height of upward fractures with the subsidence of key strata and analyzed the dynamic development process of upward fractures with the longwall face advances. Cao and Huang [13] obtained the development characteristics of fractures in shallow single seam mining and repeated mining, and the relationship between pillar staggered distance and fractures is revealed. Besides, fractal theory was used to quantitatively study the development process of fractures [14–28].

Above all, at present, based on various research methods, there are lots of studies on the upward fractures development in single seam and multiseams mining. Fractures development is a macroscopic phenomenon, which contains fracture generation and expansion fracture mechanics is an effective method to analyze the development of upward fracture; however, there are few studies in this area. Therefore, based on fracture propagation theory in fracture mechanics and physical simulation, the development law of mining-induced upward fractures was revealed in this paper, and mechanism and criterion of fracture propagation were studied.

## 2. Development Law of Mining-Induced Upward Fractures

### 2.1. Fractures Development Based on Physical Simulation Experiment

#### 2.1.1. Fractures Development of No. 1-2 Coal Seam Mining in Daliuta Coal Mine

(1) *Physical Simulation Experiment Model.* Physical simulation experiment was established to reveal the development stage of mining-induced upward fractures. Based on the mining condition of the No. 1-2 coal seam in Daliuta Coal Mine, the average thickness of the coal seam is 4 m, and its buried depth is about 73 m. The experiment model is 1.5 m long  $\times$  1.3 m wide  $\times$  0.16 m height (Figure 1). Sand was adopted as the aggregates, cementitious materials are gypsum and calcium carbonate, and the material ratio is shown in Table 1.

(2) *Fractures Development with Longwall Face Advances.* The coal seam was excavated from left to right. When the longwall face advances to 15 m, the immediate roof caves. There is no fracture development in the overburden, and the roof caving height is 1.4 m, as shown in Figure 2.

When it advances to 46 m, the overlying strata above immediate roof suddenly cave, and it is the first caving of main roof. The roof caving angle is about  $55^\circ$ , as shown in Figure 3.

When it advances to 54 m, the main roof produces the first periodic caving, the development height of fracture reaches 20.5 m, the separation height of fracture is 3.2 m, and its separation width is 31.8 m. As the longwall face advances,



FIGURE 1: Physical simulation experiment model of Daliuta Coal Mine.

when the longwall face advances to 64 m, 76 m, . . . , 120 m, the main roof produces the 2nd, 3rd, . . . , 7th periodic roof caving, respectively, and simultaneously, the fractures develop upwards, as shown in Figure 4. When it advances to 120 m, it reaches critical mining, and the mining-induced fractures have developed to the ground surface (Figure 4(d)). The relationship between fracture development height and face advances distance is shown in Figure 5.

(3) *The Relationship between Fractal Dimension and Face Advances Distance.* The two-dimensional slice image is obtained from 3DEC numerical calculation, the image obtained is often RGB color image, and it is converted into gray image, the processed gray image is imported into MATLAB, and the image is binarized by using the threshold segmentation method. The gray transformation discriminant function of binary processing is as follows:

$$f(x, y) = \begin{cases} 0, & f(x, y) \leq t, \\ 1, & f(x, y) \geq t. \end{cases} \quad (1)$$

FracLab toolbox is used to calculate the fractal dimension of the processed digital image, and the fractal dimensions of fractures with different advance distances are shown in Figure 6.

Figure 6 shows that in normal mining stage, the fractal dimension increases gradually while the longwall face advances, and when it reaches critical mining, the development height of fractures does not change significantly while the longwall face advances.

#### 2.1.2. Fractures Development of No. 4-2 Coal Seam Mining in Hongliulin Coal Mine

(1) *Physical Simulation Experiment Model.* Taking the No. 4-2 coal seam mining in Hongliulin Coal Mine as the background, the average thickness of the coal seam is 2.1 m, and its buried depth is about 115.7 m. The experiment model is 2.0 m long  $\times$  1.5 m wide  $\times$  0.2 m height (Figure 7), the geometric similarity ratio is 1:200, and the material ratio is shown in Table 2.

(2) *Fractures Development with Longwall Face Advances.* The coal seam was excavated from left to right. When it advances to 22 m, the immediate roof caves and roof of longwall face is deflected, as shown in Figure 8. When it advances to 50 m,

TABLE 1: The material ratio of physical simulation experiment.

Lithology	Thickness (m)	Depth (m)	Consumables (kg)			
			Sand	Plaster	Calcium carbonate	Fly ash
Loess	21.79	21.79	Sand (37.69): loess (37.69): silicone oil (8.29)			
Fine-grained sandstone	6.03	27.82	19.21	0.73	1.81	
Siltstone	16.86	44.68	58.23	1.91	4.60	
Fine-grained sandstone	1.77	46.45	6.04	0.23	0.53	
Siltstone	1.50	47.95	5.18	0.17	0.41	
Fine-grained sandstone	0.95	48.90	3.24	0.12	0.28	
Medium-grained sandstone	4.13	53.03	14.09	0.37	1.40	
Coarse-grained sandstone	4.37	57.4	14.91	0.39	1.49	
Siltstone	2.54	59.94	8.77	0.30	0.68	
Fine-grained sandstone	3.86	63.80	13.18	0.48	1.15	
Siltstone	1.81	65.61	6.25	0.21	0.49	
Fine-grained sandstone	1.79	67.40	6.11	0.23	0.53	
Siltstone	2.33	69.73	8.05	0.27	0.62	
Fine-grained sandstone	1.87	71.60	6.38	0.24	0.56	
Medium-grained sandstone	1.36	72.96	4.64	0.12	0.46	
No. 1-2 coal seam	4.00	76.96	5.44	0.28	1.36	5.44
Siltstone	6.04	83.00	20.84	0.72	1.63	



FIGURE 2: The immediate roof caves.



FIGURE 3: The first caving of main roof.

the overlying strata above the immediate roof suddenly cave, and it is the first caving of main roof; the roof caving angle is about  $60^\circ$ , as shown in Figure 9. When it advances to 50 m, the roof caving and fracture development are shown in Figure 10; when the longwall face reaches critical mining, the roof caving and fracture development are shown in Figure 11. It can be known that the fracture development height increases when the longwall face advances.

*2.2. Development Stage of Mining-Induced Upward Fractures.* With the longwall face advance, under the force of the concentrated tensile stress and gravity, the overlying strata gradually become flexural and then cave. At the same time, the upward fractures continue to develop upward along a certain caving angle, which is usually about  $60^\circ$ . According to the development characteristics, the development of mining-induced upward fractures can be divided into the following three stages, and it is shown in Figure 12.

- (1) Fractures generate stage: With the longwall face advances from the open cut, the vertical fractures are generated at the mining boundary, and the roof is flexural but not caved, as shown in Figure 12(a).
- (2) Fractures develop and extend stage: After the roof caves, the upward fracture develops upward along the caving angle of the roof. With the longwall face advances and the roof caves from bottom to top, the upward fracture extends upward along the caving angle of the roof, and the development height of the fracture increases with it, as shown in Figures 12(b) and 12(c).
- (3) Fractures stabilization stage: When the advance of the longwall face reaches critical mining, the development height of the upward fractures basically reaches the maximum value. Therefore, the longwall face continues to advance, and the upward fractures on the open cut side no longer developed, while the fractures on the longwall face side represent periodic development process of “fractures generation—fractures development and propagation—fractures stabilization—fractures closure-new fractures generation,” but its development height is basically invariable, as shown in Figure 12(d).

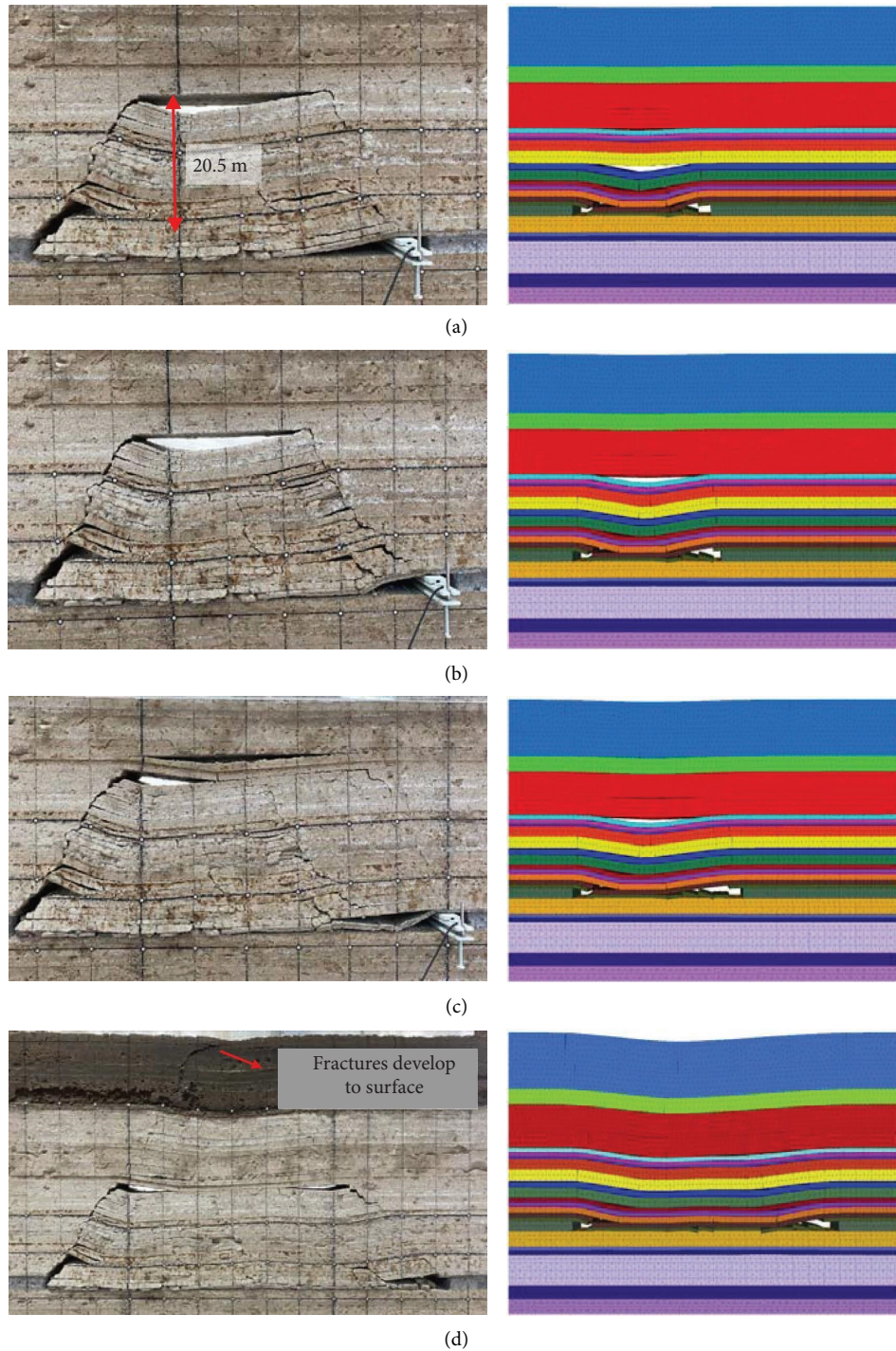


FIGURE 4: Periodic roof caving as face advances: (a) face advances to 54 m; (b) face advances to 64 m; (c) face advances to 76 m; (d) face advances to 120 m.

### 3. Development Mechanism of Upward Fractures Based on Fracture Growth Theory

**3.1. Stress Analysis of Fracture End.** The development of upward fractures is the result of the vertical force (weight of overlying strata) and concentrated tensile stress induced by roof caving. When the comprehensive stress reaches the ultimate tensile strength of rock, the rock strata will be

damaged and generate fracture. Fracture mechanics can correlate the fracture strength of rock with the stress and is an effective method to analyze the development mechanism of upward fractures; therefore, fracture mechanics were used to analyze the stress and growth process of the fracture (Figure 13).

When the gravity  $G$  of the rock layer and the overburden load  $q$  act on the vertical direction of the fracture end, it can

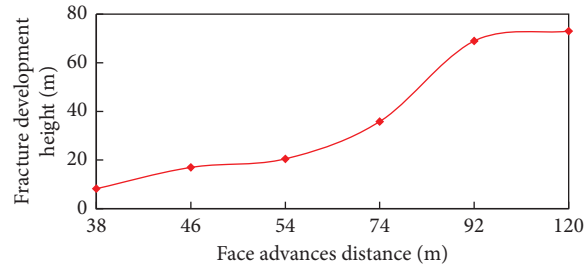


FIGURE 5: Fracture development height vs. longwall face advances.

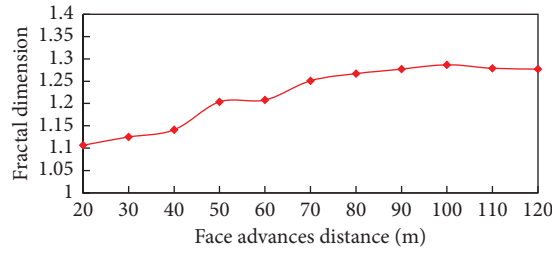


FIGURE 6: The fractal dimensions of fractures with different advance distances.



FIGURE 7: Physical simulation experiment model of Hongliulin Coal Mine.

TABLE 2: The material ratio of physical simulation experiment.

Lithology	Thickness (m)	Depth (m)	Consumables (kg)			
			Sand	Plaster	Calcium carbonate	Fly ash
Loess	39.00	39.00	Sand (56.16) : loess (16.16) : silicone oil (12.48)			
Red soil	30.80	69.80	Sand (56.16) : loess (16.16) : silicone oil (12.48)			
Siltstone	4.00	73.80	11.52	0.38	0.90	
Fine-grained sandstone	2.40	76.20	6.83	0.26	0.60	
Sandy mudstone	0.80	77.00	2.30	0.03	0.23	
Fine-grained sandstone	2.50	79.50	7.11	0.27	0.62	
Siltstone	10.60	90.10	30.53	1.02	2.37	
Fine-grained sandstone	3.00	93.10	8.53	0.32	0.75	
Medium-grained sandstone	2.10	95.20	5.97	0.15	0.60	
Fine-grained sandstone	1.50	96.70	4.32	0.14	0.34	
Medium-grained sandstone	7.40	102.60	21.05	0.52	2.11	
Fine-grained sandstone	3.30	105.90	9.39	0.35	0.82	
Coarse-grained sandstone	8.60	111.20	24.46	0.61	2.45	
Medium-grained sandstone	3.20	114.40	9.10	0.23	0.91	
Siltstone	2.40	113.60	6.91	0.23	0.54	
No. 4-2 coal seam	2.05	115.65	2.31	2.31	0.12	0.58
Medium-grained sandstone	1.40	117.05	3.98	0.10	0.40	



FIGURE 8: The immediate roof caves.

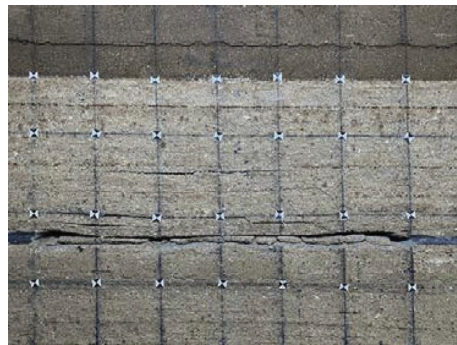


FIGURE 9: The first caving of main roof.

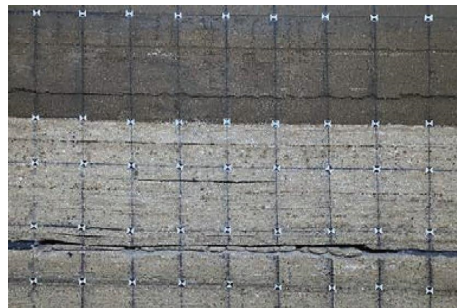


FIGURE 10: The roof caving with advances to 70 m.



FIGURE 11: The roof caving with critical mining.

lead to in-plane shear fractures (Fracture type I in Figure 14(a)). When the boundary concentrated tensile stress  $\sigma_{\theta}$  acts on the direction which is perpendicular to the upward fracture propagation direction, it can lead to tensile fractures (Fracture type II in Figure 14(b)).

The propagation of mining-induced fractures is the combined action of the previous two types of fractures. Therefore, it should be analyzed as mixed-type fractures (Fracture type I and II) in fracture mechanics, as shown in Figure 15.

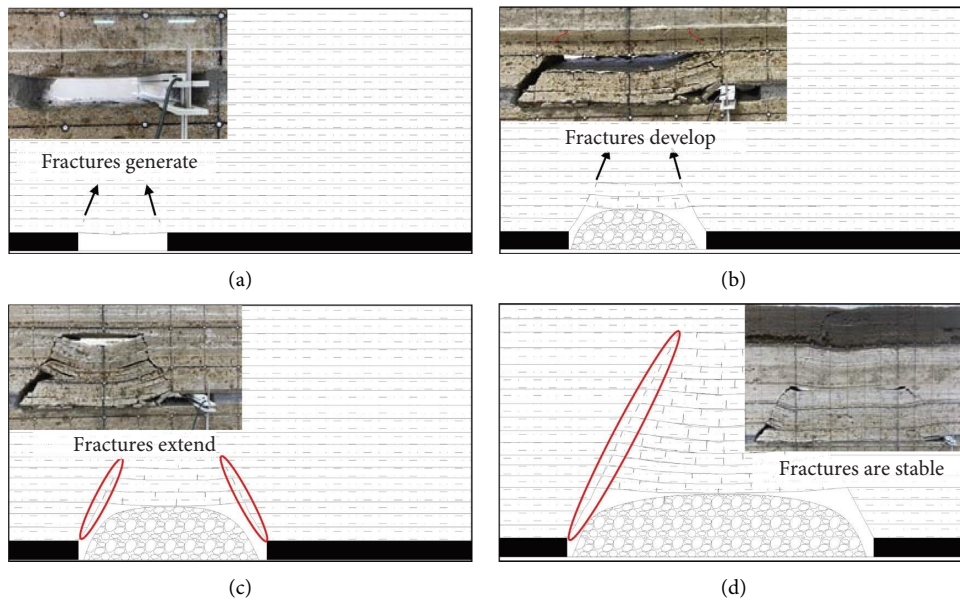


FIGURE 12: Development stage of mining-induced upward fractures: (a) fractures generate; (b) fractures develop; (c) fractures extend; (d) fractures stabilization.

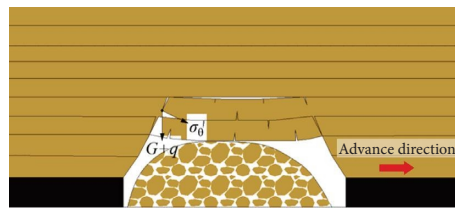


FIGURE 13: Stress analysis of fracture end.

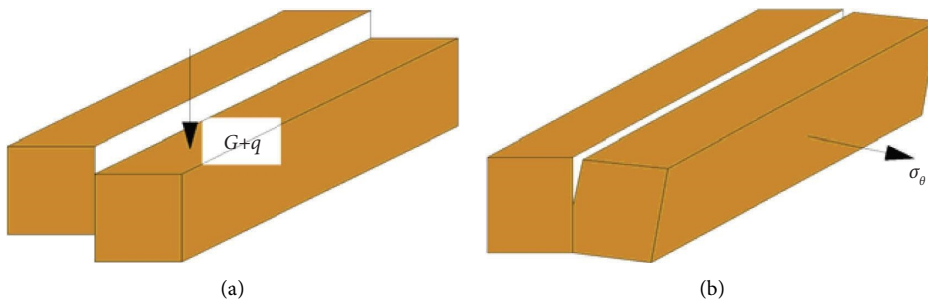


FIGURE 14: Two different fractures types: (a) in-plane shear fractures (fracture type I); (b) tensile fractures (fracture type II).

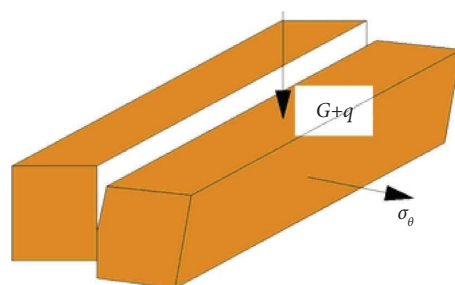


FIGURE 15: Mining-induced mixed-type fracture.

**3.2. Development Mechanism of Upward Fractures.** It is known that after longwall face mining, there are three zones along the vertical section of the rock strata. In caving zone, the caving roof represents disorder caving state, fractured zone is above caving zone, its roof shows as orderly caving, and broken roof shows that the upper part is stretched and the lower part is squeezed. In continuous deformation zone, there are no fractures that exist.

Due to the fact that the roof represents layered caving with mining, in order to analyze the development mechanism of the upward fracture in the fractured zone and determine its development height, the strata in the fractured zone were numbered from bottom to top (1, 2, . . . , n), as shown in Figure 16.

The broken propagation of strata in fractured zone is calculated layer by layer from bottom to top. When the tensile stress and the vertical stress exceed its critical strength, fracture is first generated at the top of the rock layer, and then, under the effect of combined stress, the fracture will extend downward. If it penetrates through the rock layer, it will be broken and become a channel for water or gas conduction, and at the same time, the upward fracture develops and extends upward.

**3.3. Determination Method for the Development Height of Upward Fractures.** According to the development mechanism of upward fractures, with the increase of the calculated layer in fractured zone, when the fracture of No.  $n - 1$  layer can penetrate through the layer's free surface, this rock layer is completely broken, and the upward fracture can develop upwards. When the No.  $n$  layer is calculated, if the resultant stress is not large enough and cannot result in fracture propagation, the No.  $n$  layer is not

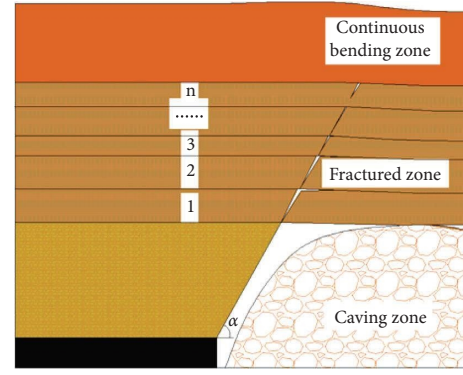


FIGURE 16: Development mechanism of upward fractures.

broken completely; therefore, the upward fractures cannot develop upwards.

Based on the critical mining conditions, the method for the development height of upward fractures can be determined. Its development height is from the top of the coal seam to the bottom of the No.  $n$  rock layer, as shown in Figure 17.

## 4. Theoretical Model and Criterion of Fracture Propagation

**4.1.  $\sigma_{(\theta)\max}$  Theoretical Model of Fracture Propagation.** According to the  $\sigma_{(\theta)\max}$  theory proposed by Li et al. [29], the parameter controlling the fracture of the rock stratum is the maximum hoop tensile stress  $\sigma_{(\theta)\max}$  at the fracture end. Based on this, the theoretical model of fracture propagation is established (Figure 18).

The stress state at the fracture end is given as

$$\begin{cases} \sigma_r = \frac{1}{(2\pi r)^{(1/2)} \cos \frac{\theta}{2}} \left[ K_I \left( 1 + \sin^2 \frac{\theta}{2} \right) + \frac{3}{2} K_{II} \sin \theta - 2 K_{II} \tan \frac{\theta}{2} \right] + \dots \\ \sigma_\theta = \frac{1}{(2\pi r)^{(1/2)} \cos \frac{\theta}{2}} \left[ K_I \cos \theta - \frac{3}{2} K_{II} \sin \theta \right] + \dots \\ \tau_{r\theta} = \frac{1}{(2\pi r)^{(1/2)} \cos \frac{\theta}{2}} \left[ K_I \sin \theta + K_{II} (3 \cos \theta - 1) \right] + \dots \end{cases}, \quad (2)$$

where  $\theta$  is the fracture propagation angle,  $^\circ$ .  $r$  is the distance from infinitesimal to fracture end,  $m$ .  $K_I$  is the strength factor of fracture type I,  $\text{MPa} \cdot \sqrt{m}$ .  $K_{II}$  is the strength factor of fracture type II,  $\text{MPa} \cdot \sqrt{m}$ .  $K_I$  and  $K_{II}$  can be calculated by the equations (3) and (4).

$$K_I = \sigma_\theta \sqrt{\pi c}, \quad (3)$$

$$K_{II} = \tau \sqrt{\pi c}, \quad (4)$$

where  $\sigma_\theta$  is the tensile stress at point A, MPa.  $\tau$  is the shear stress at point A, MPa.  $c$  is the half-length of the fracture,  $m$ , take  $c = 1$ ,  $r/c \ll 1$ .

**4.2. Establishment of Fracture Propagation Criterion.** The fracture extends in the radial direction at its end. When  $\sigma_{(\theta)\max}$  reaches the critical strength factor of the rock formation, the fracture starts to extends. According to

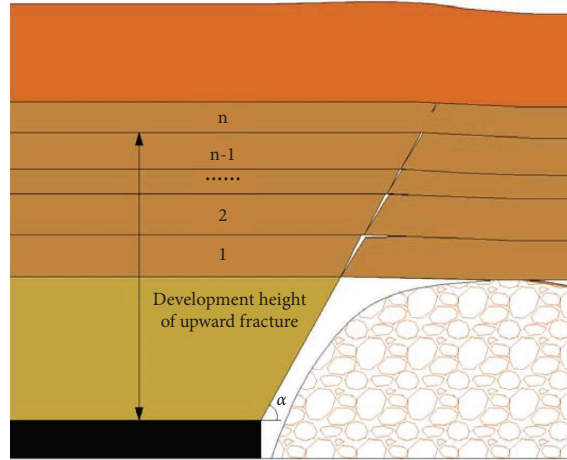


FIGURE 17: Determination of development height of upward fracture.

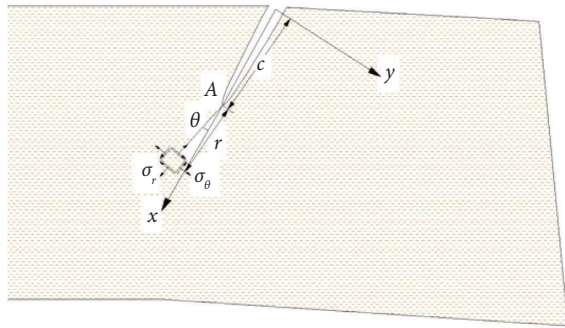


FIGURE 18: Theoretical model of fracture propagation.

equation (2), it can be expressed as equations (5) and (6) mathematically:

$$\cos \frac{\theta_0}{2} \left( \frac{K_I}{K_{Ic}} \cos^2 \frac{\theta_0}{2} - \frac{3}{2} \frac{K_{II}}{K_{Ic}} \sin \theta_0 \right) = 1, \quad (5)$$

$$\cos \frac{\theta_0}{2} [K_I \sin \theta_0 + K_{II} (3 \cos \theta_0 - 1)] = 0, \quad (6)$$

where  $K_{Ic}$  is the critical stress strength factor of fracture type I (material constant),  $\text{MPa} \cdot \sqrt{\text{m}}$ .  $K_{IIc}$  is the critical stress strength factor of fracture type II (material constant), and  $\text{MPa} \cdot \sqrt{\text{m}}$ .  $\theta_0$  is the fracture propagation initiation angle,  $^\circ$ . According to equations (5) and (6), the fracture initiation trace of the  $\sigma_{(\theta)\text{max}}$  theory is obtained as shown in Figure 19.

The criterion for fracture propagation is as follows:

- (1) According to equations (3), (4), and (6), the fracture propagation initiation angle  $\theta_0$  can be obtained.
- (2) According to equations (3)–(5) and the value  $\theta_0$  calculated above, combining with Figure 19, it can be judged whether the fracture extends (whether the upward fractures develop).

If the coordinate  $(K_I/K_{Ic}, K_{II}/K_{IIc})$  is inside the fracture initiation trace, the fractures do not extend, and the mining-induced upward fractures do not develop upwards. On the contrary, if it is outside the fracture

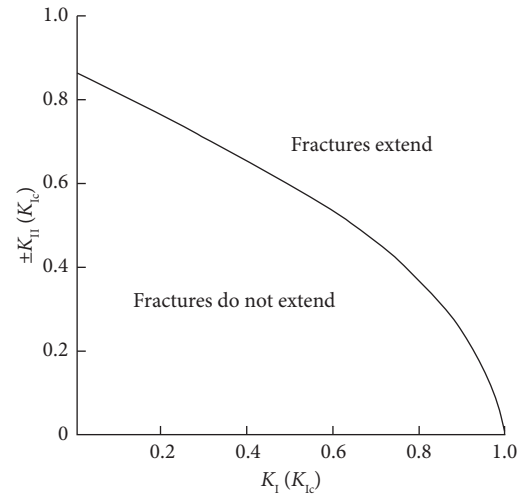


FIGURE 19: Fracture initiation trace of the  $\sigma_{(\theta)\text{max}}$  theory.

initiation trace, the fracture extends until it reaches the free surface, and the upward fracture continues to develop upwards.

## 5. Conclusions

The development of upward fractures can be divided into the following three stages: with the face advances from the open cut, the vertical fractures are generated at the mining boundary, and the roof is flexural but not caved; it is “Fractures generate stage.” After roof caves, the upward fractures extend and develop upward along the caving angle with continue advances; it is “Fractures develop and extend stage.” When the face reaches critical mining, the development height of the upward fractures is at its maximum and is basically invariable; it is “Fractures stabilization stage.”

Mining-induced fractures can be analyzed as mixed-type fractures (in-plane shear fractures and tensile fractures) in fracture mechanics; when the combined stress exceeds the critical strength of stratum, it will extend downward until

penetrate through the stratum, and the upward fracture develops and extends upwards.

The parameter controlling the fracture of the rock stratum is the maximum hoop tensile stress  $\sigma_{(\theta)\max}$  at the fracture end, the theoretical model of fracture propagation was established, and the criterion of upward fractures was proposed. If the coordinate  $(K_I/K_{Ic}, K_{II}/K_{IIc})$  is inside the fracture initiation trace, the upward fractures do not develop upwards; on the contrary, the upward fracture continues to develop upwards.

## Data Availability

The experimental data are all included within the article.

## Conflicts of Interest

The authors declare that they have no conflicts of interest.

## Acknowledgments

The authors thank the Natural Science Foundation of Inner Mongolia of China (grant number no. 2022QN05007) for its support in this study. This research was funded by the Natural Science Foundation of Inner Mongolia of China, grant number no. 2022QN05007, and Introduce Excellent Talents Support Project of Inner Mongolia, grant number no. 0701012101.

## References

- [1] W. Zhu and Y. H. Teng, "Characteristic of development of the fractured zone in mining under medium hard overburden using fully-mechanized top-coal caving method," *Applied Mechanics and Materials*, vol. 226, pp. 1312–1317, 2012.
- [2] C. L. Zhang and Y. Zhang, "Stress and fracture evolution based on abutment change in thick coal seam—a case study in China colliery," *Electronic Journal of Geotechnical Engineering*, vol. 21, no. 12, pp. 4369–4386, 2016.
- [3] Q. Bai and S. Tu, "A general review on longwall mining-induced fractures in near-face regions," *Geofluids*, vol. 2019, pp. 1–22, Article ID 3089292, 2019.
- [4] Y. Tan, H. Cheng, W. Y. Lv et al., "Calculation of the height of the water-conducting fracture zone based on the analysis of critical fracturing of overlying strata," *Sustainability*, vol. 14, no. 9, p. 5221, 2022.
- [5] H. F. Huang, Z. G. Yan, B. H. Yao, and H. J. Xu, "Research on the process of fracture development in overlying rocks under coal seams group mining in Wanli Mining Area," *Journal of Mining & Safety Engineering*, vol. 29, no. 5, pp. 619–624, 2012.
- [6] Z. J. Wen, S. L. Jing, Y. J. Jiang et al., "Study of the fracture law of overlying strata under water based on the flow-stress-damage model," *Geofluids*, vol. 2019, Article ID 3161852, 12 pages, 2019.
- [7] Z. L. Li, L. G. Wang, K. Ding et al., "Study on fracture and seepage evolution law of slope covered by thin bedrock under mining influence," *Minerals*, vol. 12, no. 3, p. 375, 2022.
- [8] E. H. Bai, W. B. Guo, Y. Tan et al., "Regional division and its criteria of mining fractures based on overburden critical failure," *Sustainability*, vol. 14, no. 9, p. 5161, 2022.
- [9] J. L. Xu, X. Z. Wang, W. T. Liu, and Z. G. Wang, "The influence of the location of the main key strata on the height of the water flowing fractured zone," *Journal of Rock Mechanics and Engineering*, vol. 28, no. 02, pp. 380–385, 2009.
- [10] J. L. Xu, W. B. Zhu, and X. Z. Wang, "Height prediction method of water flowing fractured zone based on key stratum position," *Coal Journal*, vol. 37, no. 05, pp. 762–769, 2012.
- [11] W. Z. Zhang and Q. X. Huang, "Study on the development height of upward fissures in local filling mining of shallow coal seams," *Coal Mine Safety*, vol. 45, no. 04, pp. 40–42, 2014.
- [12] B. C. Zhao, H. Sun, Y. X. Guo, and X. Yang, "Research on dynamic evolution law of water-conducting fracture in thick loose layer near shallow coal seam mining," *Coal Engineering*, vol. 53, no. 10, pp. 100–105, 2021.
- [13] J. Cao and Q. X. Huang, "Regularity and control of overburden and surface fractures in shallow-contiguous seams," *Coal Geology & Exploration*, vol. 49, no. 4, pp. 213–220, 2021.
- [14] T. Liang, X. L. Liu, and S. J. Wang, "Fractal study on the crack network evolution and permeability change in mining rock mass," *Journal of China Coal Society*, vol. 44, no. 12, pp. 3729–3739, 2019.
- [15] L. H. Guo, H. Cheng, S. L. Peng, and B. J. Fu, "Study on evolution and subsidence fractal characteristics of overlying strata in thick loose layers and thin bedrocks," *Safety In Coal Mines*, vol. 51, no. 9, pp. 59–64, 2020.
- [16] D. P. Li, H. W. Zhou, D. J. Xue, H. Y. Yi, and H. L. Gao, "Relationship between percolation and fractal properties of mining-induced crack network in coal and rock masses," *Rock and Soil Mechanics*, vol. 36, no. 4, pp. 1135–1140, 2015.
- [17] S. G. Li, W. B. Qin, Z. L. Li, Y. Ding, and H. F. Lin, "Research on fractal characterization of mined crack network evolution repeated coal mining," *Journal of Liaoning Technical University*, vol. 35, no. 12, pp. 1384–1389, 2016.
- [18] X. S. Li, Q. H. Li, Y. J. Hu et al., "Study on Three-dimensional dynamic stability of open-pit high slope under blasting vibration," *Lithosphere*, vol. 2021, no. 4, Article ID 6426650, 2022.
- [19] D. Z. Ren, X. Z. Wang, Z. H. Kou et al., "Feasibility evaluation of CO<sub>2</sub> EOR and storage in tight oil reservoirs: a demonstration project in the Ordos Basin," *Fuel*, vol. 331, Article ID 125652, 2023.
- [20] M. C. He, Q. R. Sui, M. N. Li, Z. J. Wang, and Z. G. Tao, "Compensation excavation method control for large deformation disaster of mountain soft rock tunnel," *International Journal of Mining Science and Technology*, vol. 32, no. 5, pp. 951–963, 2022.
- [21] C. Zhu, M. C. He, B. Jiang, X. Z. Qin, Q. Yin, and Y. Zhou, "Numerical investigation on the fatigue failure characteristics of water-bearing sandstone under cyclic loading," *Journal of Mountain Science*, vol. 18, no. 12, pp. 3348–3365, 2021.
- [22] Q. Wang, S. Xu, Z. X. Xin, M. C. He, H. Y. Wei, and B. Jiang, "Mechanical properties and field application of constant resistance energy-absorbing anchor cable," *Tunnelling and Underground Space Technology*, vol. 125, Article ID 104526, 2022.
- [23] C. Zhu, X. D. Xu, X. T. Wang et al., "Experimental investigation on nonlinear flow anisotropy behavior in fracture media," *Geofluids*, vol. 2019, no. 9, Article ID 5874849, 9 pages, 2019.
- [24] Y. D. Bao, J. P. Chen, L. J. Su, W. Zhang, and J. W. Zhan, "A novel numerical approach for rock slide blocking river based on the CEFDEM model: a case study from the Samaoding paleolandslide blocking river event," *Engineering Geology*, vol. 312, Article ID 106949, 2023.
- [25] Q. Wang, B. Jiang, S. Xu et al., "Roof-cutting and energy-absorbing method for dynamic disaster control in deep coal

- mine,” *International Journal of Rock Mechanics and Mining Sciences*, vol. 158, Article ID 105186, 2022.
- [26] S. B. Tang, J. M. Li, S. Ding, and L. T. Zhang, “The influence of water-stress loading sequences on the creep behavior of granite,” *Bulletin of Engineering Geology and the Environment*, vol. 81, no. 11, p. 482, 2022.
- [27] X. Liang, S. B. Tang, C. A. Tang, L. H. Hu, and F. Chen, “Influence of Water on the Mechanical Properties and Failure Behaviors of sandstone under Triaxial Compression,” *Rock Mechanics and Rock Engineering*, pp. 1–32, 2022.
- [28] Y. Wang, C. Zhu, M. C. He, X. Wang, and H. L. Le, “Macromeso dynamic fracture behaviors of Xinjiang marble exposed to freeze thaw and frequent impact disturbance loads: a lab-scale testing,” *Geomechanics and Geophysics for Geo-Energy and Geo-Resources*, vol. 8, no. 5, 154 pages, 2022.
- [29] H. Li, Z. G. Yin, J. Xu, and W. W. Zhang, *Rock Fracture Mechanics*, Chongqing University Press, Chongqing, China, 1988.

## Research Article

# Deformation Characteristics and Control Mechanisms of Deep High-Stress Large-Span Roadways

Bo Yang <sup>1,2</sup> and Jing Chai <sup>1,3</sup>

<sup>1</sup>*Xi'an University of Science and Technology, Xi'an, Shaanxi 710000, China*

<sup>2</sup>*Shanxi Institute of Energy, Jinzhong, Shanxi 030600, China*

<sup>3</sup>*Key Laboratory of Western Mine Exploitation and Hazard Prevention, Xi'an University of Science and Technology, Ministry of Education, Xi'an, Shaanxi 710000, China*

Correspondence should be addressed to Jing Chai; [chaij@xust.edu.cn](mailto:chaij@xust.edu.cn)

Received 15 September 2022; Revised 30 October 2022; Accepted 24 November 2022; Published 2 February 2023

Academic Editor: Fuqiang Ren

Copyright © 2023 Bo Yang and Jing Chai. This is an open access article distributed under the Creative Commons Attribution License, which permits unrestricted use, distribution, and reproduction in any medium, provided the original work is properly cited.

Controlling the surrounding rock in soft rock roadways under deep high stress, strong rheology, and intensive mining is critical for the safety, efficiency, and economy of mine production. In this study, the mechanical properties, large deformation mechanism, and support countermeasures of surrounding rock in the high-stress roadway in the Yuwu coal mine were systematically explored through laboratory tests, numerical calculations, and field measurements. It is shown that mudstone and sandstone are mainly composed of chlorite and kaolinite, respectively. Also, mudstone features elastoplasticity and experiences argillization and swelling in water. The mechanism of surrounding rock deformation in the high-stress roadway in the Yuwu coal mine was determined. As the V-shaped shear zone in the side corner expanded to the deep under high deviatoric stress, large-scale tensile damage occurred in the shallow surrounding rock. Consequently, discontinuous stresses in deep and shallow parts induce the expansion and fracturing of the roadway. The deformation velocity and damage degree of surrounding rock rise exponentially under different stress release coefficients, so the reduced distance of the face roof under control and timely support is important for restricting the free surface. An idea of “timely and active reinforcing the side and strengthening the bottom” was proposed. This approach made the loads on all the support objects within the working range. The overall deformation of the surrounding rock was controlled within 350 mm, ensuring the long-term stability of the roadway.

## 1. Introduction

Due to its mechanical properties and complex stress fields, deep roadway surrounding rock features significant strength attenuation and fast deformation [1–6]. Under the superimposed effect of high stress and strong mining, surrounding rock experiences continuous and discontinuous deformation and even disasters [7]. Therefore, clarifying the microscopic characteristics and macromechanical properties of deep surrounding rock and the stress release characteristics of deep roadways is crucial for developing deep roadway control technology.

In order to increase the stability of surrounding rock in deep roadways, researchers have carried out extensive work

in terms of the type, mechanism, and control technology of surrounding rock deformation. The deformation of roadway surrounding rock is mainly induced by the nature of rock strata (e.g., the significant strength attenuation due to argillization in water), stress (the postpeak rock dilation, integrity reduction, and strength attenuation caused by the joint effects of pure shear, bending and tensile shear), and structure (e.g., special geological tectonic zones) [8, 9]. Based on numerical calculations, Liu and Sun [10] proposed that the failure mode of deep roadway surrounding rock changes from tensile failure to shear failure with increased depth. Wang et al. [11] suggested a method for the support of roadways in deep mining areas with high-strength bolt-grouting. Based on a self-developed deep-ground testing

device, Xu et al. [12] generalized the whole process of roadway instability using various monitoring methods and concluded that the surrounding rock instability is induced by discontinuous stresses (as a result of internal stress drop) in the shallow and deep. Li et al. and Wang et al. [13, 14] identified the zonal fracturing characteristics of deep surrounding rock and developed a constitutive applicability model. Deep roadway control mainly enhances the coupling strength and enlarges the angle of high-stress coordinated deformation of surrounding rock. The main methods include passive support, active support, repair and reinforcement, pressure release and transfer, and the joint method [15, 16]. Different types of surrounding rock should be reinforced by different methods. Based on the reserved deformation, Yu et al. [17] proposed a comprehensive support and repair strategy using a bolt, metal mesh, shotcrete, grouting, anchor cable, and combined anchor cable. Considering the boundary shape characteristics of the plastic zone, Guo et al. [18] reported the evaluation criterion of the location of potential hazards and critical evaluation points of dynamic roadway disasters. Yang et al. [19] considered that the shallow tensile fracturing and large expansion are the root causes of roadway floor heave and roof cut-off and presented a new joint support method of “anchor bolt-anchor cable-metal mesh-sprayed concrete and shell.” Concerning the asymmetric stress and damage zone of roadways, Zhu et al. [20] introduced the “three shells” collaborative support technology for large-section chambers in deep mines. Li et al. [21] explored the influence of anchoring agent with high sand content, mechanical anchoring means, or grouting reinforcement on the anchoring force.

The failure mechanism of surrounding rocks in deep roadways has always attracted much attention. Zhao et al. [22] considered that the maximum and minimum stresses deteriorated gradually with the increase of time after roadway excavation, and the failure zones in soft rock mass expanded increasingly over time. Zhan et al. [23] analyzed the stability control theory of soft-rock roadways based on the Nishihara model and Drucker–Prague’s modification of the Mohr–Coulomb yield condition. Jia et al. [24] proposed the nonlinear creep constitutive model of soft rock and its numerical realization method by the indoor creep test of soft rock and the large-scale triaxial creep tests on-site. Zhan et al. [25] reported that combining the parts organically and coordinating their bearing performance effectively realize the stability control of large nonlinear deformation. Zhu et al. [26] divided the surrounding rock stress and roadway deformation characteristics into advance influence, rapid change, and stability stages. The new support technologies for deep soft rock roadways were put forward based on mechanism research. Li et al. [1] proposed a “double layer bolt-mesh-shotcrete and U-shaped steel” supporting scheme by numerical simulations and field tests, effectively solving the problem of large deformation and failure of deep soft rock roadway. Yuan et al. [27] introduced a method of bolt-net-cable-grout coupling support and achieved good results in practical application, effectively solving the support issues of high-stress broken soft rock roadway in deep mines. Yang et al. [28] explored a new, improved method of support

called the “bolt-cable-mesh and shell” support scheme, which could change the stress state of surrounding rock especially roadway floor. Zhao et al. [29] proposed “shotcreting, grouting anchor bolt, anchor bolt, grouting anchor cable, and anchor cable” compound timbering fashion. The rationality of the supporting technology was corroborated by theoretical analysis, engineering analogy, engineering practice, and numerical simulations.

The above studies have enriched the theory and practice concerning stability control of deep roadway surrounding rocks [30, 31]. However, these analyses were made from a macroscopic perspective, neglecting the stress release characteristics of surrounding rock corresponding to the actual roadway support timing. Therefore, considering the large buried deep roadways in the Yuwu coal mine as the case study, the microstructure, macromechanical properties, grade classification, and damage characteristics of surrounding rock under different stress release coefficients were analyzed in this paper. On this basis, a surrounding rock reinforcement method was proposed to provide a reference for supporting deep roadways in similar geological conditions.

## 2. Occurrence Conditions and Macro and Microcharacteristics of Roadway Surrounding Rock

### 2.1. Occurrence Conditions of Roadway Surrounding Rock.

The Yuwu coal mine is located southeast of Shanxi province, west of the Lu’an mine area. Its longitude and latitude range is  $112^{\circ}47' - 112^{\circ}54'$  east and  $36^{\circ}15' - 36^{\circ}25'$  north (Figure 1). The mine has its railroad line linked to the Chinese railroad system, which can realize the transportation of coal nationwide, and the transportation is very convenient. The geographical location map involves copyright and issues related to confidentiality. On average, the No. 3 coal seam of the Yuwu coal mine is 6.4 m thick. Along the floor of the S5203 transportation roadway, its main roof, immediate roof, and immediate floor are medium sandstone, sandy mudstone, and mudstone, with average thicknesses of 18 m, 1.3 m, and 3.2 m, respectively. The roadway, whose size is  $5,400 \text{ mm} \times 3,800 \text{ mm}$ , presents the phenomenon of roof water trickling in its partial area. The maximum principal stress is in the vertical direction of the mine, i.e., the vertical stress is the maximum stress, and the horizontal stress is 0.5–1.0 times as high as the vertical stress. The principal and horizontal stresses of the S5203 transportation roadway are 14.3 MPa and 13.1 MPa, respectively.

### 2.2. Macro and Microcharacteristics of the Surrounding Rock.

Samples were taken from the roof and floor of the S5203 roadway on-site and processed into a standard cylinder size (50 mm diameter  $\times$  100 mm height) in the laboratory for a uniaxial compression test. Also, rock powders with different lithologies were processed for X-ray diffraction tests to analyze their mineral compositions. The specific test results are shown in Figure 2. Mudstone has a long compression phase, strong postpeak plasticity, a small elastic modulus

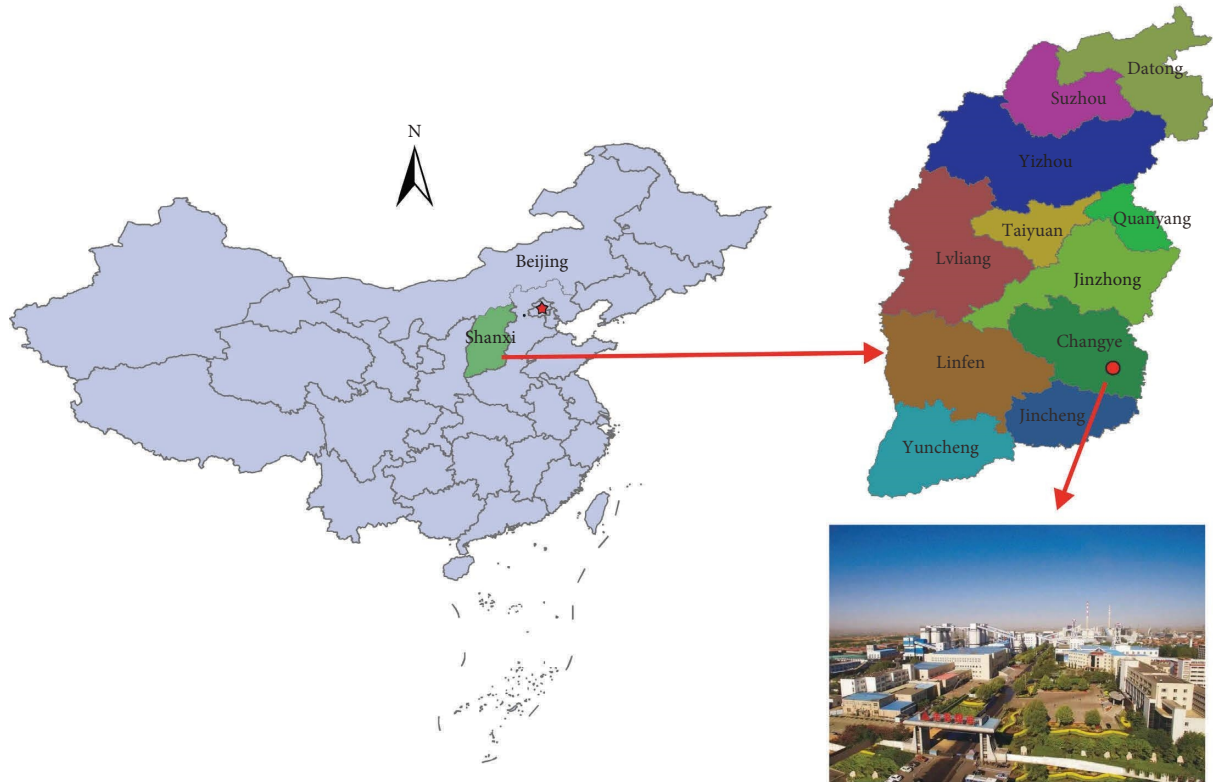


FIGURE 1: Geographic location and mining map of the Yuwu coal mine.

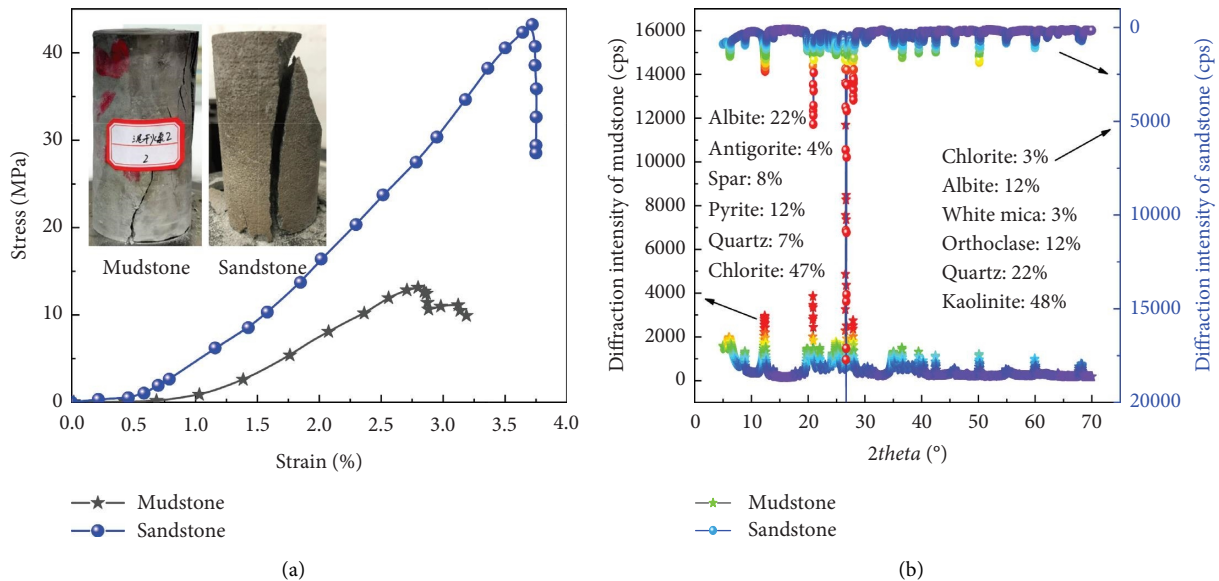


FIGURE 2: Macro and microcharacteristics of rocks of different lithologies: (a) stress-strain curves and (b) mineral compositions.

(0.8 GPa), and a low peak strength (13.1 MPa). Sandstone exhibits a high fracturing strength and a remarkable elastic brittleness, with an elastic modulus and a peak strength of 2.0 GPa and 43.2 MPa, respectively. It can be seen from the mineralogical compositions of mudstone and sandstone that mudstone is mainly comprised of sodium feldspar (22%) and chlorite (47%). Chlorite has a flaky microstructure, and

these flakes rub strongly with each other when damage occurs. However, chlorite softens while encountering water, inducing severe deformation of the roof and floor. Sandstone mainly comprises kaolinite (48%) and quartz (22%), with closely packed microscopic particles. This type of rock fractures severely when it fails, which is consistent with the laboratory observation of rock compression and fracturing.

2.3. *Grade of Roadway Surrounding Rock.* From the mechanical properties of the roof and floor of roadways, the level of ground stress, and the “Engineering Rock Classification Standard,” it can be determined that the roof of roadways belongs to the high-stress area [32]. The floor and the two sides belong to the extremely high-stress area. The strength-to-stress ratio can be expressed as follows:

$$S_r = \frac{k_v R_c}{\sigma_{\max}}, \quad (1)$$

where  $k_v$  is the integrity factor, taken as 0.3–0.5 in this paper;  $\sigma_{\max}$  is the maximum principal stress perpendicular to the direction of the roadway axis, MPa;  $R_c$  is the uniaxial compressive strength of the rock, MPa. Hence, the surrounding rock on the two sides and floor can be classified as Grade V, which is Grade II on the roof.

### 3. Stress Release and Deformation Characteristics of Surrounding Rock in a Deep Roadway

3.1. *Model Validation and Large-Scale Modeling.* In this paper, the deformation and damage characteristics of roadway surrounding rock were analyzed by the block distinct universal element code-grain boundary model (UDEG-GBM) [33, 34], as shown in Figure 3. The mechanical behavior of blocks is controlled by the mechanical properties of the crystal interface and the geometric features of the polygon. Once it exceeds the shear or tensile strength, the bond between particles breaks, producing compressive shear fractures, tensile fractures, or sliding fractures. Therefore, it can be considered an effective tool for studying the generation, initiation, and extension of fractures.

A uniaxial compression numerical model of the same size as the laboratory model was developed (including two steel plates on the roof and floor of the sample). The model employed inhomogeneous particle size distribution and a proven reasonable block length (3 mm). The upper and lower steel plates were applied with a constant velocity of 0.01 m/s in the Y-direction to guarantee a quasistatic state of the sample. The total reactive forces (which are continuously recorded) at the contact between the sample and the roof loading plate were the axial stresses.

The stress-strain responses of the sample exhibit an initial linear elastic trend without a compression phase. This is due to the disparity between the numerical calculations and laboratory results. The yielding phase was not noticeable. The sample mainly experienced axial splitting and tensile fracturing, consequently bearing macroscopic fractures parallel to the loading direction. Thus, tensile fractures were generated at the low-loading stress stage, and the shear fractures were generated at an accelerating rate during the yielding phase. Moreover, the shear fracture generation stage lasted longer, indicating that mudstone is strongly plastic.

Meanwhile, the rock compression process witnessed a shear localization effect and mixed damage of the axial splitting/shear zone, which belongs to the final phase. Sandstone had 1.3 times as many tensile fractures as

mudstone. Nevertheless, the two types of rock were close in the number of shear fractures, indicating that postpeak tensile fracturing can indirectly characterize the elastic brittleness of the sample. The numerical calculation and laboratory test results can confirm the reasonableness of the simulation parameters and methods, which can be used to analyze the scenarios of large-scale roadway fracturing.

The large-scale numerical calculation model was close to the actual geological conditions (58 m length  $\times$  38 m height). The upper boundary of the model was stress constraint, which could characterize the overlying stratum load (14 MPa), and the left, right, and lower boundaries of the model were roller supports. The numerical model, local detail image of the roadway location, and numerical calculation model are shown in Figure 4 and Table 1.

#### 3.2. Damage Characteristics of Deep Roadway Surrounding Rock

3.2.1. *Deformation and Principal Stress Evolution Characteristics of a Roadway.* The monitoring curves of displacements of the roof, floor, and the two sides at different stress release coefficients after mining are shown in Figure 5. The overall deformation of the roadway develops in a stepwise manner with a decrease in the stress release coefficient. The roadway deforms unevenly under unsupported conditions, with serious roof subsidence, floor heave, and side shrinkage occurring simultaneously. The left roof subsides for about 520 mm. The heave of the right floor is slightly larger than that of the left floor; however, both are no larger than 530 mm. The left and right sides deform for 630 mm and 930 mm, respectively. In addition, the side deformation and floor heave are consistent.

It can be seen from the principal stress evolution under different stress release effects (Figure 6) that the stress is concentrated on the roadway surface, especially on the side corners where the stress is intensively concentrated. When the deflective stress reaches the shear strength, the surrounding rock becomes damaged, and the bearing capacity of the shallow surrounding rock is reduced. As the tensile stress zone continues to expand deeper, a large stress relaxation zone around the roadway is consequently formed. Hence, roadway support should be timely provided because a large stress release coefficient (little energy release) can effectively mitigate the overall displacement of the roadway and the magnitude of the stress environment. Given the synergistic deformation of the two sides, roof, and floor, the sides and floor should be supported synergistically; otherwise, the enlarged displacement of the sides will lead to stress transfer to the floor, thus inducing floor heave.

3.2.2. *Damage and Fracturing Evolution of Surrounding Rock.* Since the instability of underground engineering surrounding rock is closely related to the stress environment, plastic zone, and extension of fractures [18], it is of great significance to clarify the generation and extension of fractures in surrounding rock after mining in deep roadways. Blue and red lines mark unit and joint shear and

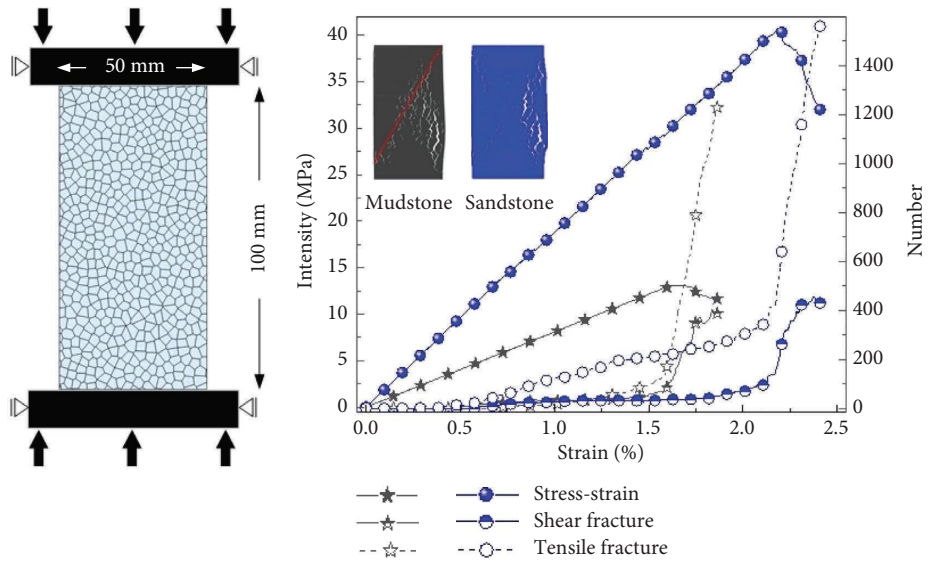


FIGURE 3: Numerical calculation model and model validation.

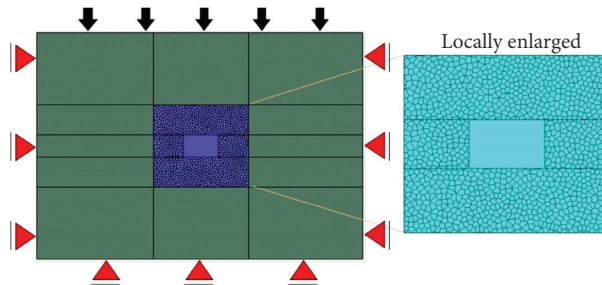


FIGURE 4: Numerical calculation model of severe deformation in a deep high-stress roadway.

TABLE 1: Numerical calculation parameters of severe deformation in a deep high-stress roadway.

Lithology	Block		Block/contact		Contact Normal/tangential stiffness (GPa)
	Elasticity modulus (GPa)	Cohesive force (MPa)	Internal friction angle (°)	Tensile strength (MPa)	
Mudstone	0.8	1.2/3.8	24/30	0.8/1.5	90/70
Sandstone	2.0	4/10	38/40	1.2/2.8	160/100
Coal seam	0.6	1.1/3.2	21/28	1.1/1.4	80/48

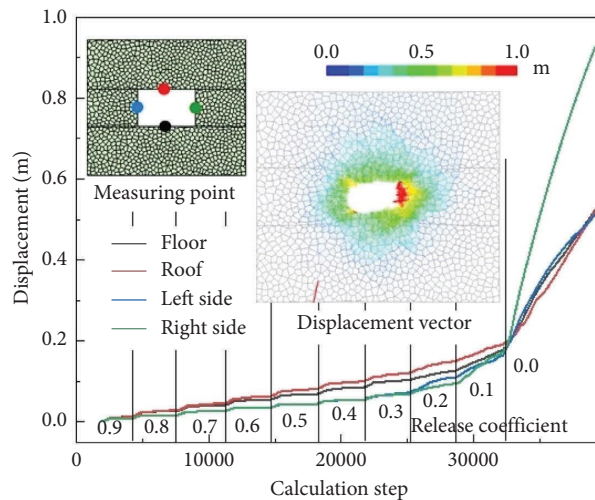


FIGURE 5: Monitoring of surrounding rock deformation at measuring points.

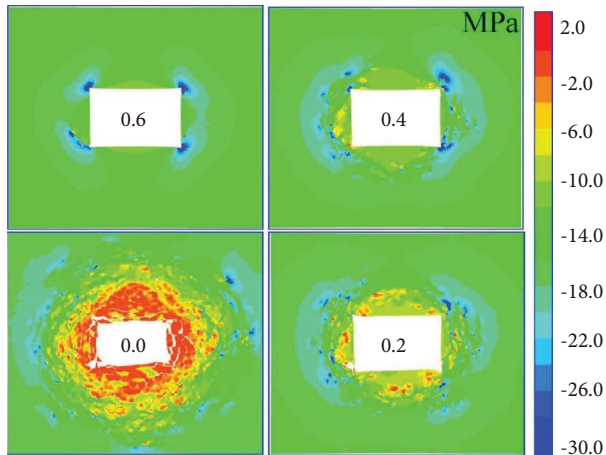


FIGURE 6: Evolution characteristics of principal stress.

tensile damages. Shear fractures that first appear in the side corners may cause shear extrusion damage, which is consistent with the principal stress distribution given in the previous study. As the V-shaped shear damage zone gradually deepens, the stress it releases will give rise to damage on the roof and floor, leaving a huge shear fracture zone in the deep and a tensile damage zone around the roadway surface. Compared with Figure 7, it is apparent that the tensile damage zone is exactly the area where surrounding rock displacement is large (Figure 5), as the tensile damage induces the fragmentation, expansion, and separation of surrounding rock. Since the surrounding rock is severely fragmented, the rock masses almost no longer rub or embed each other.

The unit damage evolution resembles the joint damage evolution, both surging at the stress release coefficient of 0.4. At a 0–30% relaxation state, the internal support pressure of the surrounding rock is sufficient to withstand spalling damage. However, the back-support pressure plummets at a 60% relaxation state, accompanied by a significant plasticity index. Spalling and roof-falling accidents are likely to occur near the roadway. Thus, it is critical to choose appropriate support measures and installation timings for the safety of workers and equipment. Installation timing is an important aspect of roadway reinforcement/support design. If the system is installed too early, the inducing roadway load may exceed the bearing capacity of the structural units. If too late, rock masses may already be irreversibly damaged and slackened.

**3.3. Deformation Mechanism of Roadway in Yuwu Coal Mine.** From the analysis presented previously, the deformation characteristics and mechanism of high-stress roadways in the Yuwu coal mine can be described as follows.

- (1) **Contradiction between high-ground stress and low-strength rock:** The ground stress is high, while the surrounding rock is loose and soft. The mining-induced stress relief on the free side increases deflective stress, and hence, the high stress damages shallow surrounding rock around the roadway. As fractures

expand from the middle of the roadway to the interior and surface, shallow surrounding rock loses its bearing capacity. In addition, the floor containing a large number of clay minerals will aggravate the deformation and damage when contacted with mine water during the mining process.

- (2) **Poor stress state around the roadway:** Due to the poor stress state of the right angle, the high stress tends to be concentrated in the side corners. After the formation of a shear zone, the shallow part of the roadway becomes a free rock layer, which indirectly increases the span of the roadway and leads to a bending of the floor. Floor damage is inconducive to roadway stability because it causes roadway contraction and exacerbates roof subsidence. This vicious cycle will eventually result in the occupation of free space on the roadway.

## 4. Deep Surrounding Rock Control Technology

**4.1. Support Idea and Scheme.** From the results presented previously and the deformation characteristics and mechanism of deep surrounding rock in the Yuwu coal mine, the deep surrounding rock should be reinforced by timely and coordinated support to the roof, floor, and sides. The joint active support of anchor bolts (cables) and double steel joists is adopted in the roadway to improve the coupling performance of deep and shallow surrounding rock. Besides, passive support is adopted to control the initial and surface deformation of surrounding rock, i.e., I-shaped steel sheds are installed on the heading face.

For the roof, it is supported by yielding bolts with an interrow spacing of 830 mm × 700 mm and anchor bolts (cables) with an interrow spacing of 1,660 mm × 700 mm (in a 3-2-3 layout). The lengths of the bolt and cable are 2,400 mm and 6,300 mm, respectively. The two sides and the roof are equipped with metal meshes and double steel ladders. The specific parameters are given in Figure 8.

**4.2. Effectiveness of Roadway Surrounding Rock Control.** In order to verify the reasonableness of the support parameters proposed above, grasp the characteristics of surrounding rock deformation of deep surrounding rock roadways in the Yuwu coal mine, and test the effect of surrounding rock control, on-site monitoring was conducted on the S5203 roadway by taking surface displacement (at cross measuring points), anchor bolt stress, and anchor cable stress as indicators. The monitoring started at 5 m from the heading face.

Surface displacements of the roadway at different times are shown in Figure 9. The roof-to-floor and side-to-side convergences were 210 mm and 140 mm, respectively. Overall, the roadway just deformed mildly, and roof subsidence was slightly larger than the floor heave. The deformation of the two sides and the roof and floor stabilized on the 10th and 15th days, respectively. Meanwhile, during excavation, a thin sandy mudstone stratum was found in the immediate roof. On the 6th day, small fractures began to

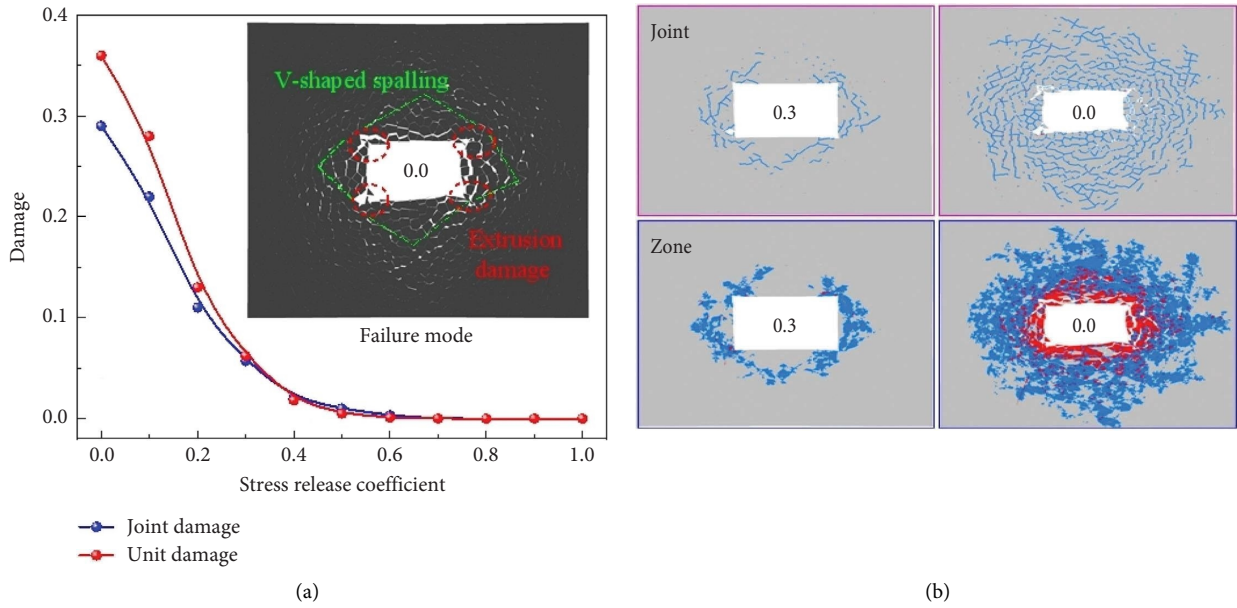


FIGURE 7: Damage and fracturing characteristics of the surrounding: (a) damage evolution of surrounding rock and (b) distribution characteristics of the plastic zone.

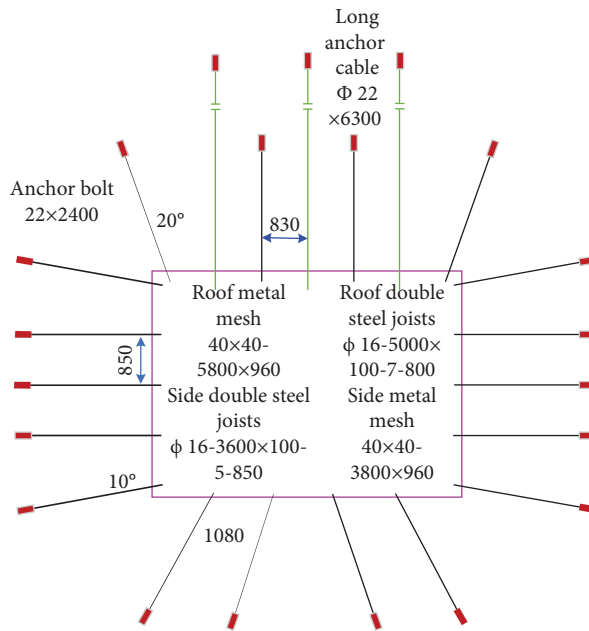


FIGURE 8: Parameters of roadway support.

appear on the roof. Subsequently, they grew wider and became more widespread, in line with serious roof subsidence during the 6th–15th days.

The anchor bolt and cable experienced a significant increase in load at the beginning of roadway excavation and began to stabilize on the 15th day. In descending order, the magnitudes of load are as follows: the roof anchor cable (190 kN), the roof anchor bolt (96 kN), the left side anchor bolt (78 kN), and the right side anchor bolt (75 kN). Such an

order is attributed to the fact that the ground stress was vertical. The anchor bolt and cable had not yet reached their yield limits, indicating that they were in a good stress state with abundant factors. Hence, they could withstand more dynamic loads. In conclusion, with these support parameters, the roadway boasts strong integrity, small surrounding rock deformation, coordinated load on support objects, and high efficiency of multiple support measures. These factors can guarantee a long lifespan of the roadway.

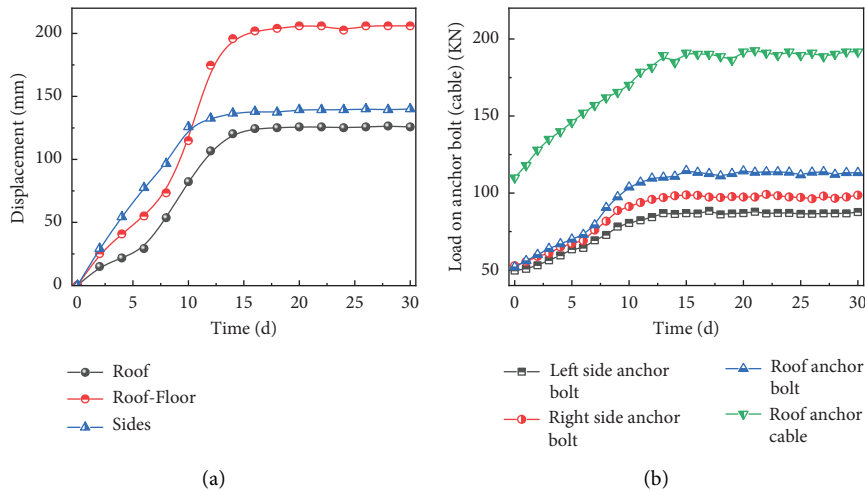


FIGURE 9: Results of on-site monitoring: (a) deformation of roadway surrounding rock and (b) load on anchor bolt (cable).

## 5. Conclusions

In this work, the microstructure, macromechanical properties, grade classification, and damage characteristics of the surrounding rock under different stress release coefficients are analyzed, and a surrounding rock reinforcement method applicable to a specific deep roadway is proposed. This method has been successfully applied to supporting deep soft rock roadways in the Yuwu coal industry. However, it has not been tested in other mines, so the study lacks breadth. The scope of application of this study lies in support of deep high-stress soft rock roadways with large span characteristics. The following conclusions are drawn.

- (1) Mudstone, which is mainly composed of sodium feldspar (22%) and chlorite (47%), has strong plasticity in the compression phase. However, mudstone will aggravate deformation during the mining process and damage the floor when encountering mine water. Sandstone mainly comprises kaolinite (48%) and quartz (22%) and exhibits pronounced elasticity and brittleness. The surrounding rock on the two sides and floor can be classified as Grade V, while that on the roof is Grade II.
- (2) The damage process of a deep soft rock roadway was successfully reproduced by the microparameter calibration model. At an over 60% relaxation state, the roadway surrounding rock will become more plastic and undergo increasingly severe displacement and damage. In this case, appropriate support timing is critical for preventing strong load or irreversible relaxation damage. Postpeak tensile fracturing can indirectly characterize the degree of elasticity and brittleness of the sample.
- (3) The mechanism of the large deformation in deep soft rock roadways in the Yuwu coal mine is as follows. The high deviatoric stress causes the formation of the deep V-shaped shear zone. The shallow large-scale

tensile free-state surrounding rock gives rise to the discontinuity of stresses in the deep and shallow surrounding rock.

- (4) An idea of “timely and active + reinforcing the side and strengthening the bottom” is proposed. Under this approach, the overall convergence of surrounding rock was managed within 350 mm. The stabilization time was about 15 d, and the anchor bolt corresponded to a large abundant factor, thus ensuring the long lifespan of roadways.

## Data Availability

The data used to support the findings of this study are included in the article.

## Conflicts of Interest

The authors declare that they have no conflicts of interest.

## Acknowledgments

This research was funded by the National Natural Science Foundation of China (52107152).

## References

- [1] G. Li, F. Ma, J. Guo, H. Zhao, and G. Liu, “Study on deformation failure mechanism and support technology of deep soft rock roadway,” *Engineering Geology*, vol. 264, Article ID 105262, 2020.
- [2] H. Xie, M. Gao, R. Zhang, G. Peng, W. Wang, and A. Li, “Study on the mechanical properties and mechanical response of coal mining at 1000 m or deeper,” *Rock Mechanics and Rock Engineering*, vol. 52, no. 5, pp. 1475–1490, 2018.
- [3] Q. Wang, S. Xu, Z. Xin, M. He, H. Wei, and B. Jiang, “Mechanical properties and field application of constant resistance energy-absorbing anchor cable,” *Tunnelling and*

- Underground Space Technology*, vol. 125, Article ID 104526, 2022.
- [4] D. Ren, X. Wang, Z. Kou et al., "Feasibility evaluation of CO<sub>2</sub> EOR and storage in tight oil reservoirs: a demonstration project in the Ordos Basin," *Fuel*, vol. 331, Article ID 125652, 2022.
  - [5] S. Tang, J. Li, S. Ding, and L. Zhang, "The influence of water-stress loading sequences on the creep behavior of granite," *Bulletin of Engineering Geology and the Environment*, vol. 81, no. 11, p. 482, 2022.
  - [6] X. Liang, S. Tang, C. A. Tang, L. Hu, and F. Chen, "Influence of water on the mechanical properties and failure behaviors of sandstone under triaxial compression," *Rock Mechanics and Rock Engineering*, vol. 2022, pp. 1–32, 2022.
  - [7] S. Xie, Y. Wu, D. Chen, R. Liu, X. Han, and Q. Ye, "Failure analysis and control technology of intersections of large-scale variable cross-section roadways in deep soft rock," *International Journal of Coal Science & Technology*, vol. 9, no. 1, p. 19, 2022.
  - [8] W. Jing, S. Liu, R. Yang, L. Jing, and W. Xue, "Mechanism of aging deformation zoning of surrounding rock in deep high stress soft rock roadway based on rock creep characteristics," *Journal of Applied Geophysics*, vol. 202, Article ID 104632, 2022.
  - [9] H. Wang, C. Jiang, P. Zheng, W. Zhao, and N. Li, "A combined supporting system based on filled-wall method for semi coal-rock roadways with large deformations," *Tunnelling and Underground Space Technology*, vol. 99, Article ID 103382, 2020.
  - [10] Q. Liu and L. Sun, "Simulation of coupled hydro-mechanical interactions during grouting process in fractured media based on the combined finite-discrete element method," *Tunnelling and Underground Space Technology*, vol. 84, pp. 472–486, 2019.
  - [11] Q. Wang, Z. Jiang, B. Jiang, H. Gao, Y. Huang, and P. Zhang, "Research on an automatic roadway formation method in deep mining areas by roof cutting with high-strength bolt-grouting," *International Journal of Rock Mechanics and Mining Sciences*, vol. 128, Article ID 104264, 2020.
  - [12] X. Xu, H. Jing, Z. Zhao, Q. Yin, J. Li, and H. Li, "Physical model experiment research on evolution process of water inrush hazard in a deep-buried tunnel containing the filling fault," *Environmental Earth Sciences*, vol. 81, no. 20, p. 488, 2022.
  - [13] G. Li, F. Ma, G. Liu, H. Zhao, and J. Guo, "A strain-softening constitutive model of Heterogeneous rock mass considering Statistical damage and its application in numerical modeling of deep roadways," *Sustainability*, vol. 11, no. 8, p. 2399, 2019.
  - [14] M. Wang, N. Zhang, J. Li, L. Ma, and P. Fan, "Computational method of large deformation and its application in deep mining tunnel," *Tunnelling and Underground Space Technology*, vol. 50, pp. 47–53, 2015.
  - [15] K. Yi, H. Kang, W. Ju, Y. Liu, and Z. Lu, "Synergistic effect of strain softening and dilatancy in deep tunnel analysis," *Tunnelling and Underground Space Technology*, vol. 97, Article ID 103280, 2020.
  - [16] Y. Kang, Q. Liu, G. Gong, and H. Wang, "Application of a combined support system to the weak floor reinforcement in deep underground coal mine," *International Journal of Rock Mechanics and Mining Sciences*, vol. 71, pp. 143–150, 2014.
  - [17] W. Yu, K. Li, and Z. Zhou, "Deformation mechanism and control technology of surrounding rock in the deep-buried large-span chamber," *Geofluids*, vol. 2020, pp. 1–22, 2020.
  - [18] X. Guo, Z. Zhao, X. Gao, X. Wu, and N. Ma, "Analytical solutions for characteristic radii of circular roadway surrounding rock plastic zone and their application," *International Journal of Mining Science and Technology*, vol. 29, no. 2, pp. 263–272, 2019.
  - [19] S.-Q. Yang, M. Chen, H.-W. Jing, K.-F. Chen, and B. Meng, "A case study on large deformation failure mechanism of deep soft rock roadway in Xin'An coal mine, China," *Engineering Geology*, vol. 217, pp. 89–101, 2017.
  - [20] C. Zhu, Y. Yuan, W. Wang, Z. Chen, S. Wang, and H. Zhong, "Research on the "three shells" cooperative support technology of large-section chambers in deep mines," *International Journal of Mining Science and Technology*, vol. 31, no. 4, pp. 665–680, 2021.
  - [21] S.-C. Li, H.-T. Wang, Q. Wang et al., "Failure mechanism of bolting support and high-strength bolt-grouting technology for deep and soft surrounding rock with high stress," *Journal of Central South University*, vol. 23, no. 2, pp. 440–448, 2016.
  - [22] Z. Zhao, Y. Tan, S. Chen, Q. Ma, and X. Gao, "Theoretical analyses of stress field in surrounding rocks of weakly consolidated tunnel in a high-humidity deep environment," *International Journal of Rock Mechanics and Mining Sciences*, vol. 122, Article ID 104064, 2019.
  - [23] Q. Zhan, X. Zheng, J. Du, and T. Xiao, "Coupling instability mechanism and joint control technology of soft-rock roadway with a buried depth of 1336 m," *Rock Mechanics and Rock Engineering*, vol. 53, no. 5, pp. 2233–2248, 2019.
  - [24] S. Jia, J. Yang, M. Gao, L. Jia, C. Wen, and G. Wu, "Experimental and numerical analysis of deformation and failure behaviour for deep roadways in soft rocks," *Bulletin of Engineering Geology and the Environment*, vol. 81, no. 11, p. 466, 2022.
  - [25] Q. Zhan, N. Muhammad Shahani, X. Zheng, Z. Xue, and Y. He, "Instability mechanism and coupling support technology of full section strong convergence roadway with a depth of 1350 m," *Engineering Failure Analysis*, vol. 139, Article ID 106374, 2022.
  - [26] Q. Zhu, T. Li, Y. Du et al., "Failure and stability analysis of deep soft rock roadways based on true triaxial geomechanical model tests," *Engineering Failure Analysis*, vol. 137, Article ID 106255, 2022.
  - [27] W. Yuan, K. Hong, R. Liu, L. Ji, L. Meng, and X. Chen, "Numerical simulation of coupling support for high-stress fractured soft rock roadway in deep mine," *Advances in Civil Engineering*, vol. 2022, Article ID 7221168, 10 pages, 2022.
  - [28] X. Yang, E. Wang, Y. Wang, Y. Gao, and P. Wang, "A study of the large deformation mechanism and control Techniques for deep soft rock roadways," *Sustainability*, vol. 10, no. 4, p. 1100, 2018.
  - [29] C. Zhao, Y. Li, G. Liu, and X. Meng, "Mechanism analysis and control technology of surrounding rock failure in deep soft rock roadway," *Engineering Failure Analysis*, vol. 115, Article ID 104611, 2020.
  - [30] Y. Wang, C. Zhu, M. He, X. Wang, and H. Le, "Macro-meso dynamic fracture behaviors of Xinjiang marble exposed to freeze thaw and frequent impact disturbance loads: a lab-scale testing," *Geomechanics and Geophysics for Geo-Energy and Geo-Resources*, vol. 8, no. 5, p. 154, 2022.
  - [31] Q. Wang, B. Jiang, S. Xu et al., "Roof-cutting and energy-absorbing method for dynamic disaster control in deep coal mine," *International Journal of Rock Mechanics and Mining Sciences*, vol. 158, Article ID 105186, 2022.
  - [32] Q.-L. Yao, Q. Xu, J.-F. Liu, L. Zhu, D.-W. Li, and C.-J. Tang, "Post-mining failure characteristics of rock surrounding coal

- seam roadway and evaluation of rock integrity: a case study,” *Bulletin of Engineering Geology and the Environment*, vol. 80, no. 2, pp. 1653–1669, 2020.
- [33] F. Gao, D. Stead, and D. Elmo, “Numerical simulation of microstructure of brittle rock using a grain-breakable distinct element grain-based model,” *Computers and Geotechnics*, vol. 78, pp. 203–217, 2016.
- [34] X. Li, Q. Li, Y. Hu et al., “Study on three-Dimensional dynamic stability of Open-Pit high Slope under Blasting Vibration,” *Lithosphere*, vol. 2021, no. 4, Article ID 6426550, 2021.

## Research Article

# Mechanism and Safety Mining Technology of Overall Instability-Induced Rockbursts of Multi-Coal Seam Spatially Isolated Working Face

Bo Sun, Sitao Zhu , Fuxing Jiang, and Gao'ang Wang

School of Civil and Resources Engineering, University of Science and Technology Beijing, Beijing 100083, China

Correspondence should be addressed to Sitao Zhu; zhositao@ustb.edu.cn

Received 4 August 2022; Accepted 8 September 2022; Published 24 September 2022

Academic Editor: Fuqiang Ren

Copyright © 2022 Bo Sun et al. This is an open access article distributed under the Creative Commons Attribution License, which permits unrestricted use, distribution, and reproduction in any medium, provided the original work is properly cited.

The isolated working face has always been the hardest hit area for the occurrence of rockburst, and the spatially isolated working face with multiple coal seams is often easily overlooked due to its hidden nature, which leads to the occurrence of rockburst accidents. This paper takes the Liuhuanggou coal mine (9–15) 08 isolated working face as the engineering background, used field research, theoretical analysis, numerical simulation, and field monitoring, investigated the coal body stress evolution law during mining, and revealed the overall instability rockburst mechanism of the working face and deduced the limit advance distance when the working face was in a state of boundary instability. The research results show the following: (1) with the increase of advancement, the overlying strata on the working face are dynamically transformed from the “C” spatial structure with hollowing on both sides to the “θ” spatial structure with coal body support in the middle; (2) when the dynamic load stress on the coal body of the working face exceeds 1.5 times its integrated compressive strength, there is a risk of overall instability rockburst; (3) when the working face advances to 430 m from the open cutting, the superimposed stress on the coal body exceeds its comprehensive compressive strength and reaches a critical instability state, which is verified by numerical simulation. Based on the analysis of the mechanics and mechanism of the overall instability rockburst of the working face, this paper proposes a set of targeted safe mining solutions: (1) The joint monitoring system of microseism-stress-drilling cutting is adopted to monitor and warn the dangerous rockburst areas. (2) The “rockburst-gas” drilling technique is used to unload the pressure on both sides of the working face and the coal wall. (3) The mining speed shall not exceed 3.2 m/d when the working face is mined before 350 m, and shall not exceed 2.4 m/d when the working face enters the influence area of mined-out LW(4-5)02 (350~550 m). The microseismic monitoring results and field practice confirmed the reasonableness and effectiveness of the safe mining technology plan.

## 1. Introduction

With the continuous mining of coal resources, the coal deposit conditions are becoming more and more complex, so that rockburst accidents occur frequently [1–8]. According to statistics, the number of rockburst mines in China has rapidly increased from 142 in 2012 to 177 as of 2017, and rockburst has become one of the most dangerous disasters in China's coal mines [9–13]. The frequent occurrence of rockburst has brought serious damage to the safety production and economic efficiency of mines. Among them, the isolated working face, which is generated by strip mining or unreasonable mining layout, is the hardest hit

area for the occurrence of rockburst. Compared with other types of working face, the stress concentration around the roadway of an isolated working face is higher, and the roof movement is also more intense. Coupled with the mining conditions, complex geological conditions, and other factors, it is more likely to occur rockburst, which brings great difficulties to the safe mining of coal resources [14–20].

There has been a lot of research on the mechanism and prevention of rockburst induced by the overall instability of the isolated working face. Zhu et al. [21, 22] scientifically classified the types of rockbursts in longwall workings by means of stress and microseismic monitoring, studied the mechanism of overall instability-induced rockbursts, and

proposed a risk assessment method for such rockbursts. Wang et al. [23] and Deng and Gu [24] analyzed the mechanism of mine seismic and rockburst triggered by isolated coal pillars using mechanical models, studied the overlying strata movement law of isolated coal pillars, and proposed reasonable width design criteria for isolated coal pillars. Liu et al. [25] explored the distribution of stress field on the isolated longwall working face by mechanical model, theoretical calculations, seismic computed tomography, and energy density, studied the stress distribution characteristics on the isolated longwall working face under three different surrounding rock conditions, and evaluated the rockburst risk of four longwall isolated working faces in ZhaoLou coal mine as an example. Xue et al. [26] revealed the mechanism of rockburst occurring in mine coal pillars from the perspective of energy evolution and the bursting liability of coal specimen through theoretical calculations and numerical simulations, proposed the energy density criteria for rockburst hazard evaluation, and analyzed the energy density factor and the characteristics of the changing trend in the vertical direction. Zhao et al. [27] established a micro-structure model of coal based on the theory of coal grain friction generating charge, studied four different friction coefficient variation laws of coal, and then used the electromagnetic radiation method for potential rockburst ground pressure hazard at isolated coal pillar working face.

The above scholars have conducted a lot of researches on the law of overburden movement of isolated working face and the prevention and control technology of rockburst of isolated working face, which provide theoretical reference for this paper, but there are fewer researches on the critical judgment basis of the overall instability rockburst of coal body and its safe mining technology when the isolated working face with multi-seam spatial distribution advances to the mined-out area. In view of this, this paper takes the Liuhuanggou coal mine (9–15) 08 isolated working face as the engineering background and studies the critical instability width of the isolated working face through mechanical analysis, theoretical calculation, and numerical simulation, in order to provide a reference for similar engineering practice.

## 2. Engineering Background

*2.1. Overview.* (9–15) 08 spatially isolated working face (SIW) of the Liuhuanggou coal mine mainly mining 9–15 coal seam. The average mining depth of the working face is 430 m, and the average thickness of the coal seam is 14 m, which belongs to an extra-thick coal seam with stable seams and a simple structure. The roof of the coal seam is dominated by gritstone and medium-grained sandstone, and there is a group of hard sandstone group with a thickness of 26.84 m about 38 m above the coal seam, which may have a large impact on the working face during mining, as shown in Table 1. According to the results of coal rockburst tendency identification, both the 9–15 coal seam and its top and bottom plates have a strong burst tendency.

(9–15) 08 spatially isolated working face (SIW) of the Liuhuanggou coal mine is the successor of (4–5) 06 longwall

TABLE 1: Stratigraphy statistics table.

Serial number	Lithology	Thickness (m)
$R_{19}$	Siltstone	1.00
$R_{18}$	Gritstone	12.80
$R_{17}$	Interbedded fine-sandstone	5.00
$R_{16}$	Siltstone	8.04
$R_{15}$	Mudstone	0.20
$R_{14}$	Fine-sandstone	3.31
$R_{13}$	Mudstone	3.42
$R_{12}$	Fine-sandstone	1.00
$R_{11}$	Mudstone	2.2
$R_{10}$	4-5 coal seam	6.94

working face (LW) SIW(9–15) 08 is partially located below the mined-out LW(4–5) 04 and (4–5) 06 of the 4–5 coal seam, and the average distance from 4–5 coal seam is about 27 m. In addition, about 110 m to the southwest of the SIW(9–15) 08 is the old mined-out area of the adjacent mine, and about 548 m to the east from the open cut is the mined-out LW(4–5) 02. It has a strike length of about 1713.2 m and an inclined length of about 130 m. The plan location is shown in Figure 1. The tendency profile is shown in Figures 2 and 3.

*2.2. Rockburst Risk Analysis.* SIW(9–15) 08 has a relatively high degree of stress concentration in the coal body of the working face due to the influence of the extra-thick coal seam, mountain stress, and the mined-out areas on both sides. When the working face advances to mined-out LW(4–5) 02, it gradually forms a spatially isolated working face with four sides of mining, the stress concentration of the coal body on the working face further rises, and the overall instability of the coal body is very likely to occur when mining the coal body in this area, so the coal wall and the trackgate have strong rockburst hazard. The beltgate has a weak rockburst hazard because it is arranged below the mined-out area. In summary, through macro evaluation, the preliminary judgment of (9–15) 08 working face rockburst hazards is shown in Figure 4. This paper focuses on the stress changes in the coal body when the SIW(9–15) 08 is advancing towards the mined-out LW(4–5) 02 and provides safe mining technology solutions based on this, with a view to providing a reference for the actual project.

## 3. Mechanism of Overall Instability Rockburst

*3.1. Overburden Spatial Structure and Stress Evolution Characteristics.* According to the actual mining situation of the coal seam in the Liuhuanggou coal mine and the actual measured data of surface subsidence, it is known that during the mining period of SIW(9–15) 08, all the mined-out areas after the mining of 4–5 coal seams are in a non-fully mined state, and the overlying strata of SIW(9–15) 08 form an asymmetric pressure arch structure [28, 29]. With the increasing advancement of the working face, the stress distribution on the coal body roughly shows 4 patterns, as shown in Figure 5.

At the early stage of mining, the coal body of SIW(9–15) 08 is affected by the mined-out areas which on both sides, the

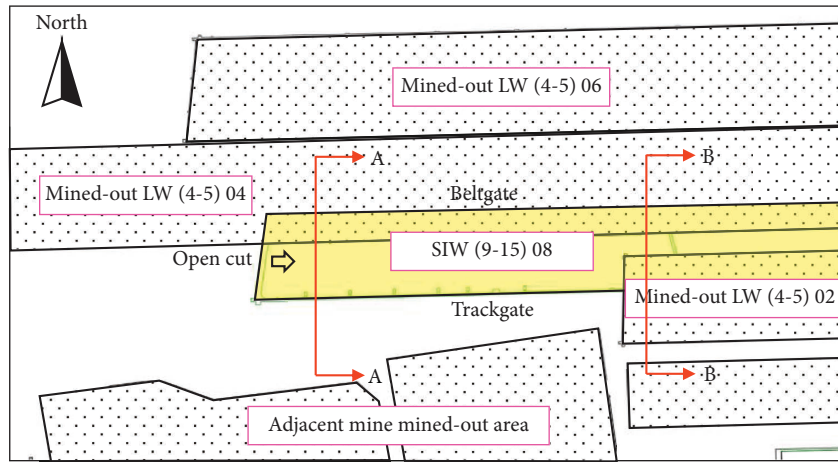


FIGURE 1: SIW(9-15) 08 plan location diagram.

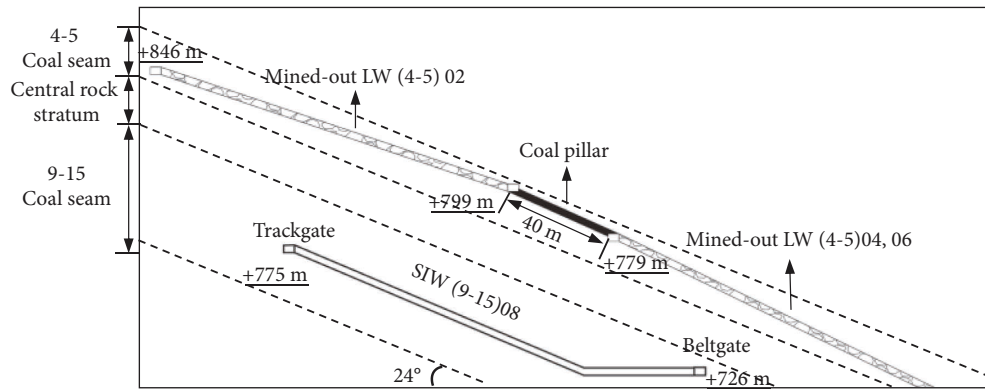


FIGURE 2: Schematic diagram of A-A tendency profile.

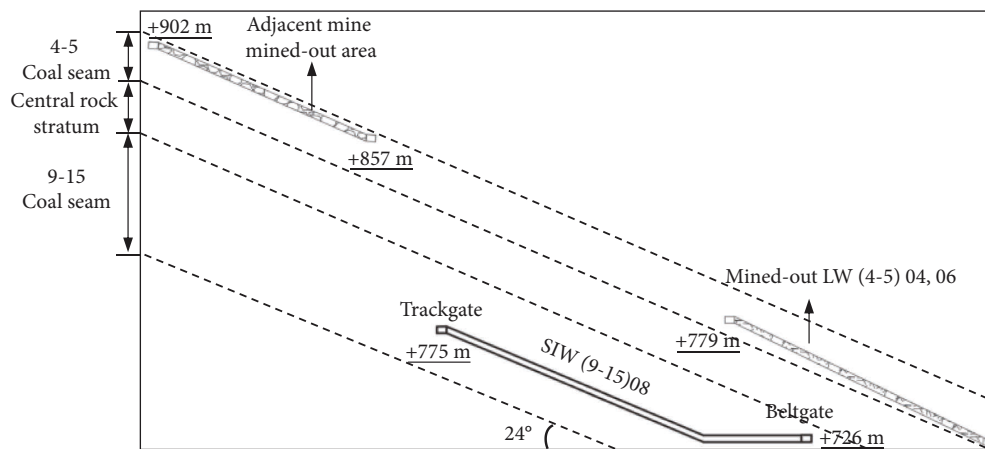


FIGURE 3: Schematic diagram of B-B tendency profile.

stress concentration of the coal body is much higher than that of the ordinary working face. But the coal body of the working face at this stage has a large bearing width, the peak stress distribution is not yet superimposed on both sides of the coal body, and the middle of the coal body is still in the original rock stress area, showing a “bimodal” distribution, as shown in Figure 5(a). There is no risk of overall instability rockburst in this stage.

At the middle stage of mining, as the working face continues to advance, the roof strata gradually break and are connected with the overlying faulted strata in the surrounding mined-out areas, forming a spatial structure similar to the “C” shape [30]. The stress peak gradually shifts to the middle of the coal body, and the stress in the center of the coal body rises above the original rock stress. At this point, the stress distribution is presented as a “saddle type,” as shown in Figure 5(b).

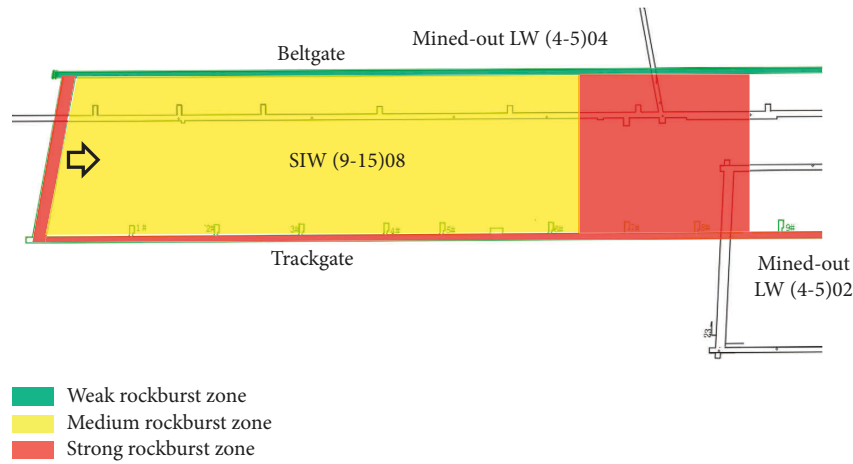


FIGURE 4: Rockburst danger zones of SIW(9-15) 08.

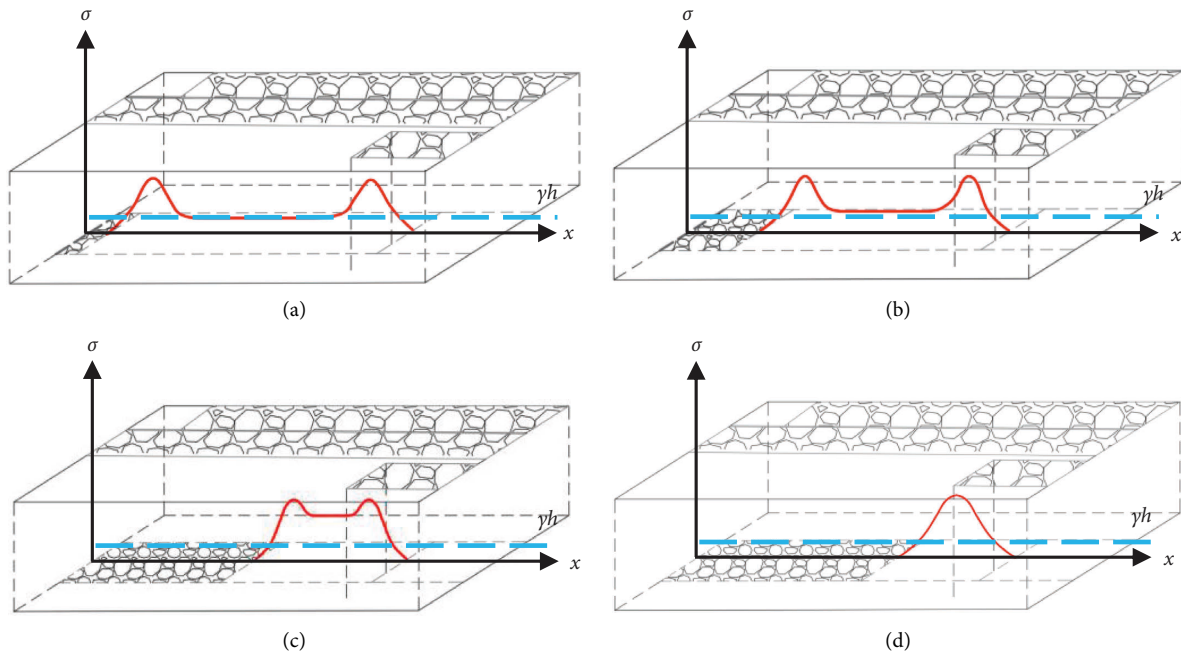


FIGURE 5: Schematic diagram of superimposed force field distribution. (a) Bimodal type. (b) Saddle type. (c) Platform type. (d) Unimodal type.

At the end stage of mining, the overburden spatial structure develops continuously upward, forming a dynamic “C” type overburden spatial structure. When the working face enters the influence range of side abutment pressure of mined-out LW(4-5) 02, the overlying strata on the working face gradually connect with the overlying broken strata of mined-out LW(4-5)02, forming a nearly “θ” type overlying rock spatial structure with coal body support in the middle [31]. At this time, the isolated coal body stress is “platform type” or even “unimodal type” distribution, as shown in Figures 5(c) and 5(d). The central region of the coal body stress increases sharply, the core stress homogenizes, and the overall instability rockburst is very easy to occur.

**3.2. Mechanism and Mechanical Analysis.** According to the previous analysis of the spatial structure and stress evolution of the overburden during the mining of (9-15) 08 working face, the mechanism of the overall instability rockburst of (9-15) 08 working face is: before working face mining, the coal body is not affected by mining disturbance, and the stress on the coal body mainly comes from the self-weight of the overlying strata and the transfer stress of the overlying strata on both sides of the mined-out areas and is in a state of stress equilibrium. During the working face mining, the isolated coal body will be affected not only by the above stresses, but also by the advanced support pressure of the working face, and gradually enter the side abutment pressure influence range of the mined-out LW(4-5)02, the advanced

support pressure of the working face and the side abutment pressure of the mined-out areas are superimposed, which further increases the risk of the overall instability rockburst of the coal body of the isolated working face.

In order to visually analyze the stresses on the coal body when the working face advances, the stresses on the isolated coal body are roughly divided into three parts: the working face inclined abutment pressure, the working face strike abutment pressure, and the self-weight of the overlying strata of the coal body.

**3.2.1. Inclined Abutment Pressure Distribution Characteristics.** According to the actual mining situation of the coal seam in the Liuhuanggou coal mine and the measured parameters of surface subsidence, it is known that the overlying strata of 4-5 coal seam are in a non-sufficient mining state after the working face of 4-5 coal seam had been mined. Since the 4-5 coal seam and 9-15 coal seam are only about 28 m apart, in order to simplify the calculation, it is assumed that (9-15) 08 working face is in the same plane as the mined-out areas on both sides. Accordingly, a static distribution model of the inclined abutment pressure of the coal body at the isolated working face is established, as shown in Figure 6.

The area  $S_1$  of the red area on the left side is shown in

$$S_1 = \frac{l_1 \sin \theta}{2} \left( H_1 - \frac{l_1 \sin \theta}{2} \right) (1 + \cot \alpha_1) + \frac{l_1^2 \sin^2 \theta}{16} (1 + \cot \alpha_1)^2 + \frac{\cot(\alpha_1 - \theta)}{2} \left( H_1 - \frac{l_1 \sin \theta}{2} \right)^2. \quad (1)$$

The area  $S_2$  of the red area on the right side is shown in

$$S_2 = \frac{l_2 \sin \theta}{2} \left( H_2 - \frac{l_2 \sin \theta}{2} \right) (1 + \cot \alpha_2) + \frac{l_2^2 \sin^2 \theta}{16} (1 + \cot \alpha_2)^2 + \frac{\cot(\alpha_2 - \theta)}{2} \left( H_2 - \frac{l_2 \sin \theta}{2} \right)^2. \quad (2)$$

The area  $S_3$  of the yellow area on the left is shown in

$$S_3 = \frac{l_1^2}{16} (1 + \cot \alpha_1). \quad (3)$$

The area  $S_4$  of the yellow area on the right is shown in

$$S_4 = \frac{l_2^2}{16} (1 + \cot \alpha_2). \quad (4)$$

Then, the average side abutment pressure on the isolated coal body is shown in

$$\bar{\sigma}_l = \sum_{i=1}^4 S_i \frac{\gamma}{d}, \quad (5)$$

where  $l_1$  and  $l_2$  are the width of the mined-out areas on both sides of the isolated working face,  $H_1$  and  $H_2$  are the burial depth of the mined-out areas on both sides;  $d$  is the width of the isolated working face;  $\alpha_1$  and  $\alpha_2$  are the strata movement angles of the mined-out areas on both sides;  $\theta$  is the dip angle

of the coal seam; and  $\gamma$  is the volume weight of the overlying strata.

**3.2.2. Strike Abutment Pressure Distribution Characteristics.** The strike abutment pressure on the isolated working face is divided into two parts: mined-out LW(4-5) 02 strike abutment pressure and advanced support pressure when the working face advances. Taking the workface open cut as the coordinate origin and the direction of workface advance as the positive direction of the  $x$ -axis to establish the coordinate system, the incremental pressure of mined-out LW(4-5) 02 bearing pressure on the isolated work face is shown in

$$\Delta \sigma_3 = \begin{cases} 0, & [0, L - 2H_{i_3} \cot \beta_3], \\ 2\sigma_{\max i_3} \left[ 1 - \frac{(L-x)}{2H_{i_3} \cot \beta_3} \right], & [L - 2H_{i_3} \cot \beta_3, L - H_{i_3} \cot \beta_3], \\ \frac{\sigma_{\max i_3} (L-x) \tan \beta_3}{H_{i_3}}, & [L - H_{i_3} \cot \beta_3, L], \end{cases} \quad (6)$$

$$\sigma_{\max i} = \frac{(L_{wi} + H_i \cot \beta) M_i \gamma}{2H_i \cot \beta}, \quad (7)$$

where  $\sigma_{\max i}$  is the maximum abutment pressure generated by the  $i$ th key stratum on the coal body on the side of the mined-out areas;  $H_i$  is the distance from the center of the thickness of the  $i$ th key stratum to the coal floor;  $\beta$  is the rock fracture angle in the mined-out areas;  $L_{wi}$  is the span of the key stratum  $i$ ; and  $L$  is the length of the working face strike direction from the mined-out area.

The workface advanced abutment pressure stress increment  $\Delta \sigma_4$  is shown in

$$\Delta \sigma_4 = \begin{cases} \frac{\sigma_{\max i} (x+a) \tan \beta}{H_{i_4}}, & [0, H_{i_4} \cot \beta], \\ 2\sigma_{\max i} \left[ 1 - \frac{(x+a)}{2H_{i_4} \cot \beta} \right], & [H_{i_4} \cot \beta, 2H_{i_4} \cot \beta], \\ 0, & [2H_{i_4} \cot \beta, L], \end{cases} \quad (8)$$

where  $a$  is the working face advance distance, taking the value range  $0 \sim L$ .

Combining equations (6)–(8), the strike average abutment pressure on the isolated coal body is shown in

$$\bar{\sigma}_t = \frac{\int_0^{L-a} \Delta \sigma_4 dx + \int_a^L \Delta \sigma_3 dx}{L-a}. \quad (9)$$

The self-weight stress of the coal body at the working face is shown in

$$\sigma_q = \gamma H, \quad (10)$$

where  $H$  is the depth of the working face.

Considering the effect of dynamic disturbance on the coal body of the isolated working face by mining activities

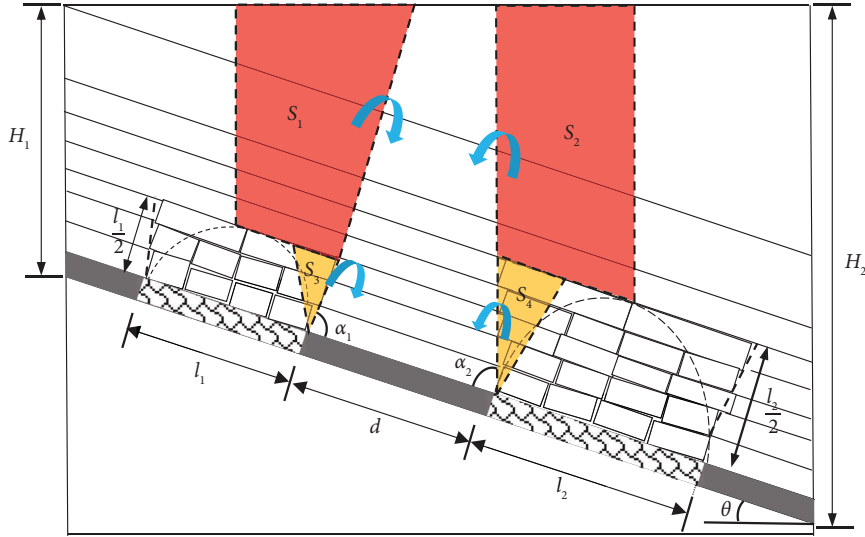


FIGURE 6: Static distribution model of inclined abutment pressure on the isolated working face.

[32, 33], introducing the dynamic load coefficient  $k$ , the average stress of the working face is shown in

$$\bar{\sigma} = k(\bar{\sigma}_l + \bar{\sigma}_t + \sigma_q). \quad (11)$$

**3.3. Analysis of the Overall Instability Rockburst Hazard of a Spatially Isolated Working Face.** The necessary condition for the occurrence of an overall instability rockburst on the coal body of an isolated working face is that the average abutment pressure on the isolated coal body exceeds 1.5 times its comprehensive compressive strength [34, 35]. We have the following equation:

$$I_c = \frac{\bar{\sigma}}{\bar{\mu}[\sigma_c]} > 1.5, \quad (12)$$

where  $[\sigma_c]$  is the uniaxial compressive strength of the coal body, MPa, and  $\bar{\mu}$  is the average comprehensive compressive coefficient of the coal body, taking the value range of 3~5.

It can be seen that when the average abutment pressure on the coal body of the isolated working face is equal to 1.5 times its comprehensive compressive strength, the isolated coal body is in the critical state of overall instability rockburst. Equation (13) can be obtained by associating equations (11) and (12):

$$k \left( \frac{\int_0^{L-a} \Delta\sigma_4 dx + \int_a^L \Delta\sigma_3 dx}{L-a} + \sum_{i=1}^4 S_i \frac{\gamma}{d} \right) = 1.5 \bar{\mu} [\sigma_c]. \quad (13)$$

Substitute the specific parameters of the working face into equation (13) and solve for the unknown  $a$  in the equation to obtain the limit advance distance of the working

face when the isolated working face reaches the critical instability state.

### 3.4. Determination of the Overall Instability Rockburst Hazard

#### 3.4.1. Estimation of Inclined Abutment Pressure.

According to the relevant parameters of the adjacent mine and the working face of 04 and 06 of 4-5 coal seam, take the depth of the mined-out areas  $H_1 = 350$  m,  $H_2 = 486$  m; the width of the mined-out area  $l_1 = 140$  m,  $l_2 = 330$  m; the rock movement angle of the mined-out areas  $\alpha_1 = \alpha_2 = 80^\circ$ ; (9-15) 08 working face width  $d = 130$  m, coal seam dip angle  $\theta = 24^\circ$ , overlying strata volume weight  $\gamma = 2.5$  t/m<sup>3</sup>.

Substitute the above parameters into equations (1)–(5) to obtain the inclined abutment pressure as shown in

$$\bar{\sigma}_l = 29.85 \text{ MPa}. \quad (14)$$

**3.4.2. Estimation of Strike Abutment Pressure.** To simplify the calculation, the overlying strata of the mined-out areas are regarded as a whole rock formation, then  $H_i = h_{\max} + M_i/2$ . According to mined-out LW(4-5) 02 and SIW(9-15) 08 drilling stratigraphic parameters and field monitoring data, take mined-out LW(4-5) 02 depth  $H_3 = 358$  m, pressure arch maximum height  $h_{\max 3} = 70$  m, working face from the mined-out area strike length  $L = 548$  m, (9-15) 08 working face buried depth  $H_4 = 430$  m,  $h_{\max 4} = 65$  m,  $\beta_4 = 74^\circ$ , key stratum span  $L_{wi} = 417$  m.

Substituting the above parameters into equations (6)–(8) to obtain the strike abutment pressure and self-weight stress as shown in

$$\Delta\sigma_3 = \begin{cases} 0, & [0, 432], \\ 0.51x - 221.38, & [432, 490], \\ 280.54 - 0.51x, & [490, 548], \end{cases} \quad (15)$$

$$\Delta\sigma_4 = \begin{cases} 0.42(x + a), & [0, 69], \\ 64.04 - 0.42(x + a), & [69, 138], \\ 0, & [138, 548], \end{cases} \quad (16)$$

$$\sigma_q = 10.75. \quad (17)$$

3.4.3. *Estimation of Limit Advance Distance.* According to the identification data of coal seam 9–15 in the Liuhuanggou coal mine, the single axis compressive strength of coal body  $[\sigma_c] = 21$  MPa, the average comprehensive compressive stress (CCS) coefficient of coal body  $\mu = 3$ , the dynamic load coefficient  $k = 1.3$ , and the comprehensive equations (14)~(17) can obtain the relationship between the average stress(AS) on the coal body of the isolated working face and the advancing degree of the working face as shown in Figure 7.

As can be seen from Figure 7, the AS on the coal body as the working face advances from the open cut to the mined-out LW(4-5) 02 is roughly divided into the following three stages:

- (1) When the working face advances 350 m in the first stage, the AS of the coal body rises slowly with the advance of the working face, and the dynamic load stress of the working face increases slowly from 59 MPa to 76 MPa.
- (2) When the working face advances 350~470 m and enters the influence range of mined-out LW(4-5) 02, the average stress on the coal body increases sharply, and the dynamic load stress on the working face increases rapidly from 76 MPa to 105 MPa. When the working face advances 430 m, the average stress on the coal body reaches the critical value of the overall instability rockburst, and the overall instability rockburst is very likely to occur.
- (3) When the working face is pushed past the stress peak point of 470 m, the AS of the coal body decreases rapidly to below the critical value with the decrease of abutment pressure on the isolated coal body.

## 4. Numerical Analysis

4.1. *Numerical Model.* According to the geology and mining conditions of the Liuhuanggou coal mine (9–15) 08 working face, the model size is established as  $L \times W \times H = 680 \text{ m} \times 700 \text{ m} \times 387 \text{ m}$ , with an inclination angle of  $24^\circ$ , using Mohr–Coulomb criterion, fixing the horizontal displacement at both ends of the model, constraining the horizontal and vertical displacement at its bottom, and the top as a free surface. Apply a uniform load on top of the model to simulate the self-weight of the overlying strata. Model X-axis direction is (9–15) 08 working

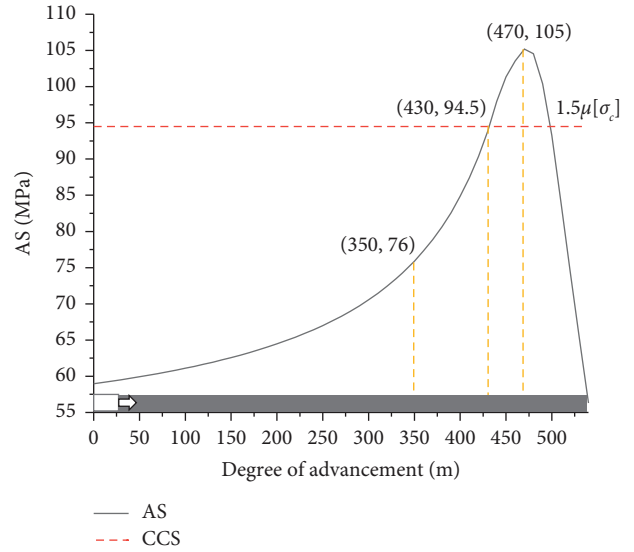


FIGURE 7: Relationship between average stress and degree of advancement of isolated coal body.

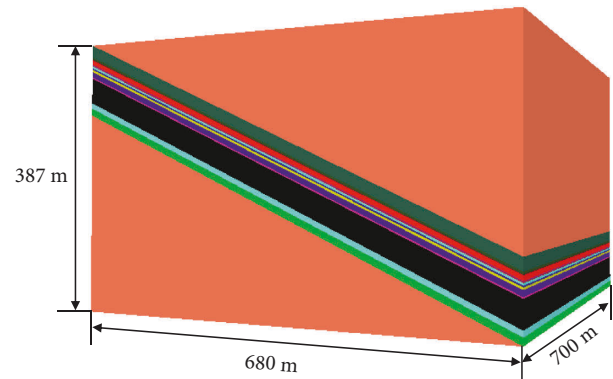


FIGURE 8: Numerical calculation model.

face tendency, and Y-axis direction is (9–15) 08 working face direction. The numerical calculation model is shown in Figure 8.

4.2. *Analysis of Stress Concentration.* According to the actual mining situation of the adjacent mine and Liuhuanggou coal mine, the excavation sequence is adjacent mine working face → (4-5) 02 working face → (4-5) 04 working face → (4-5) 06 working face. The effect on the change of stress in the coal body of (9–15) 08 working face was recorded. The details are shown in Figure 9.

As can be seen from Figure 9, with the gradual hollowing around the (9–15) 08 working face, the stress on the coal body of the working face can be broadly divided into two areas:

- (1) From Figures 9(a) and 9(c), it can be seen that when the adjacent mine working face is mined out, the working face coal body stress rises from 10.75 MPa to about 15 MPa. With the completion of mining of 04 and 06 working face of 4-5 coal seam, (9–15) 08

working face forms a spatial isolated working face with hollow mining on both sides, and the stress of coal body of working face rises obviously, from 15 MPa to about 40 MPa rapidly.

- (2) From Figure 9(b), it can be seen that after (4-5) 02 working face is mined, the stress on the coal body of (9-15) 08 working face rises to about 17.5 MPa from the original rock stress by the influence of the mined-out area. When (9-15) 08 working face advances to the mined-out area, the abutment pressure transferred from the overlying strata of the mined-out area to the isolated coal body is gradually superimposed, and the stress on the coal body further increases. When the stress on the coal body exceeds its 1.5 times comprehensive compressive strength, there is a risk of overall instability rockburst.

**4.3. Analysis of Stress Evolution during Mining.** In order to study the stress changes of the isolated coal body at different advancement degrees of the working face, based on the results of the previous theoretical calculations, measurement lines were arranged along the middle of the inclination in the coal body of (9-15) 08 working face, focusing on monitoring the stress changes of the coal body when the working face is 200 m away from mined-out LW(4-5) 02, and recording the stress changes of the coal body at every 20 m advancement of the working face, as shown in Figure 10.

As can be seen from Figure 10, when the working face advances toward the mined-out LW(4-5) 02, the abutment pressure on the isolated coal body is distributed in a single peak, and the maximum point of the abutment pressure is about 100 m in front of the working face. When the working face advances in the range of 350~430 m, the abutment pressure on the isolated coal body increases continuously, and the peak stress increases from 55 MPa to 79 MPa, which increases the risk of overall instability rockburst on the coal body. After the working face advances 430 m, the stress decreases and tends to be stable. The abutment pressure drops back to about 53 MPa. From the numerical simulation analysis, it can be obtained that when the isolated working face gradually advances to about 430 m, the coal body abutment pressure gradually increases, and the risk of overall instability rockburst is higher.

## 5. Analysis of Safe Mining Plan and Effect

Based on the previous research on the overall instability mechanism of the isolated working face, the safe mining plan is designed from the perspective of monitoring and early warning, pressure relief for the actual situation of (9-15) 08 working face.

**5.1. Monitoring and Early Warning Technical Measures.** Monitoring and early warning technology are one of the most effective methods to prevent and control rockburst [36-41]. According to the previous analysis, "microseism-stress-drilling cutting" joint monitoring is carried out within 200 m from the front of mined-out LW(4-5) 02.

**5.1.1. Microseismic Monitoring System Arrangement.** Six microseismic probes are arranged within 200 m in front of the coal body of the working face and 100 m in the back mined-out area, among which three are arranged in the trackgate and beltgate respectively, using 100 m interval and cross arrangement to focus on monitoring the area with overall instability rockburst hazard. The microseismic probe arrangement is shown in Figure 11.

**5.1.2. Online Stress Monitoring System Arrangement.** During the mining of the working face, a measuring site is arranged every 25 m along the advancing direction, two measuring points are arranged in each site, and the installation depth of the borehole stress gauge is 14 m and 8 m, respectively, with an interval of 1 m. In the process of working forward to disassemble forward in time to ensure that the monitoring range is always not less than 200 m, as shown in Figure 12.

**5.1.3. Arrangement of Drilling Cuttings Pulverized Coal Monitoring System.** Pulverized coal monitoring is carried out within 60 m of the upper part of the beltgate and the lower part of the trackgate in the working face, with a hole depth of 15 m and a spacing of 20 m, and monitored twice a week. For the early warning areas monitored by the online stress monitoring system, one drilling cutting detection hole is constructed at a location 2~5 m from the early warning point, with the same drilling parameters as above.

## 5.2. Pressure Relief and Anti-Rockburst Technical Measures

**5.2.1. Pre-Unloading Measures on Both Sides of the Working Face along the Gate.** (9-15) 08 working face beltgate is located below the mined-out areas and has weak rockburst risk, so it is mainly monitored. If the rockburst hazard is found and then take pressure relief measures. (9-15) 08 working face trackgate is located in solid coal, with strong rockburst hazard, need to construct drilling relief with large diameter to unload pressure, drilling parameters as shown in Table 2.

**5.2.2. Prepressure Relief Measures for Coal Wall at Working Face.** According to the theoretical calculation and numerical simulation results, (9-15)08 working face will form a "θ" type overburden spatial structure when it is about 120 m away from mined-out LW(4-5) 02, which has the risk of overall instability rockburst, and it is necessary to take penetration pressure relief to eliminate the elastic core of coal column.

The original design was to take deep holes in the coal wall to relieve pressure after the working face entered the overall instability danger zone, due to the difficulty of the construction of this method, considering that (9-15) 08 working face needs to extract and release the gas in the coal body before mining, the research group proposed the "rockburst-gas" drilling technology, increasing the diameter of the gas extraction holes from 94 mm to 133 mm, with a spacing of 2 m and an

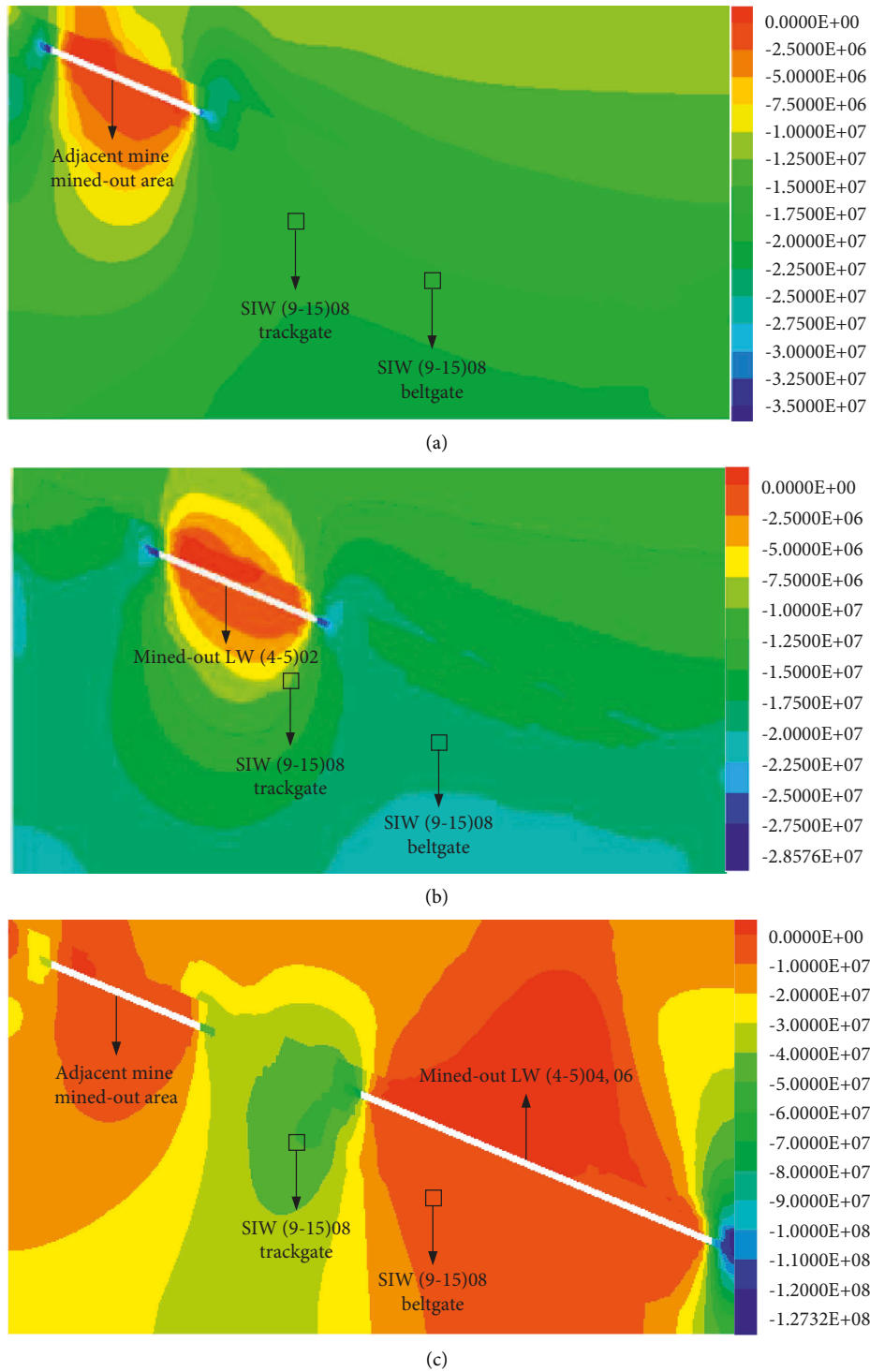


FIGURE 9: Stress evolution cloud diagram after mining at the working face. (a) Vertical stress cloud map of the adjacent mine working face after hollowing. (b) Vertical stress cloud map of the (4-5) 02 working face after hollowing. (c) Vertical stress cloud map of the (4-5) 04, 06 working face after hollowing.

inclination of  $86^\circ$ . The drill hole arrangement is shown in Figure 13.

During drilling construction, a large number of microseismic events were induced due to drilling activities. A

comparison of microseismic events before and after the drilling construction is shown in Figure 14. Figure 14(a) shows the microseismic events during the normal mining period from July 6 to July 31 at (9-15) 08 working face, and

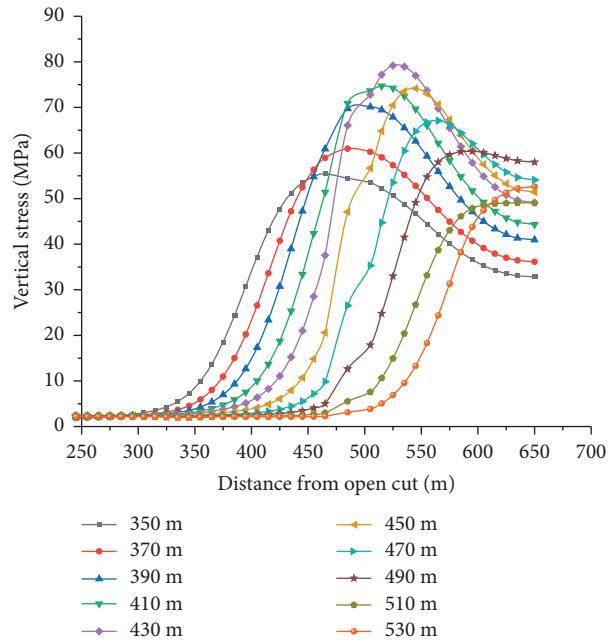
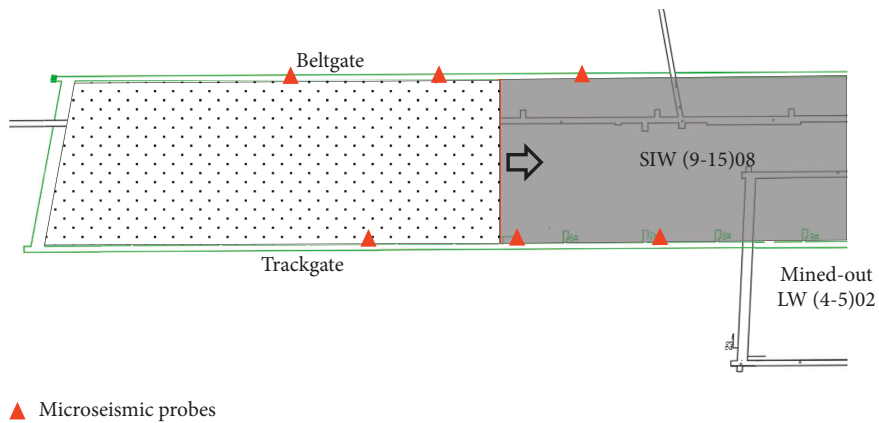


FIGURE 10: Stress changes of the isolated coal body.



▲ Microseismic probes  
FIGURE 11: Schematic layout of the microseismic monitoring system.

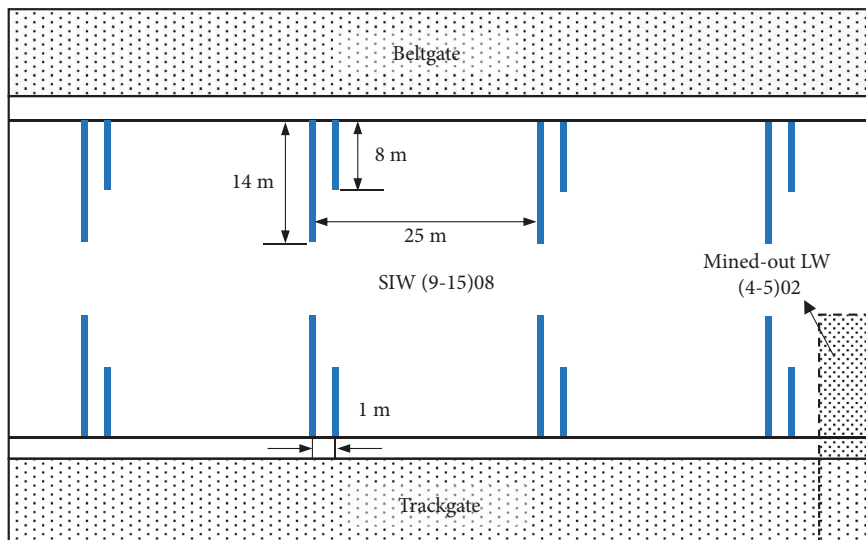


FIGURE 12: Schematic diagram of the measuring site layout.

TABLE 2: Prepressure relief measures and specific parameters of the two sides of the gate.

Rockburst hazard zone level	Measures	Parameters
Weak	Monitoring	—
Medium	Drilling relief with large diameter	Hole depth 25 m, drilling diameter 120~150 mm, hole spacing 2 m
Strong	Drilling relief with large diameter	Hole depth 25 m, drilling diameter 120~150 mm, hole spacing 1 m

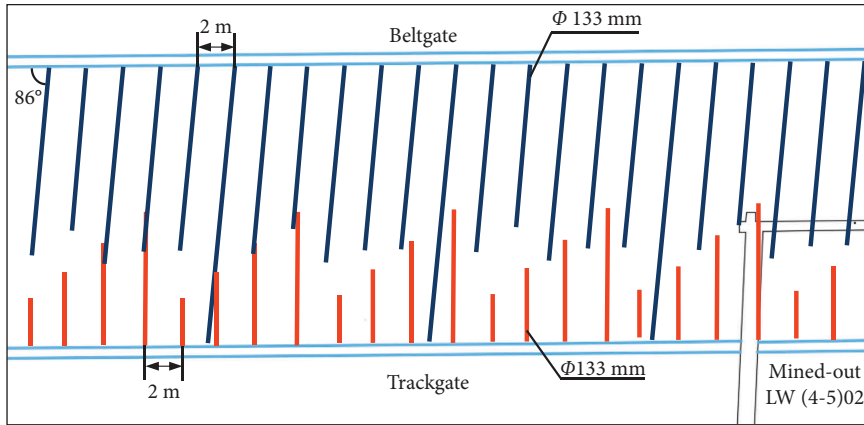


FIGURE 13: (9-15) 08 working face “rockburst-gas” drilling layout diagram.

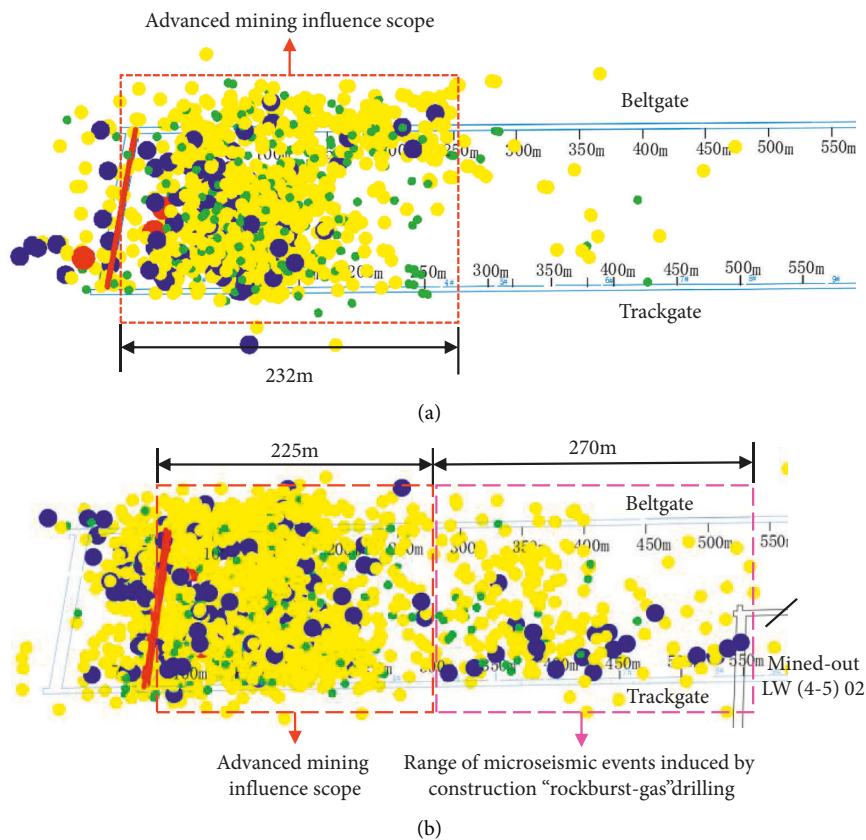


FIGURE 14: Comparison of microseismic events before and after the construction of “rockburst-gas” drilling. (a) Range of microseismic events during normal mining. (b) Range of microseismic events during drilling construction.

Figure 14(b) shows the microseismic events during the construction of the “rockburst-gas” drill hole at the coal wall of the isolated working face from August 28 to November 20.

As can be seen from Figure 14, a large number of microseismic events occurred during the construction of “rockburst-gas” drilling in the overall instability rockburst hazard

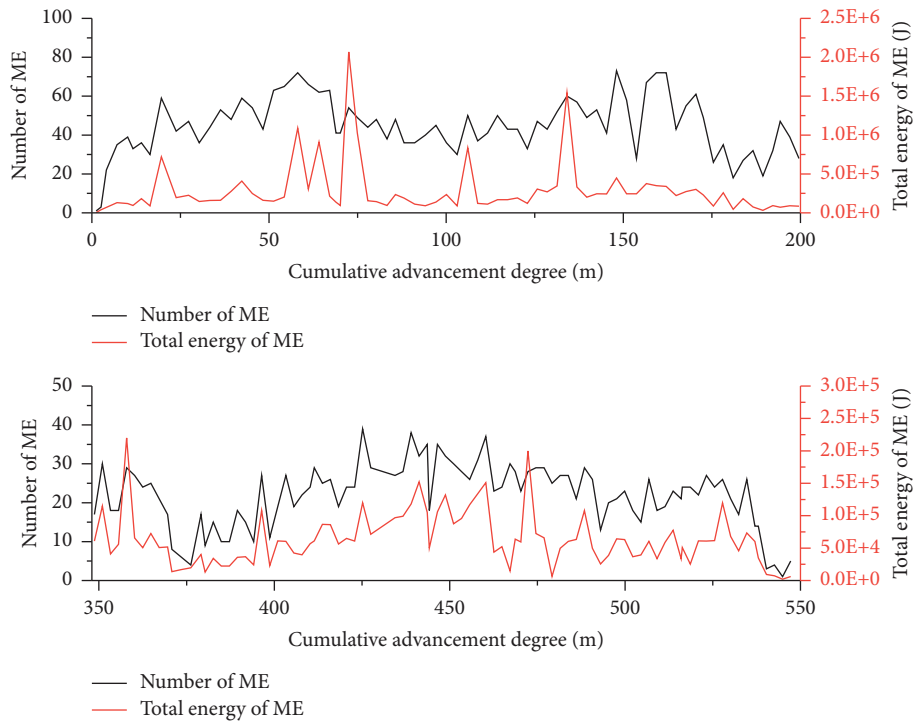


FIGURE 15: Comparison of microseismic events and total energy.

area of the working face, which released the elastic energy in the isolated coal body in advance and reduced the stress concentration in the coal column.

**5.3. Control Mining Speed.** Studies have shown that controlling the mining rate plays a crucial role in the prevention and control of rockburst [42, 43]. Excessive mining speed will lead to larger rock damage size, increased elastic energy released, abutment pressure peak in front of the coal body gradually approaching the coal wall, and the peak stress will increase.

According to the mining speed statistics of other working faces of 9–15 coal seam, the average mining speed of 9–15 coal seam is 2.8 m/d and the maximum mining speed is 5.6 m/d, which occurs in (9–15) 06 working face, during which no rockburst warning occurs. According to the results of theoretical calculation and numerical simulation, considering the high degree of stress concentration in the isolated coal body of (9–15) 08 working face and the risk of overall instability rockburst during the mining period, it is determined that the mining speed of the working face should not exceed 3.2 m/d when it is mining the fist 350 m of coal body, and the mining speed should not exceed 2.4 m/d when it enters the influence range of mined-out LW(4-5) 02 (350~550 m).

**5.4. Strengthen the Strength and Distance of Advanced Support.** From Figure 14, it can be seen that the advance disturbance range during the mining process of the working face is about 220 m, and the current advance support length of the mine is 120 m, so it is recommended to strengthen the

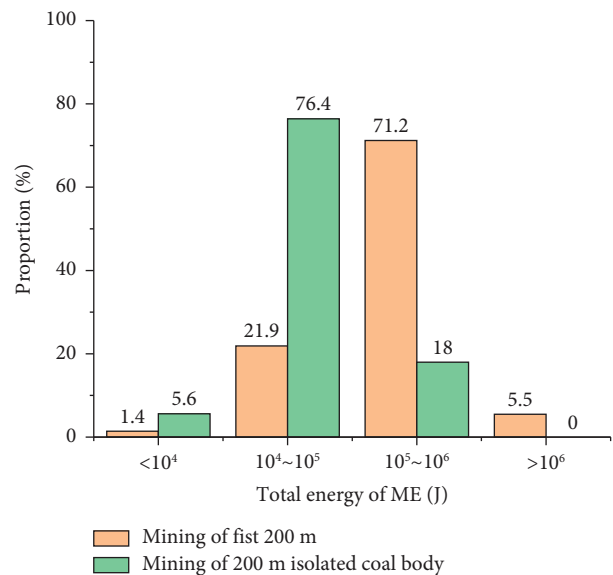


FIGURE 16: Total energy ratio of microseismic events.

advance support of the gateways of the working face to 220 m, and strengthen the strength of the advance support to improve the rockburst resistance and disturbance energy of the advance support system.

**5.5. Analysis of Prevention and Treatment Effects.** In order to test the prevention and control effect after taking targeted measures, the frequency and total energy of microseismic events (ME) occurring within 200 m of the initial advance of

the working face mining and 200 m of the advancement to the mined-out LW(4-5) 02 are compared, as shown in Figures 15 and 16.

From Figures 15 and 16, it can be seen that when the first 200 m of coal body was mined at the (9–15) 08 working face without special anti-rockburst measures, the highest number of microseismic events per day is 73. The total energy of microseismic events is up to  $2.07 \times 10^6$  J, and 71.2% is concentrated in the range of  $10^5 \sim 10^6$  J. After taking special measures for safe mining, the number of daily microseismic events during mining of the isolated coal body decreased to 10~40, and the total daily microseismic energy is all less than  $10^6$  J, mostly located in the range of  $10^4 \sim 10^5$  J (76.4%). It can be seen that after the adoption of special measures for safe mining, the daily microseismic events and total energy decreased significantly compared with the initial stage of mining, which achieved the expected results and realized the safe mining of the overall instability rockburst hazard area of the isolated coal body.

## 6. Conclusion

Based on the Liuhuanguo coal mine (9–15) 08 spatially isolated working face as the engineering background, this article studies the stress evolution law of the isolated coal body, reveals the mechanism of its occurrence of overall instability rockburst of isolated coal, and pushes to the limit width when the coal body reaches the critical instability state. According to the actual mining situation of (9–15) 08 working face, this study proposes safety mining measures for isolated coal body. The effectiveness of the safety mining measures is verified by comparing the onsite microseismic monitoring data, and the following conclusions are drawn:

- (1) Spatially isolated working face with increasing advance distance, the overlying strata show a dynamic transformation process from “C” type spatial structure to “ $\theta$ ” type spatial structure, and its susceptibility to overall instability rockburst is the result of the comprehensive effect of stress transfer from the working face and the overlying strata in the mined-out areas.
- (2) According to the actual coal body storage condition, a mechanical analysis model is established to obtain the relationship between the internal stress of the coal body and the advancement degree, and the criterion for the limited advancement distance of the working face when the critical instability state is reached is derived. The results show that the working face reaches a critical instability state when it reaches 430 m from the open cut, and there is a risk of overall instability rockburst.
- (3) Based on the results of the theoretical analysis, we have developed comprehensive prevention and control measures for monitoring and early warning, pressure relief and prevention, and control of mining speed, and proposed an innovative “rockburst-gas” drilling technology to ensure the safe mining of the isolated working face.

## Data Availability

The data used to support the findings of this study are included within the article.

## Conflicts of Interest

The authors declare no conflicts of interest.

## Acknowledgments

This work was funded by the National Natural Science Youth Fund of China (51904017), China Association for Science and Technology Young Talent Support Project (2021QNRC001), and the Major Science and Technology Innovation Project in Shandong Province, China (2019SDZY02).

## References

- [1] H. Zhou, F. Meng, C. Zhang, D. Hu, F. Yang, and J. Lu, “Analysis of rockburst mechanisms induced by structural planes in deep tunnels,” *Bulletin of Engineering Geology and the Environment*, vol. 74, no. 4, pp. 1435–1451, 2015.
- [2] C. Zhang, I. Canbulat, B. Hebblewhite, and C. R. Ward, “Assessing coal burst phenomena in mining and insights into directions for future research,” *International Journal of Coal Geology*, vol. 179, pp. 28–44, 2017.
- [3] J. Zhou, X. Li, and H. S. Mitri, “Evaluation method of rockburst: state-of-the-art literature review,” *Tunnelling and Underground Space Technology*, vol. 81, pp. 632–659, 2018.
- [4] Z. Hao, G. Sun, and G. Zhang, “Mechanism and inducing factors of rockburst events of roadways under ultrathick strata,” *Frontiers of Earth Science*, vol. 10, 2022.
- [5] X. He, C. Zhou, D. Song et al., “Mechanism and monitoring and early warning technology for rockburst in coal mines,” *International Journal of Minerals, Metallurgy and Materials*, vol. 28, no. 7, pp. 1097–1111, 2021.
- [6] J. Zhang, F. Jiang, J. Yang, W. Bai, and L. Zhang, “Rockburst mechanism in soft coal seam within deep coal mines,” *International Journal of Mining Science and Technology*, vol. 27, no. 3, pp. 551–556, 2017.
- [7] L. Xu, K. Lu, Y. Pan, and Z. Qin, “Study on rock burst characteristics of coal mine roadway in China,” *Energy Sources. Part A, Recovery, Utilization, and Environmental Effects*, vol. 44, no. 2, pp. 1–20, 2019.
- [8] B. Liu, Y. Zhao, C. Zhang, J. Zhou, Y. Li, and Z. Sun, “Characteristic strength and acoustic emission properties of weakly cemented sandstone at different depths under uniaxial compression,” *International Journal of Coal Science & Technology*, vol. 8, no. 6, pp. 1288–1301, 2021.
- [9] Y. Jiang, Y. Zhao, H. Wang, and J. Zhu, “A review of mechanism and prevention technologies of coal bumps in China,” *Journal of Rock Mechanics and Geotechnical Engineering*, vol. 9, no. 1, pp. 180–194, 2017.
- [10] J. Zuo, H. Song, Y. Jiang, S. Zhao, M. Yu, and L. Li, “Preliminary discussion on comprehensive research method for rock burst in coal mine based on Newton’s second law,” *Shock and Vibration*, vol. 2020, Article ID 8861306, 16 pages, 2020.
- [11] Q. X. Qi, Y. Z. Li, S. K. Zhao et al., “Seventy years development of coal mine rockburst in China: establishment and consideration of theory and technology system,” *Coal Science and Technology*, vol. 47, no. 9, pp. 1–40, 2019, (in Chinese).

- [12] Y. D. Jiang, Y. S. Pan, F. X. Jiang, L. M. Dou, and Y. Ju, "State of the art review on mechanism and prevention of coal bumps in China," *Journal of China Coal Society*, vol. 39, no. 2, pp. 205–213, 2014, (in Chinese).
- [13] D. Guo, P. Lv, J. Zhao, and C. Zhang, "Research progress on permeability improvement mechanisms and technologies of coalbed deep-hole cumulative blasting," *International Journal of Coal Science & Technology*, vol. 7, no. 2, pp. 329–336, 2020.
- [14] Q. Wang, S. Xu, M. He, B. Jiang, H. Wei, and Y. Wang, "Dynamic mechanical characteristics and application of constant resistance energy-absorbing supporting material," *International Journal of Mining Science and Technology*, vol. 32, no. 3, pp. 447–458, 2022.
- [15] Q. Yin, J. Wu, Z. Jiang et al., "Investigating the effect of water quenching cycles on mechanical behaviors for granites after conventional triaxial compression," *Geomechanics and Geophysics for Geo-Energy and Geo-Resources*, vol. 8, no. 2, p. 77, 2022.
- [16] P. Zhang, D. Zhang, Y. Yang et al., "A case study on integrated modeling of spatial information of a complex geological body," *Lithosphere*, vol. 2022, Article ID 2918401, 2022.
- [17] Z. Dou, S. Tang, X. Zhang et al., "Influence of Shear Displacement on Fluid Flow and Solute Transport in a 3D Rough Fracture," *Lithosphere*, vol. 2021, no. 4, 2021.
- [18] Z. Tao, Q. Geng, C. Zhu et al., "The mechanical mechanisms of large-scale toppling failure for counter-inclined rock slopes," *Journal of Geophysics and Engineering*, vol. 16, no. 3, pp. 541–558, 2019.
- [19] M. Z. Gao, B. G. Yang, J. Xie et al., "The mechanism of microwave rock breaking and its potential application to rock-breaking technology in drilling," *Petroleum Science*, vol. 19, no. 3, pp. 1110–1124, 2022.
- [20] C. Xue, A. Cao, W. Guo et al., "Mechanism and energy evolution characteristics of coal burst in mining thick, deep, and large inclined coal seams: a case study from a Chinese coal mine," *Geofluids*, vol. 2022, Article ID 7704226, 18 pages, 2022.
- [21] S. Zhu, Y. Feng, and F. Jiang, "Determination of abutment pressure in coal mines with extremely thick alluvium stratum: a typical kind of rockburst mines in China," *Rock Mechanics and Rock Engineering*, vol. 49, no. 5, pp. 1943–1952, 2016.
- [22] S. Zhu, Y. Feng, F. Jiang, and J. Liu, "Mechanism and risk assessment of overall-instability-induced rockbursts in deep island longwall panels," *International Journal of Rock Mechanics and Mining Sciences*, vol. 106, pp. 342–349, 2018.
- [23] B. Wang, S. Zhu, F. Jiang, J. Liu, X. Shang, and X. Zhang, "Investigating the width of isolated coal pillars in deep hard-strata mines for prevention of mine seismicity and rockburst," *Energies*, vol. 13, no. 17, p. 4293, 2020.
- [24] J. Deng and D. S. Gu, "Buckling mechanism of pillar rockbursts in underground hard rock mining," *Geomechanics and Geoengineering*, vol. 13, no. 3, pp. 168–183, 2018.
- [25] G. Liu, Z. Mu, J. Chen, J. Yang, and J. Cao, "Rock burst risk in an island longwall coal face by stress field," *Geoscience Journal*, vol. 22, no. 4, pp. 609–622, 2018.
- [26] Y. Xue, Z. Cao, and Z. Li, "Destabilization mechanism and energy evolution of coal pillar in rockburst disaster," *Arabian Journal of Geosciences*, vol. 13, no. 13, p. 557, 2020.
- [27] T. Zhao, Y. Yin, F. Xiao, Y. Tan, and J. Zou, "Rockburst disaster prediction of isolated coal pillar by electromagnetic radiation based on frictional effect," *The Scientific World Journal*, vol. 2014, Article ID 814050, 7 pages, 2014.
- [28] X. Shi, X. Zhang, and F. Jiang, "A case study of fracture law and stress distribution characteristics of surrounding rock of working face in deep mines," *Geotechnical & Geological Engineering*, vol. 37, no. 4, pp. 2935–2948, 2019.
- [29] C. Wang, A. Cao, G. Zhu, G. Jing, J. Li, and T. Chen, "Mechanism of rock burst induced by fault slip in an island coal panel and hazard assessment using seismic tomography: a case study from Xuzhuang colliery, Xuzhou, China," *Geoscience Journal*, vol. 21, no. 3, pp. 469–481, 2017.
- [30] J. B. Wang, M. D. Wang, E. X. Li, D. F. Dong, and L. M. Xu, "Advances and prospects of anginex as a promising anti-angiogenesis and anti-tumor agent," *Peptides*, vol. 38, no. 2, pp. 457–462, 2012.
- [31] F. X. Jiang, "Viewpoint of spatial structures of overlying strata and its application in coal mine," *Journal of Mining & Safety Engineering*, no. 1, pp. 30–33, 2006, (in Chinese).
- [32] K. Zhong, W. Zhao, C. Qin, H. Gao, and W. Chen, "Mechanical properties of roof rocks under superimposed static and dynamic loads with medium strain rates in coal mines," *Applied Sciences*, vol. 11, no. 19, p. 8973, 2021.
- [33] Z. y. Wang, L. m. Dou, and G. f. Wang, "Mechanism analysis of roadway rockbursts induced by dynamic mining loading and its application," *Energies*, vol. 11, no. 9, p. 2313, 2018.
- [34] F. X. Jiang, G. Cheng, Y. Feng, C. W. Wang, and Y. Y. Xu, "Research on coal overall instability of isolated working face with irregular gobs on both sides," *Chinese Journal of Rock Mechanics and Engineering*, vol. 34, no. S2, pp. 4164–4170, 2015, (in Chinese).
- [35] G. A. Wang, S. T. Zhu, F. X. Jiang et al., "Mechanism of rock burst induced by overall instability of isolated coal and its prevention in large well at thousands-kilometer underground," *Journal of Mining & Safety Engineering*, vol. 36, no. 05, pp. 968–976, 2019, (in Chinese).
- [36] X. l. Li, S. j. Chen, S. m. Liu, and Z. h. Li, "AE waveform characteristics of rock mass under uniaxial loading based on Hilbert-Huang transform," *Journal of Central South University*, vol. 28, no. 6, pp. 1843–1856, 2021.
- [37] F. X. Jiang, S. H. Yang, Y. H. Cheng, X. M. Zhang, Z. Y. Mao, and F. J. Xu, "A study on microseismic monitoring of rockburst in coal mine," *Chinese Journal of Geophysics*, vol. 49, no. 5, pp. 1511–1516, 2006.
- [38] L. Qiu, Z. Liu, E. Wang, X. He, J. Feng, and B. Li, "Early-warning of rock burst in coal mine by low-frequency electromagnetic radiation," *Engineering Geology*, vol. 279, Article ID 105755, 2020.
- [39] A. y. Cao, L. m. Dou, C. b. Wang, X. x. Yao, J. y. Dong, and Y. Gu, "Microseismic precursory characteristics of rock burst hazard in mining areas near a large residual coal pillar: a case study from xuzhuang coal mine, xuzhou, China," *Rock Mechanics and Rock Engineering*, vol. 49, no. 11, pp. 4407–4422, 2016.
- [40] L. Qiu, Y. Zhu, D. Song et al., "Study on the nonlinear characteristics of EMR and AE during coal splitting tests," *Minerals*, vol. 12, no. 2, p. 108, 2022.
- [41] Q. Wang, S. Xu, Z. Xin, M. He, H. Wei, and B. Jiang, "Mechanical properties and field application of constant resistance energy-absorbing anchor cable," *Tunnelling and Underground Space Technology*, vol. 125, Article ID 104526, 2022.
- [42] H. Li, Q. Qi, W. Du, and X. Li, "A criterion of rockburst in coal mines considering the influence of working face mining velocity," *Geomechanics and Geophysics for Geo-Energy and Geo-Resources*, vol. 8, no. 1, p. 37, 2022.
- [43] F. Cui, Y. Yang, X. Lai, C. Jia, and P. Shan, "Experimental study on the effect of advancing speed and stoping time on the energy release of overburden in an upward mining coal working face with a hard roof," *Sustainability*, vol. 12, no. 1, p. 37, 2019.

## Research Article

# Water Inrush Mechanism of Roof Induced by the Fault Weakening Effect in the Coal Mining

Qing Qiu <sup>1</sup>, Lulin Zheng <sup>1</sup>, Hong Lan,<sup>2,3</sup> Wen Zhang,<sup>4</sup> Hengyi He,<sup>1</sup> Chun Zhao,<sup>2</sup> Youwen Tian,<sup>2</sup> Hao Liu,<sup>3</sup> and Ruipeng Li <sup>1</sup>

<sup>1</sup>College of Mining, Guizhou University, Guiyang 550025, Guizhou, China

<sup>2</sup>Longfeng Coal Mine of Guizhou Lindong Coal Industry Development Co., Ltd., Jinsha County 551800, Guizhou, China

<sup>3</sup>College of Resource and Environmental Engineering, Guizhou University, Guiyang 550025, Guizhou, China

<sup>4</sup>College of Construction Engineering, Jilin University, Changchun 130026, Jilin, China

Correspondence should be addressed to Lulin Zheng; llzheng@gzu.edu.cn

Received 29 June 2022; Accepted 25 July 2022; Published 19 September 2022

Academic Editor: Fuqiang Ren

Copyright © 2022 Qing Qiu et al. This is an open access article distributed under the Creative Commons Attribution License, which permits unrestricted use, distribution, and reproduction in any medium, provided the original work is properly cited.

The northern Guizhou coalfield exhibits complex geological conditions and well-developed structures. Hard rock formations are damaged by faults, causing frequent water inrush accidents. To study the damaging effect of faults on roof key strata and the mechanism of water inrush accidents, this paper chose the 5914 coal mining faces of the Longfeng coal mine as the engineering background, determined the water inrush source and key strata through field investigation, hydrochemical analysis, and theoretical calculation, and used RFPA-flow numerical simulation software to simulate the hydraulic coupling effect. The characteristics of the shear stress, damage degree, and hydraulic gradient were analyzed, and finally, the high-density electrical method was employed for simulation verification. The results indicated that the key stratum can control water inrush, but under the influence of faults, the roof forms multiple separation layers, and several sudden increases in displacement occur (the sudden jump phenomenon). A stress concentration area is formed in the head-end tunnel through the fault, and the number of AE events increased to 1150. The water-force gradient exhibits a uniform local large-scale evolution process, and finally, the height of the water-conducting fracture reaches 60 m through the aquifer. This height is 3 times that without fault influence. The numerical simulation results are consistent with the theoretical calculation and field analysis results, which verifies that the fault imposes a highly significant weakening effect on the key stratum, providing data support for later engineering.

## 1. Introduction

As the third largest coal field in Guizhou, China, the northern Guizhou coalfield is rich in coal resources, but this coalfield is located in a unique tectonic location and exhibits a complex regional geological structure, including concealed structures and karst development; coupled with the influence of the Yanshan and Himalayan movements, large-scale faults and folds were formed [1], causing the geological structure and hydrogeological conditions in the northern Guizhou coalfield to be highly complex and the types of water hazards to be varied. In particular, this coalfield is seriously impacted by karst water in roof strata [2, 3]. On August 21, 2019, the Longfeng coal mine of the Guizhou

Lindong Group Mining Co., Ltd., is located in the northern Guizhou coalfield. Due to the influence of hidden faults, water inrush caused by karst cave water in the roof of the coal seam resulted in 2 deaths and a direct economic loss of more than 5 million yuan. The investigation of the accident shows that there is a fault during the excavation of the working face on June 19, and the water from goaf roof at the outlet under the mining face increased. Then, during July 22 to August 6, the roof burst several times, and on August 21, gangue and water from the roof suddenly poured into the working face, causing the accident. Nowadays, many underground projects involve water-force coupling [4, 5], and for mine water damage, the water source and water inrush channel are highly hidden. Therefore, it is necessary to

clarify the occurrence conditions of the water inrush source, action mechanism of the geological structure in regard to the water-conducting fracture, especially to study the coupling relationship between faults and the roof lithology under water-force action, and action characteristics and evolution pattern of the roof water-conducting fracture zone.

Scholars have performed much work regarding the prevention of karst water damage and the mechanism of water inrush. Based on mechanics theory, research has been conducted to determine the failure pattern of water-conducting fracture zones. Among these studies, the most representative theories include the three-zone theory [6], four-zone model [7], and key stratum theory [8]. According to the key stratum theory, when there are multiple hard strata among the overlying strata in the stope, these strata control all or part of rock mass activities, which are referred to as key strata. Based on this theory, most experts have conducted in-depth studies of filling mining, co-mining of coal and gas, prediction of water-conducting fracture zones, and other aspects [9–11]. The stress transfer path and stress distribution near key strata exhibit notable characteristics in the coal mining process [12], and the difference in the fracture deformation zone of the key stratum affects the roof waterproofing performance [13]. In addition, scholars acknowledge that the key stratum provides a good control effect on the formation of water-conducting fracture zones [14], the failure pattern of overburden rock [15], and water inrush from the mine roof and floor [16]. However, as a specific geological structure, faults are widely found in the northern Guizhou coalfield [17]. The faults destroy the continuity of coal seam and roof strata, enlarge the breaking range of surrounding rock, and seriously threaten the safe production of mine. According to statistics, 80% of water inrush accidents are related to faults [18, 19]. Faults not only control the structural morphology of water-bearing systems but also control the dynamic conditions of groundwater [20]. A lot of studies have been done on the relationship between fracture evolution and rock fracture, and it is believed that the existence of fracture seriously affects rock fracture behavior [21, 22]. When the tunnel face occurs close to a fault, the fracture activation frequency of the surrounding rock increases, and the fault can penetrate the hard waterproof layer, resulting in water inrush accidents between the surrounding rock and aquifer [23].

With the continuous development of computer technology, numerical simulation has become an important method to research the failure mechanism of roof overlying rock and the mechanism of water inrush. The commonly used numerical simulation software programs include RFPA, UDEC, and FLAC3D. Among the above software packages, RFPA numerical simulation software is based on finite element and meso-damage statistics theory, and fully considers the heterogeneity of rock material, the randomness of defect distribution, and the influence of water on rock mass fracture development which makes it to be widely used in the study of rock fracture, roof and floor rock and failure laws, and water inrush from roof and floor of coal seam. Liu et al. [24, 25] combined the RFPA and fractal theory to study the fracture evolution characteristics of sandstone and single joint

sandstone. Ma et al. [26] applied RFPA-2D to study the fracture behavior of rock mass near faults. Yu et al. [27] applied the rock fracture process analysis system RFPA-2D to analyze the dynamic development process of overburden rock failure under the influence of mining. Zhang et al. [28] simulated the hydraulic fracturing and studied the evolution law of crack propagation and acoustic emission by RFPA-flow. Wang et al. [29] used RFPA-flow to study the influence of confining pressure and pore pressure crack propagation and permeability of rock mass under uniaxial compression and, on this basis, analyzed the formation mechanism of floor water inburst channel.

Previous studies have studied the theoretical research on mine water inrush by studying the movement, deformation, and failure of roof overburden under the influence of faults and the development law of water-conducting fracture zone, but the formation of water inrush accidents involves a very complex process. Structural damage, control of key strata, and water-rock interactions constitute some of the multiple factors leading to roof water damage, and research on this aspect is scarce in the northern Guizhou coalfield. Therefore, it is necessary to select typical coal mines in the northern Guizhou coalfield as examples to study the weakening effect of faults on key strata and the mechanism of mine water inrush under the action of water and rock.

## 2. Engineering Background

In the Longfeng coal mining area, the strata are gently sloping, and the geological structure is simple, but a concealed structure is developed. During the exploration period, 11 hidden faults were exposed through drilling, and more than 100 small hidden faults were revealed. Coal seams in the area mainly occur in the Upper Permian Longtan Formation ( $P_3l$ ), and the average thickness of the Longtan Formation reaches approximately 98 m, belonging to marine and continental cross-deposits. At present, the main mining target is the 9# coal seam. The direct roof of the 9# coal seam is silty mudstone, and the upper part comprises siltstone or fine sandstone. The direct floor is argillaceous siltstone, while silty mudstone and siltstone occur locally. The overlying water-filled aquifers include the Yulongshan Member of the Triassic Yelang Formation ( $T_1Y^2$ ) and the Upper Permian Changxing Formation ( $P_3c$ ). The vertical distance between coal seam no. 9 and the bottom boundary of the Changxing Formation limestone karst water aquifers is 34.98 m, and the thickness of the Changxing Formation aquifers ranges from 24.13 to 35.50 m, with an average thickness of 29.44 m. In the absence of atmospheric water supplementation, the water level of the aquifer remains stable at approximately 50 m. The roof lithology of 5914 working face is mainly determined according to borehole ZK2-5 and drilling data of advanced geological exploration. The rock formation combination and rock parameters are shown in Figure 1.

The mining face of the Longfeng coal mine adopts the backwall-type mining method, and the roof mining method is adopted to manage the roof. Meanwhile, the 4# and 5# coal seams above the 9# have not been mined. The roof is stable and does not easily collapse, which plays an obvious controlling role on rock stratum activities, and the key stratum

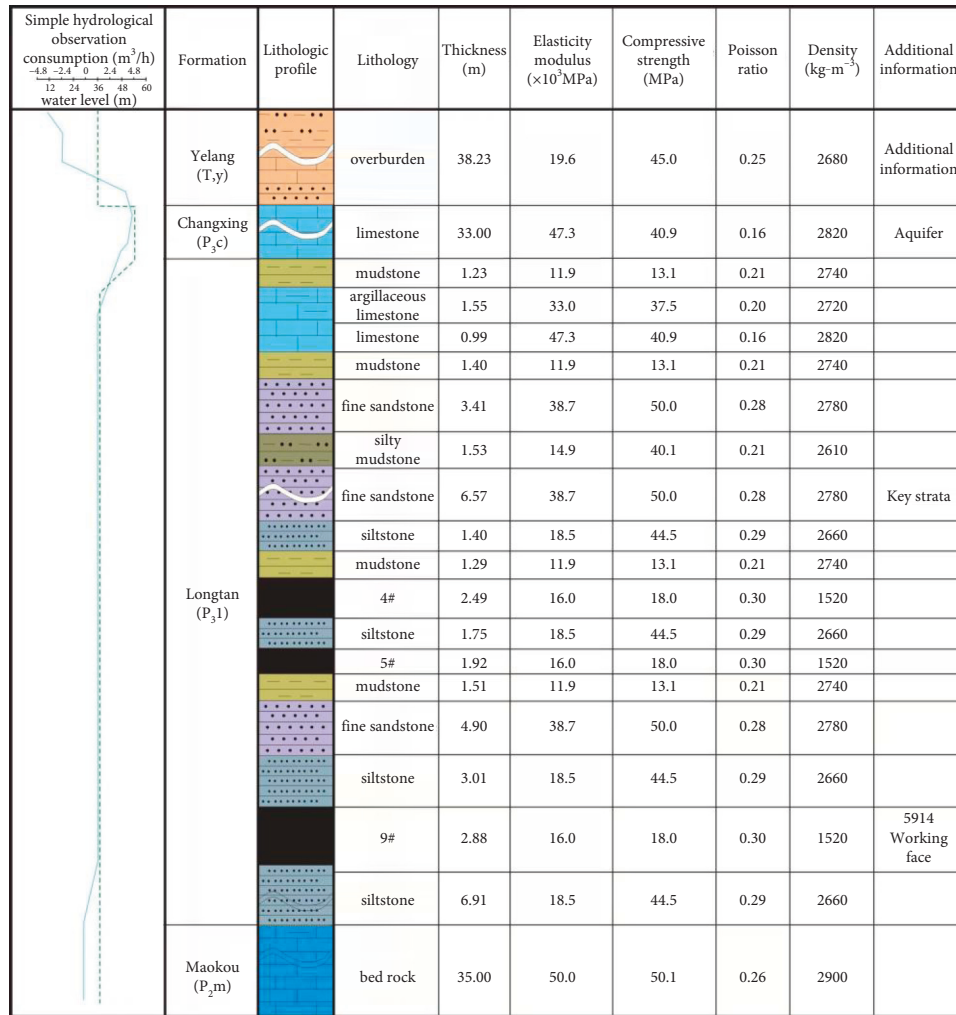


FIGURE 1: Columnar and rock formation parameter map of the ZK2-5 borehole in the Longfeng coal mine.

features are obvious. However, during the advancement of the 5914 working face of the 9# coal seam, several water gushing and slurry collapse events occurred in the roof, and the water outlet of goaf roof under mining face increased on June 19, 2019. The subsequent investigation determined that there occurred an east-west fault fracture with a dip angle of 43° and a length of 12 m above the roof in this accident. This fault is located below the key stratum, which resulted in a connection between the aquifer and C9 coal seam, thus causing the aforementioned water inrush accident. A field geological survey found that there were several similar concealed faults east of the 5914 mining face, and small faults were connected with the F1 fault traversing the northern and southern parts of the mining area, which became a potential risk factor in the later advancement process. An overview of the 5914 working face and the accident site is shown in Figure 2.

### 3. Determination of Roof Water Damage Source and Key Strata

3.1. Determination of Water Hazard Sources. To further determine the source of water damage, before the arrival

of the heavy rainfall period (thus excluding the influence of external water sources on the water sample composition under the action of precipitation), outlet water point S-1 below the working face, water interception point S-2 in a 300 m borehole in the 5914 working face, and water seepage point S-3 at the no. 11 support (the water intake point is shown in Figure 2) were considered, and water samples of the overlying aquifer were analyzed to determine the water quality. The results are listed in Table 1.

The mass concentration of Ca<sup>2+</sup> in the gushing water at S-1, S-2 and S-3 ranged from 3.55 to 48.42 mg·L<sup>-1</sup>, and the mass concentration of K<sup>+</sup> + Na<sup>+</sup> ranged from 101.06 to 129.06 mg·L<sup>-1</sup>. Moreover, the hydrochemical type of the S-1 and S-3 samples is HCO<sub>3</sub>·SO<sub>4</sub>-Mg·K + Na, and the hydrochemical type of the S-2 sample is HCO<sub>3</sub>·SO<sub>4</sub>-Mg·K + Na-Ca. Comparison reveals that the ion concentration in the water samples is similar to that in the Changxing Formation aquifer, and the water chemical type is consistent, indicating that water inrush in the 5914 mining face stems from the Permian Changxing Formation limestone karst water aquifer in the roof.

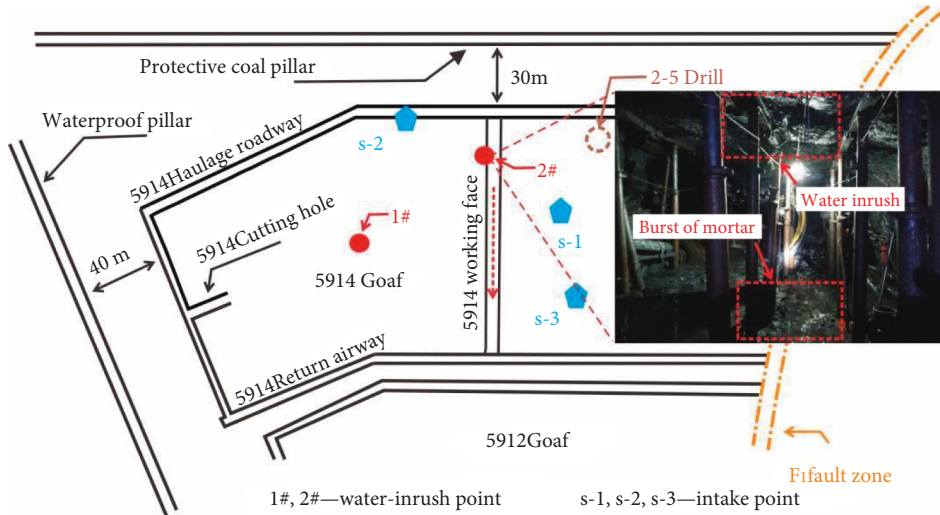


FIGURE 2: Overview of the working face and accident site.

TABLE 1: Water quality analysis results.

Sample	pH	Mass concentration of each ion/(mg·L <sup>-1</sup> )							Type of water
		Ca <sup>2+</sup>	Mg <sup>2+</sup>	K <sup>+</sup> + Na <sup>+</sup>	Cl <sup>-</sup>	SO <sub>4</sub> <sup>2-</sup>	HCO <sub>3</sub> <sup>-</sup>	NO <sub>3</sub> <sup>-</sup>	
T <sub>1</sub> y-1	7.61	77.21	2.98	10.02	13.12	33.75	286.48	4.80	HCO <sub>3</sub> -Ca
T <sub>1</sub> y-2	7.80	70.20	3.68	31.61	10.35	51.04	227.53	6.00	HCO <sub>3</sub> -Ca
P <sub>3</sub> c-1	7.70	17.96	67.86	271.22	13.93	264.25	273.17	3.60	HCO <sub>3</sub> ,SO <sub>4</sub> -Mg-K + Na
P <sub>3</sub> c-2	8.30	25.48	63.65	143.61	15.42	267.91	199.04	2.40	HCO <sub>3</sub> ,SO <sub>4</sub> -Mg-K + Na
S-1	7.94	10.65	53.20	129.06	20.49	271.24	248.71	2.80	HCO <sub>3</sub> ,SO <sub>4</sub> -Mg-K + Na
S-2	8.34	48.42	68.74	101.06	18.01	294.7	246.76	2.80	HCO <sub>3</sub> ,SO <sub>4</sub> -Mg-K + Na·Ca
S-3	7.87	3.55	50.15	115.98	28.58	196.73	216.37	2.00	HCO <sub>3</sub> ,SO <sub>4</sub> -Mg-K + Na

3.2. *Determination of the Key Stratum.* Because of the different properties of coal and rock, the breaking patterns of the rock strata are different from those of the fully mechanized mining face. The overall weight of the overburden is borne by hard and thick rock strata, which can control the roof collapse distance and are collectively denoted as the key stratum [8]. The position of the key stratum is determined according to equation (1), and a corresponding calculation model is shown in Figure 3.

If the 1 to  $m$  hard strata are deformed but the  $m + 1$  stratum is not deformed, the latter hard stratum then constitutes the second layer. Since the strata are deformed from the first layer to the  $m$ -th layer, the load on the hard strata in the first layer [30] is

$$q_{(m)1} = \frac{E_1 h_1^3 \sum_{i=1}^m h_i r_i}{\sum_{i=1}^m E_i h_i^3}, \quad (1)$$

where  $q_{(m)1}$  is the load of the  $m$ -th rock layer on the hard rock layer;  $h_i$  is the thickness of layer  $i$ ;  $m$ ;  $r_i$  is the bulk density of rock layer  $i$ , MN/m<sup>3</sup>; and  $E_i$  is the elastic modulus of rock layer  $i$ , GPa.

It is assumed that the  $m + 1$  layer is another hard layer. Since its deflection is smaller than that of the lower layer, the  $m + 1$  layer does not synchronously deform with the lower layer. Therefore, the following applies:

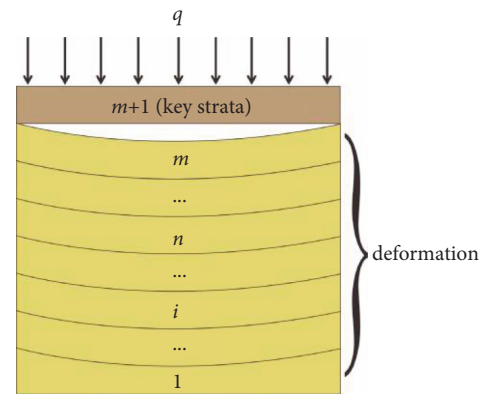


FIGURE 3: Key stratum load model.

$$q_{(m+1)l} < q_{(m)l}. \quad (2)$$

Substituting equations (1) into (2), an evaluation equation of the position of the hard rock layers can be obtained after simplification as [31]

$$E_{m+1} h_{m+1}^2 \sum_{i=1}^m h_i r_i r_{m+1} \sum_{i=1}^m E_i h_i^3. \quad (3)$$

In actual assessment, the calculation starts from the first layer of the working surface and proceeds upward layer by

layer. When equation (3) is satisfied, the corresponding rock layer is the first hard rock layer. The calculation process is continued upward until the top hard layer can be identified, after which the calculation is stopped. The specific location of hard and soft rock layers can be ensured through the above calculation process.

Based on geological drilling data of borehole ZK2-5 (Figure 1) and combined with the above derivation equation, it is concluded that the key stratum of the 5914 working face is a 6.57-m-thick fine sandstone layer (Figure 1).

#### 4. Numerical Simulation of Roof Water Gushing under the Weakening Effect of a Fault on the Key Stratum

**4.1. Model Calculation Method.** RFPA<sup>2D</sup>-flow is a numerical analysis system based on finite element theory, which can fully consider nonlinear, nonuniform, and anisotropic changes in rock strata and karst water in the process of coal seam mining and can better analyze the evolution process of roof water damage under the coupling action of seepage and stress. The mechanical parameters of the RFPA material model of the meso-structure are based on laboratory test results, the karst water aquifer follows Biot consolidation theory, and the material stress-permeability coefficient relationship can be described by a negative exponential equation [32]:

$$Kf = K_0 e^{-b\sigma}, \quad (4)$$

where  $K_0$  is the initial permeability coefficient,  $\sigma$  is the normal stress, and  $b$  is a coupling parameter.

The seepage behavior of fluid varies with the damage degree of the rock mass. Therefore, the coupling effect of seepage, stress, and damage must be considered to accurately reflect the real conditions through numerical simulation. The basic equation of fluid-solid seepage coupling is as follows:

The equilibrium equation is

$$\frac{\partial \sigma_{ij}}{\partial x_j} + \rho X_j = 0, \quad (5)$$

$$(i, j = 1, 2, 3).$$

The geometric equation is

$$\varepsilon_{ij} = \frac{1}{2}(u_{i,j} + u_{j,i}), \quad (6)$$

$$\varepsilon_v = \varepsilon_{11} + \varepsilon_{22} + \varepsilon_{33}.$$

The seepage equation is

$$K\nabla^2 p = \frac{1}{Q} \frac{\partial p}{\partial t} - \alpha \frac{\partial \varepsilon_v}{\partial t}. \quad (7)$$

The seepage-stress coupling model is

$$K(\sigma, p) = \xi K_0 e^{-\beta((\sigma_{ii/3}) - \alpha p)}, \quad (8)$$

where  $\rho$  is the density,  $\sigma_{ij}$  is the sum of the normal stresses,  $\varepsilon_v$  and  $\varepsilon_{ij}$  are the volumetric strain and normal strain,

respectively,  $\delta$  is the Kronecker constant,  $Q$  is Biot's constant,  $G$  and  $\lambda$  are the shear modulus and Ramet coefficient, respectively,  $\nabla^2$  is the Laplace operator,  $P$  is the pore water pressure, and  $\xi$ ,  $\alpha$ , and  $\beta$  are the permeability coefficient jump ratio, pore water pressure coefficient, and coupling coefficient (stress-sensitive factor), respectively. The values are determined via experiments and exhibit certain changes between different states.

Numerous experimental results have demonstrated that the permeability coefficient is not only a function of stress but also a function of the evolution of stress-induced damage and rupture. According to the coupling equation of seepage and damage, when the stress state or strain state of a given element meets a certain damage threshold, the element is damaged, and the elastic modulus of the damaged element is [33]

$$E = (1 - D)E_0, \quad (9)$$

where  $D$  is the damage variable and  $E$  and  $E_0$  are the elastic modulus of the damaged and lossless elements, respectively.

Choosing the uniaxial tensile constitutive model as an example, the seepage-damage coupling equation of the element is expressed below [34]:

When the element strength reaches the tensile strength  $f_t$  damage threshold, the following applies:

$$\sigma_3 \leq -f_t. \quad (10)$$

The damage variable is

$$D = \begin{cases} 0, & \varepsilon_{t0} \leq \varepsilon, \\ 1 - \frac{f_{tr}}{E_0 \varepsilon}, & \varepsilon_{tu} \leq \varepsilon < \varepsilon_0, \\ 1, & \varepsilon \leq \varepsilon_{tu}, \end{cases} \quad (11)$$

where  $f_{tr}$  is the residual strength and  $\varepsilon_{t0}$  and  $\varepsilon_{tu}$  are the maximum and ultimate tensile strains, respectively.

The unit permeability coefficient is

$$K = \begin{cases} K_0 e^{-\beta(\sigma_3 - \alpha p)}, & D = 0 \\ \xi K_0 e^{-\beta(\sigma_3 - \alpha p)}, & 0 \leq \varepsilon < 1 \\ \xi' K_0 e^{-\beta(\sigma_3 - p)}, & D = 1 \end{cases} \quad (12)$$

Similarly, the permeability-damage coupling equation of the uniaxial compression unit can be obtained, as shown in Figure 4.

**4.2. Model Settings.** The evolution process of roof water gushing under the weakening action of faults is considered. Based on the actual working conditions of Longfeng coal mine, the size of the model was set to 150 m × 300 m, and 300 × 600 grid cells were divided. An equivalent load of 1 MPa of the overburden layer and a 50 m water head (reflecting the water pressure of the Changxing Formation aquifer) were applied to the upper part of the model. According to the revealed faults, the dip angle of the fault is 45° and the length was set 12 m. Because only the evolution

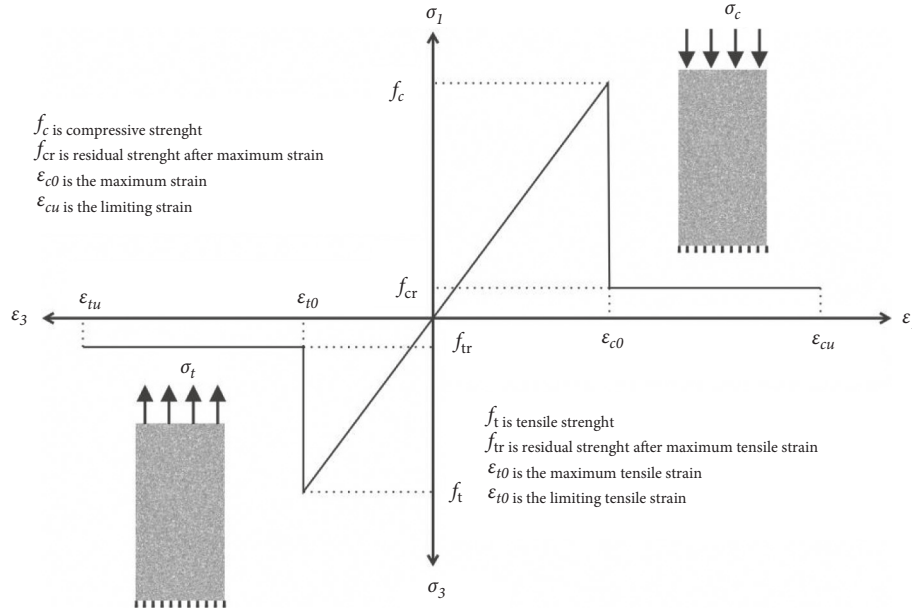


FIGURE 4: Meso-element constitutive model under uniaxial compression and tension.

process of roof water inrush under the influence of faults on the weakening of key layers was analyzed, the horizontal displacement of both sides of the model boundary and vertical displacement of the bottom surface were constrained, and fault parameters were set based on the weakening element method. The plane strain model was adopted for calculation. Due to the boundary effect, 50 m coal pillars were reserved on the left side of the model, and continuous excavation was carried out starting from the second step, with 10 m excavated at each step. The simplification of the established numerical calculation model is shown in Figure 5, and the attributes and physical and mechanical parameters of the rock strata in the model are shown in Figure 1.

**4.3. Evolution of the Shear Stress Field in the Surrounding Rock of the Roof.** Since a rock mass occurring at the intersection of the maximum and minimum principal stresses is highly prone to failure and the failure form mainly involves shear failure [35], only shear stress characteristics were analyzed. Four measuring points in the roof of the coal seam were set for  $y$ -direction displacement monitoring at the 60 m level (without fault influence), 20 m level (with minor fault influence), 10 m level (affected by the fault), and 0 m level (fault layer). The monitoring results are shown in Figure 6(d). As shown in Figure 6(a), the roof of the coal seam is affected by mining, and the maximum principal stress is distributed at the junction of soft and hard coal rock layers and the face of the mined-out area. With eastward advancement of mining, the stress in the roof shear stress concentration area uniformly increases, deformation of the surrounding rock continues to develop, and the overall failure range increases by a small margin. As shown in Figure 6(b), fault activation is clearly observed. A stress concentration distribution area emerges in both the upper

and lower areas of the fault, and the stress concentration area is connected to the working face. Fractures become connected with the fault and vertically develop toward the lower part of the key stratum. Subsequently, the activated area of the fault rapidly increases, and the surrounding rock fails and releases pressure, leading to expansion of the unconsolidated zone to greater depths. The response of the separation zone in the upper part of the fault is notable, which leads to the highest transverse development speed of the fracture in the upper part of the fault, and a longitudinal fracture gradually develops through the aquifer. With intensification of microfracture events, the seepage and scouring effects of karst water in the aquifers on the fracture result in deterioration of the mechanical properties of the fault, and the fracture rapidly penetrates through the working face and fault. As shown in Figure 6(c), the working face fissure eventually becomes connected with the fault fissure, the fissure in the upper part of the fault suddenly develops upward along with the fracture in the key stratum [36], and the phenomenon of a sudden jump occurs. The surrounding rock is increasingly damaged to form a water-conducting fracture zone, and the development height of the water-conducting fracture zone reaches approximately 55 m. Compared to the fault-free roof during the early mining period, only one separation zone is formed in the early goaf without fault influence, and the height of the fracture zone reaches approximately 25 m, which is consistent with the height of 24.68 m of the fracture zone obtained based on the Exploration Specification of Hydrogeology and Engineering Geology in mining areas (GB/T 12719-2021).

$$H = \frac{100 \Sigma M}{3.1 \Sigma M + 5.0} \pm 4.0, \quad (13)$$

where  $M$  is thickness of the coal seam, m (2.88 m); combined with the analysis results shown in Figure 6(d), it is found that the displacement of the measuring point at the 60 m level

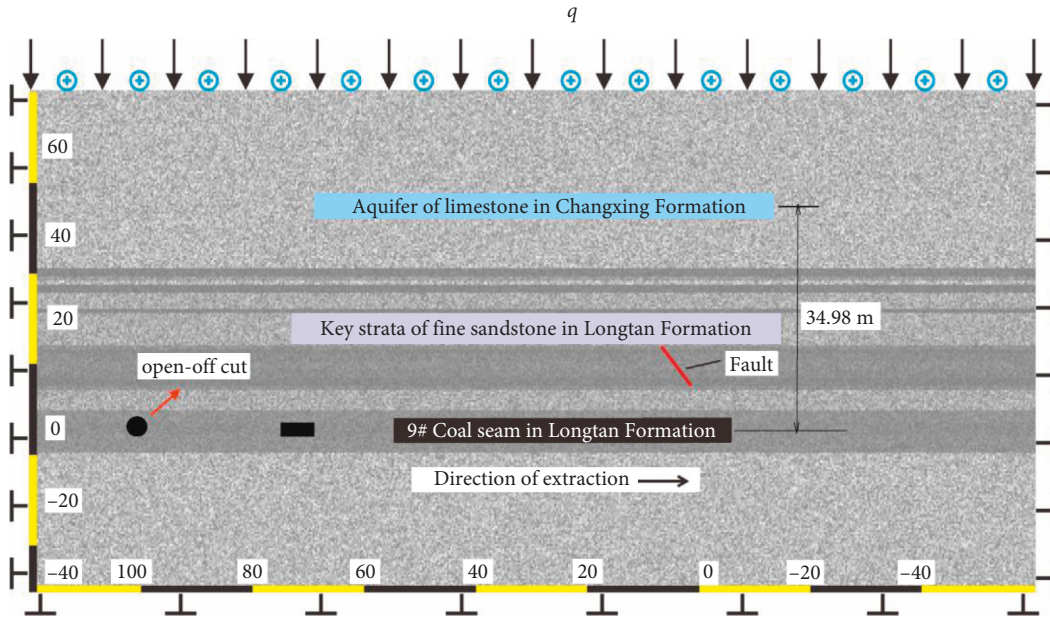


FIGURE 5: Numerical calculation model.

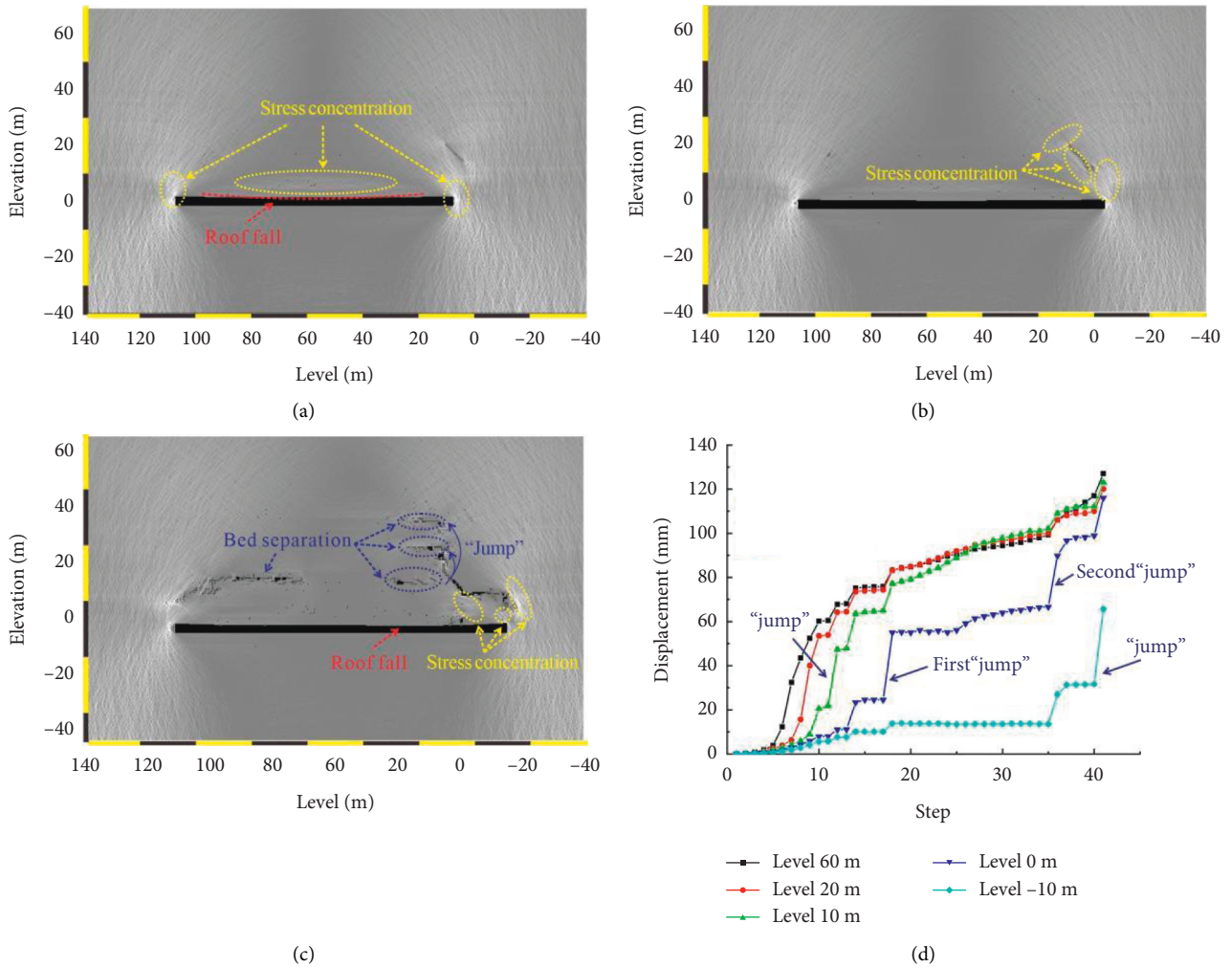


FIGURE 6: Shear stress cloud map and roof displacement analysis.

steadily increases throughout the whole process, and the key stratum provides a good control effect. Horizontal displacement of the 10 m roof measuring point occurred several times under low and continuous instability, corresponding to the process in which the stress in the footwall of the fault and upper and lower parts was gradually released at the early stage of mining, fault cracks were penetrated, and the key stratum was locally damaged. The horizontal displacement of the 0 m measuring point exhibited two clear sudden changes, which were caused by the weakening control effect of the failure of key stratum and the sudden jump phenomenon attributed to the penetration of the roof water-conducting fissure zone. After the sudden jump phenomenon occurred, a high-stress concentration area was formed in the head at  $-10$  m. After 40 steps, the displacement significantly changed. The roof closer to the fault was very prone to caving, which imposed the greatest influence on mining caving at the later stage.

Therefore, due to the presence of the key stratum, the deformation and failure of the roof are well controlled, and the development of cracks in the strata is relatively smooth. Meanwhile, the water-conducting fracture zone could not be effectively connected, which could effectively reduce the risk of roof collapse, thus reducing the possible of mine water hazard. Under the influence of faults, the roof displacement of the key stratum can vary, and three separation zones can be rapidly formed above the key stratum. The integrity of roof strata is destroyed, cracks develop, and the height of the developed water-conducting fracture is 2-3 times that of the water-conducting fracture without the influence of faults, which accelerates the formation of water inrush channels and increases the risk of a sudden influx of water from aquifers into the working face. What's more, the closer the key stratum occurs to the fault, the larger the area of the separation zone is and the higher the risk of roof collapse is. The presence of faults significantly weakens the strength of the key stratum, greatly reduces the control effect of the key stratum on the water-conducting fracture zone, increases the damage range of the roof both horizontally and longitudinally, results in the roof most obviously sinking near the fault layer, and forms a high-stress area in the unmined roof, which creates concealed conditions for water inrush accidents at the later stage.

*4.4. Damage and Failure Characteristics of the Surrounding Rock of the Roof Fault.* The acoustic emission (AE) technique is an effective method to measure the deformation and failure of rock masses, so as to effectively reflect the failure process of coal roof. In the AE event diagram, the red unit indicates tensile damage, the white unit indicates compression damage, and the black unit indicates cumulative AE damage. As shown in Figure 7(a), when the working face occurs far from the fault, the roof of the goaf is not damaged, and successive AE events of compressive and tensile failure occur uniformly. As the working face was advanced, roof delamination damage was observed, roof pressure damage reduction occurred due to the overburden, and the AE events mainly indicated tensile damage. In the process of

local damage to the surrounding rock, acoustic emission events were continuously developed in the deep surrounding rock, the AE event increment under excavation was less than 30, and the AE accumulative curve smoothly increased throughout the process. As shown in Figure 7(b), when the working face was advanced beneath the fault, the number of AE events in the fault increased to 52, and the single-step AE energy reached 156 J. Due to the insufficient bearing capacity of the fault itself, AE events mainly increased within the fault, tensile failure events largely occurred, and a small number of compressive failure events emerged at both ends of the fault. As shown in Figure 7(e), the upper part of the fault is controlled by the key stratum, and energy release is inhibited. The single-step AE energy is reduced to 86 J, AE events slowly accumulate, and the cumulative AE curve is relatively flat. With progression of the mining process, detachment occurs beneath the key stratum. When the energy accumulated in the upper part of the fault reaches a certain value, energy is first released through detachment, and AE events tend to develop toward detachment. Since the key stratum is not significantly damaged, AE events are longitudinally prevented from penetrating into the surrounding rock, and only sporadic AE events occur at the depth of the surrounding rock. As the stress in the surrounding rock at the bottom of the fault changes, AE events continue to accumulate and laterally expand along the working face. As shown in Figure 7(c), after AE events at the bottom of the fault were extended laterally across a certain distance, these AE events changed direction and followed longitudinal mining surface extension. Affected by the fault, when the working face passed beyond 20 m of the fault (Figure 7(d)), a large area of damage occurred in the key stratum, the number of AE events rapidly surged to 1530, thereby rapidly expanding toward the aquifer, and energy was concentrated in the interface area of the rock strata. However, the goaf is only affected by mining at the early stage, and the key stratum imposes a suitable control effect. Only an AE accumulation zone is formed below the key stratum, and a few AE events are distributed in the deep surrounding rock at the 0 m level. Fault activation exerts a weakening effect on the surrounding rock, which greatly increases the possibility of the formation of a water-conducting fracture zone.

*4.5. Seepage Field Evolution of the Surrounding Rock in the Roof.* The simulation results of the hydraulic gradient were analyzed (Figure 8). Under the influence of mining, the roof at the center of the goaf collapsed, along with the generation of scattered damage units, the hydraulic gradient curve expanded toward the roof in the middle of the goaf, but the key stratum exerted a satisfactory control effect on fracture development, and the overall hydraulic gradient curve was characterized by a small amplitude and uniform downward extension. When roof damage occurs, as shown in Figure 8(b), the water gradient curve continues below the scattered distribution of the failure unit, the hydraulic gradient curve is relatively smooth but now continues below the heading toward the fault, i.e., fault activation occurs, and

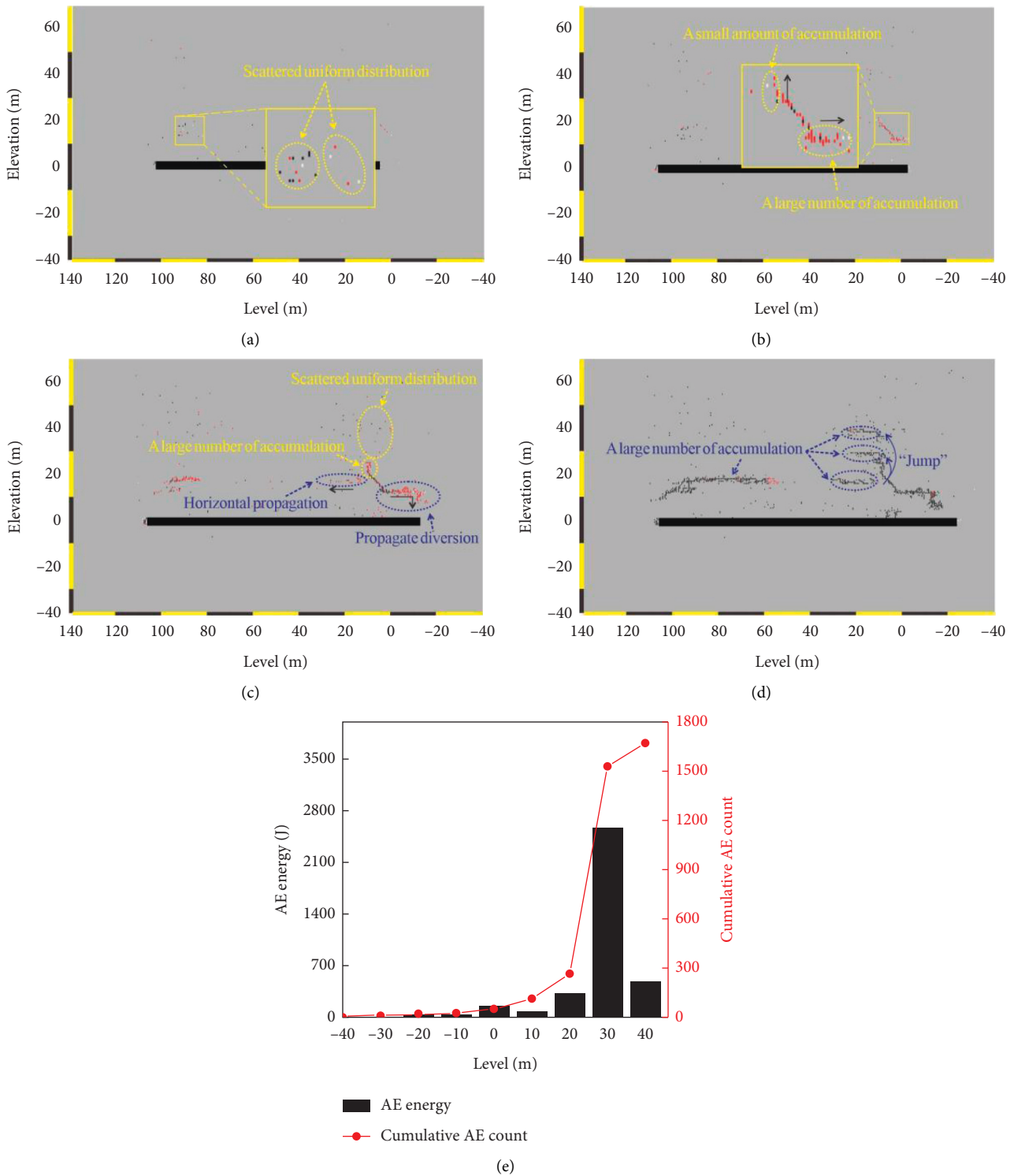


FIGURE 7: Analysis of the observed AE phenomena.

the hydraulic gradient curve changes along the direction of the fault, suggesting that fault activation seriously affects the distribution of the seepage field in the surrounding rock. At 10 m across the fault (Figure 8(c)), a wide range of fracture zones is formed in front and at the rear of the goaf. Through comparison of the front and rear of the goaf, it can be found that although the roof is significantly damaged, the front

goaf experiences uniform change, while the rear goaf occurs under the influence of the fault. Moreover, the key stratum is damaged, and a water-conducting fracture zone is rapidly formed. The seepage gradient in the rock sharply increases, the water-conducting fracture zone becomes connected with the aquifer and working face, a seepage path is established, seepage fluid softens the rock mass around the fracture, and

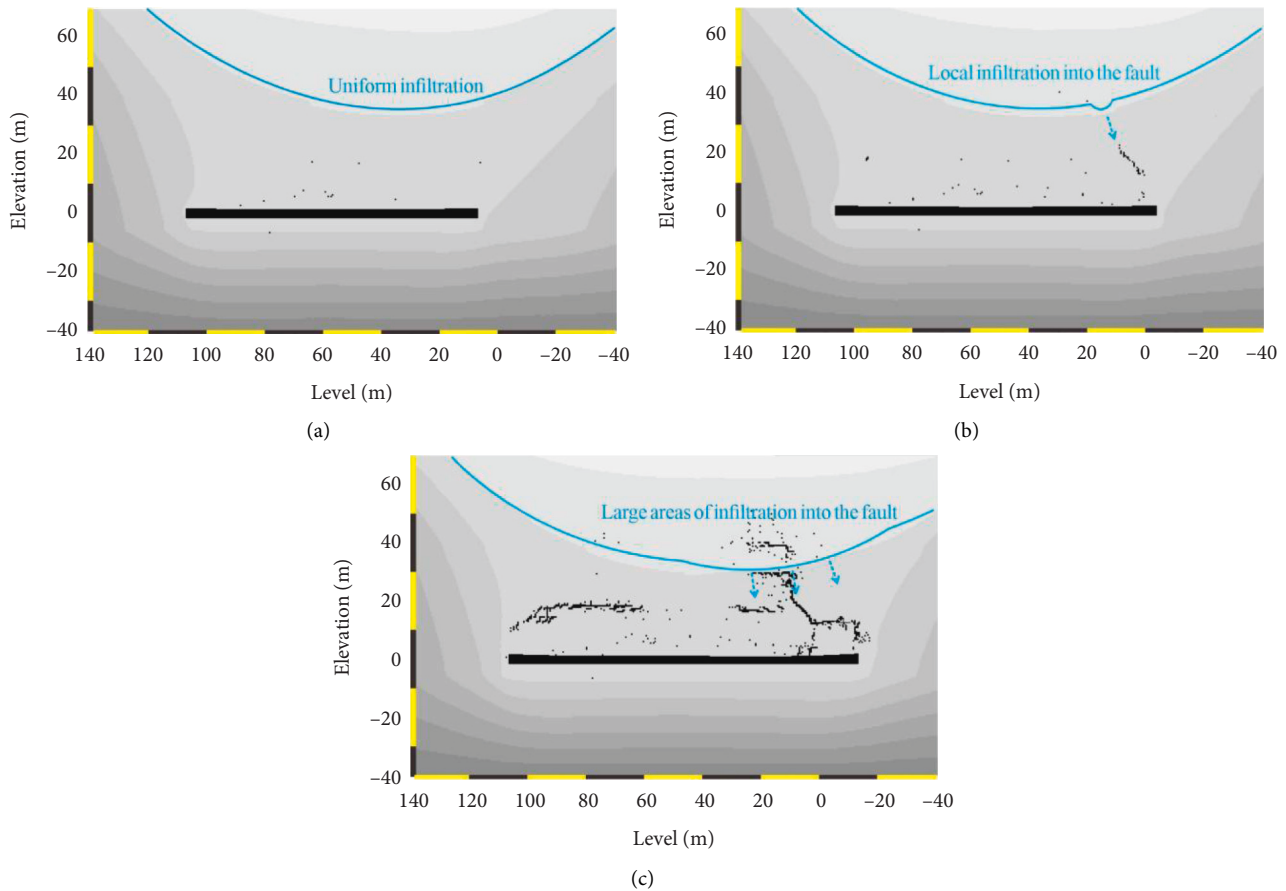


FIGURE 8: Diagram of hydraulic gradient evolution.

a water inrush accident occurs. In addition, the fault causes the roof in the eastern mining area to form a high-water pressure area, which reduces the security of later production.

### 5. Measurement of the Water-Conducting Fracture Zone and Analysis of Water Inflow in the Working Face

The high-density electrical method combined with geological data retrieved from the ZK2-5 borehole column chart was used to carry out transverse and longitudinal geophysical projections. The geophysical interpretation results are shown in Figure 9.

The above geophysical images show that the fracture zone in the mining area is irregularly developed, and concealed karst water may be widely distributed. A low-resistance zone is distributed sporadically from 0–640 m along the material detection line, which mainly involves a fissure in the Yelang Formation karst aquifer and is speculated to be a local fissure attributed to caving of the goaf roof at the early stage. At the position of the survey line from 631–1000 m, there is a strip-shaped low-resistivity anomaly, which is a fracture in the Changxing Formation aquifer. At the location of the water gushing accident in the 800 m working face, there occurs a funnel-shaped low-resistivity area, and the

lower part of the low-resistivity area tends to be connected with the coal seam, which is speculated to be the water-conducting fracture zone in the working face and Changxing Formation aquifer. By analyzing the 600–900 m position in the mining area of the working face, it can be found that when the working face occurs 600–750 m from the fault, the resistance value does not change significantly, and there are no numerous fractures. The key stratum suitably controls fracture expansion. When the working face is located near 800 m (below the fault), the fissure rapidly expands, and a fissure zone is formed within a large area, generating a large funnel-shaped low-resistance area. The regional vertical distance is approximately 60 m and is tilted toward the east. This indicates that after the working face passes through the fault, the fault continuously influences the surrounding rock fissures, and stress concentration increases the extension range of the surrounding rock fissures behind the fault.

According to Figure 10, when the working face occurred 50 m from the fault on May 18, 2019, the water outflow remained stable, and the water inflow reached approximately 40 m<sup>3</sup>/h. On June 19, the mining face passed the fault by 10 m, and a large amount of water gushing suddenly occurred in the roof of the goaf, with the water amount reaching approximately 240 m<sup>3</sup>/h (i.e., the 1# water inrush point). To ensure the safety of the working face, slow manual advancement should occur. From July 22 to August 6, 30 m

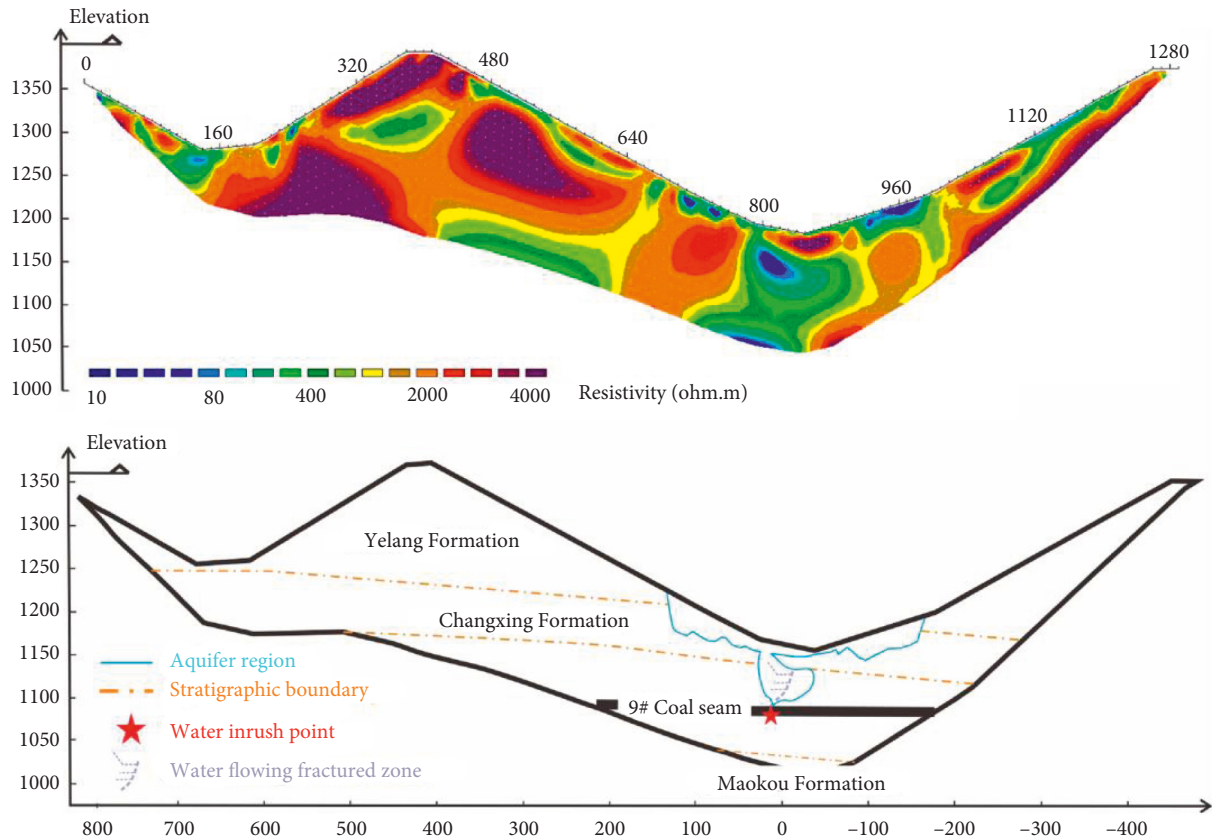


FIGURE 9: Image of the resistivity formation profile.

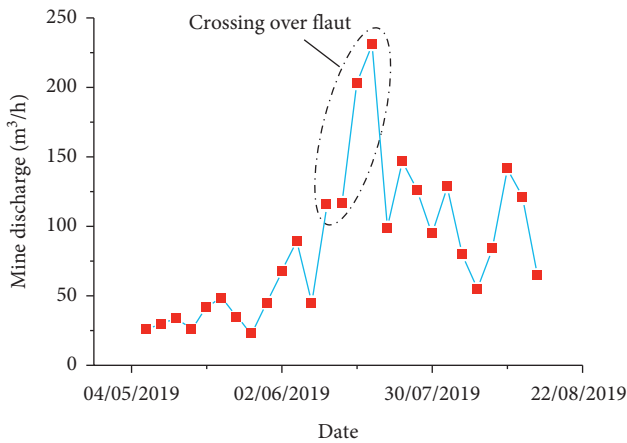


FIGURE 10: Overview of water gushing in the working face.

through the fault, roof water inrush and slurry collapse events occurred several times in the 13–24 m section of the working face, and the roof of the working face collapsed. Each water inrush accident generated an inflow of 132 m<sup>3</sup>/h, accompanied by a gap at the support (i.e., the 2# water inrush point). The whole water inrush process was uniform before crossing the fault and surged after the fault. Combined with the above numerical analysis, it could be concluded that at the early stage of uniform water inrush, the surrounding rock was broken due to its proximity to the structural area, tectonic stress, and mining pressure, but the

surrounding rock of the working face did not produce a plastic zone connected with the aquifer, resulting in a small amount of consistent water seepage. Ten meters passed the fault, the sudden jump phenomenon occurred in the water-conducting fracture zone, and karst water quickly gushed out of the working face, resulting in a sudden surge in water. At 30 m after the fault, frequent and notable water gushing occurred due to the formation of a high-stress water pressure concentration area in the working face, resulting in multiple water gushing events accompanied by slurry collapse, which is consistent with the evolution trend of the roof fracture zone in the numerical simulations.

In summary, the key stratum exerts a good control effect on the stability of the roof of the surrounding rock. In the absence of structural influence, the development height of the fracture zone is 25 m, and no water inrush accidents occur. Later, due to the influence of faults, the control effect of key strata is weakened, the height of the fracture zone increases to 60 m, and the water inflow increases greatly. Therefore, it necessary to prospect the geological structure of working face in advance. In view of the situation that the working face encounters faults, special mining scheme should be formulated to reduce the stress concentration near the fault and prevent the occurrence of water inrush accident.

### 6. Conclusion

- (1) Through a geological survey, it was found that there is a fault zone in the east of mining face 5914. Based

on the key stratum theory, the fine sandstone layer above the no. 9 coal seam was identified as the key stratum, and the water hazard source was determined as the Changxing Formation aquifer via hydrochemistry.

- (2) The numerical simulation results of RFPA-flow show that without the influence of faults, the AE events were evenly distributed within a small range in the deep surrounding rock due to the presence of key layers. With the tunneling of the working face, the shear stress concentration phenomenon appears below the key strata, and deformation occurred at the center of the roof. The fracture zone gradually formed a separation zone below the key stratum, and the final fracture height reached approximately 25 m.
- (3) Under the action of fault weakening, AE events at the early stage converged at the hinge point of the fault and key stratum and then rapidly expanded both horizontally and longitudinally. The number of AE events surged to 1150, and the observed fissures were consistent with the AE phenomenon. Moreover, the sudden jump phenomenon occurred vertically, after which the fissures quickly penetrated the aquifer and formed a water-conducting fissure zone. The height reached 60 m, which is 2~3 times as high as that in the case of no faults.
- (4) In the process of working face tunneling, the hydraulic gradient curve is characterized by small amplitude and uniform downward extension due to the existence of key strata. However, when the working face is driven to the affected area of the fault, the hydraulic gradient curve extends to the working face in a large area, which increase the risk of water damage accidents in the later period.

## Data Availability

Some or all data, models, or codes generated or used during the study are available from the corresponding author upon request.

## Conflicts of Interest

The authors announced that there are no conflicts of interest regarding the publication of this paper.

## Acknowledgments

This work was supported by the National Natural Science Foundation of China (No. 52164006), Guizhou Provincial Science and Technology Projects (No. [2022]248), the National Natural Science Foundation for Young Teachers of Guizhou University (No. [2020] 81), and Risk Assessment of Water Hazard in No. 13 Coal Seam Floor in No. 2 Mining Area of Longfeng Coal Mine and Research on Water Prevention and Control Measures (No. K21-0111-025).

## References

- [1] W. J. B. Sun, Y. J. Zuo, S. Y. Wang et al., "Pore structures of shale cores in different tectonic locations in the complex tectonic region: a case study of the Niutitang Formation in Northern Guizhou, Southwest China," *Journal of Natural Gas Science and Engineering*, vol. 80, Article ID 103398.
- [2] X. G. Cheng, W. Qiao, G. F. Li, and Z. Yu, "Risk assessment of roof water disaster due to multi-seam mining at Wulunshan Coal Mine in China," *Arabian Journal of Geosciences*, vol. 14, no. 12, p. 1116, 2021.
- [3] B. Kong, Z. Y. Cao, T. Sun, C. Qi, and y. Zhang, "Safety Hazards in Coal Mines of Guizhou China during 2011–2020," *Safety Science*, vol. 145, Article ID 105493, 2022.
- [4] S. H. Prassettyo and M. Gutierrez, "Effect of transient coupled hydro-mechanical response on the longitudinal displacement profile of deep tunnels in saturated ground," *Tunnelling and Underground Space Technology*, vol. 75, pp. 11–20, 2018.
- [5] F. Song, A. Rodriguez-Dono, and S. Olivella, "Hydro-mechanical modelling and analysis of multi-stage tunnel excavations using a smoothed excavation method," *Computers and Geotechnics*, vol. 135, Article ID 104150.
- [6] W. J. Yu, W. J. Wang, G. S. Wu, X. Yu, and W. Peng, "Three zones and support technique for large section incline shaft crossing goaf," *Geotechnical & Geological Engineering*, vol. 35, no. 5, pp. 1921–1931, 2017.
- [7] L. Q. Shi, X. Y. Qu, X. G. Yu et al., "Theory and practice on the division of the "water pressure-free zone" in a mining coal seam floor," *Arabian Journal of Geosciences*, vol. 13, no. 20, p. 1079, 2020.
- [8] J. L. Xie and J. L. Xu, "Effect of key stratum on the mining abutment pressure of a coal seam," *Geosciences Journal*, vol. 21, no. 2, pp. 267–276, 2017.
- [9] Y. P. Liang, B. Li, and Q. L. Zou, "Movement type of the first subordinate key stratum and its influence on strata behavior in the fully mechanized face with large mining height," *Arabian Journal of Geosciences*, vol. 12, no. 2, p. 31, 2019.
- [10] B. Li, Y. P. Liang, and Q. L. Zou, "Determination of working resistance based on movement type of the first subordinate key stratum in a fully mechanized face with large mining height," *Energy Science & Engineering*, vol. 7, no. 3, pp. 777–798, 2019.
- [11] H. D. Duan, S. Y. Zhu, S. W. Cao, and M. Zhang, "Safe feasibility of retaining sand-proof coal rock pillars in full-mechanized caving mining of extra-thick coal seam," *Arabian Journal of Geosciences*, vol. 14, no. 9, p. 778, 2021.
- [12] T. J. Kuang, Z. Li, W. B. Zhu et al., "The impact of key strata movement on ground pressure behaviour in the Datong coalfield," *International Journal of Rock Mechanics and Mining Sciences*, vol. 119, pp. 193–204, 2019.
- [13] T. Zhang, Q. Gan, Y. X. Zhao et al., "Investigations into mining-induced stress–fracture–seepage field coupling effect considering the response of key stratum and composite aquifer," *Rock Mechanics and Rock Engineering*, vol. 52, no. 10, pp. 4017–4031, 2019.
- [14] J. Sun and X. X. Miao, "Water-isolating capacity of an inclined coal seam floor based on the theory of water-resistant key strata," *Mine Water and the Environment*, vol. 36, no. 2, pp. 310–322, 2017.
- [15] Y. J. Zhou, M. P. Li, X. D. Xu, and M. Li, "A study on dual-load-zone model of overlying strata and evolution law of mining stress," *Computers, Materials & Continua*, vol. 58, no. 2, pp. 391–407, 2019.

- [16] W. G. Du, J. Chai, D. D. Zhang, and W. Lei, "The study of water-resistant key strata stability detected by optic fiber sensing in shallow-buried coal seam," *International Journal of Rock Mechanics and Mining Sciences*, vol. 141, p. 104604.
- [17] Z. H. Wu, M. T. Tang, Y. J. Zuo et al., "Acoustic Emission-Based Numerical Simulation of Tectonic Stress Field for Tectoclase Prediction in Shale Reservoirs of the Northern Guizhou Area, China," *Energy Geoscience*.
- [18] W. J. Sun, W. F. Zhou, and J. Jiao, "Hydrogeological classification and water-inrush accidents in China's coal mines," *Mine Water and the Environment*, vol. 35, no. 2, pp. 214–220, 2016.
- [19] J. J. Zhang, K. J. Xu, G. Reniers, and G. You, "Statistical analysis the characteristics of extraordinarily severe coal mine accidents (ESCMAs) in China from 1950 to 2018," *Process Safety and Environmental Protection*, vol. 133, pp. 332–340, 2020.
- [20] J. H. Zhao, L. Bo, C. Juntao, and J. Ning, "Mechanism of seepage-stress fault water-inrush and grouting seal," *Arabian Journal of Geosciences*, vol. 13, no. 11, p. 404, 2020.
- [21] Y. Wang, W. K. Feng, and C. H. Li, "On anisotropic fracture and energy evolution of marble subjected to triaxial fatigue cyclic-confining pressure unloading conditions," *International Journal of Fatigue*, vol. 134, p. 105524.
- [22] Y. Wang, D. Q. Liu, J. Q. Han, C. Li, and H. Liu, "Effect of fatigue loading-confining stress unloading rate on marble mechanical behaviors: an insight into fracture evolution analyses," *Journal of Rock Mechanics and Geotechnical Engineering*, vol. 12, no. 6, pp. 1249–1262, 2020.
- [23] W. B. Sun, Y. C. Xue, T. T. Li, and W. Liu, "Multi-field coupling of water inrush channel formation in a deep mine with a buried fault," *Mine Water and the Environment*, vol. 38, no. 3, pp. 528–535, 2019.
- [24] H. Liu, Y. J. Zuo, Z. H. Wu et al., "Fractal analysis of mesoscale failure evolution and microstructure characterization for sandstone using DIP, SEM-EDS, and micro-CT," *International Journal of Geomechanics*, vol. 21, no. 9, 2021.
- [25] H. Liu, L. L. Zheng, Y. J. Zuo et al., "Study on mesoscopic damage evolution characteristics of single joint sandstone based on micro-CT image and fractal theory," *Shock and Vibration*, pp. 1–18, Article ID 6547028, 2021.
- [26] K. Ma, F. Z. Yuan, D. Y. Zhuang, Q. Li, and Z. Wang, "Study on rules of fault stress variation based on microseismic monitoring and numerical simulation at the working face in the dongjiahe coal mine," *Shock and Vibration*, pp. 1–12, 2019.
- [27] X. Yu, K. Zhao, Q. Wang et al., "Relationship between movement laws of the overlaying strata and time space of the mined-out," *Geofluids*, 2020.
- [28] L. Y. Zhang, Z. Q. Qu, Y. Chen et al., "Numerical simulation of hydro-force coupled crack propagation," *Fresenius Environmental Bulletin*, vol. 28, pp. 4923–4934, 2019.
- [29] J. N. Wang, W. T. Liu, and J. J. Shen, "Investigation on the fracturing permeability characteristics of cracked specimens and the formation mechanism of inrush channel from floor," *Shock and Vibration*, vol. 2021, pp. 1–12.
- [30] J. L. Xu, W. Qin, and D. Y. Xuan, "Accumulative effect of overburden strata expansion induced by stress relief," *Journal of China Coal Society*, vol. 45, no. 1, pp. 35–43, 2020.
- [31] X. Y. Qin, Y. H. Zhang, and Z. A. Huang, "Breaking mechanism and control technology of hard roof in deep and thin coal seam protective layer," *Journal of Central South University*, vol. 52, no. 11, pp. 4010–4020, 2021.
- [32] X. X. Men, C. A. Tang, Z. Han, and T. Ma, "Numerical simulation to influence of perforation angle on fracture propagation under hydraulic fracturing," *Journal of Northeastern University*, vol. 34, no. 11, pp. 1638–1641, 2013.
- [33] T. H. Yang, C. A. Tang, and W. C. Zhu, "Coupling analysis of seepage and stresses in rock failure process," *Chinese Journal of Geotechnical Engineering*, vol. 4, pp. 489–493, 2001.
- [34] T. H. Yang, C. A. Tang, and H. Y. Liu, "Numerical model of the instability-failure process of the coal-bed floor due to confined water-inrush," *Journal of Geomechanics*, vol. 3, pp. 281–288, 2003.
- [35] G. H. Zou, C. Zhang, and D. Tian, "Study on the formation mechanism of water conducting channel of overburden strata crossing fault Group in fully mechanized caving face," *Metal Mine*, vol. 5, pp. 65–70, 2021.
- [36] K. Yang and S. Liu, "Rule of multi-key strata movement-fracture evolution-dynamics of gas emission in deep long distance lower protective layer mining," *Journal of Mining & Safety Engineering*, vol. 37, no. 5, pp. 991–1000, 2020.